



HAL
open science

How are stars born?: The second gravitational collapse and its consequences

Adnan Ali Ahmad

► **To cite this version:**

Adnan Ali Ahmad. How are stars born?: The second gravitational collapse and its consequences. Astrophysics [astro-ph]. Université Paris Cité, 2024. English. NNT : 2024UNIP7012 . tel-04886879

HAL Id: tel-04886879

<https://theses.hal.science/tel-04886879v1>

Submitted on 14 Jan 2025

HAL is a multi-disciplinary open access archive for the deposit and dissemination of scientific research documents, whether they are published or not. The documents may come from teaching and research institutions in France or abroad, or from public or private research centers.

L'archive ouverte pluridisciplinaire **HAL**, est destinée au dépôt et à la diffusion de documents scientifiques de niveau recherche, publiés ou non, émanant des établissements d'enseignement et de recherche français ou étrangers, des laboratoires publics ou privés.



UNIVERSITÉ PARIS CITÉ

CEA Saclay, Département d'Astrophysique
Laboratoire de Modélisation des Plasmas Astrophysiques
École doctorale STEP'UP (560)

How are stars born? The second gravitational collapse and its consequences

Par **ADNAN ALI AHMAD**

Thèse de doctorat de **PHYSIQUE DE L'UNIVERS**

Dirigée par **MATTHIAS GONZÁLEZ**

Et par **PATRICK HENNEBELLE**

Présentée et soutenue publiquement le 30/09/2024

Devant un jury composé de :

PR. ROMAIN TEYSSIER
PR. ROLF KUIPER
PR. CORINNE CHARBONNEL
CR EVELYNE ALECIAN
PR. MATTHIAS GONZÁLEZ
DR PATRICK HENNEBELLE

Princeton University
University of Duisburg-Essen
Observatoire de Genève
CNRS
Université Paris Cité
CEA

Rapporteur
Rapporteur
Examinatrice
Examinatrice
Directeur de thèse
Directeur de thèse

Résumé / Abstract

Titre: Comment les étoiles se forment-elles ? Le second effondrement et ses conséquences

Mots clefs: formation stellaire ; étoile ; disque ; accretion ; radiation ; gravité ; turbulence ; champ magnétique

Résumé: Les étoiles se forment à la suite de l'effondrement de cœurs denses gravitationnellement instables. Ce processus, bien qu'il se soit produit d'innombrables fois dans l'Univers, reste mal compris en raison des défis liés à l'observation des régions de formation d'étoiles, ainsi que des difficultés théoriques associées à la modélisation d'un processus hautement non linéaire dans lequel l'hydrodynamique autogravitante, les champs magnétiques, le transfert radiatif et la turbulence se produisent tous simultanément et présentent un réseau complexe d'interactions. À cet égard, les simulations numériques ont offert des informations inestimables qui ont ouvert la voie à une grande partie de notre compréhension dans ce domaine. Plus particulièrement, ceux-ci ont révélé une séquence évolutive en deux étapes dans laquelle se forme un premier cœur en équilibre hydrostatique, qui lui-même s'effondre à nouveau pour former une protoétoile. Ce deuxième effondrement gravitationnel est un processus hautement dynamique et, en tant que tel, constitue une entreprise difficile d'un point de vue numérique. Au cours de ma thèse, j'ai réalisé des simulations magnétohydrodynamiques résistives radiatives de pointe de l'effondrement de cœurs denses turbulents jusqu'à des densités stellaires. La plage dynamique impliquant 25 ordres de grandeur en densité et 8 en étendue spatiale est abordée avec le code de maillage adaptatif RAMSES. Les propriétés de la protoétoile nouvellement née et celles de son disque circumstellaire sont

étudiées avec un niveau de détails sans précédent, et les calculs vont au-delà de nombreux articles antérieurs. Je présenterai les informations que nous avons acquises sur certaines questions majeures liées à la formation des étoiles grâce à ces simulations. Tout d'abord, j'ai effectué des calculs d'hydrodynamique radiative en symétrie sphérique dans le but d'étudier les propriétés et le comportement de la protoétoile, où j'ai constaté qu'elle était turbulente à la naissance malgré sa stabilité aux mouvements convectifs. Cela est dû à une instabilité au niveau du choc d'accrétion qui se déclenche peu après la naissance de la protoétoile. La turbulence est ensuite entretenue par l'accrétion. Cela a des implications sur les modèles d'évolution pré-stellaire, ainsi que sur l'évolution du champ magnétique implanté dans la protoétoile à la naissance. À la suite de cela, j'ai réalisé des simulations avec de la turbulence dans le cœur dense initial, qui conduisent à la formation de disques circumstellaires entourant la protoétoile. Les propriétés du disque naissant, ainsi que son évolution dans le temps, sont étudiées en détail. De manière remarquable, nous constatons qu'un disque circumstellaire se forme suite à la rupture rotationnelle de la protoétoile lorsqu'elle accrete rapidement les matériaux de son environnement. Enfin, j'ai réalisé des simulations prenant en compte les champs magnétiques, qui modifient drastiquement la dynamique du gaz par freinage magnétique. Nous constatons qu'un champ magnétique d'un kilogauss est implanté dans

la protoétoile à la naissance, et malgré le freinage magnétique, elle atteint néanmoins la vitesse de rupture et forme un disque circumstellaire. La magnétisation du disque provoque un transport efficace du moment cinétique, ce qui conduit à des propriétés du disque différentes de celles des essais hydro-

Résumé substantiel: Les étoiles se forment à la suite de l'effondrement de cœurs denses gravitationnellement instables. Ce processus, bien qu'il se soit produit d'innombrables fois dans l'Univers, reste mal compris en raison des défis liés à l'observation des régions de formation d'étoiles, ainsi que des difficultés théoriques associées à la modélisation d'un processus hautement non linéaire dans lequel l'hydrodynamique auto-gravitante, les champs magnétiques, le transfert radiatif et la turbulence se produisent tous simultanément et présentent un réseau complexe d'interactions. À cet égard, les simulations numériques ont offert des informations inestimables qui ont ouvert la voie à une grande partie de notre compréhension dans ce domaine. Plus particulièrement, ceux-ci ont révélé une séquence évolutive en deux étapes dans laquelle se forme un premier cœur en équilibre hydrostatique, qui lui-même s'effondre à nouveau pour former une protoétoile. Ce second effondrement gravitationnel est un processus hautement dynamique et, en tant que tel, constitue un défi d'un point de vue numérique.

Au cours de ma thèse, j'ai réalisé des simulations magnétohydrodynamiques résistives radiatives de pointe de l'effondrement de cœurs denses turbulents jusqu'à des densités stellaires. La plage dynamique impliquant 25 ordres de grandeur en densité et 8 en étendue spatiale est abordée avec le code de maillage adaptatif RAMSES. Les propriétés de la protoétoile et celles de son disque circumstellaire sont étudiées avec un niveau de détails sans précédent, et les calculs vont au-delà de nombreux articles antérieurs. Je présenterai les informations que nous avons acquises sur certaines questions majeures liées à la formation stellaire grâce à ces simulations.

dynamiques. Ces résultats ont mis en lumière les plus petites échelles spatiales pertinentes pour la formation et l'évolution des disques protostellaires et circumstellaires, approfondissant ainsi notre compréhension des objets qui deviendront plus tard des systèmes planétaires.

Tout d'abord, j'ai effectué des calculs d'hydrodynamique radiative en symétrie sphérique dans le but d'étudier les propriétés et le comportement de la protoétoile, où j'ai constaté qu'elle était turbulente à la naissance malgré sa stabilité aux mouvements convectifs. Cela est dû à une instabilité au niveau du choc d'accrétion qui se déclenche peu après la naissance de la protoétoile. La turbulence est ensuite entretenue par l'accrétion. Cela a des implications sur les modèles d'évolution pré-stellaire, ainsi que sur l'évolution du champ magnétique implanté dans la protoétoile à sa naissance. Nous avons également étudié le comportement de la protoétoile dans les mois qui suivent sa naissance, ainsi que celui de son choc d'accrétion radiatif. À la suite de la formation de la protoétoile, son rayon augmente rapidement au fil du temps. Cela est dû à la nature sous-critique de son choc d'accrétion, qui peine à évacuer l'énorme quantité d'énergie cinétique injectée par accrétion. Cependant, à mesure que la proto-étoile gonfle, la densité (et donc la profondeur optique) du choc d'accrétion diminue de manière continue, ce qui augmente son efficacité radiative. Nous constatons également que la protoétoile n'est pas complètement ionisée à la naissance. Cependant, à mesure que la protoétoile accrete du matériau de son environnement, la quantité de masse sous forme ionisée en son sein augmente de manière continue au fil du temps. Par conséquent, la conductivité électrique de la proto-étoile augmente avec le temps. De plus, nous estimons que la dissociation de l'hydrogène moléculaire et l'ionisation de l'hydrogène atomique et de l'hélium ne représentent qu'environ 6 % de l'énergie totale injectée par l'accrétion. Ainsi, la consom-

mation d'énergie de ces processus joue un rôle insignifiant dans la régulation du rayon de la protoétoile. Néanmoins, nous prévoyons que la haute conductivité électrique de la protoétoile, combinée à la turbulence dans son intérieur, pourrait modifier de manière significative son champ magnétique, même avant le début de la combustion du deutérium.

À la suite de ces simulations à symétrie sphérique, j'ai réalisé des simulations avec de la turbulence dans le cœur dense initial, ce qui conduit à la formation de disques circumstellaires entourant la protoétoile. Les propriétés du disque naissant, ainsi que son évolution dans le temps, sont étudiées en détail. De manière remarquable, nous constatons qu'un disque circumstellaire se forme à la suite de la rupture rotationnelle de la protoétoile lorsqu'elle accrete rapidement les matériaux de son environnement. Ce disque nouvellement formé est chaud, dense, très turbulent et évolue dans des délais très courts en raison des taux d'accrétion élevés. La protoétoile est enfouie dans ce disque et aucun front de choc ne sépare les deux. À mesure que l'accrétion se poursuit, le disque engloutit complètement la protoétoile et se propage vers l'extérieur en raison d'une quantité de moment cinétique excessif, ainsi que l'accrétion. La masse du disque dépasse celle de la protoétoile d'un facteur ≈ 7 , ce qui signifie que la majorité de la masse après le second effondrement gravitationnel réside dans le disque et que son autogravité domine la dynamique du gaz en son sein. La pression thermique apporte également une contribution notable sur la dynamique. Dans le cas où un disque externe existe avant le second effondrement, ce disque circumstellaire se forme à l'intérieur de celui-ci, et les deux fusionnent après que le disque interne s'étend sur des rayons suffisamment grands. Malgré les différentes histoires évolutives à des échelles spatiales plus grandes, la structure du disque et de l'étoile formée à la suite du second effondrement gravitationnel est identique, mais nous remarquons néanmoins une légère dispersion causée par les conditions initiales turbulentes. Cela est dû à la formation du pre-

mier cœur de Larson dans toutes nos simulations, un objet à l'équilibre hydrostatique qui garantit que le second effondrement se produira dans des conditions à peu près similaires. L'existence d'un disque circumstellaire permet également de créer une cavité au niveau des régions polaires. Cette cavité permet à la protoétoile de rayonner dans un milieu optiquement mince, permettant ainsi à son choc d'accrétion d'atteindre un régime supercritique en ~ 2 ans et de rayonner la grande majorité de son énergie d'accrétion. Grâce à l'analyse physique du front de choc dans nos simulations, l'hypothèse ad hoc d'un choc d'accrétion rayonnant la majorité de l'énergie entrante, qui est utilisée dans les modèles d'évolution préstellaire pour accorder leurs prédictions aux observations, s'est désormais avérée vraie. Quant à la structure du système, afin de découpler physiquement la protoétoile de son disque et de réduire sa vitesse de rotation aux valeurs observées, les mécanismes de freinages doivent transporter une quantité suffisante de moment cinétique de l'intérieur du disque vers l'extérieur. Les champs magnétiques sont susceptibles de jouer ce rôle.

Enfin, j'ai réalisé des simulations prenant en compte les champs magnétiques, qui modifient drastiquement la dynamique du gaz par freinage magnétique. Conformément aux résultats précédents de la littérature, l'approximation MHD idéale conduit à un freinage magnétique très efficace qui empêche la formation d'un disque circumstellaire (c'est ce que l'on appelle la catastrophe du freinage magnétique). Le résultat du second effondrement gravitationnel serait donc une accumulation centrale et sphérique de matière qui conduit à la naissance d'une protoétoile sphérique, avec des nappes de courant dépassant de la surface stellaire. Les propriétés de la protoétoile naissante sont similaires à celles obtenues dans des simulations hydrodynamiques à symétrie sphérique. La protoétoile présente également un intérieur très fortement turbulent. Lorsque l'on tient compte de la diffusion ambipolaire, l'efficacité du freinage magnétique est considérablement

réduite vers le gaz à haute densité, ce qui permet à la protoétoile nouvellement née d'atteindre la vitesse de rupture et de se débarrasser d'une partie de son matériel de surface pour former un disque circumstellaire autour d'elle. La protoétoile est enfouie dans son disque circumstellaire, dont la naissance et l'évolution sont qualitativement similaires aux simulations RHD que nous avons précédemment effectuées, car le rapport de pression thermique avec les pressions magnétiques à l'intérieur du disque dépasse de loin l'unité. Cependant, la magnétisation du disque provoque un transport efficace du moment cinétique, ce qui conduit à des propriétés quantitatives du disque différentes de celles des simulations hydrodynamiques. Néanmoins, le disque naissant s'étend vigoureusement dans la direction radiale. Ce résultat a des implications pour le problème du moment cinétique, puisque nous montrons que la protoétoile doit atteindre une vitesse de rupture pour former un disque circumstellaire. En tant que tels, les processus de transport du moment cinétique doivent ralentir la protoétoile sur des échelles de temps considérablement plus longues que le temps de chute libre du cœur dense du nuage. Quant à la puissance du champ magnétique implanté dans la protoétoile, nous constatons que celui-ci est de l'ordre du kilogauss. Les études observationnelles récentes sur l'intensité des champs magnétiques dans les jeunes objets stellaires, bien que peu nombreuses en termes de taille d'échantillon, rapportent une valeur moyenne d'un kilogauss et favorisent l'hypothèse d'un champ fossile sur l'origine des champs magnétiques dans les étoiles. Cela signifie que ce dernier est hérité de la naissance protostellaire et que nos simulations du second effondrement gravitationnel sont en accord avec les observations. Afin d'implanter un tel champ dans la protoétoile, le flux magnétique au sein du cœur dense est diffusé par diffusion ambipolaire jusqu'à une valeur de $\sim 0,1$ G au sein du premier cœur de Larson. Après le second effondrement, la limite MHD idéale est retrouvée car toutes les particules de poussière sont sublimées et le gaz commence à

s'ioniser, et la moitié de la masse de la protoétoile se révèle être sous forme ionisée. Une intensité de champ d'environ 0,1 G dans le premier cœur de Larson semble également être en accord avec les mesures paléomagnétiques des météorites du système solaire, les observations de maser d'eau dans les jets protostellaires et en accord avec les études observationnelles de la taille des disques. Ces simulations prenant en compte des champs magnétiques ont montré l'importance de l'inclusion de la diffusion ambipolaire dans les calculs. Si cette dernière n'était pas incluse, la protoétoile serait dépourvue de disque circumstellaire puisqu'elle n'atteint jamais la vitesse de rupture, et elle aurait une intensité de champ magnétique bien supérieure à celle observée dans les jeunes objets stellaires. De plus, les propriétés du disque naissant dans nos simulations MHD sont affectées par les mécanismes de freinages efficaces fournis par le champ magnétique. Ceux-ci transportent une quantité considérable de matière vers la protoétoile, ce qui réduit la densité du disque. Ce résultat a des répercussions sur les simulations à plus grande échelle qui cherchent à simuler des échelles de temps beaucoup plus longues, car elles omettent les régions les plus internes au profit d'une particule puits qui accumule la matière de son environnement avec un seuil d'accrétion donné. Actuellement, lors de la mesure de ce que devrait être ce seuil d'accrétion, nous trouvons une différence d'un ordre de grandeur entre les simulations RHD et MHD, soulignant ainsi la nécessité de résistivités adéquates de la poussière, car elles dictent l'intensité du champ magnétique dont héritent les structures formées après le second effondrement gravitationnel, et par extension, la densité du disque. En résumé, grâce à ces simulations du second effondrement gravitationnel, nous avons acquis des connaissances sur un certain nombre de problèmes imprégnant le domaine de la formation des étoiles. Ces simulations de pointe ont révélé le comportement du gaz aux plus petites échelles spatiales pertinentes à la naissance des étoiles et des disques circumstellaires.

Title: How are stars born? The second gravitational collapse and its consequences

Keywords: star formation; stars; protostars; accretion; disks; turbulence; radiation; magnetic fields

Abstract: Stars form as a result of the collapse of gravitationally unstable molecular cloud cores. This process, despite having occurred countless times in the Universe, remains poorly understood because of the challenges involved in observing star forming regions, as well as the theoretical difficulties associated with modelling a highly non-linear process in which self-gravitating hydrodynamics, magnetic fields, radiative transfer, and turbulence, all play out simultaneously and exhibit a complex web of interactions. In this regard, numerical simulations have offered invaluable insights that have pioneered much of our understanding in the field. Most notably, these have revealed a two-step evolutionary sequence in which a first core in hydrostatic equilibrium forms, which itself collapses to form a protostar. This second gravitational collapse is a highly dynamical process, and as such, is a challenging undertaking from a numerical point of view.

During my thesis, I have carried out state-of-the-art radiative resistive-magnetohydrodynamics simulations of the collapse of turbulent dense cores to stellar densities. The dynamical range involving 25 orders of magnitude in density and 8 in spatial extent is tackled with the adaptive mesh refinement code RAMSES. The properties of the nascent protostar and that of its circumstellar disk are studied in unprecedented detail, and the calculations are pushed beyond many previous papers in the literature in my attempt to model the early main accretion phase. The results of these simulations have offered valuable insights on some of star formation's outstanding issues.

Firstly, I carried out radiative-

hydrodynamics calculations in spherical symmetry with the goal of studying the properties and behavior of the nascent protostar, where I found that it is turbulent at birth despite its stability against convective motion. This is due to an instability at the accretion shock that is triggered shortly following protostellar birth. The turbulence is then sustained by accretion. This has implications for pre-stellar evolutionary models, as well as on the evolution of the magnetic field implanted in the protostar at birth.

Following that, I have carried out simulations with turbulence in the initial dense core, which lead to the formation of circumstellar disks surrounding the protostar. The properties of the nascent disk, as well as its evolution over time, are studied in detail. Remarkably, we find that a circumstellar disk is formed following the rotational breakup of the protostar as the latter rapidly accretes materials from its surroundings.

Finally, I have carried out simulations accounting for magnetic fields, which drastically alter the gas dynamics through magnetic braking. We find that a magnetic field of kilogauss strength is implanted in the protostar at birth, and despite magnetic braking, it nevertheless reaches breakup velocity and forms a circumstellar disk. The magnetization of the disk causes efficient angular momentum transport, which leads to different disk properties than in the hydrodynamical runs.

These state-of-the-art results have shed light on the smallest spatial scales relevant to protostellar and circumstellar disk formation and evolution, thus furthering our understanding of the objects that later become fully-fledged planetary systems.

Tough time never last, only tough people last...

-Demi Demi

Remerciements

This thesis manuscript is the result of a three year endeavor that required a tremendous amount of work. Countless hours were spent discussing ideas with my peers, working through equations on paper and whiteboard, and developing and debugging code that generated a huge amount of data that had to be post-processed and analyzed. Carrying out research in theoretical astrophysics, and particularly in stellar formation theory, requires a huge amount of intellectual effort and institutional support. Behind each published paper is a mountain of labor that is often under appreciated.

In addition to the technical expertise offered by my host team, as well as the accessibility to modern supercomputing hardware, I was immersed in a world of research in which rapid progress is being made. New connections between different physical processes are constantly being drawn, and theoretical models are regularly refined and readjusted in order to conform to new observational constraints. Pushing the boundaries of stellar formation theory necessarily entails that one has access to the immense wealth of knowledge and resources being poured in the field, which stresses the importance of open science policies that greatly facilitate collaborative efforts.

Ultimately, carrying out research depends not only on one's abilities, but also in having the privilege and opportunity to work in the right institutes that can offer the funding required for computing power, instrument access, access to scientific publications, and conference missions. In these regards, I was immensely privileged, as none of the work presented in this thesis would have been possible without them.

Je vais maintenant passer au français pour remercier les personnes avec qui j'ai partagé de très bons souvenirs, à la fois avant et durant la thèse.

Je tiens tout d'abord à remercier mes deux encadrants, Matthias et Patrick, grâce à qui j'ai d'abord obtenu un stage de M2, et qui m'ont ensuite fait confiance pour poursuivre le travail en thèse. Vous m'avez guidé tout le long, du concours à l'école doctorale jusqu'aux répétitions de soutenance, et vous avez fait preuve d'immense générosité. Matthias, tu as été patient et calme avec moi, restant toujours composé, pédagogique, et rationnel lorsque je traçais ma voie (parfois de manière erratique) dans le domaine. Peu de doctorants ont le privilège d'avoir des encadrants qui leurs donnent tant de liberté sur leur sujet, et je t'en remercie. Patrick, tu sais déjà à quel point je suis impressionné par la facilité avec laquelle tu navigues la théorie complexe de formation stellaire, et la rapidité avec laquelle tu parviens à trouver des connections entre des mécanismes physiques. Ta tendance à toujours réfléchir plus grand, à vouloir placer chaque nouveau résultat dans un contexte plus large, est quelque chose qui m'a marqué et que je chercherai toujours à refaire.

Ange, merci d'avoir organisé tant de repas chez toi, d'avoir été à l'écoute lors des moments difficiles, et d'avoir été un soutien vis-à-vis de la situation au proche-orient. Ça m'a beaucoup fait plaisir de pouvoir parler du Liban avec toi.

Je tiens ensuite à remercier les membres de mon équipe LMPA, en commençant par notre cher Thierry. Les innombrables discussions scientifiques que l'on a eues ensemble, allant de la simple thermodynamique à SASI, m'ont toujours passionné. Ton intuition sur la physique est impressionnante, et la rapidité avec laquelle tu t'es amélioré aux échecs me terrifie. Merci, pour toutes ces discussions, pour ta générosité, ton amitié.

Ugo, je ne pense pas que je peux mettre dans de simples mots à quel point tu m'as marqué ces trois dernières années. Tu m'as mis à l'escalade, tu m'as aidé d'innombrables fois pour déboguer RAMSES, et les discussions sur la science que l'on a eu m'ont permis de mieux appréhender le domaine. Tu es mon modèle.

Mes co-bureaux, Valentin et Gabriel, merci pour tous les moments passés ensemble, à la fois au labo et en dehors. Votre soutien, particulièrement cette dernière année durant la rédaction, m'a donné beaucoup de force. Je n'oublierai jamais les délires que l'on a partagés. Je vous souhaite le meilleur pour la suite.

Tine, merci pour tes conseils (mention spéciale à ton goût de colormaps), pour les discussions conviviales lors des pauses de thé/café, ainsi que les moments où l'on a exploré Kyoto ensemble.

Arturo, ta bonne humeur et tes ondes positives m'ont toujours réchauffé le cœur. C'était toujours un plaisir de te voir au labo.

Noé, pour tout ton aide avec les aspects techniques lorsque j'ai débarqué, ainsi que pour ton amitié durant ma première année de thèse.

Anne-Cécile, pour ta bonne humeur et pour tes partages de goûter au labo.

Paul, pour tous les moments que l'on a passés ensemble, ainsi que les discussions politiques.

Tung, pour avoir obtenu le stage auquel j'ai candidaté, ce qui m'a amené à travailler sur mon sujet actuel.

Merci également aux membres de l'équipe objets compact au LMPA ; Mattéo, Raphaël, et Jérôme, pour ces trois années enrichissantes.

Je souhaite également remercier les stagiaires qui sont passés au labo cette dernière année. Pierre-Louis, pour ton amitié et les séances de grimpe. Georges et Solange, pour vos stages enrichissants. Marie, pour ta bonne humeur et tes jolis dessins.

Il y a également les collaborateurs de notre équipe au labo ; Marie-Anne, Maxime et Nacho. Anaëlle, merci pour toutes les discussions sur le côté observationnel qui m'ont été très utiles. Merci également d'avoir été une source d'inspiration pour moi ces trois dernières années ; la facilité avec laquelle tu appréhendes des sujets complexes, ton caractère fort, et ton empathie, m'ont marqué.

Je remercie également les doctorants du laboratoire, avec qui j'ai partagé beaucoup de beaux moments.

Julia, pour ton soutien, ton empathie, ta gentillesse, ton intelligence émotionnelle, et tes gâteaux délicieux.

Loris, pour tous ces beaux moments que l'on a passés ensemble, que ce soit dans le sport ou dans la cuisine. Merci d'avoir été là pour moi dans mes moments difficiles, et

merci également pour le brainrot.

Clara, pour avoir partagé ta joie et ta bonne humeur, et ton amour des chats. Tu m'as soutenu en prêtant ton oreille à de nombreuses reprises cette dernière année, et je t'en remercie.

Achrène, on a partagé trop peu de moments ensemble mais chacun de ces moments restera un souvenir précieux. Ta force, ton intelligence, et ton empathie m'ont beaucoup inspiré.

Jack, on a passé peu de temps ensemble au labo avant ta migration à l'ENS, mais tu as été un bel ami avec qui j'ai beaucoup rigolé (et dérapé).

Leïla, on a fait un beau duo en tant que co-représentant des doctorants. J'ai beaucoup apprécié travailler avec toi, et je suis content que l'on soit devenu amis au fil du temps. Merci d'avoir été le cobaye, avec Fabian, de mes expériences culinaires.

Nicolas, pour avoir partagé ton goût du cinéma, ainsi que d'avoir joué à BAR avec moi.

Tristan, Maxime, Eva, Felipe, Guillaume, Teneman, et Hugo, avec qui j'ai passé des bons moments au labo et en dehors.

Il y a également les amis en dehors du labo, sans qui je serais devenu fou.

Anis, merci pour ton amitié, pour ton soutien, et ton aide durant ces trois dernières années. Ton intelligence et ta persévérance m'ont beaucoup inspiré, et je suis fier de t'appeler mon frère.

Axel, merci pour toutes les fois où j'avais besoin de quelqu'un à qui parler et que tu étais là pour moi. Ton empathie et ta gentillesse brille au point de m'éblouir. Je suis très heureux d'avoir rencontré une des plus belles personnes dans ma vie durant le master à Nice. Je t'aime mon frère.

Amar, merci pour tes conseils, ton écoute, et pour ton honnêteté. Tu m'as rappelé à plusieurs reprises ma valeur, et tu as beaucoup contribué à mes introspections ces deux dernières années.

Sarah, merci pour ta joie, ton humour, ton empathie, et pour toutes les discussions sur l'histoire.

Merci également à toutes les personnes que j'ai rencontré à Nice, après avoir débarqué en France il y a maintenant huit ans.

Héloïse, tu es une des plus belles personnes que j'ai rencontré dans ma vie. Merci pour toutes les fois où tu as demandé mes nouvelles, toutes les fois que tu m'as prêté ton oreille, et merci pour les cookies absolument incroyables. Tu brilles aussi intensément qu'une proto-étoile, et je le dis en tant que spécialiste du sujet.

Kevin, nos innombrables soirées jeux-vidéos sont parmi mes souvenirs préférés ces trois dernières années. Les soirées Divinity, Project Zomboid, Dying Light, et Baldur's Gate 3 était formidables. Cependant, je pense qu'ils l'étaient simplement parce que je les faisais avec toi, et que c'était l'occasion de discuter avec un frère que j'aime beaucoup. Tu es une très belle personne, et j'espère que plus de personnes ai le plaisir de rencontrer le phénomène que tu es.

Juliette, je pense sincèrement que sans ton aide durant la licence je ne serais jamais arrivé là où j'en suis aujourd'hui. Ton intelligence, ta discipline, et ta gentillesse m'ont beaucoup inspiré. Merci également d'avoir partagé mon goût pour l'humour nul, et

pour être aussi passionné que moi du monde du seigneur des anneaux. Les peu de fois que l'on s'est vu durant ces trois ans de thèse m'ont toujours ensoleillé ma journée.

Ines, on n'était pas très amis quand on s'est rencontré mais tu es vite devenue une des plus belles personnes dans ma vie. Je suis très content que l'on ait pu naviguer à travers nos émotions et que l'on ait évolué ensemble ces huit dernières années.

Anthony, merci pour tes innombrables conseils, ta gentillesse, et pour ton oreille toujours prête à écouter. Tu es une belle personne, un frère, avec qui j'ai beaucoup apprécié partager, et j'espère que l'on continuera de partager durant les longues années à venir. Ylan, tu m'as marqué dès notre première rencontre devant l'amphithéâtre de géophysique. Tu m'as beaucoup aidé à être à l'aise avec moi-même, et d'avoir confiance en moi-même. Je te remercie énormément pour ça.

Anastasia, merci pour tous les moments que l'on a passé ensemble à Nice. Tu es une belle personne avec beaucoup d'amour à donner, et ça m'a toujours fait plaisir d'échanger avec toi.

Daniela, thank you for all the moments we have spent together. I'm so happy to have met you during the master's, and the countless hours we spent laughing together were very memorable moments. I hope we get to see each other again in the future.

Jules, mon meilleur ami, tu sais déjà à quel point tu m'as marqué dans la vie, à quel point je suis fier de t'appeler mon frère, à quel point je t'aime. Je ne pense pas que je partage tant de centre d'intérêts avec qui que ce soit d'autre. On a grandi ensemble, évolué ensemble, et on continuera de naviguer la vie ensemble. Merci pour avoir été une constante dans ma vie, et ce depuis le collège.

Abbas, mon grand frère, merci pour ton accueil en France, et pour m'avoir guidé durant mes premières années. J'aurais été perdu sans toi.

أمي وابي ، سندي في كل شي ، هذه أطروحة مخصصة لكم . شكرن لي كل تعبكن ، كول
تضحية ، كل نقطة عرق الذي سماح هذال نجاح . أمي ، حبك الدافئ وتشجيعك أوصلني إلى ما
أنا الآن . أبي ، مروتتك ، تواضعك ، ذكائك ، كرمك ، هي ما يجعلك قدوة لي في الحياة . شكرًا
لكما ، بدونكما لن أكون شيئًا .

Contents

Résumé / Abstract	i
Remerciements	ix
List of figures	xviii
1 The birth of stars - Introduction	1
1.1 Molecular clouds: stellar foundries	2
1.1.1 From clouds to stars	3
1.1.2 Turbulence and its spectra	4
1.2 Gravitational collapse in star forming clouds	4
1.2.1 The empirical sequence	9
1.3 The pivotal role of angular momentum during the collapse	9
1.3.1 Formation of circumstellar disks	11
1.3.2 Transport processes in circumstellar disks	12
1.3.3 Magnetic fields	16
1.4 The magnetic flux problem	23
1.4.1 Observational constraints	23
1.4.2 Magnetic field strength predicted by simulations	25
1.4.3 Fossil field, or dynamo generated?	25
1.5 The luminosity problem	28
1.5.1 Lower accretion rates	29
1.5.2 Protostellar outbursts	30
1.5.3 Radiative efficiency of protostars	31
1.6 This work	31
2 Modelling the star formation process	33
2.1 The fluid equations	33
2.1.1 MHD equations	34
2.1.2 Virial theorem	36
2.1.3 Hydrostatic equilibrium	37
2.2 Radiative transfer	37
2.2.1 Flux limited diffusion approximation	40
2.3 Numerical methods	42
2.3.1 Time discretization	42
2.3.2 Finite volume method	43
2.3.3 Parallel computing	46

2.3.4	The RAMSES astrophysical code	47
2.4	Analyzing and visualizing simulated astrophysical data	49
2.4.1	Parallelized data analysis	49
2.4.2	Coordinate transforms	50
2.4.3	Raycasting	52
2.4.4	3D Visualizations	54
3	The second collapse	61
3.1	The state of the art	61
3.2	Paper I: The nascent protostar	65
3.2.1	Theoretical background: Convective instability	66
3.3	Paper II: Birth of circumstellar disks	92
3.4	MHD simulations	111
3.4.1	Context	111
3.4.2	Numerical setup	114
3.4.3	Large scale structures	114
3.4.4	The second collapse	118
3.4.5	Magnetic field structure	124
3.4.6	Disk expansion: comparison with the hydro case	130
3.4.7	Discussions	132
3.4.8	Conclusion	135
3.5	Miscellaneous results	138
3.5.1	Merger of First Larson cores	138
3.5.2	Multigroup simulations	138
4	Conclusion and Perspectives	141
4.1	The insights gained by second collapse calculations	142
4.2	Perspectives	145
	Appendix A Useful code snippets	147

List of Figures

1.1	Pillars of creation	2
1.2	Schematic overview of the birth of the protostar	7
1.3	The two-step evolutionary sequence	8
1.4	The empirical sequence	10
1.5	Distribution of angular momentum throughout a gravitational collapse	11
1.6	Angular momentum exchange between two annuli	13
1.7	Gravitational instabilities in self-gravitating disks	15
1.8	Observations of magnetic field strengths	17
1.9	MRN resistivities	20
1.10	JWST view of L1527 IRS	21
1.11	Schematic overview of jets and outflows	22
1.12	Observed magnetic field strengths in YSOs	24
1.13	Magnetic field amplification during the collapse	26
1.14	Luminosity distribution of young stellar objects	29
2.1	Frequency integrated opacity table	39
2.2	Schematic representation of the finite volume method	44
2.3	Schematic representation of parallel computing	47
2.4	Example of an AMR grid	48
2.5	Schematic overview of a parallelized pipeline	50
2.6	Change of basis	52
2.7	Schematic representation of raycasting	53
2.8	Raycast cells	54
2.9	Example of a volume render	56
2.10	3D streamlines	57
2.11	Example of a 3D isocontour	58
2.12	Example of a ROI render	58
2.13	3D printing pipeline	60
3.1	State of the art of second collapse calculations	62
3.2	Schematic representation of convection	67
3.3	Large scale structure comparison between runs IMHD and NIMHD.	117
3.4	Magnetic field properties during the collapse	118
3.5	Illustration of stellar criterion	120
3.6	Temperature and density evolution after second collapse.	121
3.7	Radiative flux and radial velocity evolution after second collapse.	122
3.8	Averaged radial profiles of run IMHD	125

3.9	Averaged radial profiles of run NIMHD	126
3.10	Magnetic field strength and morphology in the resistive case	129
3.11	Magnetic field strength and morphology in the ideal MHD limit	130
3.12	Comparing the disk evolution in the hydro and MHD case	132
3.13	Structural and kinematic comparison between run NIMHD and HD	133
3.14	Merger of two first Larson cores	139
3.15	Disk properties comparison in gray and multigroup simulation	140
3.16	Slices comparing a gray and multigroup simulation	140

Chapter 1

The birth of stars - Introduction

Our own star, the Sun, is the energy source fueling life on our planet. When it sets below the horizon, its blinding light scattered across the atmosphere is obscured, revealing the thousands of visible stars adorning the night sky. These stars are the building blocks of our Universe, numbering approximately 10^{24} . Despite this, their birth mechanism is as of yet not fully understood, owing to observational and theoretical hurdles that significantly hamper breakthroughs in the field. Nevertheless, advancements in stellar formation theory are of considerable interest to a wide range of fields in astrophysics. For instance, extra-solar planetary systems display a diverse range of properties, which calls for a deeper understanding of the initial conditions of their birth process. Such planetary systems are formed from circumstellar disks of gas and dust, which are a natural consequence of the conservation of angular momentum during the stellar formation process. Of course, this process also dictates the initial conditions of the star itself, which joins the main sequence approximately 10^7 yrs after its birth ([Stahler & Palla 2004](#)). Another example is the physics of the interstellar medium (ISM), the diffuse gas that permeates galaxies, whose properties are heavily affected by feedback effects from stars. Finally, galaxies themselves are agglomerations of stars (as well as dark matter), whose birth mechanism imprints itself on the resulting properties of the galaxy. It is thus of crucial interest to tackle the challenge of star formation.

In this chapter, we will provide an overview of our current understanding of star formation by showcasing our theoretical grasp of the physical processes involved, all the while presenting the observational constraints that have guided much of our efforts. This process is fundamentally multi-scale, both in density and in spatial extent, and involves a complex interplay of several physical processes such as self-gravitating hydrodynamics, magnetic fields, radiative transfer, and turbulence. Of course, it is not possible for us to fully describe all the scales involved in star formation, and as such we will limit ourselves to the ones relevant to the work done during this thesis, where we have taken a keen interest in the collapse of dense cores within molecular clouds and how such a process results in the birth of stars and circumstellar disks. Before joining the fray in a complex topic such as this, let us first introduce some context and basic

concepts that are relevant in understanding the major issues permeating the field¹.

1.1 Molecular clouds: stellar foundries



Figure 1.1: The pillars of creation: a giant molecular cloud giving birth to stars, as photographed in the optical band by the Hubble Space Telescope (left) and in the near-infrared by the James Webb Space Telescope (right). JWST’s infrared view allows one to see through the opaque dust, thus revealing nascent stars. Image credits: NASA, ESA, CSA, STScI, Hubble Heritage Project (STScI, AURA).

Young stars are formed in giant molecular clouds, primarily composed of hydrogen in molecular form (H_2) and helium, with trace amounts of heavier elements (mainly oxygen, carbon, and nitrogen). These clouds are found all throughout our Milky Way galaxy, and their huge mass reservoir of dust and gas is what feeds the birth of new stars and the planetary bodies orbiting them. [Figure 1.1](#) displays perhaps the most famous cloud complex of all: the pillars of creation, situated in the eagle nebula. The opaque dust, which represents approximately 1% of the mass content of the cloud, obscures the newly-formed stars embedded within it in the visible band. In the near-infrared, this problem is alleviated, as the optical depth of the cloud is significantly lower at these wavelengths and thus allows us to peer through the cloud and witness the birth of stars.

Star formation is ultimately a cycle, in which the diffuse gas of the interstellar medium (ISM) is compressed into stars, before being ejected back into it through outflows, winds and supernovae. In doing so, elements heavier than hydrogen and helium that have been produced through stellar nucleosynthesis find their way into the ISM, where they mix with the original diffuse gas mixture. The gas then condenses once more to form new molecular clouds, and the cycle repeats itself.

¹A more exhaustive description originating from first principles will be made in Chapter 2

Understanding how these cloud complexes form stars is a difficult undertaking. Firstly, they are opaque to optical radiation, and although the problem is alleviated in the infrared, their high densities ensure that their optical depths remain high. Secondly, the closest star forming region to the solar system, the Rho Ophiuchi cloud complex, is situated at ~ 165 pc (Klose 1986), which makes it very difficult to attain the sub-AU resolution required to study the small scale physics relevant to star formation. Nevertheless, significant progress has been made in this regard, particularly with the advent of high resolution millimeter and sub-millimeter instruments, as well as the launch of more sophisticated space-borne instruments. These have probed star-forming regions of our galaxy with unprecedented details, thus providing us with ever more sophisticated observational constraints. Furthermore, the increasing amount of computing power available has allowed for theorists to run ever-more complex simulations that describe a wide variety of physical processes involved in star formation.

1.1.1 From clouds to stars

The main difficulty in observing molecular clouds lies in the fact that they are mainly made of H_2 molecules, which are notoriously difficult to observe in the infrared due to their molecular structure. As such, cloud structures, ranging from 10^4 to $10^6 M_\odot$ in mass, have been traditionally observed through a tracer molecule: carbon monoxide, which emits at 2.6 mm (Wilson et al. 1970). Molecular clouds generally have a temperature of 10 K and a mean density of n_{H_2} of 100 cm^{-3} (Solomon et al. 1987; Scoville et al. 1987; Chevance et al. 2023). A hierarchy of structures has been observed in them (Larson 1981; Chieze 1987), in which the mass and size display a correlation. There is a significant debate (and even controversy) in the literature regarding the precise nature of molecular clouds and how they form stars; whether they are transient overdensities of the ISM that are formed by the converging flows of turbulence (e.g., Mac Low et al. 1998; Padoan & Nordlund 1999), or structures close to equilibrium that persist for millions of years (e.g., Larson 1981; McKee 1999, see the review of Bergin & Tafalla 2007). The difficulty in assessing this stems from the complex web of interactions between gravity, magnetic fields, cosmic rays, radiation, and feedback effects from protostars that are at play. Each of these processes and their effects on star formation is an active field of research in which rapid progress is currently being made, although a comprehensive theory of star formation that links all the relevant scales, from galaxies to individual stars all the while accounting for all the relevant physics, has yet to be achieved.

During this thesis, we have considered the smallest spatial scale relevant to proto-stellar birth; that of a dense core (of size $\sim 10^{-2}$ pc). It is the densest structure possibly formed by a molecular cloud, one whose eventual collapse triggers the birth of stars. In their survey Könyves et al. (2015) report a significant fraction of these (45 – 69%) are gravitationally bound, meaning that they are likely collapsing and in the process of forming stars. Note however, that star formation is not an isolated process, it is dictated by its environment and nascent stars themselves affect their surroundings through feedback effects.

1.1.2 Turbulence and its spectra

Observations that probe the kinematics of the gas within clouds confirm the ubiquitous nature of turbulence within them (e.g., [Schneider et al. 2011](#)). It is found across all scales relevant to star formation ([Larson 1981](#)). In essence, it is the means by which kinetic energy is re-distributed across spatial scales through random, chaotic motions. So far, there exists no theory capable of describing the behavior of turbulence, however one may do so statistically ([Frisch 1995](#)). Turbulence in the ISM differs from that which is commonly found on Earth: it is compressible and magnetized, and affects a huge range of densities. We will nonetheless present the classical theory of incompressible turbulence as postulated by [Kolmogorov \(1941\)](#) in his dimensional analysis.

Turbulence is triggered when inertial forces in the fluid greatly outweigh dissipative viscous forces. This occurs when the Reynolds number (Re) of the flow exceeds a $\sim 10^2$. It can be expressed as

$$Re = \frac{UL}{\nu}, \quad (1.1)$$

where U is the bulk velocity of the flow, L its characteristic scale, and ν its viscosity. When this occurs, kinetic energy is transferred to smaller and smaller scales, until particle collisions themselves convert said energy into heat. In this sense, turbulence is a cascading process of energy transfer. Through energy conservation, the energy dissipation rate ϵ at each scale l is given by ([Hennebelle & Falgarone 2012](#))

$$\epsilon \propto \frac{v_l^2}{\tau_l} = \frac{v_l^3}{l}, \quad (1.2)$$

where v_l and $\tau_l = l/v_l$ are the characteristic velocity and turnover time at scale l . The kinetic energy at each scale E_l ($\propto v_l^2$) and its corresponding power spectrum $P(k)$ can then be expressed in Fourier space as

$$E(k) \sim \epsilon^{2/3} k^{-5/3}, \quad (1.3)$$

$$E(k) = \int P(\vec{k}) \delta(|\vec{k}| - k) d\vec{k}, \quad (1.4)$$

where $k = 2\pi/l$ is the wave number. The power spectrum of velocity in incompressible turbulent flows is $P(k) \propto k^{-11/3}$.

1.2 Gravitational collapse in star forming clouds

In this section, we briefly summarize the main evolutionary stages describing the gravitational collapse of dense cloud cores. This is not meant to be a thorough review of the state of the art, but rather an overview presenting the most commonly admitted mechanisms and physical processes at play during the birth of stars.

Jeans instability

Our journey begins when the conditions of collapse are satisfied; namely, when outward pointing forces can no longer offer enough resistance to the inward pull of gravity (Jeans 1902). Let us first consider a dense core within a molecular cloud, and approximate it as being a spherical distribution of mass. Furthermore, let us assume that said core is mainly supported by thermal pressure gradient forces. As we will see later on, this is a gross oversimplification of the criterion for stability, but it nonetheless allows us to introduce the concept of the Jean's mass M_J . In this scenario, triggering the gravitational collapse of the dense core requires one to exceed the threshold mass value M_J . This critical value can be derived using simple physical arguments: if a gravitational collapse is triggered, sound waves will propagate through the cloud and will eventually bounce back to re-establish a thermal pressure balance. The characteristic time for this to occur is the sound crossing time t_s , and if it is shorter than the free fall time t_{ff} (i.e the characteristic time over which the cloud collapses under its own gravity), then the cloud has time to re-establish a pressure balance and it remains in hydrostatic equilibrium. If however $t_s > t_{\text{ff}}$, the cloud cannot re-establish a pressure balance and the gravitational collapse is unimpeded. t_{ff} and t_s are given by

$$t_{\text{ff}} = \sqrt{\frac{3\pi}{32G\rho}}, \quad (1.5)$$

$$t_s = \frac{R}{c_s}, \quad (1.6)$$

where R is the radius of the dense core and c_s is the isothermal sound speed. Therefore, in order to trigger a gravitational collapse, the condition $t_{\text{ff}} < t_s$ has to be satisfied. This occurs at a length scale λ_J , known as the Jeans length:

$$\lambda_J = c_s \sqrt{\frac{3\pi}{32G\rho}}. \quad (1.7)$$

The Jean's mass is then simply the mass enclosed within λ_J :

$$M_J = \frac{4\pi}{3} \lambda_J^3 \rho. \quad (1.8)$$

This quantity represents the maximum mass a spherical dense core of constant density and temperature may have before being prone to gravitational collapse.

The prestellar phase

Let us now assume that a dense core is about to undertake the process of gravitational collapse and give birth to a star. Much of our theoretical understanding of the formation of low mass protostars was pioneered by Richard Larson during his PhD. His most notable contribution to the field is the discovery of a two step evolutionary sequence describing the collapse of a gravitationally unstable dense core to stellar densities (Fig. 1.2). It can be summarized as follows (Larson 1969):

- As the dense core collapses in on itself, the gas approaches a density profile of $\rho \propto r^{-2}$. During the collapse, the gravitational binding energy is irradiated away in the infrared by dust grains, thus the gas maintains a constant temperature as it contracts. Eventually, the rising density causes the gas to become optically thick, after which radiative cooling by dust grains becomes inefficient. This causes the gas to heat up adiabatically, thus allowing it to reach a state of hydrostatic equilibrium. This gives birth to the first Larson core, an object of radius ~ 5 AU and mass $\sim 10^{-2} M_{\odot}$. The first core continues to accrete material from its surroundings and contracts adiabatically, first with a polytropic index γ_{eff} of $5/3$ ², and once the rotational degrees of freedom of H_2 molecules are excited (at ~ 100 K), γ_{eff} reduces to $7/5$.
- Once the temperature in the center of the first Larson core reaches ≈ 2000 K, the thermal dissociation of H_2 molecules is triggered. This process is highly endothermic, consuming ≈ 4.48 eV per molecule (Stahler & Palla 2004). The gravitational binding energy that was previously adiabatically heating the gas is instead consumed by the dissociation process, which causes γ_{eff} to drop to 1.1 (Saumon et al. 1995). As such, the first core loses thermal pressure support against gravity, and a highly dynamical second collapse ensues³. Once most of the H_2 molecules are dissociated, compressive heating resumes and hydrostatic equilibrium is once again achieved. This gives birth to the second Larson core (i.e., the protostar), of radius $\approx 2 R_{\odot}$, mass $\sim 10^{-3} M_{\odot}$, and temperature $\sim 10^4$ K. The temperatures in the protostellar interior are so high that atomic hydrogen and helium begin to ionize, however the protostar is thermally stable and no longer susceptible to further collapse (Tomida et al. 2013).

This evolutionary sequence is summarized in Fig. 1.3, which illustrates the thermodynamical history at the center of the collapsing cloud core. During each step of this process, angular momentum conservation causes the gas to rotate around the center of mass, thus forming a circumstellar disk. We will see later however, that numerous physical processes can cause a loss of angular momentum during the collapse.

The protostellar phase

The birth of the second Larson core ushers in the *protostellar phase*, often referred to as the *main accretion phase*, as the newly-formed protostar builds up the vast majority of its final mass throughout its duration. Once most the first core is accreted, the protostar directly accretes hot molecular gas from its surroundings, whose density profile quickly approaches free-fall ($\rho \propto r^{-1.5}$ and $v_r \propto r^{-0.5}$, Shu 1977). The majority of the luminosity output of the protostar is produced by the shock front as it converts a fraction of the incoming kinetic energy into radiation (i.e., accretion luminosity). This is owing to the fact that deuterium burning (${}^1\text{H} + {}^2\text{H} \rightarrow \gamma + {}^3\text{He}$) has not yet been triggered as it requires a temperature of 10^6 K. As such, the interior radiates a cooling

² H_2 behaves as a monoatomic gas at low temperatures

³The first core's free-fall time is ~ 10 yr, whereas the free-fall time of the dense core is $\sim 10^4$ yr.

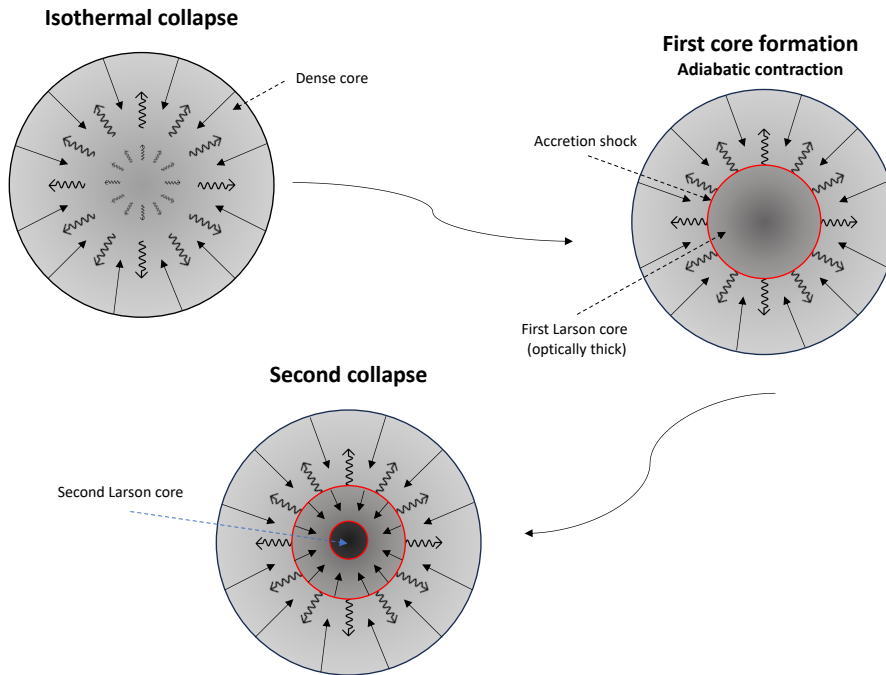


Figure 1.2: A schematic overview of the birth of the protostar, showcasing the main stages of the gravitational collapse of a dense core to stellar densities. Solid black lines indicate the direction of collapse. The isothermal collapse phase is characterized by an efficient radiative cooling of the core as it contracts. The first core forms as a result of a buildup of thermal pressure after optical thickness is achieved, which then collapses in on itself after the onset of H_2 dissociation, thus giving birth to the protostar.

flux that struggles to escape due to high optical depths. Observations of protostellar objects currently in this phase report the presence of circumstellar disks (e.g., [Maury et al. 2019](#); [Tobin et al. 2020](#)), formed through the conservation of angular momentum during the collapse. They also report the presence of high velocity jets and outflows ([Arce et al. 2007](#)), which suggests the presence of strong magnetic fields driving them⁴. Understanding how the protostar evolves during this phase in tandem with the newly-formed circumstellar disk is a contemporary challenge of stellar formation theory, as a huge dynamical range needs to be considered along a wide array of physical processes that dictate the evolution of these two objects. The advent of high resolution millimeter and submillimeter instruments has greatly facilitated the study of deeply embedded sources, as the wealth of data gathered has significantly constrained theoretical models, although much progress is yet to be made.

The pre-main sequence phase

At the end of the *protostellar phase*, the protostar has accreted the majority of its surroundings. Our theoretical understanding of this phase is greatly abetted by the

⁴Although more circumstantial, thermal pressure gradients may also drive outflows.

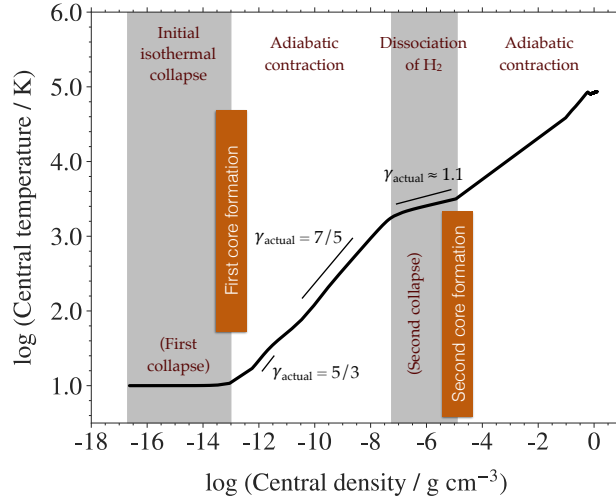


Figure 1.3: The two-step evolutionary sequence describing the collapse of a dense cloud core to stellar densities. The black curve displays the evolution of the central temperature with respect to central density (analogous to time), which tracks the thermodynamical evolution of the gas. Figure taken from [Bhandare et al. \(2020\)](#).

work done in stellar physics, as adequate approximations can be made to describe the evolution of the protostar using the stellar structure equations (e.g. [Palla & Stahler 1991](#); [Chabrier et al. 2000](#)). In addition, having accreted the majority of its surrounding dusty envelope, the protostar now becomes visible in the optical, thus providing H-R diagrams that can validate evolutionary models. The newly cleared stellar environment allows for the protostar to radiate away a significant portion of the energy it has accreted, and its contraction timescale (the Kelvin-Helmholtz timescale t_{KH}) becomes smaller than its accretion timescale t_{acc} . These two quantities can be expressed as

$$t_{\text{KH}} = \frac{GM_*^2}{L_* R_*}, \quad (1.9)$$

$$t_{\text{acc}} = \frac{M_*}{\dot{M}_*}, \quad (1.10)$$

where M_* is the protostar’s mass, R_* its radius, L_* its luminosity, and \dot{M}_* its mass accretion rate. t_{KH} represents the time required for the protostar to radiate away its gravitational binding energy, and t_{acc} represents the time required for the protostar to build its current mass. When $t_{\text{KH}} < t_{\text{acc}}$, the protostar begins its contraction which occurs over a period of 10 Myr, thus resulting in the release of an immense amount of gravitational energy. Since the protostar is a gravitationally bound object, a loss of energy causes an increase in temperature.⁵ Thus, the contraction further heats the protostellar interior until it reaches a temperature of 10^6 K in its central regions, by which point deuterium burning begins. This process releases ≈ 5.5 MeV per reaction, which cannot be transported away through radiative means. As a result, convection

⁵This is due to the Virial theorem ([Sec. 2.1.2](#)), which states that should the gravitational binding energy of the star be reduced (e.g., through a contraction), then half of the energy is lost by the star through radiation, while the other half is converted into internal energy, causing it to heat up.

sets in all throughout the protostar (Hayashi 1961), which transports additional deuterium towards the central regions that sustains the fusion process (Stahler et al. 1980). Eventually, the temperature in the central regions exceed 10^7 K, thus triggering Hydrogen fusion. This signals the end of the pre-main sequence phase, and the protostar enters the main sequence as a ZAMS (Zero Age Main Sequence) star.

1.2.1 The empirical sequence

The challenge of star formation lies not only in the abundance of physical processes that add significant complexity to theoretical works, but also in the difficulty involved in obtaining concrete observational constraints from star forming regions. The immense reservoir of gas and dust in which the nascent star is embedded obscures much of its outgoing radiation. The envelope reprocesses said radiation and mainly emits in the infrared, however a greater fraction of stellar light escapes unhampered as the system evolves over time. As such, young stellar objects (YSOs) have historically been classified according to the slope of their spectral energy distributions (SEDs, Lada & Wilking 1984; Lada 1987; Andre et al. 1993), in what is now known as *the empirical sequence* (Fig. 1.4).

The class 0 phase represents a period in which the protostar is entirely embedded within its envelope, where a negligible amount of its radiation manages to peer through without being re-processed. During this phase, $M_{\text{env}} > M_* \sim M_{\text{d}}$, where M_{env} and M_{d} are respectively the mass of the envelope and of the disk.

After having accreted a large fraction of the envelope, the protostar begins to reveal itself in optical wavelengths as its radiation manages to peer through the envelope, which is itself becoming thinner as its mass content is accreted by the nascent protostar and circumstellar disk. The system enters what is known as the class I phase, which lasts $\sim 5 \times 10^5$ yr (Evans et al. 2009). During this phase, $M_* > M_{\text{env}} \sim M_{\text{d}}$.

Once the majority of the envelope has been accreted by the star and disk, the system transitions to the class II phase, where strong optical and UV emissions are observed with $M_* \gg M_{\text{d}}$ and $M_{\text{env}} \sim 0$. This phase is believed to last 10^6 yrs.

Once the disk has been accreted by the nascent star, the system transitions to the class III phase, which is characterized by the presence of a debris disk; an object mainly made of dust aggregates created by the planet-forming processes.

1.3 The pivotal role of angular momentum during the collapse

A salient question in stellar formation theory relates to the angular momentum budget of dense cores and how this quantity evolves both during and after the gravitational collapse. Rotational motion offers centrifugal support against gravity, and the ratio of rotational to gravitational energy of a dense core of size R , mass M , rotating at an

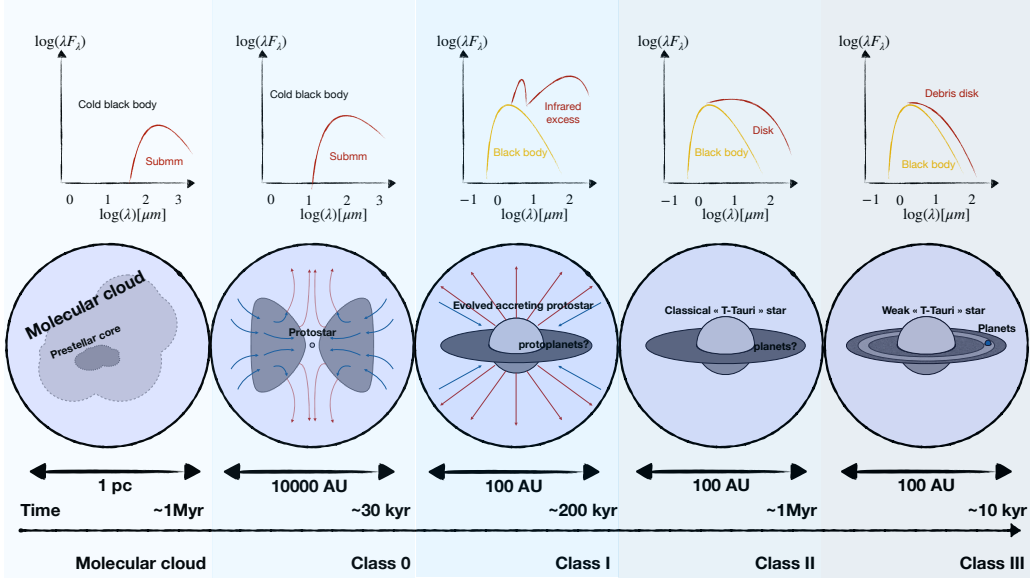


Figure 1.4: A schematic overview of the empirical evolutionary sequence of star formation, starting from a pre-stellar dense core and ending with a fully-fledged star, as inferred from observations (André 2002). Image taken with permission from Lebreuilly (2020).

angular velocity of Ω , can be expressed as:

$$\frac{E_{\text{rot}}}{E_{\text{grav}}} \sim \frac{R^3 \Omega^2}{GM} = \frac{j^2}{GMR}, \quad (1.11)$$

where j is the core's specific angular momentum. Equation 1.11 shows that should angular momentum be conserved during the collapse, the centrifugal force becomes increasingly dominant over gravity. This implies the existence of a *centrifugal barrier*, a region in which centrifugal support outweighs gravity, and thus in which further collapse is halted. Let us now consider a quantitative estimate of the radius of this centrifugal barrier, in which we assume typical values for the quantities involved in our balance equation: $\Omega \sim 10^{-14} \text{ s}^{-1}$ (Goodman et al. 1993), $M \sim 1 M_{\odot}$, and $R \sim 0.1 \text{ pc}$. This would result in a centrifugal barrier at $r \approx 460 \text{ AU}$, which is far too large for such a low mass object. As such, Eq. 1.11 shows that the conservation of angular momentum would not allow for a star to form, as the resulting protostar would be rotating far above its breakup velocity. This problem is known as the *angular momentum problem* in star formation (Bodenheimer 1995). Thus, during the stellar formation process, a significant fraction of the original angular momentum budget of the dense core must be lost. This is illustrated in Fig. 1.5, which displays the specific angular momentum of the various spatial scales involved in the stellar formation process, from dense prestellar cores to the Sun. The figure shows that about 7 orders of magnitude in specific angular momentum must be lost before the star joins the main sequence.

However, angular momentum itself is not a properly defined quantity. Indeed, to measure it, one must consider an origin point in an inertial frame of reference, and in the context of collapsing dense cores, this is often assumed to be the center of mass.

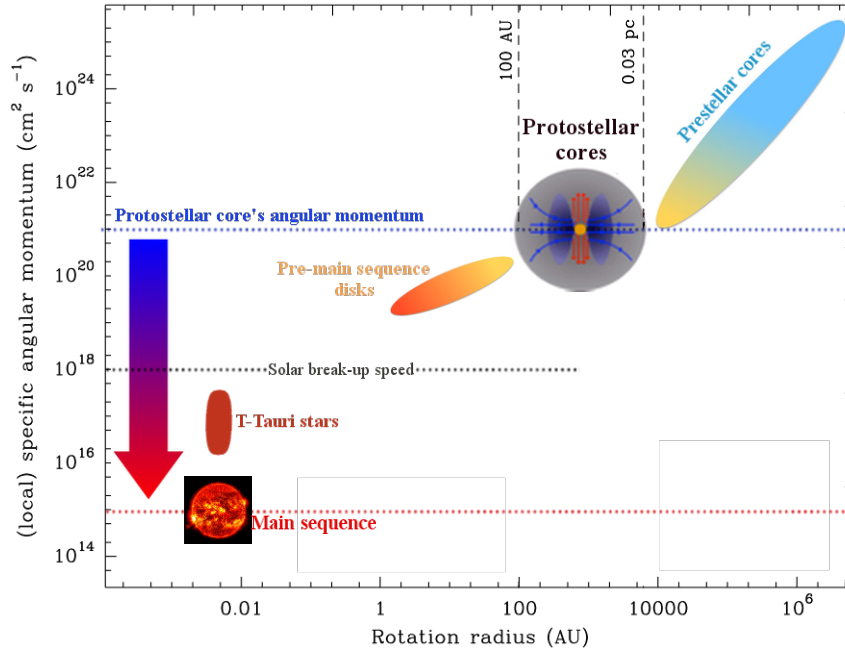


Figure 1.5: Distribution of the specific angular momentum at various scales, as inferred from observations. Image credits: A. Maury & A. Belloche ’s star formation course.

The problem arises in the fact that dense cores are not axisymmetric distributions of gas, and so the center of mass is not necessarily the center of collapse. A natural consequence of this fact is that the gravitational collapse itself can generate a torque that produces angular momentum, sufficiently so to form a circumstellar disk around the newly formed protostar (Verliat et al. 2020). Therefore, it is difficult to ascertain the origin of angular momentum in young stellar objects (Verliat et al. 2020; Xu & Kunz 2021; Lee et al. 2021), or the scales from which it is inherited. In addition to this, dense cores are known to be magnetized (Crutcher 2012). As we will show later on during this section, this will introduce a torque on the gas that will deplete its angular momentum.

The process by which angular momentum is lost or redistributed is an activate field of research. Below, we summarize the main physical processes at play in this regard.

1.3.1 Formation of circumstellar disks

A natural consequence of our approximate analyses in Equation 1.11 is the formation of a centrifugally supported circumstellar disk orbiting the protostar. A naive application of this conservation law would result in a disk whose radius is of the order of the centrifugal barrier ($\sim 10^2$ AU), a result that is at odds with surveys of class 0 disks which show that disks of radii $r > 100$ AU are rare. Indeed, the CALYPSO survey of Maury et al. (2019) reports that about 75% of their sample of 19 class 0 disks have radii $r < 60$ AU, whereas the VANDAM survey of Tobin et al. (2020) reports that 65% of their sample of 146 class 0/I disks have radii $r < 50$ AU. This points towards the fact that a significant portion of the angular momentum of the dense core

is lost during the collapse itself, most likely as a result of magnetic fields acting on the fluid. This is further supported by measurements of the specific angular momentum of class 0/I disks, which seems to be two orders of magnitude below that of dense cores (Williams & Cieza 2011). Thus, a further 5 orders of magnitude reduction is needed to explain the rotation rates of main sequence stars. Below, we summarize the mechanisms responsible for internal torquing within the disk once it has formed, and the role of magnetic fields, both in setting the initial disk size by transporting angular momentum during the isothermal collapse phase as well as its role in driving disk winds, is further discussed in Sec. 1.3.3.

1.3.2 Transport processes in circumstellar disks

We must thus explore what mechanisms are at play in transporting angular momentum in circumstellar disks. Before delving into the details of said mechanisms, it is useful to first explore what the implications of angular momentum transport are using a toy model. Let us consider two annuli of masses m_1 and m_2 and specific angular momenta j_1 and j_2 , orbiting a protostar of mass M_* (see Fig. 1.6). Let us further assume that these annuli are fully supported by the centrifugal force, such that their orbital radii are $r_{1,2} = j_{1,2}^2/GM_*$. Let us now assume that these two annuli exchange angular momentum through some torque mechanism such that the inner ring loses angular momentum through $j_1 \rightarrow j_1 - \delta j$, and in the process raising the outer ring's angular momentum $j_2 \rightarrow j_2 + \delta j$. Centrifugal balance implies that this would cause a contraction of the inner ring, while the outer ring expands to a larger radius. A crude approximation of the exchanged angular momentum can be expressed as⁶

$$\delta J = \delta m_1 \sqrt{GM_* r_1} = \delta m_2 \sqrt{GM_* r_2} , \quad (1.12)$$

$$\Rightarrow \frac{\delta m_1}{\delta m_2} = \sqrt{\frac{r_2}{r_1}} . \quad (1.13)$$

Since $r_2 > r_1$, an exchange of angular momentum implies that $\delta m_1 > \delta m_2$. In other words, the inner ring receives more mass than the outer ring. This demonstrates the natural tendency of circumstellar disks to concentrate mass in the central regions while angular momentum is expelled outwards. The salient question now lies in determining what dissipative processes can extract angular momentum.

Viscous shear

The most natural way to invoke a dissipation of angular momentum in circumstellar disks is through shear. The previously mentioned balance between the centrifugal and gravitational forces causes the gas to rotate at the *keplerian velocity*:

$$v_k = \frac{j}{r} = \sqrt{\frac{GM_*}{r}} . \quad (1.14)$$

⁶This is crudely assuming that the angular momentum difference owing to a change of *specific* angular momentum is lower than that caused by the mass exchange.

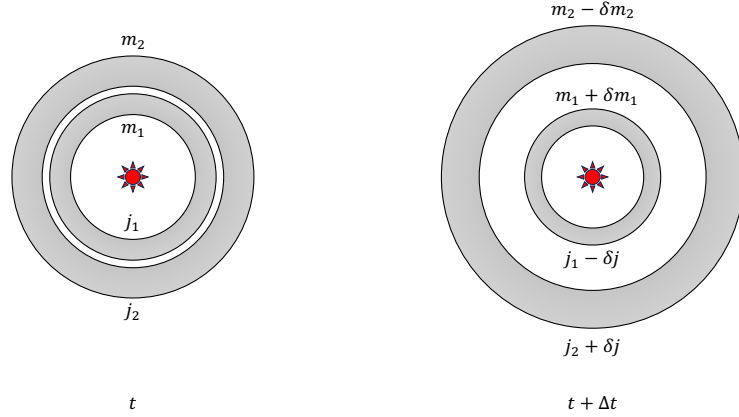


Figure 1.6: Schematic representation of angular momentum transport within a circumstellar disk, in which two annuli exchange angular momentum. The inner ring contracts and gains mass in the process, whereas the outer ring expands and loses mass.

This equation implies that throughout the disk, the gas rotates at different velocities (i.e., the flow is sheared). Thus, molecular viscosities will drag the inner regions and transfer their angular momentum to the outer regions. The typical timescale by which this occurs is aptly named the *viscous timescale* (Lynden-Bell & Pringle 1974):

$$t_\nu = \frac{r^2}{\nu}, \quad (1.15)$$

where ν is the molecular viscosity of the gas. It can be expressed as

$$\nu \sim v_{\text{th}} \lambda_{\text{p}}, \quad (1.16)$$

where λ is the particle mean free path and v_{th} is their thermal speed:

$$v_{\text{th}} = \sqrt{\frac{3\kappa_{\text{B}}T}{m_{\text{H}}}}, \quad \lambda_{\text{p}} \sim 1/n\sigma, \quad (1.17)$$

where n is the number density of molecules with a collisional cross-section of σ . Taking σ to be the size of an H_2 molecule and conditions appropriate to circumstellar disks at 1 AU, we have $\sigma \sim 3 \times 10^{-16} \text{ cm}^{-2}$, $n \sim 10^{15} \text{ cm}^{-3}$, and $v_{\text{th}} \sim 1 \text{ km s}^{-1}$. Thus, we obtain $\nu \sim 3 \times 10^5 \text{ cm}^2 \text{ s}^{-1}$, and $t_\nu \sim 2 \times 10^{13} \text{ yr}$. This timescale is three orders of magnitude above the age of the universe, which allows us to safely conclude that viscous shear is not the dominant process behind the transport of angular momentum in circumstellar disks.

Turbulent diffusion

In order to explain the dissipation of the disks in timescales comparable to those inferred from observations, let us introduce the α -disk model of Shakura & Sunyaev (1973) and

Lynden-Bell & Pringle (1974). The main idea behind it lies in invoking turbulence in circumstellar disks as a mechanism of transport of angular momentum. Indeed, the low viscosity of these objects also implies that they will be highly turbulent, since their Reynolds number defined as

$$Re = \frac{c_s h}{\nu}, \quad (1.18)$$

where h is the scale height of the disk and c_s the sound speed, is $\sim 10^{11}$. This gargantuan Reynolds number means that viscous forces are entirely negligible through a broad range of spatial scales, and turbulence is ubiquitous in circumstellar disks. However, describing turbulence and turbulent transport analytically is a difficult undertaking, and the α -disk model mimics said transport by introducing a *turbulent viscosity*:

$$\nu_t = \alpha c_s h, \quad (1.19)$$

where α is a dimensionless parameter that dictates the vigour of turbulent transport. Its value may be inferred from the observational lifetimes of circumstellar disks, which are of the order of 10^{6-7} yr (Haisch et al. 2001). Thus, through Eq. 1.15, we have $\alpha \sim 10^{-3} - 10^{-1}$. An example of a work in the literature that uses this prescription of angular momentum transport is Hueso & Guillot (2005), who found that this would result in disks whose sizes are > 100 AU.

This model is of course extremely simplified, as the full physics behind the transport of angular momentum is reduced to a diffusive term. Nevertheless, assuming a constant α both in space and in time allows for a comprehensive theory describing circumstellar disks. Further constraining this parameter would require one to model the origin of turbulence, which in circumstellar disks is rather complex (Armitage 2011). A widely accepted and robust mechanisms of turbulence generation in circumstellar disks are gravitational instabilities (Lodato & Rice 2004). Whatever the source of this turbulence may be, its transport of angular momentum in numerical simulations is often reported in terms of an effective α :

$$\alpha_R = \frac{\langle \delta v_r \delta v_\phi \rangle_\rho}{\langle P \rangle_\rho}, \quad (1.20)$$

where v_r and v_ϕ are respectively the radial and azimuthal velocities, P the thermal pressure, and the angle brackets denote a density weighted average over space. The subscript is meant to differentiate this effective viscosity from that of gravitational torques discussed below. The "R" stands for Reynolds, as Eq. 1.20 is often called the Reynolds stress tensor.

Gravitational instabilities

Previously, we have only considered the star's gravity in our balance equations. Furthermore, we have neglected any thermal pressure gradients present within the circumstellar disk. These approximations however, are not entirely valid for newly-formed circumstellar disks whose mass is comparable to that of the protostar. This allows for

gravitational instabilities to develop when the following stability criterion is violated (Toomre 1964):

$$Q = \frac{c_s \omega}{\pi G \Sigma} < 1, \quad (1.21)$$

where Σ is the disk's surface density and ω its epicyclic frequency:

$$\omega^2 = \frac{1}{r^3} \frac{\partial(r^4 \Omega^2)}{\partial r}, \quad (1.22)$$

where Ω is the disk's angular velocity. This parameter describes the ratio of inward pointing gravitational forces to outward pointing pressure gradient and centrifugal forces, all the while accounting for the fact that any instabilities are immediately sheared apart by differential rotation. When $Q \sim 1$, gravitational instabilities are triggered, and globally trailing spiral waves permeate the disk (see Fig. 1.7, left). In addition to being a source of turbulence, the non-axisymmetric spiral wave generates an azimuthal component to the gravitational potential, thus causing a *gravitational torque* in the disk which transports angular momentum outward. As with turbulent transport, the transport of angular momentum through gravitational torques is reported in terms of an effective α :

$$\alpha_G = \frac{\langle \delta g_r \delta g_\phi \rangle_\rho}{4\pi G \langle P \rangle_\rho}, \quad (1.23)$$

where g is the gravitational potential.

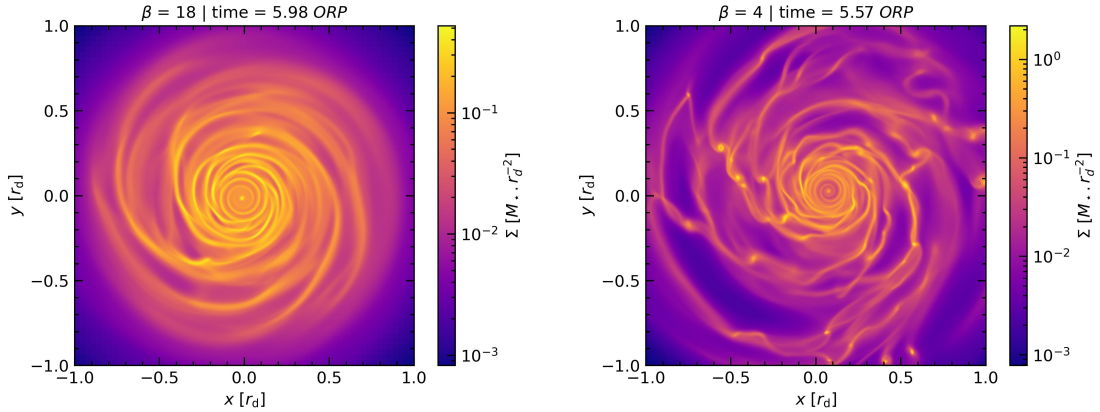


Figure 1.7: Simulations by Brucy & Hennebelle (2021) of self-gravitating circumstellar disks, showing the presence of globally trailing spiral arms generated through gravitational instabilities (left), which can fragment into gravitationally bound objects should the disk be able to cool efficiently enough (right). The visualized quantity is the column density, with brighter colors indicating higher values.

If however pressure and tidal shearing are unable to damp the instability and prevent further collapse, the disk will fragment into gravitationally bound objects (Fig. 1.7, right). This paves the way to form a multiple star system, all the while extracting a significant amount of angular momentum from the disk. Determining the precise barrier beyond which fragmentation is inevitable is unfortunately not straightforward, as a recent study by [Brucy & Hennebelle \(2021\)](#) showed that it is better described by a probabilistic approach. Said probabilities strongly depend on how efficiently the disk is able to cool, such that an efficiently cooling disk needs to transport angular momentum rapidly in order to generate the heat required to maintain its equilibrium. In this sense, gravitational torques within circumstellar disks may act as a sort of thermostat, acting to bring Q as close as possible to marginal stability ([Paczynski 1978](#); [Lodato & Rice 2004](#); [Lodato 2007](#)).

1.3.3 Magnetic fields

Magnetic fields have been detected in the vast majority of star forming regions ([Crutcher 2012](#)), and in particular in dense cloud cores ([Kirk et al. 2006](#); [Jones et al. 2015](#); [Kandori et al. 2018](#); [Myers & Basu 2021](#)). Two main techniques are commonly used to measure them: either Zeeman splitting ([Crutcher & Kemball 2019](#)) or mapping of linearly polarized dust emissions at submillimeter wavelengths ([Lazarian 2007](#); [Andersson et al. 2015](#)).

The field interacts with the gas through the Lorentz force, which can be decomposed into a pressure and tension term⁷ ([Spruit 2013](#); [Hennebelle & Inutsuka 2019](#)). In CGS units, it has the following form:

$$f_L = \frac{(\vec{\nabla} \times \vec{B}) \times \vec{B}}{4\pi} = -\vec{\nabla} \left(\frac{B^2}{8\pi} \right) + \frac{(\vec{B} \cdot \vec{\nabla})\vec{B}}{4\pi}. \quad (1.24)$$

The strength of magnetic fields in dense cores has been measured in the range of $10^{-5} - 10^{-3}$ G, and said measurements are often expressed in terms of a normalized mass-to-flux ratio ([Hennebelle & Falgarone 2012](#))

$$\mu = \frac{M/\phi_B}{(M/\phi_B)_{\text{crit}}}, \quad (1.25)$$

where $\phi_B = \pi r^2 B$ is the magnetic flux. The denominator in the above equation is the critical mass-to-flux ratio μ_{crit} beyond which gravitational collapse is halted by magnetic pressure. It has been computed numerically by [Mouschovias & Spitzer \(1976\)](#)

$$\mu_{\text{crit}} = \left(\frac{M}{\phi_B} \right)_{\text{crit}} = \frac{0.53}{\pi} \sqrt{\frac{5}{G}}. \quad (1.26)$$

Values of μ below 1 are called *magnetically subcritical*, whereas values above 1 are called *magnetically supercritical*. In [Fig. 1.8](#), the magnetic field strength measured

⁷The MHD equations will be introduced in Chapter 2.

along the line of sight is plotted as a function of surface density. We see that diffuse gas tends to be in the subcritical regime, whereas the higher density gas (such as dense cores for instance) is supercritical. Thus, in the context of collapsing dense cores, although the magnetic pressure does not provide enough support to counteract gravity, it may nonetheless extract a significant amount of angular momentum; an effect known as *magnetic braking* (Mouschovias 1985). This is done through the magnetic torque $\vec{\nabla} \cdot (-r B_\phi \vec{B} / 4\pi)$, a term arising from magnetic tension and which represents the field's inherent resistance to torsion. Thus, should the gas twist any field lines through rotational movements, torsional Alfvén waves are generated. These waves are carried along the field lines and extract angular momentum. Thus, the role of magnetic fields in the context of the *angular momentum problem* has been the subject of intensive study in recent years. The transport of angular momentum by magnetic fields within disks is also often reported in terms of an effective α :

$$\alpha_B = -\frac{\langle B_\phi B_p \rangle_\rho}{4\pi \langle P \rangle}, \quad (1.27)$$

where B_ϕ and B_p are respectively the toroidal (azimuthal) and poloidal (vertical and radial) components of the magnetic field vector.

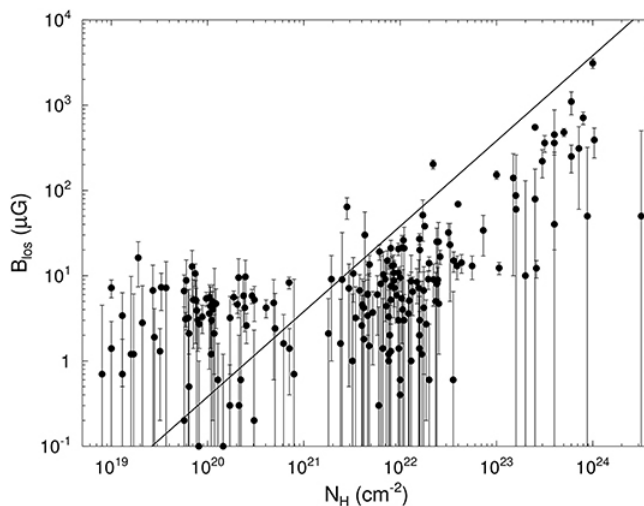


Figure 1.8: Magnetic field strengths measured along the line of sight and plotted as a function of surface density. The solid black line displays the value beyond which magnetic subcriticality is achieved (see Eq. 1.25). Image taken from Crutcher & Kemball (2019).

Magnetic braking catastrophe

The first simulations to tackle the gravitational collapse of dense cloud cores while accounting for magnetic fields were done under the *ideal MHD approximation* (Allen et al. 2003; Matsumoto & Tomisaka 2004; Galli et al. 2006; Price & Bate 2007; Hennebelle & Teyssier 2008; Hennebelle & Fromang 2008), which assumes that the gas is a perfect conductor of the electric current. Under said approximation, the magnetic field

strength observed in dense cores is enough to efficiently transport the vast majority of the gas’s angular momentum during the isothermal collapse phase, thus preventing the formation of a circumstellar disk; a problem known as the *magnetic braking catastrophe*.

In order to reduce the efficiency of magnetic braking, turbulence has been invoked as a possible regulator. Indeed, molecular clouds are highly turbulent structures (Larson 1981; Miville-Deschênes et al. 2017), whose large scale motions cascade down to the scale of dense cores. By creating stochastic motion, the field lines are tangled and reconnection is driven (i.e., changes to the magnetic field’s topology, Lazarian & Vishniac 1999). This causes a diffusion of the magnetic field as the collapse proceeds, and hence reduces the efficacy of magnetic braking; enough-so to form a circumstellar disk (Seifried et al. 2012; Santos-Lima et al. 2012; Joos et al. 2013).

Another mechanism by which the efficiency of magnetic braking can be reduced is by considering a misalignment of the magnetic field with respect to the rotation axis. This has an observational basis, as the survey of Hull et al. (2013) found that the outflows emanating from protostellar cores are not necessarily aligned with the large scale magnetic field. If one assumes that said outflows are aligned with the angular momentum vector of the disk, then this would also imply that the rotation axis of dense cores is misaligned with respect to the magnetic field threading it. Under this hypothesis, circumstellar disks may form in ideal MHD simulations (Hennebelle & Ciardi 2009; Joos et al. 2012; Li et al. 2013; Krumholz et al. 2013; Masson et al. 2016; Gray et al. 2018).

Diffusive processes

In recent years, the most significant correction brought to the *ideal MHD approximation* is the inclusion of magnetic resistivities. Since dense cores are not fully ionized (Umebayashi & Nakano 1990; Bergin & Tafalla 2007), the magnetic field cannot, through the Lorentz force, interact directly with the bulk material of the molecular gas which is made of neutral species. This interaction happens through ions, which collide with the neutral species and transfer their momentum to them. Thus, a coupling between the magnetic field and the gas is predicated upon a high concentration of ions. However, the measured electron fractional abundance in dense cores is of the order of 10^{-7} (Bergin & Tafalla 2007). Therefore, a departure from the *ideal MHD approximation* is expected to occur during the collapse, and *non-ideal effects* need to be considered should one wish to accurately model the interaction of the fluid with the magnetic field; namely, *ambipolar diffusion*, *ohmic dissipation*, and the *Hall effect*. It is helpful to visualize each of these effects in the induction equation, which describes the temporal evolution of the magnetic field in the moving fluid (Maury et al. 2022):

$$\begin{aligned} \frac{\partial \vec{B}}{\partial t} = & \vec{\nabla} \times (\vec{v} \times \vec{B}) - \vec{\nabla} \times (\eta_{\text{O}} \vec{\nabla} \times \vec{B}) + \vec{\nabla} \times \left[\frac{\eta_{\text{A}}}{|\vec{B}|^2} ((\vec{\nabla} \times \vec{B}) \times \vec{B}) \times \vec{B} \right] \\ & - \vec{\nabla} \times \left[\frac{\eta_{\text{H}}}{|\vec{B}|} (\vec{\nabla} \times \vec{B}) \times \vec{B} \right], \end{aligned} \quad (1.28)$$

where η_0 , η_A , and η_H are respectively the Ohmic, ambipolar, and Hall resistivities. The first term on the right hand side of Eq. 1.28 represents the advection of the magnetic field in the fluid. The second term is Ohmic dissipation, which represents the collisions between electrons and neutral species. The third term is ambipolar diffusion, which represents the drift between the bulk of the gas made up of neutrals, and the ions. Finally, the fourth term is the Hall effect, which represents the drift between the ions and electrons.

All of these resistive effects manifest themselves at different densities during the collapse (see Fig. 1.9). The most significant of them is undoubtedly *ambipolar diffusion*, which consistently acts at the widest range of spatial scales; from the dense core to the first Larson core, where it begins to wane.

Ohmic dissipation begins to manifest itself towards the higher density regime, such as within the first Larson core and the circumstellar disk.

The *Hall effect* manifests itself in a more complicated manner. Should the magnetic field's orientation be flipped, Eq. 1.28 shows that the ambipolar diffusion and Ohmic dissipation terms flip signs, whereas the Hall's effect term does not. This means that the orientation of the magnetic field with respect to the rotation axis significantly alters the Hall effect's contribution to the induction equation (Braiding & Wardle 2012). As such, simulations incorporating the Hall effect (e.g., Tsukamoto et al. 2015a; Wurster et al. 2016; Marchand et al. 2019; Wurster & Lewis 2020b) have investigated an anti-aligned and aligned configuration. In the former, the Hall effect supplements ambipolar diffusion and further reduces magnetic braking, whereas in the latter configuration, magnetic braking is enhanced. Thus, the Hall effect has a more circumstantial contribution to magnetic resistivities.

At the temperatures regime in which H_2 molecules are dissociated ($T > 2000$ K, generally reached when densities exceed $\sim 10^{-9}$ g cm $^{-3}$ during the collapse), almost the entirety of the fluid's dust content is vaporized, and atomic hydrogen and helium begin to ionize. This leads to a stark reduction in magnetic resistivities, and the magnetic field recouples with the gas. This entails a recovery of the *ideal MHD approximation* within the protostar following the second collapse.

Simulations that have accounted for magnetic resistivities, be it ambipolar diffusion, ohmic dissipation, or the Hall effect, have consistently reported the formation of a circumstellar disk (e.g., Machida & Matsumoto 2011; Tsukamoto et al. 2015a,b; Zhao et al. 2016; Masson et al. 2016; Wurster et al. 2018; Zhao et al. 2018; Vaytet et al. 2018; Machida & Basu 2019; Lebreuilly et al. 2020, 2021; Wurster & Lewis 2020b; Lee et al. 2021; Wurster et al. 2021). These diffusive processes provide a more robust way to avert the *magnetic braking catastrophe* than turbulence or misalignment, whose outcomes appear to be more circumstantial. Most importantly, they predict disk sizes of $\sim 10^1$ AU (Hennebelle et al. 2016), which is in broad agreement with observations. In reality, a combination of misalignment, turbulence, and diffusive processes is expected in nearly all dense cores, which should allow for the vast majority of newly-formed stars to possess a circumstellar disk orbiting them regardless of their birth environment.

A final detail worth mentioning is the fact that accounting for all magnetic resistivity effects requires a detailed *chemical network* capable of describing the abundance of

charged species according to the temperature and density regime the fluid resides in. In addition to this, a dust grain model describing their size and density distribution needs to be included to determine the surface area available for chemical reactions, such as ion-electron recombination (Marchand et al. 2016; Zhao et al. 2020). The Mathis-Rumple-Nordsieck distribution (Mathis et al. 1977) is most commonly used for this purpose, however its validity has been called into question by recent studies of dust size distributions during the collapse (Lebreuilly et al. 2023; Kawasaki & Machida 2023; Tsukamoto et al. 2023a). These studies shed new uncertainties on the efficiency of these diffusive processes, which further highlights their sensitivity with respect to the micro-physics involved during the collapse.

Finally, the main physical process behind the creation of ionized species in dense cores are cosmic rays. Observations suggest that the cosmic ray ionization rate is $\zeta^{\text{H}_2} \sim 10^{-18} - 10^{-16} \text{ s}^{-1}$ (Padovani et al. 2009), however these values may vary depending on the environment in which the dense core finds itself, as strong shock cavities in protostellar jets may produce cosmic rays that supplement the background values (Padovani et al. 2015, 2016).

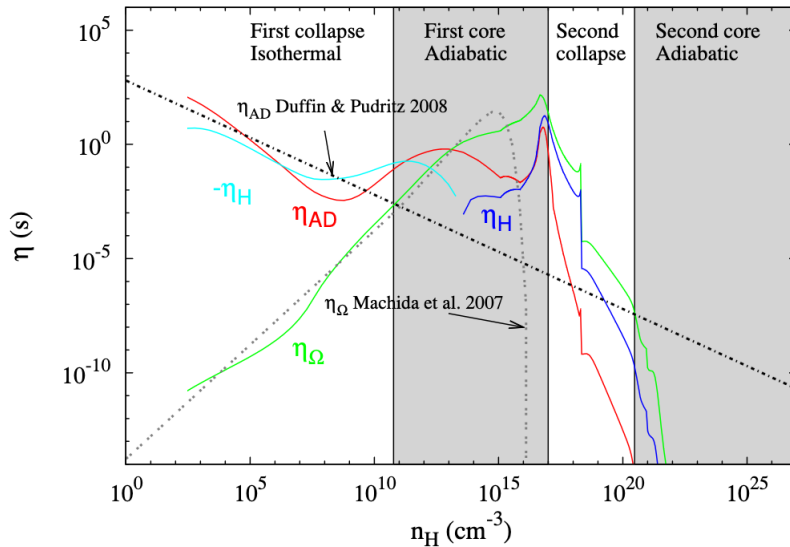


Figure 1.9: Ambipolar resistivity (red), Ohmic resistivity (green), negative Hall resistivity (cyan), and positive Hall resistivity (blue) as a function of density. The resistivities are computed assuming an MRN (Mathis et al. 1977) dust size distribution. Image credits: Marchand et al. (2016).

Jets and outflows

A key physical process capable of re-distributing angular momentum are jets and outflows. These are often observed in the optical or near-infrared wavelengths, although the focus has recently shifted to submillimeter wavelengths in order to study molecular line emissions in more embedded sources (Ray & Ferreira 2021; Tsukamoto et al. 2023b). Jets are highly collimated hypersonic ejecta traveling at a Mach number of

20 – 30 ($\sim 100 \text{ km s}^{-1}$, [Hartigan et al. 2011](#)), whereas outflows have a wide opening angle and are much lower velocity in comparison (traveling at Mach numbers of a few). [Figure 1.10](#) shows a NIRC*am* view of L1527 IRS, which reveals an extended density cavity along the polar regions of the protostar in which material is ejected.

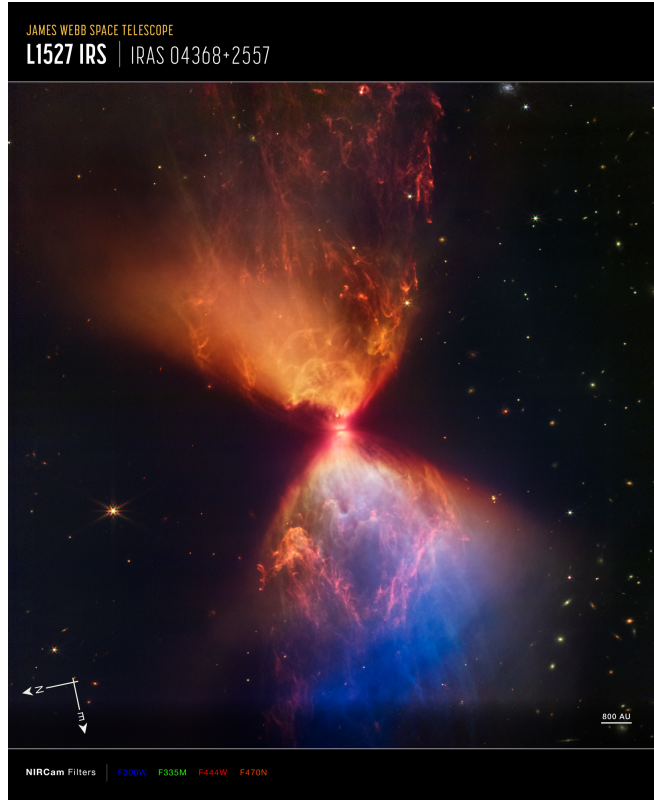


Figure 1.10: JWST NIRC*cam* image of L1527 IRS revealing the presence of an outflow and its low density cavity. The thin dark band in the center of the image is a circumstellar disk obscuring the nascent protostar’s light. Image credits: NASA, ESA, CSA, STScI.

The stark contrast in ejecta velocity between jets and outflows points toward a difference in their launching mechanism. Indeed, the hypersonic jet velocity corresponds roughly to the escape velocity when measured at the surface of the protostar, which suggests that it is the protostar itself that is propelling the material ([Ray & Ferreira 2021](#)). The lower velocity of outflows suggests that the ejecta is propelled at larger spatial scales, and as a result they are expected to carry a higher amount of mass and angular momentum as they entrain more material ([Machida et al. 2008](#)). A schematic overview of the structure of jets and outflows is provided in [Fig. 1.11](#).

The dense core collapse calculations we have previously mentioned have also reported the launching of these outflows. The driving of these two processes is explained by two physical mechanisms: the former is driven by the *magnetocentrifugal mechanism* ([Blandford & Payne 1982](#); [Ouyed & Pudritz 1997](#)), where the gas is accelerated by the magnetocentrifugal force, whereas the latter is driven by the *magnetic tower mechanism* ([Lynden-Bell 1996](#); [Lovelace et al. 2002](#)), where a strong magnetic pressure gradient

is responsible for the outward propulsion of high velocity material. Hence, it relies on a strong twisting of the magnetic field. Such twisting can be achieved at first core densities, where ambipolar diffusion and Ohmic dissipation have sufficiently diffused the magnetic field strength to the point where the magnetic field is dragged by the fluid. The rotation of the first core bends the field lines around it, thus providing the toroidal component needed to launch an outflow. The same phenomena is reproduced within the circumstellar disk, which drives what is commonly referred to as a "disk wind" that continuously extracts angular momentum.

The twisting of field lines is reproduced at the scale of the protostar itself following the second collapse. Although the ideal MHD approximation is recovered within it owing to the high degree of ionization, thermal pressure gradient and centrifugal forces far outweigh magnetic pressure forces (Vaytet et al. 2018; Machida & Basu 2019; Wurster & Lewis 2020b). Hence, the field lines bend around the newly-formed (and rapidly rotating) protostar, allowing the launching of a highly collimated jet through the *magnetic tower mechanism*.

We note however, that the prevalence of jets and outflows in these calculations is not fully established yet, as Wurster & Lewis (2020b); Wurster et al. (2022) report that turbulence in the dense core seems to be delaying (and even suppressing in some cases) the onset of outflows and jets. We also note that thermal pressure gradients may drive outflows, although these are more circumstantial and are predicated upon efficient heating of the envelope by stellar radiation. Finally, in massive star formation, radiation pressure may also drive or at least aid in the creation of outflows (Yorke & Sonnhalter 2002; Kuiper et al. 2010, 2011), although Mignon-Risse et al. (2021) has shown that the magnetic field remains the dominant factor in this regard.

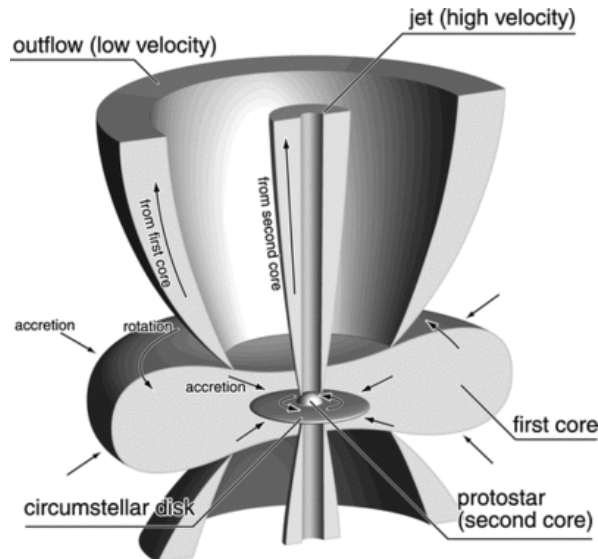


Figure 1.11: Schematic representation of jets and outflows. Image credits: Machida et al. (2008).

1.4 The magnetic flux problem

In the previous section, we have discussed magnetic fields in the context of the *angular momentum problem*, with a particular focus on how magnetic braking affects the formation and evolution of disks. A closely connected problem to that of angular momentum is the *magnetic flux problem* (Mouschovias 1985). Under the ideal MHD approximation, the magnetic flux $\phi_B = \pi r^2 B$ is conserved during the collapse. As such, a collapsing dense core of size $R \sim 10^{-2}$ pc with an initial magnetic field strength of $\sim 10^{-5}$ G would give birth to a protostar ($R \sim 1 R_\odot$) whose magnetic field strength is $\sim 10^6$ G should flux freezing hold. This is approximately three orders of magnitude above the magnetic field strength observed in young stellar objects ($\sim 10^3$ G, Johns-Krull 2007; Johns-Krull et al. 2009; Yang & Johns-Krull 2011), and therefore a considerable amount of magnetic flux has to be lost by the time the protostar becomes visible. We have mentioned in the previous section the role of magnetic resistivities in defusing the flux to the point where circumstellar disks are able to form. In this section, we shift our focus to the magnetic flux inherited by the protostar at the time of its birth.

1.4.1 Observational constraints

Direct measurements

Direct measurements of the magnetic field strength in protostars can be made using Zeeman broadening of spectral lines (e.g., Robinson 1980; Johns-Krull & Valenti 1996; Johns-Krull 2007; Yang et al. 2008). Since such measurements require the stellar photosphere to be visible, they can only be made during the class I and more evolved stages, and to our knowledge, only Johns-Krull et al. (2009) and Flores et al. (2019, 2024) presented measurements of magnetic field strength in class I sources. The fact that such detections only happened so recently illustrates the difficulty of performing these measurements. Nevertheless, two works have surveyed the magnetic field strength of a total sample of 28 young stellar objects (YSOs): Johns-Krull (2007); Yang & Johns-Krull (2011). Their resulting measurements of photospheric magnetic field strengths and fluxes with respect to stellar age are displayed in Fig. 1.12.

Firstly, it seems that the magnetic field strengths display a moderate amount of scatter with respect to stellar age, however the mean value is of the order of $\sim 10^3$ G. Secondly, the magnetic flux seems to be decreasing with stellar age.

We also note the recent study by Flores et al. (2024), which surveyed a sample of 42 class I sources and found a mean magnetic field strength of 4.2 kG, although the authors of the study did not report the ages of their sources. Finally, in more evolved class II and III sources, there is a relative abundance of magnetic field strength measurements, with over 100 samples having been observed. These also seem to report a similar value of ~ 1 kG (Yang et al. 2005; Johns-Krull 2007; Lavail et al. 2017; Donati et al. 2019; Sokal et al. 2020; López-Valdivia et al. 2021; Flores et al. 2022).

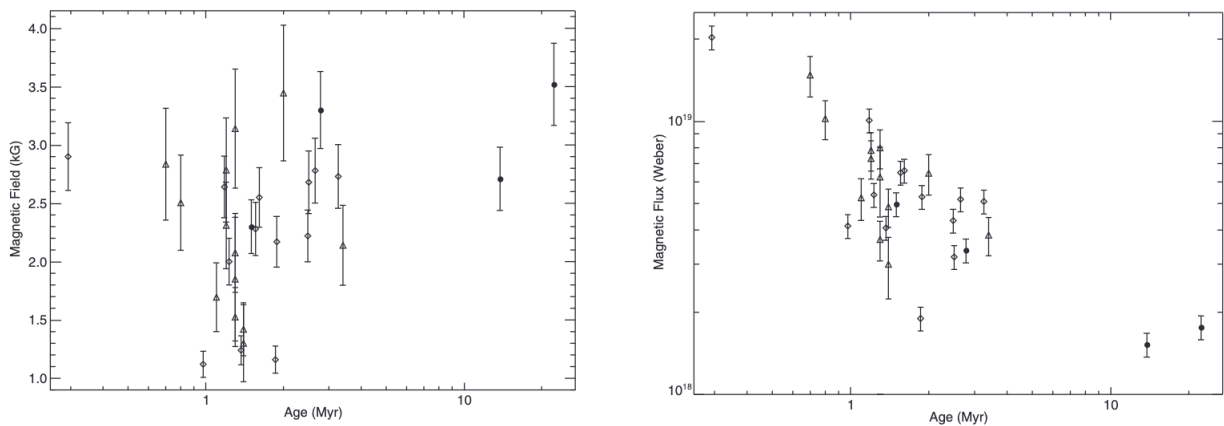


Figure 1.12: Observed magnetic field strengths (left) and magnetic flux (right) of a sample of 28 young stellar objects from [Johns-Krull \(2007\)](#) and [Yang & Johns-Krull \(2011\)](#) as a function of stellar age. Image credit: [Yang & Johns-Krull \(2011\)](#).

Indirect measurements

The magnetic field strength may be indirectly inferred from other kinds of observations. For instance, the disk size surveys of [Maury et al. \(2019\)](#) and [Tobin et al. \(2020\)](#) indicate that disk radii must be of the order of $\sim 10^1$ AU. This indicates that although magnetic braking is present in dense cores, the magnetic field is not strong enough to prevent the formation of circumstellar disks. As such, disk sizes may be linked to magnetic field strengths through models of magnetically-regulated disks such as those of [Hennebelle et al. \(2016\)](#).

Another indirect measurement comes from a recent study by [Moscadelli et al. \(2023\)](#), who observed water masers in a jet at distances < 100 AU from the star and inferred from them a magnetic field strength of $0.1 - 0.7$ G.

Finally, our own solar system can also provide us with constraints. Ancient meteorites recovered on Earth can be analysed with natural remanent magnetization techniques, which allows for a direct and precise measurement of the magnetic field strength at the time of their formation within the protosolar disk (see the review of *paleomagnetism* by [Weiss et al. 2021](#)). The resulting measurements report a field strength of 0.54 ± 0.21 G 1.22 Myr after the birth of the Sun.

These three indirect measurements provide a constraint on the magnetic field strength in MHD simulations. As we will show below, the ~ 0.1 G magnetic field strength inferred from these observations can provide constraints on MHD simulations of collapsing dense cores. This comes from the fact that the measurements are likely to reflect the magnetic field present in more diffuse gas, where densities are close to those of first Larson cores and circumstellar disks.

1.4.2 Magnetic field strength predicted by simulations

Constraints on the magnetic field strength implanted in the protostar at birth requires a self-consistent modelling of the collapse of the dense core to stellar densities. Due to the challenges in performing such simulations, only a handful of studies have done so by including magnetic fields (see the review by [Teyssier & Commerçon 2019](#)). In addition, the stringent time-stepping constraints following protostellar birth precludes them from advancing sufficiently in time to predict magnetic field strengths in more evolved systems such as class I protostars. Nevertheless, some interesting results were obtained in said simulations, particularly by those that account for magnetic resistivities.

Indeed, diffusive processes prevent flux freezing from occurring during the collapse, such that the resulting protostar inherits significantly less magnetic flux from the collapse of the first core. As an illustrative example, [Fig. 1.13](#) shows the magnetic field strength distribution as a function of density during the second collapse calculations of [Vaytet et al. \(2018\)](#), where they have compared the resulting measurements under the ideal and non-ideal (with ambipolar diffusion and Ohmic dissipation) MHD approximation. In the former (red distribution), flux freezing causes the implantation of a magnetic field of strength 10^6 G in the protostar, whereas in the latter (blue distribution), ambipolar diffusion creates a plateau of ~ 0.1 G at first core densities. Once the second collapse sets in, the high temperatures sublimate all dust particles and begin ionizing atomic species, such that flux freezing is recovered. However, the reduction in magnetic flux prior to the second collapse means that the second core inherits a significantly weaker magnetic field of $\sim 10^3$ G, in accordance with the observations of more evolved systems.

The robustness of the results reported by [Vaytet et al. \(2018\)](#) are difficult to establish. Firstly, non-ideal MHD simulations having reached the second collapse stage are sparse, and secondly, these studies use different codes, resolutions, chemical networks, cosmic ray ionization rates, and initial conditions that render a comprehensive comparison difficult to make. For instance, [Tsukamoto et al. \(2015b\)](#) reports an implanted magnetic field of $\sim 10^2$ G when accounting for ambipolar diffusion and Ohmic dissipation. [Wurster et al. \(2018\)](#); [Wurster & Lewis \(2020b\)](#), accounting for all non-ideal effects, also report a field strength of $\sim 10^2$ G. However the more recent study of [Wurster et al. \(2022\)](#) investigated the effects of numerical resolution in their SPH simulations and reports an unconverged field strength of $\sim 10^3$ G. What is converged however, is the field strength at first core densities (~ 0.1 G, e.g. [Tsukamoto et al. 2018](#); [Vaytet et al. 2018](#); [Mignon-Risse et al. 2021](#)), and so we expect flux freezing during the second collapse to be able to produce at most a field of $\sim 10^3$ G in the protostar, with any values higher than that being generated by a dynamo process.

1.4.3 Fossil field, or dynamo generated?

We have thus far established from current observational constraints that the magnetic field strength in YSOs is of the order of 10^3 G. Second collapse simulations can obtain

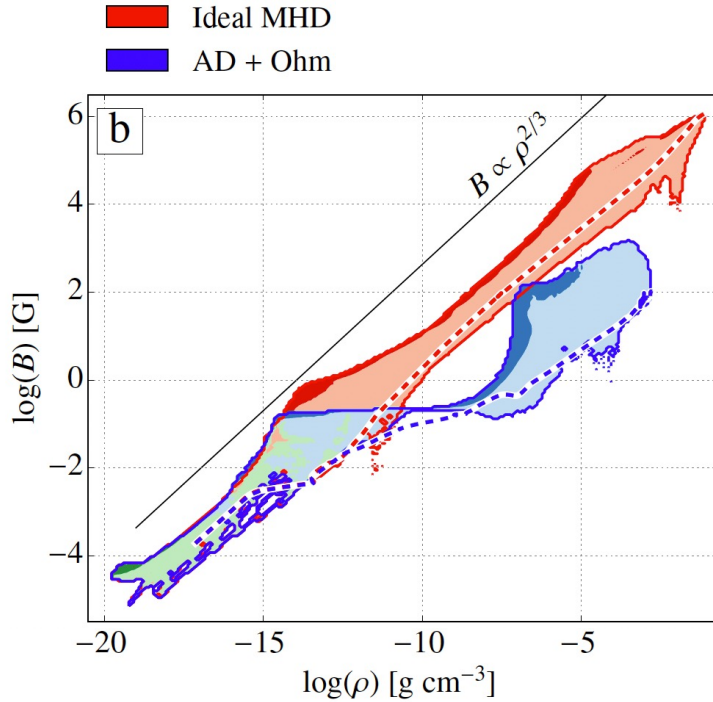


Figure 1.13: Distribution of the magnetic field strength as a function of density under the ideal MHD approximation (red), and non-ideal MHD with the inclusion of ambipolar and Ohmic diffusion (blue). Image credit: [Vaytet et al. \(2018\)](#).

such magnetic field strengths provided that the first core has a field of $\sim 10^{-1}$ G, which seems to be in accordance with paleomagnetic measurements of solar system meteorites, water maser observations, and in broad agreement with disk size surveys. It is thus possible to obtain the kG magnetic fields reported by observations at stellar birth. The salient question now lies in determining how this magnetic field dynamically evolves until the protostar becomes visible. Suppose that a 10^3 G field is implanted in the protostar at birth. The main resistive process capable of diffusing it is Ohmic dissipation, whose characteristic timescale is

$$t_O = \frac{R_*^2}{\eta_O}. \quad (1.29)$$

The Ohmic resistivity is dictated by the concentration of charged species, and due to the high temperatures found within the protostar ($\sim 10^4$ K), all dust grains are sublimated and atomic gas begins to ionize. This causes t_O to reach a value of 10^{10} yr ([Cowling 1945](#); [Wurster et al. 2022](#)), which would mean that a fossil field could survive throughout an entire stellar lifetime. However, Ohmic dissipation is not the only dissipative process capable of reducing the magnetic field in protostars. Turbulent diffusion, much like how it diffuses angular momentum in disks, is capable of diffusing magnetic fields in stars by tangling the field lines to a typical length scale of turbulence.

This occurs at a timescale of

$$t_d = \frac{R_*^2}{\eta_d}, \quad (1.30)$$

where η_d is the turbulent magnetic diffusivity. Works in pre-main sequence evolution have shown that the protostar is fully turbulent once deuterium burning begins in the stellar core (Stahler & Palla 2004), and Bhandare et al. (2020) have shown that protostars display strong turbulent motion even prior to the onset of thermonuclear reactions. Therefore, there exists strong turbulence capable of diffusing the magnetic field in protostars.

The magnetic flux shown in Fig. 1.12 is decreasing with stellar age, however, we know from pre-main sequence evolution that the protostar also contracts as it joins the main sequence (Hayashi 1961; Stahler 1983). As such, the decrease in magnetic flux implies a decrease in magnetic field strength as the protostar evolves. This seems to indicate that turbulent diffusion is indeed at play, and that the magnetic field in protostars is *not generated* through dynamo action. Thus, if the sample of 28 YSOs presented in Johns-Krull (2007); Yang & Johns-Krull (2011) is representative of the magnetic field strength in most low mass stars, then this provides a constraint on second collapse calculations: they *must* be able to implant a 10^3 G field in the protostar at birth.

The question now shifts to the strength of this turbulent decay process: if t_d is too short (i.e., turbulent diffusion is too efficient), then the protostar requires some kind of dynamo action to maintain its magnetic field. However, if the structure of the fossil magnetic field and the interior of the protostar is such that turbulent diffusion is alleviated, then a dynamo process is no longer necessary to explain observations. Works in the literature that address this are unfortunately sparse. Tayler (1987) presented analytical estimates of the magnetic field's evolution in a fully convective star (as is expected of classical T Tauri stars, Hayashi 1961), and argued that a fossil field could survive through the pre-main sequence stage. Moss (2003) expanded on this work by providing additional analytical estimates. They arrived to similar conclusions, and argue that the existence of a radiative interior as predicted for protostars of mass $> 2.5 M_\odot$ (Palla & Stahler 1993) would alleviate the total diffusion of the magnetic field. However, Durney et al. (1993); Chabrier & Küker (2006) argue that the turbulent diffusion in pre-main sequence stars is too efficient (with $t_d \sim 10^4$ yr), and put-forth the hypothesis of a convective dynamo to explain observations. In addition, Chabrier & Küker (2006); Dobler et al. (2006) predict a positive correlation between the magnetic field strength and the stellar rotation rate, however Johns-Krull (2007); Yang & Johns-Krull (2011) find no such correlation. This theoretical uncertainty regarding the magnetic field evolution in protostars stresses the need for further studies that tackle the subject. In order to better constrain models, additional studies reporting on the strength and structure of the magnetic fields implanted in protostars following the second collapse are required.

Ultimately, unravelling the origin of magnetic fields in stars will lie on additional progress in our understanding of the interior structure of protostars (i.e., pre-main sequence evolution) and dynamo theory. Further observational constraints on the magnetic field strengths of class I and more evolved sources will greatly constrain theoretical

efforts in this regard, particularly in confirming or expanding upon the trends observed in previous surveys.

1.5 The luminosity problem

Following the first surveys of protostellar luminosities (Beichman et al. 1986; Kenyon et al. 1990), a discrepancy between theoretical models of star formation and observations was discovered by Kenyon et al. (1990). The median protostellar luminosity \tilde{L} was found to be an order of magnitude lower than the expected theoretical value. Protostars shine by radiating away the potential gravitational energy of the gas they accrete at the accretion shock, with an accretion luminosity L_{acc} of

$$L_{\text{acc}} = f_{\text{acc}} \frac{GM_* \dot{M}_*}{R_*}, \quad (1.31)$$

where f_{acc} is the fraction of the accretion energy that is radiated away. Here, we define f_{acc} as being the *radiative efficiency* of the protostellar shock front, where values of ≈ 1 correspond to supercritical (i.e., cold) accretion, and values < 1 correspond to subcritical (i.e., hot) accretion. In the literature, a mechanical meaning is often attributed to f_{acc} , whereby the shock front is assumed to be supercritical and this parameter simply refers to the fraction of mass brought by \dot{M}_* that lands in the protostar (e.g., Offner & McKee 2011).

By assuming that a typical protostar forms in 0.1–0.2 Myr, has a radius of 2 R_{\odot} and a mass of 0.5 M_{\odot} , the mass accretion rates should be on average $(2.5 - 5) \times 10^{-6} M_{\odot} \text{ yr}^{-1}$ and thus typical protostellar luminosities should be in the 10–20 L_{\odot} range (by assuming that $f_{\text{acc}} = 1$). However, the observational sample of Kenyon et al. (1990) suggested that $\tilde{L} \sim 1.6 L_{\odot}$. Later infrared surveys by the Spitzer space telescope (Evans et al. 2009; Dunham et al. 2014, 2015) and the Herschel observatory (Fischer et al. 2017) confirmed the low median luminosity of protostars (Fig. 1.14). This problem is known as *the luminosity problem*.

Before delving into the proposed solutions to the problem, let us first consider why the protostar *must* radiate away the majority of its gravitational binding energy. If we neglect protostellar radiation and assume that the entire gravitational energy of a dense core is injected into the protostar, the Virial theorem reads (Stahler & Palla 2004):

$$\frac{1}{2} \frac{GM_*^2}{R_*} = \Delta E_{\text{int}}, \quad (1.32)$$

where ΔE_{int} is the energy consumed in the dissociation of H_2 molecules and the ionization of atomic hydrogen and helium. Assuming that the entirety of molecular hydrogen is dissociated and ionized, and that helium is similarly fully ionized, this reads

$$\Delta E_{\text{int}} = \frac{X_{\text{H}} M_*}{m_{\text{H}}} \left(\frac{\Delta E_{\text{H}_2}}{2} + \Delta E_{\text{H}^+} \right) + \frac{X_{\text{He}} M_*}{4m_{\text{H}}} (\Delta E_{\text{He}^+} + \Delta E_{\text{He}^{2+}}). \quad (1.33)$$

Here, X_{H} and X_{He} are the mass fractions of hydrogen and helium species in the gas, whose values are respectively 0.73 and 0.27. ΔE_i is the energy required to achieve the following reactions:

$$\begin{aligned}
 \text{H}_2 &\rightarrow 2\text{H} : 4.48 \text{ eV} = \Delta E_{\text{H}_2} , \\
 \text{H} &\rightarrow \text{H}^+ + \text{e}^- : 13.60 \text{ eV} = \Delta E_{\text{H}^+} , \\
 \text{He} &\rightarrow \text{He}^+ + \text{e}^- : 24.59 \text{ eV} = \Delta E_{\text{He}^+} , \\
 \text{He}^+ &\rightarrow \text{He}^{2+} + \text{e}^- : 54.40 \text{ eV} = \Delta E_{\text{He}^{2+}} .
 \end{aligned}
 \tag{1.34}$$

For a $1 M_{\odot}$ protostar, $\Delta E_{\text{int}} \approx 3.2 \times 10^{46}$ erg. Thus, under the extreme scenario in which $f_{\text{acc}} = 0$, Eq. 1.32 yields a protostellar radius of $\approx 58.5 R_{\odot}$, a value far in excess of typical stellar sizes. This implies that f_{acc} *must* be high throughout the protostellar mass buildup.

Below, we provide a brief summary of the solutions proposed by Kenyon et al. (1990), which have dominated the discourse surrounding the *luminosity problem*. For a more in-depth review, the reader is referred to Fischer et al. (2023).

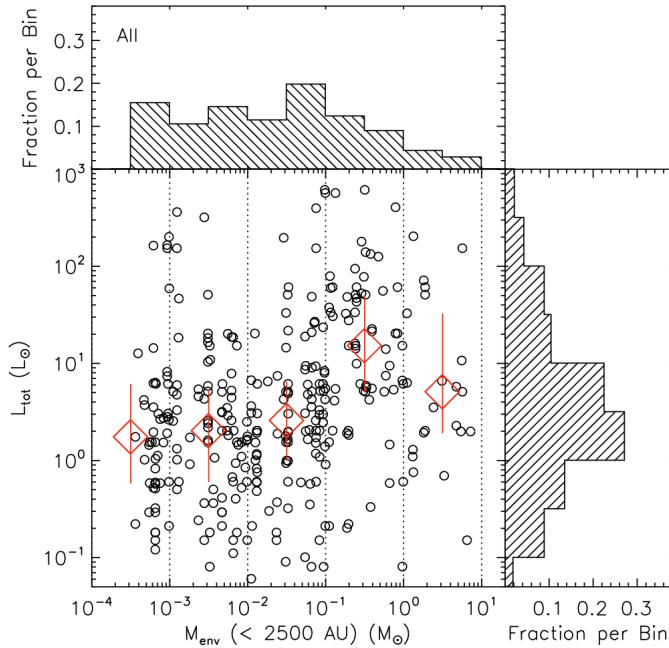


Figure 1.14: Herschel survey by Fischer et al. (2017) of the total luminosity of 324 protostars, plotted as a function of the envelope mass inside 2500 AU. The red diamonds are median luminosity values in each mass bin, which are denoted by the dotted vertical lines. The top (resp. right) histogram shows the luminosity (resp. mass) distribution as a function of envelope mass (resp. luminosity). Image credit: Fischer et al. (2017).

1.5.1 Lower accretion rates

Kenyon et al. (1990) cited a longer star formation time, and hence lower average accretion rates, as a possible way to reduce the discrepancy between predictions and

observations. The results of more recent surveys by the Spitzer space telescope seem to indicate that this is indeed the case, with the inferred protostellar lifetimes being in the range of 0.46 to 0.72 Myr (Evans et al. 2009; Dunham et al. 2015), thus reducing the predicted mean luminosity by a factor 2.3 to 3.6. Furthermore, the extinction-corrected measurements of Evans et al. (2009) also contributed to reducing the discrepancy, as they report a mean protostellar luminosity of $\approx 5 L_{\odot}$.

Offner & McKee (2011) investigated this purported solution to the luminosity problem, and found that its predictions falls within the mean luminosity values provided by Evans et al. (2009) should one consider a mechanical energy loss of $\approx 0.25\%$ (via outflows and jets) and a modest amount of episodic accretion onto the protostar. Thus, the scenario of longer star formation time is viable to match current observational data. As such, the *classical luminosity problem* as stated by Kenyon et al. (1990) in which the \tilde{L} was lower than the theoretically predicted values was solved. However, the longer star formation times were not able to reproduce the large spread in luminosities that span several orders of magnitude (see Fig. 1.14). It has been found that more complex models with time-dependant accretion rates may explain observational data (Dunham et al. 2014; Fischer et al. 2017), however the alternative scenario of episodic accretion is also viable.

1.5.2 Protostellar outbursts

Episodic accretion is the mechanism causing short, large amplitude variations in protostellar luminosities that are commonly referred to as *outbursts*. It was originally invoked by Kenyon et al. (1990), who argued that it could explain how stars build up their mass with periods of high mass accretion and high luminosity, in between longer periods of quieter low mass accretion rates. Observationally, outbursts are commonly observed, the most famous example of which are FU Ori and Ex Lup events (Audard et al. 2014). However, other types of outbursts have been observed, and the order of magnitude increase in stellar luminosity varies from object to object (Fischer et al. 2023).

From a theoretical standpoint, there exists a number of viable mechanisms to trigger bursts of accretion onto the protostar. These include gravitational instabilities in circumstellar disks (Vorobyov & Basu 2010, 2015), or variability in larger scale inflows as reported by Padoan et al. (2014). Furthermore, the magneto-rotational instability (MRI, Balbus & Hawley 1991) is believed to occur in the inner-most (and hence, most highly ionized) regions of more evolved class I and II stars (see the review by Lesur et al. 2023), and may trigger a sudden accretion of mass built-up near the star (Armitage 2011; Ohtani et al. 2014).

Thus, *episodic accretion* is a viable mechanism to reproduce the spread observed in protostellar luminosities. Since a number of models seem to match observational data, Fischer et al. (2017) argue that the field must go beyond the use of protostellar luminosity as a prognostic tool to infer how the mass build-up of protostars occurs.

1.5.3 Radiative efficiency of protostars

So far, we have discussed the luminosity problem exclusively through the lens of accretion, while assuming that $f_{\text{acc}} = 1$. This is mainly due to the ad-hoc argument brought forth by the energy balance equation (Eq. 1.32), rather than on a rigorous analysis of the radiative physics of the accretion shock. In addition, pre-main sequence evolution works such as those of Palla & Stahler (1993); Hosokawa & Omukai (2009); Baraffe et al. (2009, 2012, 2017) rely on a *supercritical* shock front to match their models with observations.

Assessing the radiative efficiency of protostars requires a self-consistent modelling of the shock front, in which one describes its formation after the collapse of the first core (i.e., second collapse calculations). Studies having done-so under the assumption of spherical symmetry find that although the first core has a supercritical shock front that radiates away most of the incoming accretion energy, the second core exhibits a strongly subcritical shock front that absorbs most of it into its internal energy budget (e.g., Narita et al. 1970; Commerçon et al. 2011; Bhandare et al. 2018; Vaytet et al. 2013; Bhandare et al. 2020). Although Larson (1969); Winkler & Newman (1980); Masunaga & Inutsuka (2000) did not explicitly measure the radiative efficiency of the shock front, their protostars initially swell to very large radii before quickly contracting. This shows that in their calculations, the protostar’s Kelvin-Helmholtz timescale t_{KH} is initially longer than the accretion timescale t_{acc} . If one assumes that the protostellar interior’s contribution to the total luminosity output is negligible, then $t_{\text{KH}}/t_{\text{acc}} \approx 1/f_{\text{acc}}$. Thus, a contracting protostar in their calculations implies $f_{\text{acc}} \approx 1$.

Expanding the calculations to account for all three dimensions allows for a more realistic measurement of f_{acc} , one which better reflects the accretion shock’s environment. Measurements are once again unfortunately sparse, with Bate et al. (2014) and Vaytet et al. (2018) reporting a strongly subcritical accretion shock ($f_{\text{acc}} \approx 0$), however Vaytet et al. (2018) also note that the polar regions of the protostar radiates much more efficiently.

Although the protostellar accretion shock is the primary means by which luminosity is produced, and hence the means by which we are able to observe star-forming regions, little is known about its radiative behavior and how said behavior changes over time. Providing a self-consistent proof of the supercriticality of the protostellar accretion shock is of fundamental importance to validate a great number of models in star formation.

1.6 This work

Throughout the introduction, I have introduced some of the current challenges in stellar formation theory that have so far eluded a concise answer. These problems could all benefit from a rigorous study of the protostar itself: its interior structure, accretion shock, and circumstellar disk. As such, during my thesis, I have carried out state of

the art self-consistent simulations of the birth of low mass protostars by describing the gravitational collapse of turbulent dense cores, the second collapse following the dissociation of H_2 molecules, and the subsequent entry into the main accretion phase. To do so, the adaptive mesh refinement radiative-magneto-hydrodynamics astrophysical code **RAMSES** (Teyssier 2002) was employed. By performing some of the highest resolution simulations in stellar formation theory, we have described the birth and early evolution of low mass protostars and their circumstellar disks with unprecedented detail. This has allowed us to offer new insight into some of the outstanding issues described in the introduction. The questions tackled during the thesis are the following:

- What are the physical properties of the nascent protostar and its interior?
- What radiative behavior does the protostar exhibit both at birth, and following the formation of a circumstellar disk?
- What is the angular momentum inherited by the protostar following the second gravitational collapse, and how does this quantity evolve as the protostar accretes material from its surroundings?
- How do magnetic fields influence the formation of the protostar, and what insights can the second collapse offer on the magnetic flux problem?
- How do the newly-formed protostar and disk interact with each other, and how do they jointly evolve?

To answer these questions, we first began by carrying out radiative-hydrodynamics simulations in spherical symmetry in order to focus our attention on the nascent protostar, its interior structure, and the radiative behavior of its accretion shock. Following that, we included angular momentum in the dense core by accounting for turbulence, and studied how this influenced the nascent protostar and circumstellar disk. Finally, we carried out our simulations with magnetic fields, both under the ideal and non-ideal approximations, albeit with a much shorter horizon of predictability owing to stringent time-stepping.

I first begin by introducing the theoretical background needed to model the star formation process in Chapter 2, as well as the basic principles of high performance computing and the workings of the **RAMSES** code. The results of my simulations are presented in Chapter 3, alongside any additional theoretical background that aids in understanding them. Finally, I discuss the wider implications of my results, offer my main conclusions, and present my future perspectives in Chapter 4.

Chapter 2

Modelling the star formation process

During the previous chapter, we have introduced the major challenges and issues permeating the field of star formation, all the while presenting a basic overview of the physical processes involved in the birth of stars. In this chapter, we shift our focus to providing the reader with the theoretical baggage required to rigorously model the star formation process. This is by no means meant to be a thorough overview, as each concept addressed in this chapter merits its own lecture, however the reader should obtain a working understanding of the basic physics at play in star formation. In addition, the sheer abundance of complex, non-linear physical processes involved in star formation, many of which are acting across a huge dynamical range, requires one to leverage the ever-increasing amount of computational power available and run sophisticated numerical simulations. For this reason, we have used the **RAMSES** astrophysical code, whose basic functioning and numerical methods will also be presented in this chapter.

2.1 The fluid equations

The gas and dust mixture permeating galaxies and composing molecular clouds can be described under the fluid approximation, which holds so long as the distance between individual particles is smaller than their mean free paths. Due to their incredibly high Reynolds number, they can be described by the *Navier-Stokes equation* under the zero viscosity approximation (i.e., the *Euler equations*). Under their conservative form, these read:

$$\frac{\partial \rho}{\partial t} + \vec{\nabla} \cdot \rho \vec{v} = \vec{0} , \quad (2.1)$$

$$\frac{\partial \rho \vec{v}}{\partial t} + \vec{\nabla} \cdot (\rho \vec{v} \otimes \vec{v} + P \mathbb{I}) = -\rho \vec{\nabla} \phi , \quad (2.2)$$

$$\frac{\partial E_{\text{tot}}}{\partial t} + \vec{\nabla} \cdot [\vec{v}(E_{\text{tot}} + P)] = -\rho \vec{v} \cdot \vec{\nabla} \phi , \quad (2.3)$$

where ρ is the gas density, \vec{v} its velocity, and P its thermal pressure. [Equation 2.3](#) describes the conservation of energy, where E_{tot} is the sum of the internal energy of

the gas (E), and its kinetic energy

$$E_{\text{tot}} = E + \frac{1}{2}\rho v^2 . \quad (2.4)$$

Equation 2.1 is the continuity equation, which describes the conservation of mass, and Equation 2.2 describes the conservation of momentum. In the latter equation, ϕ is the gravitational potential, which may be described via the *Poisson equation*:

$$\nabla^2\phi = 4\pi G\rho . \quad (2.5)$$

These equations govern the fluid's motion, however, they do not have a general closed-formed solution. Note that there are five equations, while the system possesses six unknown variables (ρ , v_x , v_y , v_z , P , and E_{tot}). In order to close the system, an equation of state linking the gas' thermal pressure to its internal energy is required. During this thesis, we have used the tabulated equation of state of [Saumon et al. \(1995\)](#), which describes a gas mixture of 73% H and 27% He. It accounts for the dissociation of H_2 molecules and the ionization of atomic hydrogen and helium.

2.1.1 MHD equations

As mentioned in the introduction, molecular clouds are composed of magnetized fluids. Although in this thesis, we have taken an interest in high density gas which exhibits magnetic subcriticality (i.e., thermal pressure gradient forces far outweigh magnetic pressure forces), magnetic fields nonetheless play a very significant role in the gas' dynamics and must be taken into account when attempting to model the fluid's behavior. Thus, we will describe in this section the equations of magneto-hydrodynamics (MHD). In essence, MHD describes an ionized collisional plasma, where the charged particles' motion create currents sustaining magnetic fields, which in turn generate electric fields through induction. The charged particles in the fluid are subjected to the Lorentz force

$$\vec{F}_L = \vec{j} \times \vec{B} , \quad (2.6)$$

where \vec{j} is the current density.

Ideal MHD

Under the ideal MHD approximation, the fluid is a perfect conductor. Accounting for the magnetic field in this approximation requires one to augment the Euler equations with the Lorentz force. After combining Eq. 2.6 with Maxwell's equations and Ohm's law, the fluid equations for momentum, energy, and magnetic field evolution become (in cgs units):

$$\frac{\partial\rho\vec{v}}{\partial t} + \vec{\nabla} \cdot \left[\rho\vec{v} \otimes \vec{v} + \left(P + \frac{|\vec{B}|^2}{2} \right) \mathbb{I} - \vec{B} \otimes \vec{B} \right] = -\rho\vec{\nabla}\phi , \quad (2.7)$$

$$\frac{\partial E_{\text{tot}}}{\partial t} + \vec{\nabla} \cdot \left[\vec{v} \left(E_{\text{tot}} + P + \frac{|\vec{B}|^2}{2} \right) - \vec{B}(\vec{B} \cdot \vec{v}) \right] = -\rho \vec{v} \cdot \vec{\nabla} \phi, \quad (2.8)$$

$$\frac{\partial \vec{B}}{\partial t} = \vec{\nabla} \times (\vec{v} \times \vec{B}). \quad (2.9)$$

Equation 2.9 is the induction equation, which describes the evolution of the magnetic field as it is advected in the fluid. Under this approximation, *flux freezing* holds, meaning that the magnetic flux of the fluid is conserved irregardless of the distortions of the flow. This means that the magnetic topology is preserved, and the magnetic field is never dissipated. The magnetic flux is expressed as a surface integral over an open surface

$$\phi_B = \int \vec{B} \cdot d\vec{S}, \quad (2.10)$$

and flux freezing can be expressed as

$$\frac{\partial \phi_B}{\partial t} + (\vec{v} \cdot \nabla) \phi_B = 0. \quad (2.11)$$

This shows that during a fluid displacement, the magnetic field frozen in the fluid is displaced alongside it. As such, the magnetic field can be transported and compressed during the flow. In the context of gravitational collapse, flux freezing would cause the magnetic field to scale as $\rho^{2/3}$.

Ambipolar diffusion

Since molecular clouds are weakly ionized, resistive effects need to be accounted for in the MHD equations. One needs to consider the fact that the fluid is made up of neutral species, positively charged ions, and negatively charged electrons. In this thesis, we have accounted for ambipolar diffusion, which adds a heating term in the energy conservation equation and diffuses the magnetic field in the induction equation:

$$\begin{aligned} \frac{\partial E_{\text{tot}}}{\partial t} + \vec{\nabla} \cdot \left[\vec{v} \left(E_{\text{tot}} + P + \frac{|\vec{B}|^2}{2} \right) - \vec{B}(\vec{B} \cdot \vec{v}) \right. \\ \left. - \frac{\eta_A c^2}{4\pi |\vec{B}|^2} [((\vec{\nabla} \times \vec{B}) \times \vec{B}) \times \vec{B}] \times \vec{B} \right] = -\rho \vec{v} \cdot \vec{\nabla} \phi, \end{aligned} \quad (2.12)$$

$$\frac{\partial \vec{B}}{\partial t} = \vec{\nabla} \times (\vec{v} \times \vec{B}) + \vec{\nabla} \times \left[\frac{\eta_A c^2}{4\pi |\vec{B}|^2} ((\vec{\nabla} \times \vec{B}) \times \vec{B}) \times \vec{B} \right] \quad (2.13)$$

One can see that the ideal MHD limit is recovered when $\eta_A \rightarrow 0$. In order to obtain η_A , a resistivity table from [Marchand et al. \(2016\)](#) is used. The table provides the resistivity as a function of density, temperature, and magnetic field strength, which allows for on-the-fly interpolations in each computational cell during the simulation. It originates from a chemical network accounting for neutral and charged species in the gas, as well as dust grains which can catalyze certain chemical reactions. These grains

may also carry the electrical charge themselves, their size distribution in [Marchand et al. \(2016\)](#) are described by the MRN ([Mathis et al. 1977](#)) size distribution. The resistivities also depend on the cosmic ray ionization rate, which is assumed to be the fiducial value of 10^{-17} s^{-1} ([Spitzer & Tomasko 1968](#); [Pineda et al. 2024](#)).

2.1.2 Virial theorem

The birth of stars begins when gravity outweighs all other forces. A useful tool allowing for the study of the stability of structures in the Universe is the *Virial theorem analysis*, which may be applied to dense cores or any other object in which one expects a semblance of *hydrostatic equilibrium*. Under the ideal MHD approximation, the non-conservative form of the momentum equation can be written as (from [Eq. 2.7](#))

$$\rho \left[\frac{\partial \vec{v}}{\partial t} + (\vec{v} \cdot \nabla) \vec{v} \right] = -\nabla P - \rho \nabla \phi - \nabla \left(\frac{B^2}{8\pi} \right) + \frac{(\vec{B} \cdot \nabla) \vec{B}}{4\pi}, \quad (2.14)$$

where we have simply re-written the Lorentz force in [Eq. 2.7](#) as the sum of a tension and pressure term. Since we are interested in deriving a global equilibrium from this equation (which expresses a local behavior), we multiply it by the position vector \vec{r} and integrate it over a volume. Under the simplifying assumption that the medium is uniform and isotropic, and by taking the first order moment of [Eq. 2.14](#), this yields

$$\frac{1}{2} \frac{d^2 I}{dt^2} = 2E_{\text{kin}} + 2E_{\text{ther}} + E_{\text{grav}} + E_{\text{mag}}, \quad (2.15)$$

where E_{kin} , E_{ther} , E_{grav} , and E_{mag} are respectively the kinetic, thermal, gravitational, and magnetic energy contained within the volume. They are expressed as

$$E_{\text{kin}} = \frac{1}{2} \int \rho v^2 dV, \quad (2.16)$$

$$E_{\text{ther}} = \frac{1}{\gamma - 1} \int P dV, \quad (2.17)$$

$$E_{\text{grav}} = \frac{1}{2} \int \rho \phi dV, \quad (2.18)$$

$$E_{\text{mag}} = \frac{1}{8\pi} \int B^2 dV, \quad (2.19)$$

where γ is the gas' adiabatic index and dV is a volume element. I is the moment of inertia

$$I = \int \rho r^2 dV. \quad (2.20)$$

On the right hand side of [Eq. 2.15](#), all elements barring E_{grav} are positive. Stability against collapse implies that the sum of the kinetic, thermal, and magnetic components in [Eq. 2.15](#) are greater than $-E_{\text{grav}}$. Thus, this is equivalent to $d^2 I / dt^2 \geq 0$.

The Virial theorem thus allows one to measure an object's stability against collapse through energy measurements, which is convenient in large numerical simulations as said energy measurements are simple to perform.

2.1.3 Hydrostatic equilibrium

The defining characteristic of stars, protostars, and dense cloud cores, is the fact that a balance is reached between thermal pressure gradient forces and gravity. Since said thermal pressure gradients are isotropic, this will naturally cause the hydrostatic object to assume a spherical shape. A force balance thus yields

$$\frac{1}{\rho} \frac{\partial P}{\partial r} = -\frac{\partial \phi}{\partial r} . \quad (2.21)$$

Inserting Poisson's equation (Eq. 2.5) into the above expression yields

$$-\frac{1}{r^2} \frac{\partial}{\partial r} \left(\frac{r^2}{\rho} \frac{\partial P}{\partial r} \right) = 4\pi G \rho . \quad (2.22)$$

Solving this equation requires an assumption of an equation of state. Generally, a polytropic equation of state $P = K\rho^\gamma$ is used, which leads to the famous Lane-Emden equations modelling the interior of stars. If an isothermal equation of state is used ($\gamma = 1$), this leads to the famous singular isothermal sphere profile of Shu (1977), which is often used to model dense cloud cores.

The attainment of hydrostatic equilibrium following the second gravitational collapse is what defines the birth of the protostar. It is also hydrostatic equilibrium that dictates its interior structure, as well as its evolution over time.

2.2 Radiative transfer

As previously mentioned, the birth of stars is heavily affected by radiative processes that considerably change the thermodynamical behavior of the gas. However, accounting for this fundamental process is difficult, and many studies crudely mimic its effects using a barotropic equation of state, whereby the gas' pressure depends only on density. In this section, we will provide the basics of radiation hydrodynamics (RHD). The concepts and equations presented here have been described more exhaustively by Mihalas & Mihalas (1984); González et al. (2006); Commerçon (2009), and González et al. (2015), from which we draw heavy inspiration.

We first begin by introducing some basic definitions. The specific intensity I describes the transport of photons across space and time. It is described by 3 spatial coordinates, a solid angle coordinate, the photon frequency, and time. Hence, $I = I(\vec{r}, \vec{n}, \nu, t)$, where \vec{r} is the position vector, \vec{n} the radiation propagation directional vector, t the time, and ν the radiation frequency.

Astrophysical media have a defined temperature and as such their radiation fields may be described by the *Planck function*

$$B_\nu(T) = \frac{2h\nu^3}{c^2 (e^{h\nu/k_B T} - 1)} , \quad (2.23)$$

where h is the Planck constant, k_B the Boltzmann constant, and c the speed of light. B_ν describes a specific intensity, and the associated radiative energy density may be obtained by integrating it across all frequencies (i.e., *Stefan-Boltzmann's law*)

$$E_r = \frac{4\pi}{c} \int_0^\infty B_\nu(T) d\nu = a_R T^4 , \quad (2.24)$$

where a_R is the radiation constant.

When radiation passes through a medium such as an astrophysical gas, it interacts with it through absorption, emission, and scattering processes. Absorption and scattering decrease the specific intensity I of the radiation field as light propagates through the gas; a process known as *extinction* (Mihalas & Mihalas 1984). The amount of extinction can be described by the *extinction coefficient* χ :

$$\chi(\vec{x}, \vec{n}, \nu, t) = \kappa(\vec{x}, \vec{n}, \nu, t) + \sigma(\vec{x}, \vec{n}, \nu, t) , \quad (2.25)$$

where κ is the thermal absorption coefficient and σ is the scattering coefficient. Generally, two absorption coefficients are considered: the Planck mean opacity κ_P and Rosseland mean opacity χ_R

$$\kappa_P = \frac{\int \kappa(\nu) B_\nu d\nu}{\int B_\nu d\nu} , \quad (2.26)$$

$$\chi_R = \frac{\int \frac{\partial B_\nu}{\partial T} d\nu}{\int \frac{1}{\chi(\nu)} \frac{\partial B_\nu}{\partial T} d\nu} . \quad (2.27)$$

Often, radiative hydrodynamics neglects scattering for added computational performance, and only the absorption coefficients are considered. In this case, the Rosseland mean opacities is written as κ_R . During this thesis, scattering was neglected. The reason why mean opacities are used is the greatly improved computational performance it provides. The different weighing schemes used in κ_P and κ_R allows one to describe different regimes of the radiation field: the latter is valid in the *diffusion limit*, where the photon mean free path is shorter than all other length scales of the system and the radiation field displays an isotropic behavior, whereas the former is more valid in the *free streaming limit*.

Since the absorption coefficient varies widely according to the astrophysical environment, it is helpful to measure a medium's extinction using the optical depth τ :

$$\tau = \int_0^l \chi dl , \quad (2.28)$$

where l is the total length of propagation through the medium. A region having an optical depth of $\tau \approx 0$ is referred to as an *optically thin region*, whereas a region with $\tau \gg 1$ is referred to as an *optically thick region*. The emissions of the medium may similarly be expressed by an *emissivity coefficient*

$$\eta(\vec{x}, \vec{n}, \nu, t) = \eta_{\text{th}}(\vec{x}, \vec{n}, \nu, t) + \eta_{\text{S}}(\vec{x}, \vec{n}, \nu, t) , \quad (2.29)$$

where η_{th} and η_{S} are respectively the thermal and scattering components. This allows us to write the radiative transfer equation

$$\left[\frac{1}{c} \frac{\partial}{\partial t} + \vec{n} \cdot \vec{\nabla} \right] I(\vec{x}, \vec{n}, \nu, t) = \eta(\vec{x}, \vec{n}, \nu, t) - \chi(\vec{x}, \vec{n}, \nu, t) I(\vec{x}, \vec{n}, \nu, t) . \quad (2.30)$$

Essentially, the above equation describes the evolution of the specific intensity across space and time: energy is gained through emissive processes, lost through absorption, and re-distributed through scattering. It displays an asymptotic behavior; at high opacities, the *diffusion limit* is reached where photons interact very intensely with the medium in which they are embedded. At low opacities, the *transport limit* is reached, where the photons are freely streaming and seldom interact with their host medium.

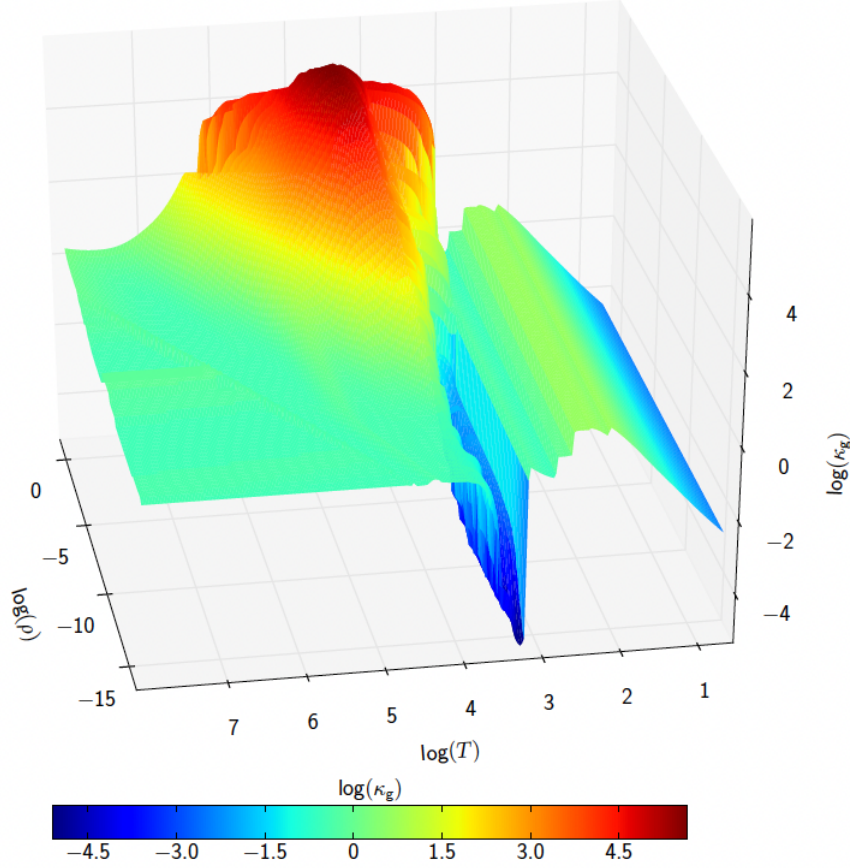


Figure 2.1: Rosseland mean opacities integrated across the $[10^5; 10^{19}]$ Hz frequency range and displayed as a function of (ρ, T) . Image taken from [Vaytet et al. \(2013\)](#).

Opacities

Determining χ requires a detailed knowledge of the gas and dust composition of the medium. During this thesis, we have used the opacity table pieced together by [Vaytet et al. \(2013\)](#), which provides the opacity of the fluid in densities of $[10^{-19}; 10^2]$ g cm^{-3} and temperatures of $[5; 10^7]$ K. The opacities were originally produced by [Semenov et al. \(2003\)](#); [Ferguson et al. \(2005\)](#); [Badnell et al. \(2005\)](#), and describe respectively the opacities of interstellar dust grains (which are assumed to be spherical grains of silicate), molecular gas, and atomic gas. At $T < 1500$ K, the opacity of the interstellar medium is dominated by dust grains, which make up approximately 1% of the mass

content of the fluid and are described by an MRN size distribution (Mathis-Rumple-Nordsie, Mathis et al. 1977). Above 1500 K, H_2 dominates the opacities of the fluid, and after its dissociation at ~ 2000 K, the atomic opacities dominate.

During a simulation, the Plank and Rosseland mean opacities need to be computed as a function of (ρ, T) for each photon frequency. The approach taken by Vaytet et al. (2013) is to compute an opacity table for each spectral bin using Delaunay triangulation, from which κ_{R} and κ_{P} may be easily interpolated during the simulation. Figure 2.1 displays the opacity table of Vaytet et al. (2013) in the *gray approximation*, i.e., integrated across all frequencies. This is the opacity table that we have used in the vast majority of our simulations.

2.2.1 Flux limited diffusion approximation

Integrating the radiative transfer equations with all six degrees of freedom is extremely demanding computationally, and almost impossible to perform within hydrodynamical simulations with current computational hardware. Indeed, this would require the use of Monte-Carlo based methods or ray-traced algorithms that solve the radiative transfer equation across space and time with frequency-dependence. Although very accurate, from a computational standpoint this is orders of magnitude costlier than solving the hydrodynamical equations. As such, accurate radiative transfer schemes are reserved for post-processing purposes, where one would produce synthetic observations of simulated objects. Within RHD simulations, approximations are often used to significantly reduce the computational cost. The approximation used during this thesis is the *flux limited diffusion approximation*, which essentially consists in reducing the radiative transfer equation to a diffusion equation by taking the zeroth order moment of Eq. 2.30. This is of course valid in the *diffusion limit* (i.e., in regions of high optical depth), however its accuracy diminishes in the *free-streaming limit* (i.e., optically thin regions) as the isotropic nature of the radiation field in this limit is no longer valid. Accounting for radiative transfer under the FLD approximation consists of augmenting the momentum equation with a radiative force term, the energy equation with the work done by said force and the radiative pressure, and solving for a radiative energy equation (Commerçon et al. 2011, 2014; González et al. 2015):

$$\frac{\partial \rho \vec{v}}{\partial t} + \vec{\nabla} \cdot [\rho \vec{v} \otimes \vec{v} + P \mathbb{I}] = -\rho \vec{\nabla} \phi - \lambda \vec{\nabla} E_r, \quad (2.31)$$

$$\frac{\partial E_{\text{tot}}}{\partial t} + \vec{\nabla} \cdot [\vec{v}(E_{\text{tot}} + P)] = -\rho \vec{v} \cdot \vec{\nabla} \phi - \lambda \vec{v} \cdot \vec{\nabla} E_r - \kappa_{\text{P}} \rho c (a_{\text{R}} T^4 - E_r), \quad (2.32)$$

$$\frac{\partial E_r}{\partial t} + \vec{\nabla} \cdot (\vec{v} E_r) + \mathbb{P}_r : \vec{\nabla} v = \kappa_{\text{P}} \rho c (a_{\text{R}} T^4 - E_r) - \vec{\nabla} \cdot \vec{F}_r, \quad (2.33)$$

where \vec{F}_r is the radiative flux vector, which under the FLD approximation is

$$\vec{F}_r = -\frac{c \lambda \vec{\nabla} E_r}{\rho \kappa_{\text{R}}}. \quad (2.34)$$

Here, λ is the Minerbo flux limiter (Minerbo 1978), which regulates \vec{F}_r to ensure causality in the diffusion and free-streaming limits according to

$$\lambda = \begin{cases} 2 / \left(3 + \sqrt{9 + 12R^2} \right) , & \text{if } 0 \leq R \leq 3/2 \\ \left(1 + R + \sqrt{1 + 2R} \right)^{-1} , & \text{if } 3/2 < R \leq \infty \end{cases} \quad (2.35)$$

where $R = |\nabla E_r| / (\kappa_r E_r)$. Under the *diffusion limit*, $\lambda \rightarrow 1/3$ and in the *free-streaming limit*, $\lambda \rightarrow 1/R$. This causes the radiative flux to reach $-c\nabla E_r / 3\kappa_R$ in optically thick regions (i.e., radiative energy is diffused isotropically), and cE_r in optically thin regions (i.e., radiative energy is simply advected at the speed of light).

\mathbb{P}_r is the radiative pressure tensor, given by

$$\mathbb{P}_r = \left(\frac{1 - \chi}{2} \mathbb{I} + \frac{3\chi - 1}{2} \vec{n} \otimes \vec{n} \right) E_r , \quad (2.36)$$

where χ is given by (Levermore 1984)

$$\chi = \lambda + \lambda^2 R^2 . \quad (2.37)$$

Under the *diffusion limit*, \mathbb{P}_r becomes isotropic and reaches a value of $E_r/3$.

Solving the RHD equations in RAMSES is done in a two step approach: firstly, the mass, momentum and energy equations are solved using an explicit scheme (see Sec. 2.3) while accounting for radiative terms, and the radiative energy equation is solved implicitly using a conjugate gradient method (Commerçon et al. 2011, 2014).

Multigroup flux limited diffusion

In the previous section, we have presented the FLD method in the *gray approximation* in which we have considered a single spectral bin. In RAMSES, the *multigroup FLD* approach has also been implemented by González et al. (2015), which allows for one to consider multiple photon frequencies. This can be particularly useful when doing second collapse calculations, as the temperature range causes a large spread in photon frequencies being produced. The multigroup FLD equations are the more general form of those presented in the previous section:

$$\frac{\partial \rho \vec{v}}{\partial t} + \vec{\nabla} \cdot [\rho \vec{v} \otimes \vec{v} + P \mathbb{I}] = -\rho \vec{\nabla} \phi - \sum_{g=1}^{N_g} \lambda_g \vec{\nabla} E_g , \quad (2.38)$$

$$\frac{\partial E_{\text{tot}}}{\partial t} + \vec{\nabla} \cdot [\vec{v}(E_{\text{tot}} + P)] = -\rho \vec{v} \cdot \vec{\nabla} \phi - \sum_{g=1}^{N_g} \left[\kappa_{P_g} \rho c (\Theta_g(T) - E_g) - \lambda_g \vec{v} \cdot \vec{\nabla} E_g \right] , \quad (2.39)$$

$$\frac{\partial E_g}{\partial t} + \vec{\nabla} \cdot [\vec{v} E_g] + \mathbb{P}_g : \vec{\nabla} \vec{v} = \vec{\nabla} \cdot \left[\frac{c \lambda_g}{\rho \kappa_{R_g}} \vec{\nabla} E_g \right] + \kappa_{P_g} \rho c (\Theta_g(T) - E_g) + \vec{\nabla} \vec{v} : \int_{\nu_{g-1/2}}^{\nu_{g+1/2}} \partial_\nu (\nu \mathbb{P}_\nu) d\nu , \quad (2.40)$$

where N_g is the total number of spectral bins, E_g the radiative energy within a spectral bin, and Θ_g is the energy carried by photons that have a Planck distribution inside their spectral bin. Solving for the radiative energy equation in the multigroup approach requires the use of a bi-conjugate gradient method (van der Vorst & Melissen 1990; González et al. 2015).

The multigroup approach offers greater fidelity, as it can account for multiple photon frequencies. However, it significantly increases the computational cost, as the radiative energy equation has to be solved for multiple spectral bins.

2.3 Numerical methods

In physics, a primary function of a theory is to be able to make predictions that are later validated by experiments. In astrophysics, it is not possible to do so, as we lack the means to manipulate the heavens, and so laboratory astrophysics is rather small compared to other fields of physics. In addition, astrophysical phenomena span huge timescales when compared to human lifetimes, and as we have shown countless times in this manuscript, they involve a complex interplay of numerous physical processes that render analytical modelling incredibly challenging. As such, numerical simulations have become a cornerstone of theoretical astrophysics, allowing theorists to model complex phenomena through billions upon billions of calculations per second¹. The results of these simulations are then compared to observations, which allows for a fine-tuning of the model, or in the case of gross mismatch, a complete revision. This has allowed for countless breakthroughs in our understanding of astrophysical phenomena, and the unabated increase in computing power will undoubtedly usher-in more breakthroughs. In this section, we will provide an overview of the basic principles behind creating and running a simulation.

2.3.1 Time discretization

Simulations describe the evolution of a physical model over discrete time intervals. Let \vec{U} be a vector containing all relevant variables of the system (e.g., density, momentum, energy, etc...), and \vec{F} the vector that describes its evolution over time:

$$\frac{d\vec{U}}{dt}(t) = \vec{F}(\vec{U}(t), t) . \quad (2.41)$$

Discretizing the above equation in time yields

$$\frac{d\vec{U}}{dt}(t) = \frac{\vec{U}(t + \Delta t) - \vec{U}(t)}{\Delta t} + O(\Delta t) . \quad (2.42)$$

Plugging the above equation back into Eq. 2.41 yields

$$\vec{U}(t + \Delta t) = \vec{U}(t) + \vec{F}(\vec{U}(t), t)\Delta t + O(\Delta t^2) . \quad (2.43)$$

¹As of the writing of this manuscript, we have just reached the era of the *exascale*, meaning that supercomputers can now perform a staggering 10^{18} floating point operations per second.

This is known as an *explicit* time integration scheme, in which obtaining the state of the system at $t + \Delta t$ requires knowledge of the system at t . This scheme is generally straightforward to implement, however it is known to be numerically unstable unless a sufficiently small timestep is used. Indeed, stability in explicit discretization schemes requires one to satisfy the Courant-Friedrichs-Lewy (CFL) condition, which states that a signal travelling at speed a cannot cross more than a single cell of size Δx in a timestep:

$$\Delta t \leq \frac{\Delta x}{a} \quad (2.44)$$

In the particular case of solving the Euler equations in 1D, the CFL condition is:

$$\Delta t \leq \frac{\Delta x}{v + c_s} , \quad (2.45)$$

where c_s is the sound speed, and v the fluid velocity.

We may also write a different scheme:

$$\vec{U}(t + \Delta t) = \vec{U}(t) + \vec{F}(\vec{U}(t + \Delta t), t + \Delta t)\Delta t + O(\Delta t^2) , \quad (2.46)$$

which is known as an *implicit* time integration scheme. The advantage of this scheme over its *explicit* counterpart is that it offers unconditional numerical stability, however it requires one to solve a simultaneous set of equations, which in complex systems tends to be a daunting task.

2.3.2 Finite volume method

In the previous section, we have discussed the time discretization of our system of equations. Here, we will discuss the spatial discretization that is employed in **RAMSES**; the *finite volume method*.

We may write the previously presented conservative form of the hydrodynamics equations as

$$\frac{\partial \vec{U}}{\partial t} + \vec{\nabla} \cdot \vec{F}(\vec{U}) = 0 \quad (2.47)$$

where \vec{U} is a state vector containing the conservative variables, and \vec{F} is the flux vector that is linearly reconstructed from \vec{U} . In the particular case of the Euler equations in their conservative form (equations 2.1, 2.2, and 2.3), the state and flux vectors are $\vec{U} = (\rho, \rho\vec{v}, E)$ and $\vec{F} = (\rho\vec{v}, \rho\vec{v} \otimes \vec{v} + P\mathbb{I}, \vec{v}(E + P))$. Should we discretize the spatial domain the same way as we have done in time, then we would be employing a scheme known as the *finite differences method*, which fails to conserve the conservative variables of the system. This would result in a very diffusive and unstable scheme, one that particularly fails to describe shock fronts. The *finite volume method* on the other hand, divides the spatial domains into cells rather than fixed grid points, on which an average value of a conserved quantity U is evaluated. In 1D, this reads:

$$U_i = \frac{1}{\Delta x} \int_{x_{i-1/2}}^{x_{i+1/2}} U dx , \quad (2.48)$$

where $\Delta x = x_{i+1/2} - x_{i-1/2}$ (see panel (a) of Fig. 2.2). This method is designed to correctly reproduce the structure of discontinuous solutions, and as such is used in almost all Eulerian hydrodynamics codes in astrophysics.

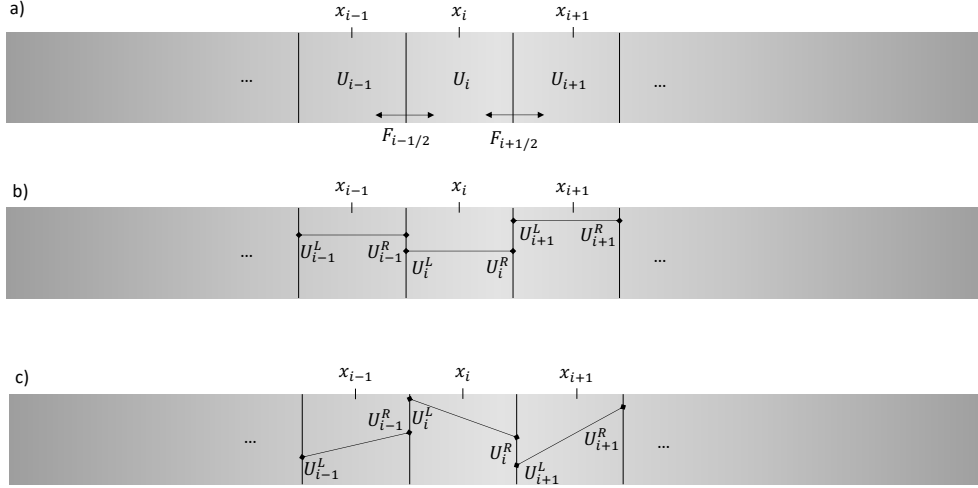


Figure 2.2: Schematic representation of the finite volume method, in which conservative quantities are averaged within cells (a). The flux can be recovered using a piecewise constant (b) or piecewise linear (c) reconstruction. Higher order schemes use parabolic flux reconstructions.

Godunov's method

In order to solve the general form of the hydrodynamical equations, we integrate Eq. 2.47 over space and time, which yields

$$\int_{x_{i-1/2}}^{x_{i+1/2}} \int_{t^n}^{t^{n+1}} \left(\frac{\partial \vec{U}}{\partial t} + \vec{\nabla} \cdot \vec{F}(\vec{U}) \right) dx dt = 0 . \quad (2.49)$$

In a 1D system, the above equation yields

$$\frac{1}{\Delta t} (\vec{U}_i^{n+1} - \vec{U}_i^n) = -\frac{1}{\Delta x} (\vec{F}_{i+1/2} - \vec{F}_{i-1/2}) , \quad (2.50)$$

where $\vec{F}_{i\pm 1/2}$ is the flux crossing the cell interface:

$$\vec{F}_{i\pm 1/2} = \int_{t^n}^{t^{n+1}} \vec{F}(\vec{U}_{i\pm 1/2}) dt . \quad (2.51)$$

In essence, Eq. 2.50 states that the average value of a conserved quantity in a given cell changes according to the net change between the incoming and outgoing fluxes, which are evaluated at the cell interfaces (hence the $\pm 1/2$ subscripts, see panel (a) of Fig. 2.2). The problem is thus reduced to reconstructing the state vector \vec{U} at each cell

interface and computing the numerical flux across it. This method, called *Godunov's method* (Godunov & Bohachevsky 1959), is particularly useful in hydrodynamics, as the numerical flux is conserved to machine precision and thus can be applied to solving the Euler equations in their conservative form.

There are a number of ways to reconstruct \vec{U} at each cell interface. For instance, one may consider a constant value for \vec{U} inside the cell (*piecewise constant reconstruction*), or a linear function with a slope (*piecewise linear reconstruction*), or for even higher order schemes, polynomial functions are considered (*piecewise parabolic reconstruction*). The first two geometrical reconstructions of the state vector \vec{U} are illustrated in panels (b) and (c) of Fig. 2.2.

Riemann problem

Irregardless of the manner in which the state vector \vec{U} is reconstructed, a discontinuity exists at each cell interface, and computing the correct numerical flux across said discontinuity is a problem known as the *Riemann problem*. Solving the Riemann problem requires one to estimate the speed of the characteristic waves of the system. Each of these wave speeds may be represented as an eigenvalue of the Jacobian matrix A of \vec{F} :

$$\frac{\partial \vec{U}}{\partial t} = -A(\vec{U}) \vec{\nabla} \cdot \vec{U} . \quad (2.52)$$

The characteristic wave speeds of the system are therefore the eigenvalues of $A(\vec{U})$. In a purely hydrodynamical case (i.e., solving the Euler equations), there are three wave speeds to consider: a contact discontinuity (sometimes called the entropy wave) travelling at velocity v , and the nature of the two other waves depends on the setup at play. For instance, these may be a shock wave travelling at velocity $v + c_s$ and a rarefaction wave traveling at $v - c_s$.

In a fully three-dimensional MHD simulation, one needs to consider a total of seven eigenvalues, representing two fast and two slow magneto-sonic waves, two Alfvén waves, and the contact discontinuity. The magneto-sonic wave speed can be expressed as

$$v_{\text{ms}} = \frac{1}{\sqrt{2}} \sqrt{c_s^2 + v_A^2 \pm \sqrt{(c_s^2 + v_A^2)^2 - 4c_s^2 v_{A,x}^2}} , \quad (2.53)$$

where c_s is the gas sound speed and $v_A = B/\sqrt{4\pi\rho}$ is the Alfvén speed. Considering all seven eigenvalues is costly, as a large number of iterations needs to be performed. This may prove to be too costly when running a simulation, and as such, *approximate Riemann solvers* are used. One example is the *Roe solver*, which linearizes the Jacobian matrix and estimates all characteristic wave speeds. Other solvers, although more approximate, greatly alleviate the numerical cost by considering a curated selection of these waves. For instance, the HLL (Harten–Lax–van Leer) solver considers only the fast magneto-sonic waves, whereas HLLC (Harten–Lax–van Leer with contact) also considers the contact discontinuity. In our RAMSES simulations, we have used the HLLD solver, which is similar to HLLC but also accounts for the Alfvén waves.

Flux limiters

When using schemes of second order and above, capturing strong discontinuities and shock fronts in the flow causes spurious oscillations to develop. This is because of *Godunov's theorem*, which states that in order for a numerical scheme to be *Total Variation Diminishing* (TVD, i.e., not producing spurious oscillations), then it must be at most first order accurate (Harten 1983). In order to obtain higher accuracy for smooth solutions while avoiding spurious oscillations around shock fronts, *flux limiters* are used. These allow for the use of higher order schemes when smooth waves are present, and limit the numerical flux using lower order schemes in the presence of strong gradients in order to preserve TVD. Various flux limiters are available, the most popular of which are *minmod*, *superbee* (Roe 1986), and *Van-Leer* (van Leer 1974). In our RAMSES simulations, we have used the *minmod* flux limiter. Note that in second order schemes in which a *piecewise linear reconstruction* is used, flux limiters are often referred to as *slope limiters*, as limiting the numerical flux implies changing the slope of the reconstruction within each cell.

2.3.3 Parallel computing

When running a simulation, the calculations can be divided into many smaller independent tasks that may be executed simultaneously rather than in sequence. The results of each independent task are then combined to obtain a final global result. When the memory requirements of a simulation are such that they cannot be run on a single computer (or node if run on a cluster), then the CPUs must operate with distributed (i.e., not shared) memory, and information relevant to the calculations such as boundary conditions for instance, need to be communicated (see Fig. 2.3). This is the basic principle of *parallel computing*, which has proven to be particularly useful in *computational fluid dynamics* where calculations need to be performed on a large number of cells or particles, and thus whose calculations stand to benefit greatly from parallelism. CPU communications are handled through the Message Passing Interface (MPI), which allows the code to scale with an increasing number of processors.

Load balancing

When performing simulations that run in parallel, the workload of each CPU has to be determined in a manner that ensures its equal distribution, which would allow for better scalability and optimal performance. In astrophysical codes however, this is often difficult to achieve, particularly when attempting to simulate the birth of stars, as the highly dynamical gravitational collapse tends to concentrate the vast majority of the mass of the system in a very small volume. This often leads to a phenomena called *load imbalance*, where underloaded CPUs need to wait for overloaded CPUs to finish their computations before proceeding to the next iteration. Load imbalance is unfortunately unavoidable in many star formation simulations, and the ultimate goal of *load balancing* is to reduce CPU idle time as much as possible.

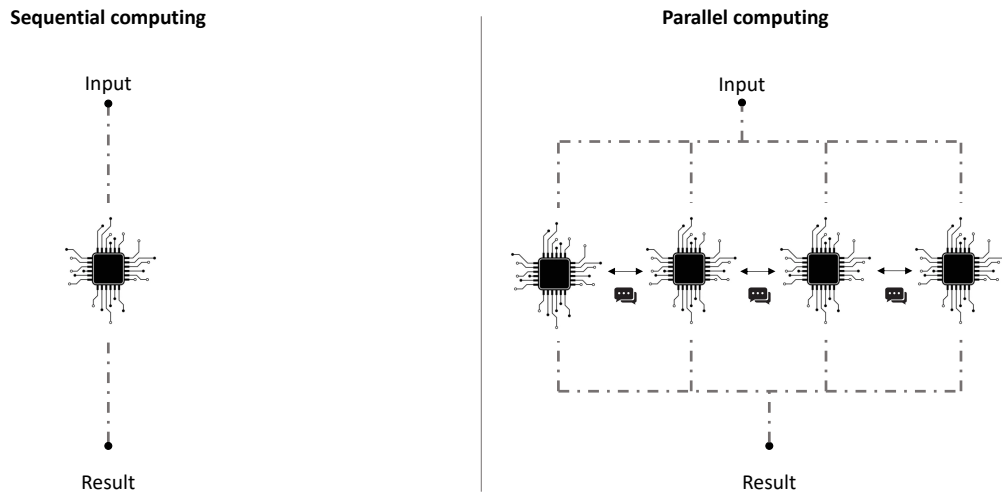


Figure 2.3: Schematic representation of the basics of parallel computing. Instead of performing a single task on a CPU (left), the task is split into independent parts that are treated simultaneously by multiple CPUs, the results of which are combined in the end (right). In the case where the memory pool is not shared, the CPUs communicate any information relevant to their calculations.

2.3.4 The RAMSES astrophysical code

During this thesis, we have used the RAMSES MHD code (Teyssier 2002). This Eulerian hydrodynamics code makes use of the finite volume method. Since its first release in 2002, it has over the years been enhanced with a large cast of modules that allow it to treat a wide variety of astrophysical phenomena: cosmological simulations (e.g., Kaviraj et al. 2017; Chabanier et al. 2020), galaxy simulations (e.g., Teyssier et al. 2010), star formation (e.g., Vaytet et al. 2018; Lebreuilly et al. 2021; Colman et al. 2024), among other applications. In this section, we will present the basic functioning and features of this code.

Adaptive Mesh Refinement

The most important feature RAMSES has to offer is adaptive mesh refinement (AMR). As mentioned previously, star formation is a highly dynamical process in which one must consider a huge dynamical range, both in density and in spatial extent. As such, it is impossible to simulate the birth of stars with a uniform, fixed grid. AMR allows one to increase the resolution in regions of interest (such as high density gas in the collapsing cloud), while maintaining a coarser resolution in regions that do not require finer details (see Fig. 2.4). This allows for a huge gain in computational time, while also significantly alleviating the memory constraints of simulations.

During a simulation, **RAMSES** continuously checks each cell and flags them for refinement according to a user-specified criterion (generally, one based on the local Jeans length). Should a cell be flagged, it is then subdivided into eight finer cells. This process is repeated throughout the simulation until the maximum refinement level is reached. Note that cells can also be flagged for de-refinement during the simulation. This hierarchy of cells is organized in a *tree-based structure* (Khokhlov 1998), and load balancing within it is done by decomposing the simulation domain along a Hilbert space-filling curve.

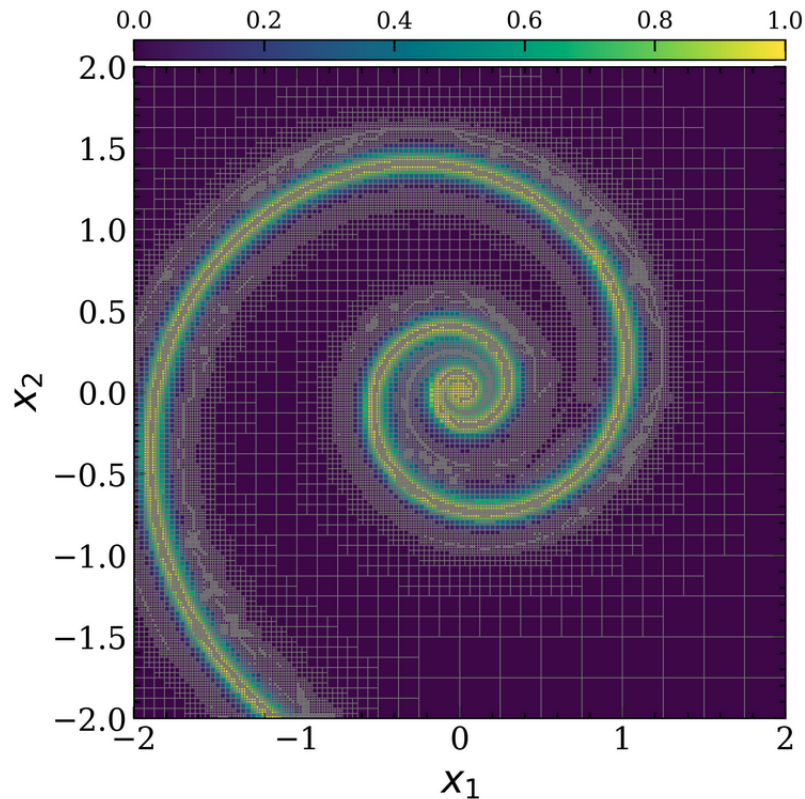


Figure 2.4: Example of an AMR grid. Image taken from the [NDTAMR repository](#).

Sub-cycling

Since AMR allows for regions of the simulation to be described with varying levels of refinement, they do not all possess the same timestep constraints. Finer levels have more stringent CFL conditions, and the coarser levels need not be updated with such small timesteps. The usage of *sub-cycling* in **RAMSES** allows for the coarser levels to maintain their more lenient timesteps, essentially remaining idle while finer levels perform their calculations, saving an invaluable amount of computation time in the process. The time step at each level ℓ however, needs to be synchronized with the finer levels by remaining a multiple of 2 of finer timesteps. As such, the timestep at each level is a multiple of 2 of that in finer levels.

Constrained transport

RAMSES solves for the MHD equations, which adds a significant challenge as one has to ensure that the divergence-free condition of the magnetic field is met. For this, the code uses the constrained transport scheme (Evans & Hawley 1988; Fromang et al. 2006), where the induction equation is re-written using the Stokes theorem as

$$\frac{\partial}{\partial t} \int_S \vec{B} \cdot d\vec{s} = - \int_l (\vec{B} \times \vec{v}) \cdot d\vec{l} . \quad (2.54)$$

By using this approach, the magnetic field components are computed at the cell interfaces using an evaluation of the electromotive force on cell edges. By summing said force across all cell interfaces, the integral cancels out and the divergence-free condition of the magnetic field is met to machine precision.

2.4 Analyzing and visualizing simulated astrophysical data

When running astrophysical simulations, terabytes of data are created and dumped into a hard-drive. The data then needs to be visualized and analyzed in order to extract a meaningful physical interpretation from the simulation. However, owing to the complicated grid structure found in AMR simulations, as well as the sheer volume of data to comb through, analyzing simulation data requires one to use a variety of data analysis techniques. The purpose of this section is to present how I tackled the problem by showcasing some of the most common data visualizations and analysis techniques that I used during my thesis. The **Osyris** python software was my preferred tool to read and visualize RAMSES data, although the techniques presented here are not exclusive to it and may be used in a variety of softwares.

2.4.1 Parallelized data analysis

In modern times, astrophysical simulations are generating an ever increasing amount of data. This makes analyzing the raw output of the simulations ever more challenging, and conventional methods are proving to be increasingly time-consuming. I was confronted with this problem early in my thesis, where each of my simulations produced thousands of snapshots of $\sim 3-4$ GB, totaling $\sim 3-4$ TB, and the prospects of waiting an increasing amount of hours for my post-processing pipelines to complete hindered my performance. I thus set-out to create a parallelized post-processing pipeline using MPI, which proved immensely useful in speeding-up my data analysis routines.

Generally, most post-processing tasks are embarrassingly parallel since the hold-up is simply the fact that a single processor has to comb through hundreds (if not thousands) of simulation outputs. As such, these do not require MPI parallelism as no communication between CPUs is required. However, some tasks are so intensive in RAM memory consumption that parallelism is required in order to spread said RAM

memory across multiple nodes. This is generally done with very heavy simulations, where CPUs spread across different nodes will read different domains of the simulation in order to alleviate RAM memory constraints, and then communicate any information relevant to the calculations. Finally, a post-processing pipeline parallelized with MPI may still be used in embarrassingly parallel tasks owing to its versatility. A schematic overview of the post-processing pipeline is shown in Fig. 2.5. The first step consists of probing the simulation outputs, and the workload is distributed across all CPUs. Ideally, the workload may be distributed according to the output folder size, as that would offer greater scalability, however I have found it much simpler to distribute an equal number of folders to each CPU, as that ensures that said CPU is handling a non-discontinuous simulation time span. Once the workload is distributed, each output folder is read iteratively and the user’s set of instructions is executed. If necessary, communications between CPUs may be performed during this step. Once the tasks are executed, the post-processing results are saved to disk. This parallelized pipeline allowed me to obtain significant speed-ups in analyzing RAMSES simulations. The entire simulation could be post-processed in minutes instead of dozens of hours. Although most post-processing applications are embarrassingly parallel, the framework I have built during this thesis may be expanded upon in the future to handle increasingly heavy simulations. A bare-bones version of it is accessible via [github](#).

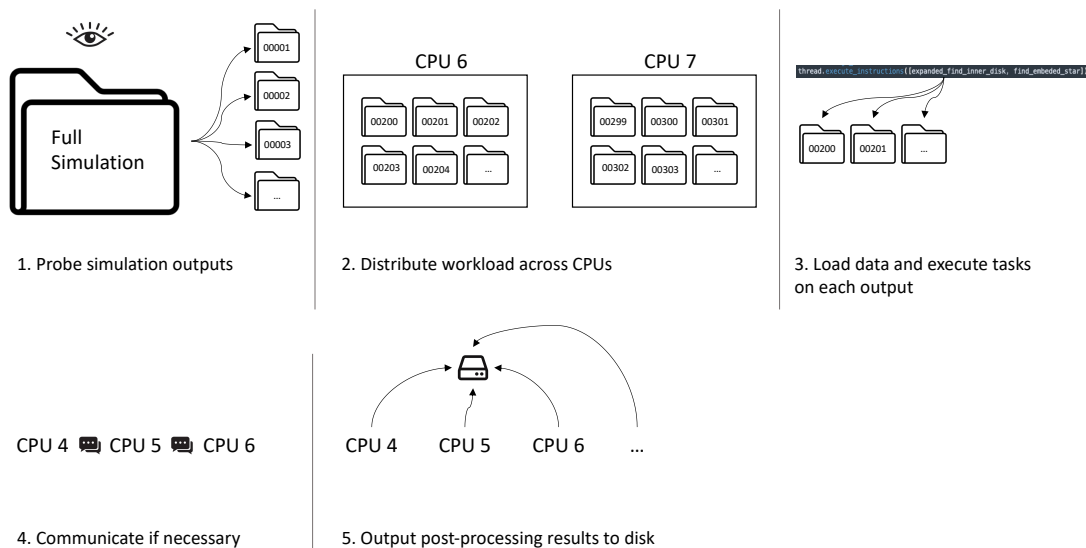


Figure 2.5: A schematic overview of an (almost) embarrassingly parallel simulation post-processing pipeline.

2.4.2 Coordinate transforms

It is often useful to transform the cartesian coordinates dumped by RAMSES into spherical or cylindrical coordinates. This is useful to study the distribution of gas and its

kinematics in structures that form as a result of a hydrostatic equilibrium or conservation of angular momentum, such as protostars or their circumstellar disks. However, depending on the simulation setup, the user often requires to define these coordinates in a new basis, rather than compute them directly in the original **RAMSES** grid. In order to perform this change of basis, I implemented two rather simple coordinate transform techniques into the **Osiris** software: a translation of position vectors and their rotation and that of all other vector quantities (e.g., velocity or magnetic field) using a rotation matrix.

The translation is a simple difference between two position vectors:

$$\vec{r}' = \vec{r} - \vec{r}_0, \quad (2.55)$$

where \vec{r}_0 is the new origin point in the original basis. In order to rotate an arbitrary vector \vec{v} by an angle of θ , the rotation matrix R_m is used:

$$R_m(\theta) = \cos(\theta)\mathbb{I} - \sin(\theta)[\vec{v}]_{\times} + (1 - \cos(\theta))(\vec{v} \otimes \vec{v}), \quad (2.56)$$

where $[\vec{v}]_{\times}$ is the cross product matrix of \vec{v} ²

$$[\vec{v}]_{\times} \hat{=} \begin{pmatrix} 0 & -v_z & v_y \\ v_z & 0 & -v_x \\ -v_y & v_x & 0 \end{pmatrix}. \quad (2.57)$$

As such, an arbitrary vector \vec{v} expressed in the new basis as \vec{v}' is simply

$$\vec{v}' = R_m \vec{v}. \quad (2.58)$$

A schematic representation of the change of basis is provided in [Fig. 2.6](#). Once this done, spherical and cylindrical components of vector quantities may be computed. The radius r , colatitude θ , azimuth ϕ , and cylindrical radius are computed as:

$$r = \sqrt{x^2 + y^2 + z^2}, \quad (2.59)$$

$$\theta = \arccos\left(\frac{z}{r}\right), \quad (2.60)$$

$$\phi = \arctan\left(\frac{y}{x}\right), \quad (2.61)$$

$$r_{cyl} = \sqrt{x^2 + y^2}. \quad (2.62)$$

All other arbitrary (non-position) vectors $\vec{F}_{x,y,z}$ have their spherical components $\vec{F}_{r,\theta,\phi}$ computed through

² $[\vec{a}]_{\times} \vec{b} = \vec{a} \times \vec{b}$. $[\vec{a}]_{\times}$ can be implemented in NumPy as $\vec{a} \times (-\mathbb{I})$.

$$\begin{pmatrix} F_r \\ F_\theta \\ F_\phi \end{pmatrix} = \begin{pmatrix} \sin(\theta)\cos(\phi) & \sin(\theta)\sin(\phi) & \cos(\theta) \\ \cos(\theta)\cos(\phi) & \cos(\theta)\sin(\phi) & -\sin(\theta) \\ -\sin(\phi) & \cos(\phi) & 0 \end{pmatrix} \begin{pmatrix} F_x \\ F_y \\ F_z \end{pmatrix}, \quad (2.63)$$

and into their cylindrical counterpart $F_{r,\phi,z}$ through

$$\begin{pmatrix} F_r \\ F_\phi \\ F_z \end{pmatrix} = \begin{pmatrix} \cos(\phi) & \sin(\phi) & 0 \\ -\sin(\phi) & \cos(\phi) & 0 \\ 0 & 0 & 1 \end{pmatrix} \begin{pmatrix} F_x \\ F_y \\ F_z \end{pmatrix}. \quad (2.64)$$

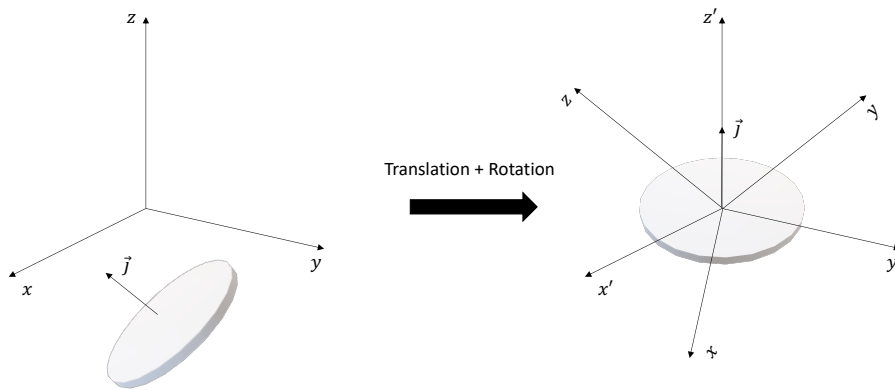


Figure 2.6: Illustration of the change of basis performed prior to coordinate transforms. An off-center disk whose angular momentum vector is misaligned with the z axis is centered and rotated, such that the new z axis (z') is aligned with the angular momentum vector of the disk, and the new x, y plane (x', y') is parallel to the disk midplane.

2.4.3 Raycasting

When performing simulations that lead to the formation of irregular structures, such as flared disks for instance, it is often helpful to draw profiles or compute quantities along a line of sight. Ray casting is a particularly useful technique in this regard. In simple terms, it consists in computing the intersection point between a ray and the six planes formed by each cube face. The fact that it is a simple computation of intersection points means that it can also be easily sped-up by GPU hardware (for instance, through a `cupy` implementation).

To illustrate how this was implemented, [Fig. 2.7](#) provides a schematic representation

of raycasting on the x-y plane. Here, the ray (which crosses the origin point for simplicity) is a straight line represented by the function $f(x) = ax$, where a is the slope of the ray when projected unto the x-y plane. Let (c_x, c_y) be the cell center and dx the cell length.

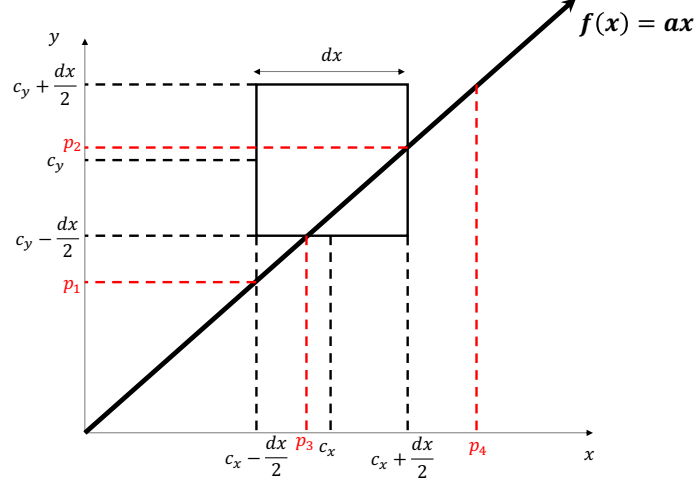


Figure 2.7: A schematic representation of raycasting on a 2D x-y plane. Performing fully 3D raycasting requires one to do the same in the z-x and z-y planes.

In order to determine whether the ray intersects with the cell or not, 4 coordinates need to be computed: p_1 , p_2 , p_3 , and p_4 :

$$\begin{aligned}
 p_1 &= a \left(c_x - \frac{dx}{2} \right) , \\
 p_2 &= a \left(c_x + \frac{dx}{2} \right) , \\
 p_3 &= a^{-1} \left(c_y - \frac{dx}{2} \right) , \\
 p_4 &= a^{-1} \left(c_y + \frac{dx}{2} \right) .
 \end{aligned} \tag{2.65}$$

As such, an intersection in the x-y plane occurs if one of the following conditions is met:

1. $(c_y + \frac{dx}{2} > p_1) \ \& \ (c_y - \frac{dx}{2} < p_1)$
2. $(c_y + \frac{dx}{2} > p_2) \ \& \ (c_y - \frac{dx}{2} < p_2)$
3. $(c_x + \frac{dx}{2} > p_3) \ \& \ (c_x - \frac{dx}{2} < p_3)$
4. $(c_x + \frac{dx}{2} > p_4) \ \& \ (c_x - \frac{dx}{2} < p_4)$

In order to perform a full 3D raycasting, this needs to be done on the z-x and z-y planes, and a ray intersects with a cube if an intersection is found in all three planes. In Fig. 2.8, we show an example of a raycasting using data extracted from a **RAMSES** simulation. The green cubes are cells having intersected with the ray, where we can see larger (i.e., coarser) cells at larger radii. The plot on the top-left corner of the figure shows the associated density profile measured along the ray.

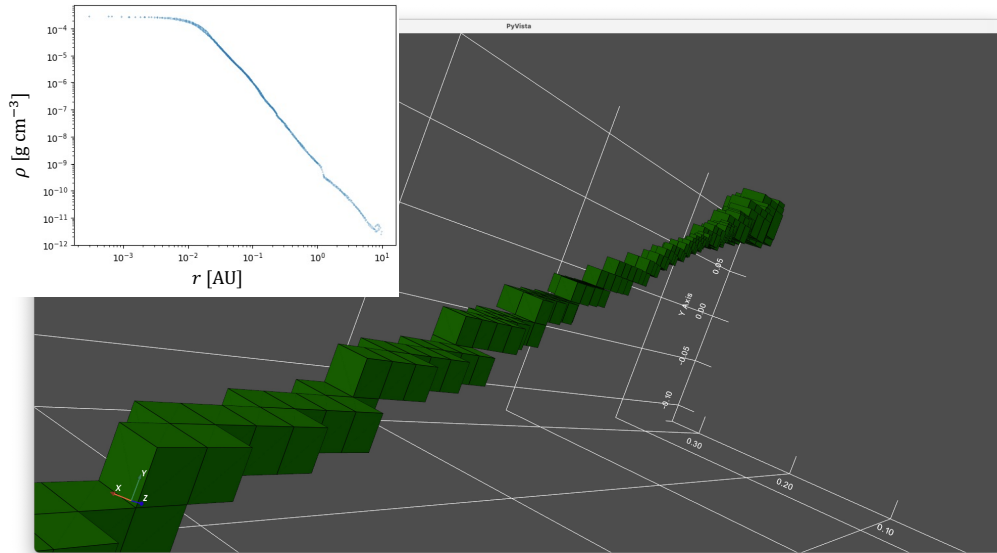


Figure 2.8: An illustration of raycasting on cells in a **RAMSES** simulation. The green cubes are cells that intersect with a ray. The plot on the top-left corner shows the density profile measured along the ray.

2.4.4 3D Visualizations

When performing 3D simulations, it is often difficult to intuitively grasp, through 2D projections or slices of the data in the form of images, the full form of the structures created within them, as well as the spatial distribution of materials. The ability to interactively visualize an astrophysical object, be it a magnetized protostar, a circumstellar disk, or a molecular cloud filament, from multiple viewpoints, offers a significant speedup in one’s ability to fully understand their structure and kinematics. This in turn allows for a better understanding of the physical processes at play within them. Indeed, astrophysics is a highly visual field, in which a proper mental map of the objects involved is crucial. In this regard, 3D visualization tools allow for a myriad of possibilities, many of which go beyond mere data visualization and may be used in public outreach related purposes.

The main difficulty in visualizing simulated astrophysical plasmas in 3D is the fact they are a continuous spatial distribution of matter, in which objects of interest are often high density structures that are deeply embedded in, or surrounded by immense amounts of gas. In addition, as mentioned previously, 3D AMR simulations are often

very heavy, which makes 3D rendering a RAM intensive task.

I also emphasize the fact that 3D visualizations work best when they are interactive. This makes them very convenient for personal or public outreach purposes, however 3D figures intended to be published in scientific journals require a significantly higher amount of polish in order for them to be readily readable. Below, I cover the 3D visualization techniques I used during the thesis. My software of choice in producing these is `Pyvista` (Sullivan & Kaszynski 2019), although they are readily available in a number of 3D visualization softwares. In [Appendix A](#), snippets of code used to create some of the figures shown below are listed.

Volume rendering

A very common technique used in visualizing embedded structures is *volume rendering*. It consists in generating 2D images from a 3D scalar field, by mapping said scalar onto the image at the user’s viewpoint using a *transfer function*. This transfer function is applied on all viewing rays, and a sum is performed as the ray travels through the dataset. Generally, sigmoid, linear, or logarithmic transfer functions are used. The main advantage of this method is that it allows for a visualization of the data without an explicit extraction of a geometrical surface.

Performing a volume render requires the user to create a *uniform dataset*, which can be done in `RAMSES` using the well known `amr2cube` function, or by stacking a set of 2D image slices (see snippets 1 and 3). Thus, this technique *must* be applied on a subset of the simulation domain, in which one trades the volume of visualized data for finer details, as creating a cube as fine as the finest level is too RAM intensive.

[Fig. 2.9](#) shows an example of a volume render of a subset of a simulation containing an embedded circumstellar disk ([snippet 5](#) shows how to do this). A linear opacity map is applied as a transfer function, and in order to obtain optimal visual parameters, an interactive widget varying the opacity distance (i.e., the distance over which the opacity of the scalar field is summed) is used.

Streamlines

Among the most challenging quantities to visualize in 3D are vector fields such as velocity or magnetic fields. Streamlines allow for a much simpler analysis of kinematics, however they are also a 3D tool that benefits greatly from interactivity, as their results depend on their launching position. The approach here is similar to that of a volume render: one must first create a cube of the vector field. To do so, it is possible to make 2D image stacks of the x , y , and z components of the vector field, which are then mapped onto a 3D grid (see snippets 2 and 4).

[Figure 2.10](#) shows two examples of 3D streamlines: one showing the polar accretion onto a circumstellar disk (left) and the other showing an interactive placement of magnetic field streamlines around a second Larson core (see snippets 6 and 7). The latter was particularly useful in finding the presence of current sheets, which are characterized by loops of the magnetic field lines on the surface of the protostar. The velocity streamlines

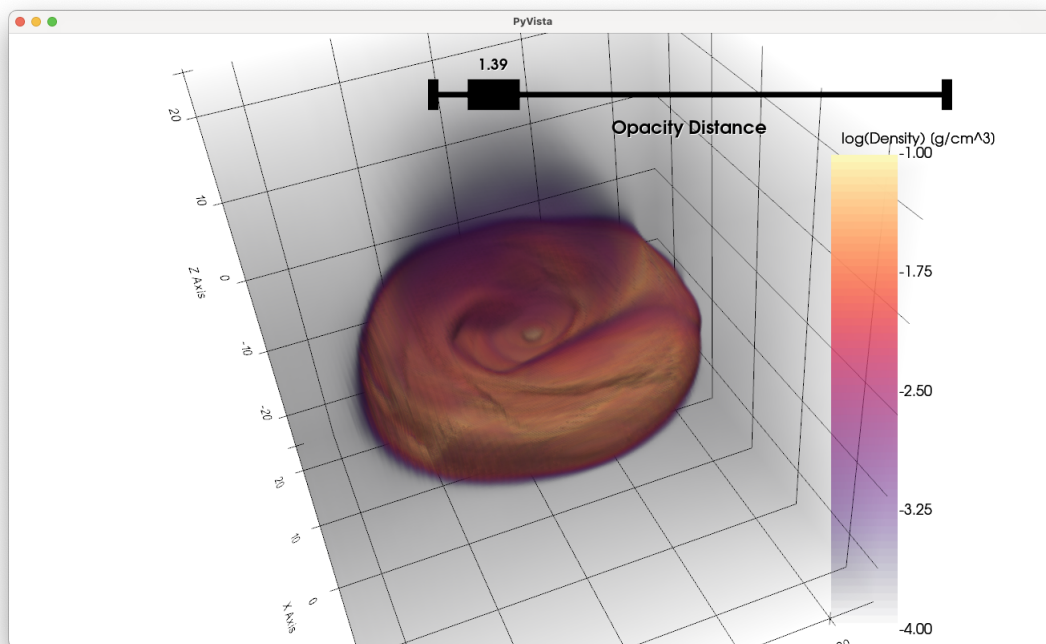


Figure 2.9: An example of a volume render of a cube extracted from a **RAMSES** simulation containing a circumstellar disk. The visualized scalar field is the gas density.

on the left showed how the gas is funneled toward the star in the polar regions.

Iso-contouring

It is often helpful to extract geometrical surfaces from the dataset, which is generally done by defining said surface as being an iso-contour of a scalar quantity. The extracted surface is made of voxels (i.e., volume elements), and as such may appear to be too pixelated. For aesthetic purposes, it is possible to smooth an iso-contour using the Laplace algorithm, which is implemented in most 3D visualization softwares. Note however, that applying a smoothing algorithm generally causes the surface to shrink in size. An example of an iso-contour is provided in [Fig. 2.11](#) (see also [snippet 8](#)), in which a star forming clump (from [Lebreuilly et al. 2024](#)) is extracted and smoothed for aesthetic purposes.

Region of interest renders

Often times, the object one wishes to render is far too extended spatially, such that a volume render would become so coarse in resolution that it is no longer capable of accurately capturing the finer details that one wishes to visualize. A possible solution is to perform a ROI (Region Of Interest) render, in which only cells satisfying a user-defined criterion that accurately captures the structure they wish to visualize

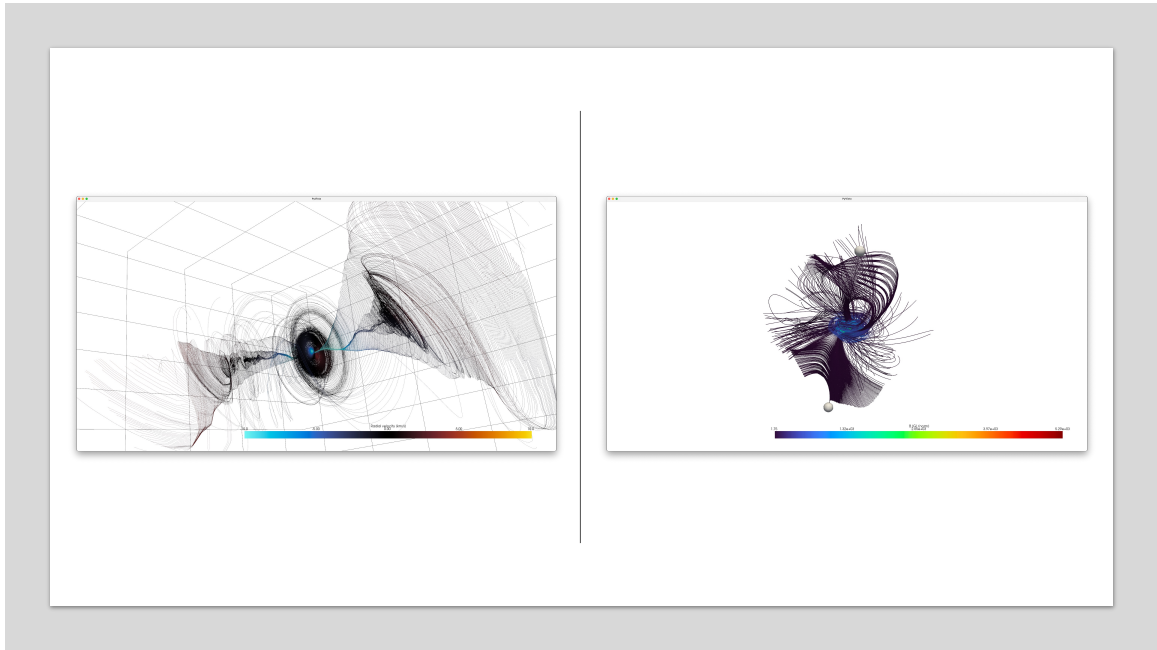


Figure 2.10: An example of 3D visualization of gas kinematics using streamlines. Left: visualization of the polar infall of material onto a circumstellar disk using velocity vector field streamlines, onto which the radial velocity is color-coded. Right: Interactive streamline placement in a visualization of magnetic field lines within and around a second Larson core, where the white balls can be moved by the user to modify the launching point of the streamlines.

are selected and visualized as a point-scatter plot (see [snippet 9](#)). Great care should nonetheless be taken to ensure that the resulting surface is not overly cumbersome to load onto RAM memory.

[Figure 2.12](#) shows an example of the 3D visualization of a star-forming molecular cloud filament, which was done by extracting all cells within a given density range. These were then visualized as a point-scatter plot with a linear opacity transfer function. This visualization shows that what appear as very thin filaments in 2D projections are in fact more spatially extended sheets of matter.

3D printing

So far, the 3D visualization techniques we've covered are very adequate for a wide variety of purposes. However, as mentioned previously, they work best when interactive. When attempting to communicate scientific ideas to a wider audience, particularly non-experts, a static 3D figure rendered on a screen is not as effective (or captivating) as an interactive model. One approach consists of hosting an interactive 3D digital scene on a website, however this is often cumbersome to create. Furthermore, it has been shown that possessing a physical model of the astrophysical object promotes interactivity on behalf of the user, and greatly aids in capturing the audience's attention and interest ([Madura 2017](#)), be it at conferences or public outreach events.

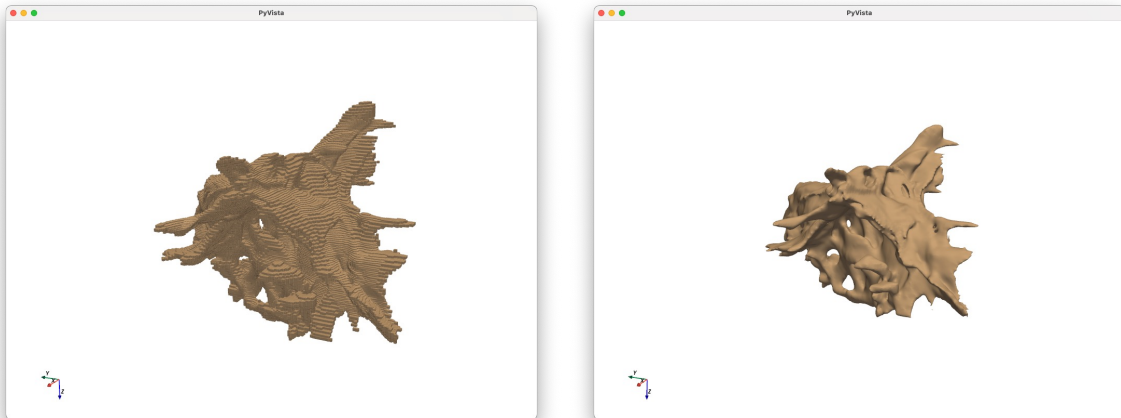


Figure 2.11: An example of an iso-contour of the density field of the star forming clump of [Lebreuilly et al. \(2024\)](#). Left: raw iso-contour surface as extracted from the data cube. Right: the iso-contour surface after 8000 iterations of the Laplace smoothing algorithm.

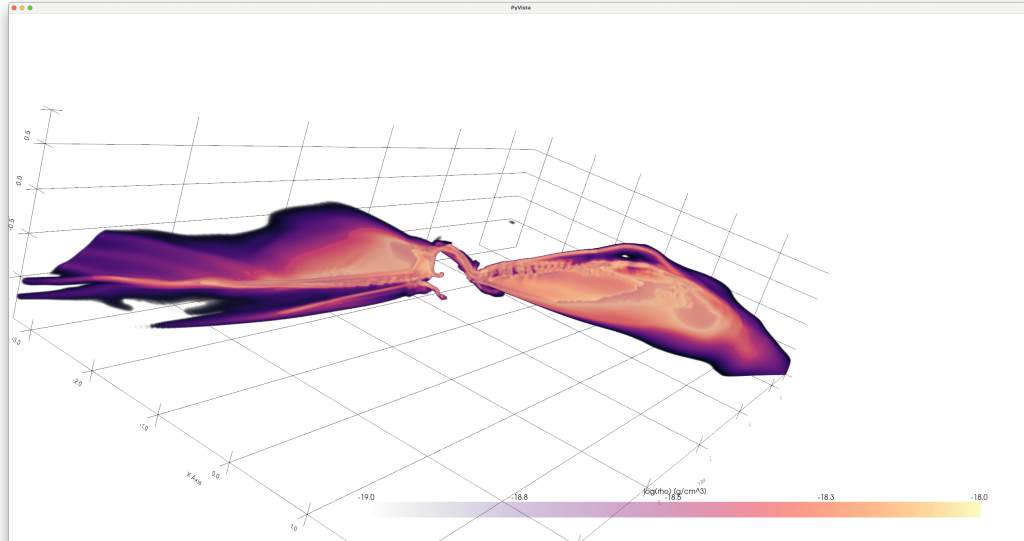


Figure 2.12: An example of an ROI (region of interest) render, in which a molecular cloud filament is extracted from a **RAMSES** simulation and visualized as a point-scatter plot, with a linear opacity transfer function.

In this regard, 3D printing has proven to be particularly useful. It consists of melting plastic and adding it layer by layer to create the object. The hardware used in 3D printing has in recent years become increasingly affordable, and even lower-end ma-

chines may produce impressive results. Typical costs for printers are ~ 4000 euros, a modest sum for astrophysical research institutes. Below, I provide an outline of the procedure I used to print astrophysical objects formed in my simulations or that of my colleagues. [Figure 2.13](#) displays an overview of the procedure.

1. Extracting surface features. One must first begin by creating a cube representing a subset of the simulation domain. This will allow for the extraction of a surface feature using an iso-contouring of a scalar quantity. Multiple surface features may be extracted using this approach. The 3D model must then be dumped into a file format compatible with 3D printers (most commonly, these are .stl or .obj). In panel (a) of [Fig. 2.13](#), a second Larson core formed in an ideal MHD simulation³ is extracted and visualized using Pyvista. Turbulent eddies may be seen at the surface of the star, and current sheets protrude from its surface. Within the current sheets, the transition from the level of refinement $\ell = 26$ to $\ell = 25$ may be seen, as coarser voxels are rendered on screen.
2. Manual cleanup (optional). After the features are extracted, it is often useful to load the model onto a 3D modelling software (e.g., Blender) in order to remove any undesired voxels that were not filtered out by the iso-contouring, such as those that are disconnected from the rest of the object and are floating in empty space.
3. Slicing the 3D model. After creating a satisfactory 3D model, one must then load it onto a slicing software, generally provided by the 3D printer manufacturer. For example, "Ultimaker Cura" was used during this thesis. Slicing consists in generating the set of instructions for the 3D printer in order to perform the layer-by-layer printing. In this step, the type of plastic to be used has to be specified, where tougher plastics (such as tough polylactic acid) can be used for less fragile results. It is also important to specify which plastic is used as support beams. Generally, it is recommended to provide an infill of at least 20% in order to guarantee the rigidity of the structure. After the slicing is completed, the model may be sent directly to the 3D printer through the local network or by first saving it onto a USB key that is latter plugged into it. Panel (b) of [Fig. 2.13](#) displays this step.
4. Printing. This step generally requires > 10 hours, where the printer works autonomously (panel c of [Fig. 2.13](#)). After completion, the support beams must be removed, and the 3D printed object is recovered (panel d of [Fig. 2.13](#)).

³This simulation is presented in [Sec. 3.4](#) of the present manuscript.

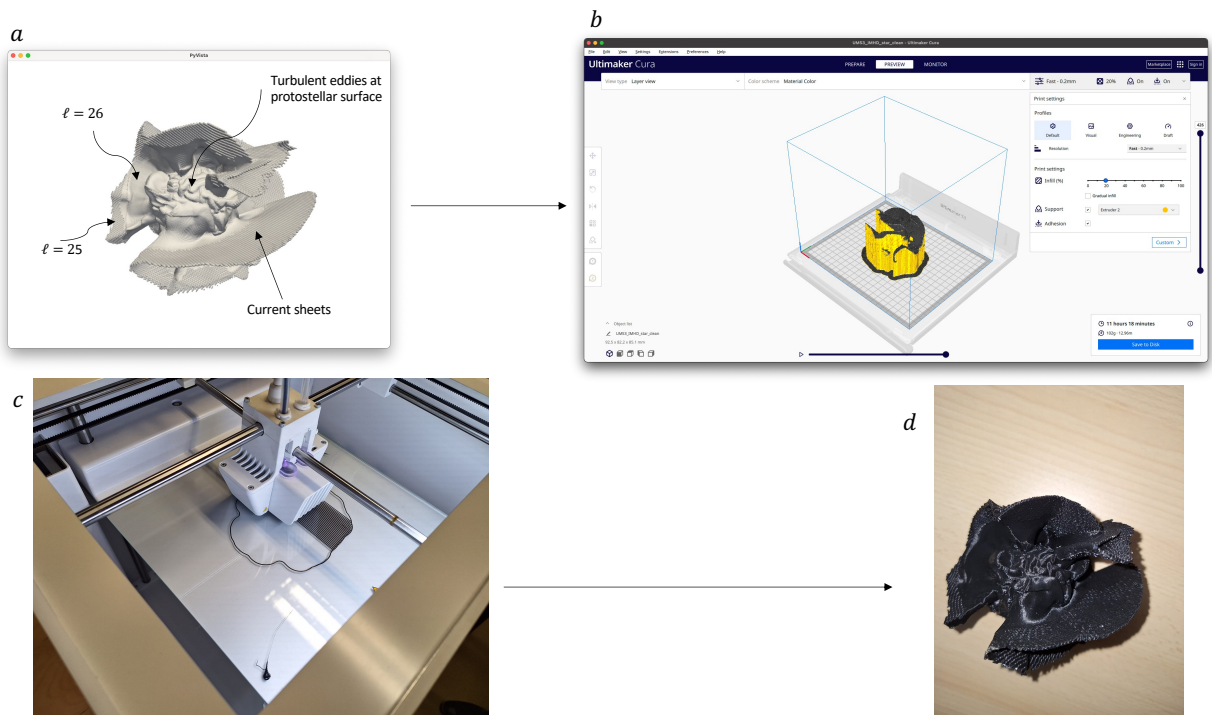


Figure 2.13: The procedural pipeline involved in 3D printing an astrophysical object formed during a simulation (see text). In this example, a second Larson core formed under the ideal MHD approximation is extracted from the simulation (a), sliced in the Ultimaker Cura software (b), sent to the 3D printer (c), and printed in full (d). The yellow structure in (b) are the support beams, which have been removed in (d).

Chapter 3

The second collapse

3.1 The state of the art

In the current state of the art, there are a variety of ways in which the second gravitational collapse is simulated. An exhaustive review of all the codes and numerical techniques can be found in [Teyssier & Commerçon \(2019\)](#). These can be summarized as:

- 1D simulations tackling the problem in spherical symmetry. This is the original approach taken by [Larson \(1969\)](#) in his pioneering second collapse calculation. It allows for a simple setup that is quite easy to implement and which can be dynamically evolved across very long timescales while including detailed physical processes (such as multigroup radiative transfer for instance). However, it does not allow for one to account for the effects of rotation and magnetic fields, which are crucial to modelling disk evolution. Nevertheless, it allows for a detailed modelling of the protostar and its evolution, which is expected to be a spherical object by virtue of its hydrostatic equilibrium. Works in the literature having used this method include those of [Larson \(1969\)](#); [Narita et al. \(1970\)](#); [Larson \(1972\)](#); [Appenzeller & Tscharnuter \(1975\)](#); [Winkler & Newman \(1980\)](#); [Masunaga & Inutsuka \(2000\)](#); [Vaytet et al. \(2013, 2014\)](#); [Vaytet & Haugbølle \(2017\)](#); [Stamer & Inutsuka \(2018\)](#); [Bhandare et al. \(2020\)](#). The majority of these works have run their calculations until the complete accretion of the original dense core by the nascent protostar, and they broadly report a final protostellar radius of $R_* \sim 2 R_\odot$ at $M_* = 1 M_\odot$.
- 2D simulations leveraging polar coordinates. Although simpler than tackling the problem in 3D, these are much more versatile than 1D calculations as they allow models to account for rotation and magnetic fields. Generally, 2D models compute the collapse with a polar symmetry (face-on view) in which the thin disk approximation and vertically integrated column densities are used; or in so called "2.5D" simulations that tackle the collapse with an azimuthal symmetry (edge-on view). This method was adopted by numerous works in the literature

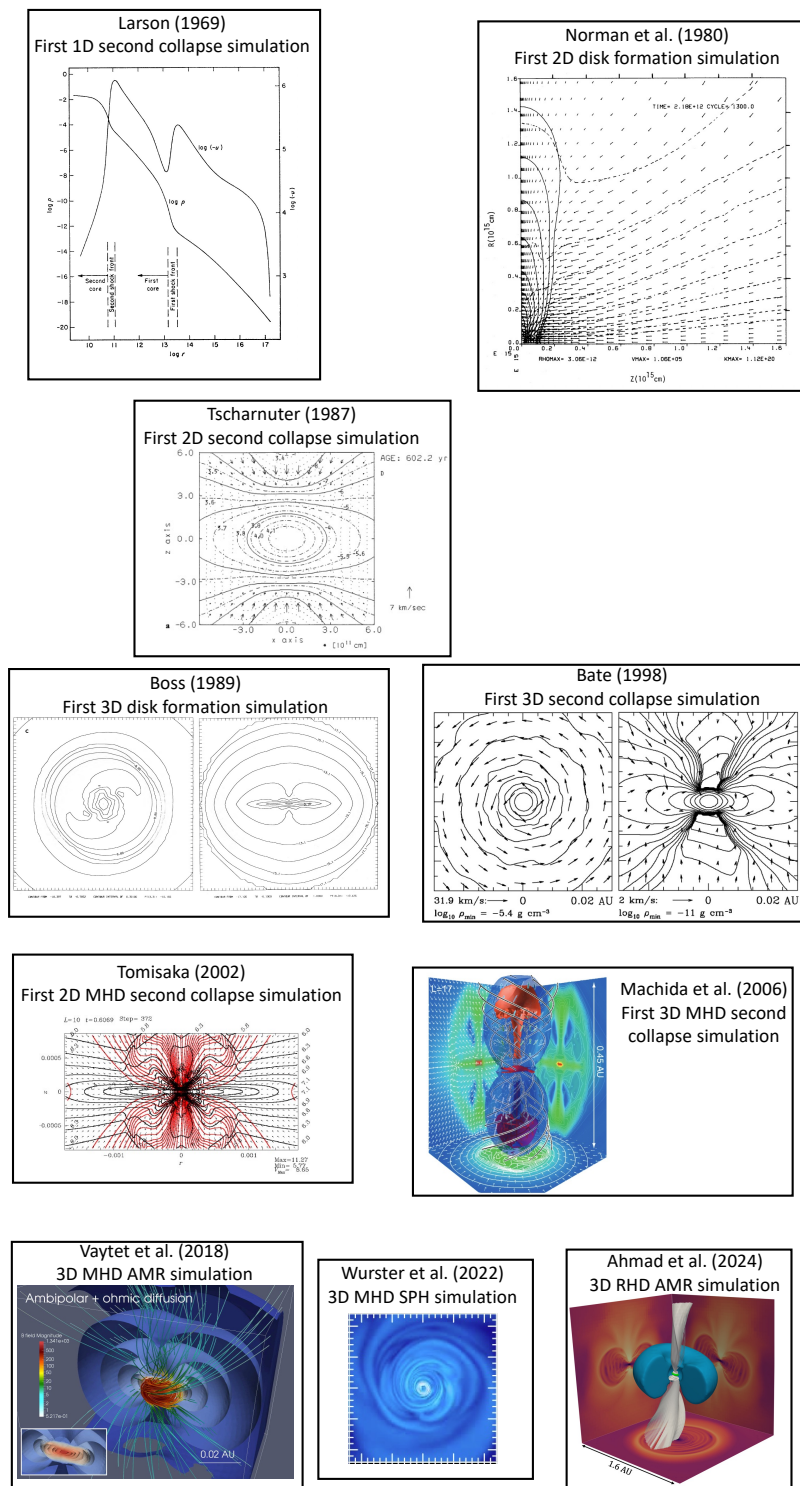


Figure 3.1: A curated selection of some historical notable works in the literature (first seven plots), with a selection of modern equivalents (last three plots). The details of said works are discussed in the main text.

such as Tscharnuter (1987); Tomisaka (2002); Tscharnuter et al. (2009); Dapp & Basu (2010); Schönke & Tscharnuter (2011); Dapp et al. (2012); Bhandare et al. (2020). It is often used in simulations that study disk evolution across long timescales, although that often requires one to omit the protostar from the calculations in order to alleviate the stringent time-stepping constraints.

- 3D simulations using nested-grid techniques. This is a popular choice of a grid that allows for one to tackle the huge dynamical range involved while implementing a Eulerian technique, and many papers in the literature employ it owing to its ease of implementation.¹ It consists in nesting finer and finer grids inside one another, thus offering consistently finer spatial resolution in the center of the computational domain. Although this is immensely useful in second collapse calculations, it resolves the central regions with an unnecessarily high resolution in the beginning of the calculation, and restricts the creation of fine and complex structures to the central regions. Works that use this method include those of Machida et al. (2006, 2007, 2008); Saigo et al. (2008); Machida et al. (2011); Machida & Matsumoto (2011); Tomida et al. (2013, 2015); Machida & Basu (2019). Pioneering 3D Eulerian calculations were almost always performed using this method.
- 3D simulations using Smoothed Particle Hydrodynamics (SPH). Instead of solving the fluid equations on a fixed grid or mesh, a mesh-free method is adopted where particles of fixed mass represent the fluid. As such, this is a *Lagrangian method* in which individual particles carry the fluid's properties. Particles cluster in regions of increasing density during the collapse, thus making the method ideal for tackling the dynamical range involved in star formation. This method has so far allowed the inclusion of the most complete physical process involved in protostellar birth. For instance, the only simulations having reached the second collapse phase and thereafter while including all three non-ideal MHD effects (Ohmic, Ambipolar, and Hall effect) were carried out with SPH. Its Lagrangian nature also allows for a much better conservation of angular momentum than Eulerian methods, particularly those that utilize cartesian grids, as they can trivially describe advection. It does however present numerous constraints: firstly, while the spatial resolution naturally follows regions of increasing density as the particles cluster around them, lower density regions remain poorly resolved. In addition, the mass of each particle often remains fixed, meaning that attaining higher resolutions requires one to significantly increase the number of particles in the simulation. Finally, this method struggles to adequately capture shock fronts, and an *artificial viscosity* term is often added to the equations in order to prevent spurious oscillations. Works in the literature making use of this method include those of Bate (1998); Whitehouse & Bate (2006); Stamatellos et al. (2007); Bate (2010, 2011); Bate et al. (2014); Tsukamoto et al. (2015b); Wurster et al. (2018); Wurster & Lewis (2020b); Wurster et al. (2021, 2022).
- 3D simulations using Adaptive Mesh Refinement (AMR, see Sec. 2.3.4). This

¹By "ease of implementation", I mean relative to other Eulerian 3D methods. It is still immensely challenging to develop a code capable of tackling the second collapse using a nested-grid technique.

is perhaps the most difficult approach, as it requires one to consider a complicated grid structure on top of solving the already highly complex hydrodynamical equations. The versatility of an AMR mesh allows for one to circumvent both the disadvantages of static nested grids and the diffusivity of SPH methods. It is however immensely difficult to implement, and its computational cost is often much greater than either nested grids or SPH simulations. The user-specified refinement criterion also allows one to accurately model the flow at any scale, and provides much more control over spatial resolution than that allowed by SPH. As such, prior to this thesis, only two of studies have used AMR codes to tackle the second collapse: [Banerjee & Pudritz \(2006\)](#) and [Vaytet et al. \(2018\)](#). The stringent time-stepping constraints following the second collapse, coupled with the poorer load-balancing schemes of AMR techniques following protostellar birth, and the heavy computational cost of numerical MHD solvers has forced both of these studies to stop their calculations almost immediately following the birth of the protostar.

In [Fig. 3.1](#), a curated selection of some notable works in the literature are displayed (see [Teyssier & Commerçon 2019](#) for a review of historical works). The first plot shows the first ever second collapse calculation of [Larson \(1969\)](#), who pioneered much of theoretical star formation. This calculation, carried out in 1D spherical symmetry, established the two-step evolutionary sequence of protostellar birth. Performing the simulations in 2D required the advent of much more powerful computers, as a fine spatial resolution is required to resolve the collapsing cloud in the center. The first correct 2D collapse calculation was that of [Norman et al. \(1980\)](#), whose higher resolution coupled with a more sophisticated angular momentum conserving scheme allowed for a much more realistic description of the collapsing dense core. Although they did not reach the adiabatic stage, they succeeded in describing the formation of a disk structure in their axially-symmetric calculations. Notably, they confirmed [Larson \(1969\)](#)'s central density peak and the power-law tail. [Tscharnutter \(1987\)](#), studying a similar setup, managed to push the calculations all the way to the second collapse stage and described the birth of a 2D protostar. The calculations, which could now describe both the formation of circumstellar disks and protostars, showed that first and second Larson cores are flattened structures due to the centrifugal force.

Fully 3D simulations came soon-after with [Boss \(1989\)](#), who was the first to simulate a 3D collapse. By now, a considerable amount of effort in the field was devoted to understanding stellar multiplicity (i.e., the formation of multiple star systems), and the fragmentation of a gravitationally unstable disk was the favored hypothesis to explain the observed binary separations. [Boss \(1989\)](#) was able to show that disks exhibit gravitational instabilities, causing the development of spiral waves within them that may then form bound fragments. The immense cost of 3D simulations meant that the first 3D second collapse calculation came nearly nine years later, with [Bate \(1998\)](#)'s SPH study. Stellar multiplicity was still the main focus of the time and in this study, it was discovered that the first core fragments into bound objects should it rotate too quickly. This would then lead to the formation of tight binaries, separated by a few AU in orbital distance. Later, developments in the field focused on the addition of more complex physics such as magnetic fields, which were first considered in [Tomisaka](#)

(2002)’s 2D study, and later studied in 3D by Machida et al. (2006), who also considered magnetic resistivities in their calculations. These studies were able to describe the birth of magnetically launched outflows and jets, as well as the transport of angular momentum by magnetic fields. Nowadays, the state of the art consists in leveraging the immense amount of computational resources available to run higher resolution simulations in which individual physical processes may be investigated. These simulations now largely include the effects of radiative transfer in their calculations, which is critical to properly model the thermal behavior of the gas.

Since the goals of my thesis involved a detailed self-consistent study of the nascent protostar and circumstellar disk, as well as their radiative behavior, a Eulerian method capable of adequately capturing shock fronts is naturally best suited for the task. My host team had an expertise in one such code: the **RAMSES** code, whose use of adaptive mesh refinement allowed it to tackle the dynamical range involved in second collapse calculations. In addition, a rich variety of physical modules such as magnetic fields under the ideal and non-ideal MHD limit, as well as radiative transfer (both gray and multigroup) are already implemented in the code, which allowed me to experiment with different numerical and physical setups.

3.2 Paper I: The nascent protostar

The early works of my PhD focused on simulating the main stages of the collapse of an isolated dense core resulting in the birth of a protostar: the initial isothermal phase, the formation of the first Larson core, the second collapse following the dissociation of H_2 molecules, and the subsequent main accretion phase. This required the use of the detailed equation of state of Saumon et al. (1995), which describes a gas mixture of H_2 , H , H^+ , He , He^+ , and He^{2+} . In addition, radiative transfer was accounted for under the FLD approximation, and the tabulated opacities pieced together by Vaytet et al. (2013) was used in this regard. The physics at scales larger than that of the first Larson core itself have already been thoroughly investigated in the literature, and as such, were not extensively studied during my PhD. I stress however that the flow at these scales was still modelled in order to produce a self-consistent calculation describing the second collapse stage.

In order to circumvent the stringent computational cost associated with simulating the second gravitational collapse while maintaining a very high spatial resolution, I carried out the first calculations in spherical symmetry. Although one may rightfully question the use of a fully three-dimensional code to simulate what is essentially a uni-dimensional flow, this was done with two objectives in mind. Firstly, in this setup, a gravitationally unstable dense core devoid of any angular momentum collapses in on itself. This causes the entirety of the collapsing gas to fall into the nascent protostar, thus dedicating the vast majority of the simulation’s computational resources to it. Secondly, the results of Bhandare et al. (2020)’s 2D simulations seemed to suggest that protostars are *convective* at birth, even prior to deuterium burning in their core. This

substantial result has multiple implications: convective motion is an efficient energy transport and mixing mechanism within the protostar, and as such will play an important role in regulating the mass-radius relationship of young stellar objects prior to their first observational appearance. In addition, the vigorous convective motion described in Bhandare et al. (2020) will undoubtedly affect the magnetic field implanted in the protostar at birth. Thus, this result has implications for the *magnetic flux problem* described in Sec. 1.4. Whether this will diffuse the magnetic flux within the protostar, or in the contrary, trigger an early dynamo process, is outside the scope of this thesis. Our goals were to model the formation of the protostar and in the process, reproduce Bhandare et al. (2020)'s findings, and to present an exhaustive quantification of this turbulence and its effects on the protostar. Performing the simulations in 3D naturally allows for a better description of turbulent motion. What followed is perhaps the most detailed ever 3D study of a nascent protostar, in which turbulent motion within the protostar was resolved for the first time in three dimensions. Before presenting the paper, published in *Astronomy & Astrophysics (680, A23)*, let us first present some theoretical background on convective instabilities within stars.

3.2.1 Theoretical background: Convective instability

Convection in stars and protostars occurs when other energy transport mechanisms, namely radiative transport and conduction, can no longer efficiently carry energy outward. What follows is a *mechanical* transport of energy, where it is advected vertically by buoyant parcels of fluid that rise from the hotter layers of the star to cooler layers, and once they've cooled down, fall back down to hotter layers. Convection is a *local* phenomena in protostars, and determining where it occurs requires a criteria for *convective instability*. Consider for instance a parcel of fluid of density ρ_1 and pressure P_1 , that rises vertically a distance Δr to a lower density medium ρ_2 and pressure P_2 (see Fig. 3.2). Since the star is in hydrostatic equilibrium, the buoyant cell maintains pressure balance with its surroundings. During the displacement, the parcel must thus expand to lower its thermal pressure, and in the process its density, where it goes from ρ_1 to $\rho_* < \rho_1$. If the drop in density is such that the buoyant cells keeps traveling upward (i.e., $\rho_* < \rho_2$), then the protostar is convectively unstable at this location. If however, the cell's density is lower than that of its surroundings (i.e., $\rho_* > \rho_2$), then the cell sinks back down. Thus, we must determine the density after displacement ρ_* , and for this, let us assume that the displacement is an adiabatic process, meaning that heat flow from the buoyant parcel to its surroundings is slower than the displacement time itself. As such, we have

$$\rho_* = \rho_1 \left(\frac{P_2}{P_1} \right)^{1/\gamma} . \quad (3.1)$$

Due to hydrostatic equilibrium, a pressure gradient dP/dr exists and we may write

$$\frac{P_2}{P_1} = 1 + \frac{1}{P_1} \frac{dP}{dr} \Delta r , \quad (3.2)$$

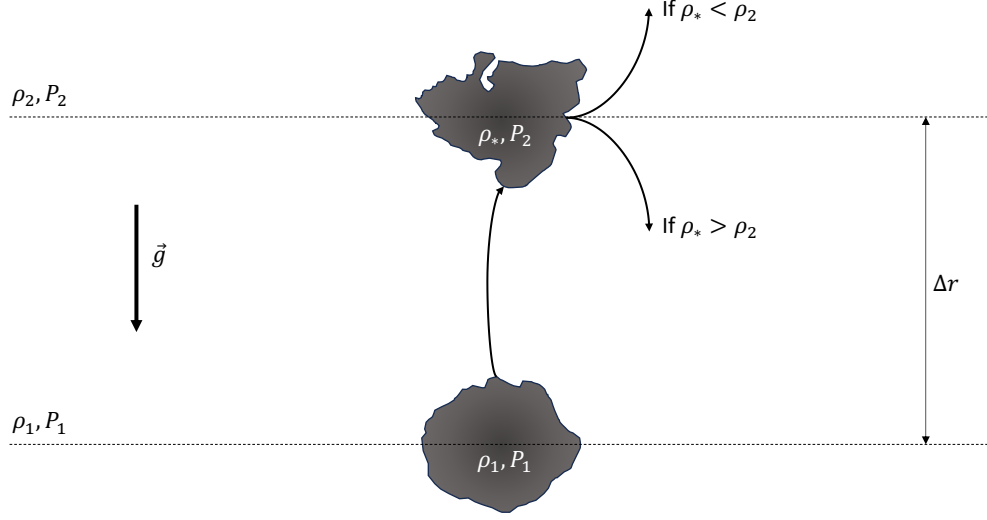


Figure 3.2: Schematic representation of convection within protostars. A buoyant cell with density ρ_1 , embedded within a medium with density ρ_1 and pressure P_1 , rises vertically a distance Δr to a medium of density ρ_2 and pressure P_2 . If the density of the rising cell is greater than that of its newfound medium, it will sink back down, otherwise it will keep rising buoyantly.

$$\Rightarrow \frac{\rho_*}{\rho_1} = 1 + \frac{1}{\gamma P_1} \frac{dP}{dr} \Delta r . \quad (3.3)$$

ρ_2 may similarly be expressed as

$$\frac{\rho_2}{\rho_1} = 1 + \frac{1}{\rho_1} \frac{d\rho}{dr} \Delta r , \quad (3.4)$$

$$\frac{\rho_2}{\rho_1} = 1 + \frac{1}{P_1} \frac{dP}{dr} \Delta r - \frac{1}{T_1} \frac{dT}{dr} \Delta r , \quad (3.5)$$

where we have made use of the ideal gas law $P = \rho \frac{k_B T}{\mu m_H}$. We may thus write

$$\frac{\rho_* - \rho_2}{\rho_1} = \left(\frac{1}{\gamma} - 1 \right) \frac{1}{P_1} \frac{dP}{dr} \Delta r + \frac{1}{T_1} \frac{dT}{dr} \Delta r . \quad (3.6)$$

Since in protostars both dP/dr and dT/dr are negative, we may write the following criterion for stability:

$$\left| \frac{dT}{dr} \right| < \left(1 - \frac{1}{\gamma} \right) \frac{T_1}{P_1} \left| \frac{dP}{dr} \right| . \quad (3.7)$$

The above equation is a formulation of Schwarzschild's criterion for stability against convection (Schwarzschild 1906). If the temperature gradient within the protostar is

steeper than the right hand side of Eq. 3.7 (which represents the adiabatic temperature gradient), then convection will take place. It is often reformulated using the entropy S :

$$\frac{dS}{dr} = c_P(\nabla - \nabla_{\text{ad}}) \frac{d \ln P}{dr} , \quad (3.8)$$



where c_P is the heat capacity of the gas, $\nabla = d \ln T / d \ln P$ is the logarithmic temperature gradient and $\nabla_{\text{ad}} = (\gamma - 1) / \gamma$ is the adiabatic temperature gradient. Since $dP/dr < 0$, convective instability implies that $dS/dr < 0$.² Should there be superadiabaticity (i.e., $\nabla > \nabla_{\text{ad}}$), then convection will transport energy and work to bring the gradient back to adiabaticity, meaning that entropy will be nearly constant in a convection zone. A constant entropy means that any such zone may be modelled as being a polytrope and thus greatly facilitates analytical modelling of protostellar interiors. This shows the importance of turbulence, and the implication of Bhandare et al. (2020)'s findings on the structure of protostars prior to deuterium burning.

Note that during the above derivation, we have ignored gradients in mean molecular weights, which is not always a valid assumption as ionization processes take place throughout the protostar. A more advanced calculation taking this into account would lead to the Ledoux criterion for convective instability (Ledoux 1947). In any case, convective instability always requires that $dS/dr < 0$.

In our studies, we have used a tabulated equation of state, and as such, we had direct access to the entropy content of each cell in our simulations. Hence, convective instabilities could directly be probed by measuring dS/dr .

²Equation 3.7 is equivalent to $\nabla < \nabla_{\text{ad}}$.

The birth and early evolution of a low-mass protostar

A. Ahmad¹, M. González¹, P. Hennebelle², and B. Commerçon³

¹ Université Paris Cité, Université Paris-Saclay, CEA, CNRS, AIM, 91191 Gif-sur-Yvette, France
e-mail: adnan.ali.ahmad1998@gmail.com

² Université Paris-Saclay, Université Paris Cité, CEA, CNRS, AIM, 91191 Gif-sur-Yvette, France

³ Univ. Lyon, ENS de Lyon, Univ. Lyon 1, CNRS, Centre de Recherche Astrophysique de Lyon, UMR5574, 69007 Lyon, France

Received 20 April 2023 / Accepted 2 October 2023

ABSTRACT

Context. Understanding the collapse of dense molecular cloud cores to stellar densities and the subsequent evolution of the protostar is of importance to model the feedback effects such an object has on its surrounding environment, as well as describing the conditions with which it enters the stellar evolutionary track. This process is fundamentally multi-scale, both in density and in spatial extent, and requires the inclusion of complex physical processes such as self-gravity, turbulence, radiative transfer, and magnetic fields. As such, it necessitates the use of robust numerical simulations.

Aims. We aim to model the birth and early evolution of a low-mass protostar. We also seek to describe the interior structure of the protostar and the radiative behavior of its accretion shock front.

Methods. We carried out a high resolution numerical simulation of the collapse of a gravitationally unstable $1 M_{\odot}$ dense molecular cloud core to stellar densities using 3D radiation hydrodynamics under the gray flux-limited diffusion approximation. We followed the initial isothermal phase, the first adiabatic contraction, the second gravitational collapse triggered by the dissociation of H_2 molecules, and ≈ 247 days of the subsequent main accretion phase.

Results. We find that the subcritical radiative behavior of the protostar's shock front causes it to swell as it accretes matter. We also find that the protostar is turbulent from the moment of its inception despite its radiative stability. This turbulence causes significant entropy mixing inside the protostar, which regulates the swelling. Furthermore, we find that the protostar is not fully ionized at birth, but the relative amount of ionized material within it increases as it accretes matter from its surroundings. Finally, we report in the appendix the results of the first 3D calculations involving a frequency-dependent treatment of radiative transfer, which has not produced any major differences with its gray counterpart.

Key words. stars: formation – stars: low-mass – stars: protostars – radiative transfer – gravitation – methods: numerical

1. Introduction

Despite its common occurrence in the Universe, understanding the collapse of gravitationally unstable dense molecular cloud cores, mostly composed of hydrogen and helium, to stellar densities is a challenging task to overcome in stellar formation theory. This does indeed entail both complex physics and observational challenges that have so far proved extremely difficult to tackle. Newly formed protostellar cores have a typical radius of about $\sim 2 R_{\odot}$ and are deeply embedded in their opaque parent molecular cloud core. When coupled with the fact that most stars form in regions of our galaxy situated at ~ 100 pc within relatively short timescales, observational breakthroughs have been sparse (e.g., [Andre et al. 1993](#); [Maury et al. 2019](#), see additionally the review by [Dunham et al. 2014](#)). From a theoretical standpoint, the challenge arises from the complex interplay between numerous physical processes: self-gravitating hydrodynamics, magnetic fields, radiative transfer, and turbulence. In addition, phase transitions such as molecular hydrogen dissociation also need to be taken into account. As a result, an analytical description of protostellar birth is virtually impossible and the field is dominated by numerical models.

The first of such works was that done by [Larson \(1969\)](#), who computed the collapse of a dense molecular cloud core to stellar densities in 1D spherical symmetry. In this pioneering work, Larson identified a two stage evolutionary sequence resulting in

the birth of a low-mass protostar. Initially, as the cloud core collapses, any compressive heating generated by the gravitational contraction is immediately radiated away in the infrared by dust grains. This initial isothermal phase is followed by an adiabatic heating phase after the gas density reaches $\sim 10^{-13} \text{ g cm}^{-3}$, where the optical depth exceeds unity and radiative cooling becomes inefficient. As a result, the central regions build enough thermal pressure support to reach a state of hydrostatic equilibrium: this is the birth of the first Larson core. It continues its contraction adiabatically with a polytropic index γ_{eff} of five-thirds, which then changes to seven-fifths once temperatures exceed 85 K and the rotational degrees of freedom of H_2 are excited.

Once the temperature of the first Larson core exceeds 2000 K, the thermal dissociation of H_2 is triggered, which is a highly endothermic process that consumes 4.48 eV per molecule ([Stahler & Palla 2004](#)). As a result, the energy provided by the compressive heating is mostly spent on the dissociation process instead of providing additional thermal pressure support. This breaks the state of hydrostatic equilibrium, and a violent second collapse ensues with $\gamma_{\text{eff}} \approx 1.1$. The extreme rise in density and temperature following this event gives birth to a new protostellar object in hydrostatic equilibrium: the second Larson core¹. The protostar continues accreting material from the infalling envelope, and angular momentum conservation leads to the formation

¹ We sometimes refer to this object as the protostar.

of a circumstellar disk. Once core temperatures exceed 10^6 K, deuterium burning begins, thus ending the pre-stellar phase.

This evolutionary sequence has so far been well accepted for low-mass protostars. Since the work done by Larson (1969), the field has developed ever more robust codes to tackle the 21 orders of magnitude in density and eight in spatial extent, in fully 3D simulations in order to include the effects of magnetic fields, rotation, turbulence, as well as radiation (for a detailed summary of each milestone reached over the years, see Teyssier & Commerçon 2019). These advancements were brought about by the ever increasing amount of computing power available. However, this growing complexity of the simulations has also meant that their computational costs has increased. As a result, there is a vast parameter space to explore and determine the role different physical processes play, but this task is hindered by the technical costs of the simulations. Such technical difficulties have significantly constrained the time stepping in self-consistent 3D simulations, and current state-of-the-art papers struggle to integrate the calculations past a few years after the birth of the protostar (e.g., Vaytet et al. 2018 reached 24 days using adaptive mesh refinement, Wurster & Lewis 2020a reached 4 yr using smooth particle hydrodynamics, whereas the 1D code in Masunaga & Inutsuka 2000 reached 1.3×10^5 yr). Such constraints have forced researchers interested in larger timescales to omit the expensive calculations of the protostar by replacing it with a sink particle (Bate et al. 1995; Bleuler & Teyssier 2014), effectively reducing the feedback effects the protostar has on larger spatial scales to a sub-grid model (e.g., Vorobyov & Basu 2015; Tomida et al. 2017; Hennebelle et al. 2020a; Wurster & Lewis 2020b; Lebreuilly et al. 2021).

Despite the many advancements achieved over the years, the difficulties in integrating the simulations across large timescales has meant that the evolution of the protostar is still poorly understood. Since protostellar feedback plays a significant role in the formation and fragmentation of its surrounding disk, the temperature and structure of its envelope, as well as the overall dynamics of molecular clouds (Hennebelle et al. 2020b, 2022; Grudić et al. 2022), understanding the physics at the protostellar scale is of crucial importance. Hence, our goal is to model the birth of the protostar and study its evolution through time in a self-consistent 3D manner. We place a special focus on the interior structure of the protostar, its accretion shock, and the inner turbulent motions, in order to understand its behavior. Since previous studies in the literature involving nonideal magnetohydrodynamics have shown that protostars are born with weak magnetic field strengths, ranging from 10^{-1} – 10^3 G (Vaytet et al. 2018; Wurster & Lewis 2020a; Wurster et al. 2022), the thermal pressure is orders of magnitude above the magnetic pressure. Hence, we have decided to omit magnetic fields from our study and have constrained ourselves to a radiation-hydrodynamics (RHD) model under the gray flux-limited diffusion (FLD) approximation. This provides the added benefit of reducing the computational cost of the simulations. Our simulations were carried out using the adaptive mesh refinement (AMR) code RAMSES (Teyssier 2002). In addition, we have for the first time carried out a 3D simulation with frequency-dependent radiative transfer leading to the formation of the protostar. Its results are in agreement with its gray counterpart, and we have reported them in the appendix.

In Sect. 2, we present the numerical methods and the initial conditions used in this work. The birth of the protostar, its evolution through time, and its chemical composition are presented

in Sect. 3. Finally, the behavior of the turbulence found within the protostar is studied in Sect. 4.

2. Model

2.1. RAMSES with multigroup flux limited diffusion

Our simulations were carried out using the 3D adaptive mesh refinement and finite-volume code RAMSES (Teyssier 2002). In order to include radiative transfer, we have used the flux-limited diffusion module developed by Commerçon et al. (2011a, 2014), and its extension to a multigroup description by González et al. (2015). Since the protostar and its evolution over time are our subject of interest, we have naturally chosen the gray (single-group) approximation, which allows for better performance. However, we have also run a simulation with a multigroup description in order to compare it with its gray counterpart, the results of which are presented in Appendix C. Hence, for the sake of clarity, we present our governing equations in their general (multigroup) form, which consist of the Euler equations coupled with a radiative energy equation (González et al. 2015):

$$\frac{\partial \rho}{\partial t} + \nabla \cdot [\rho \mathbf{v}] = 0, \quad (1)$$

$$\frac{\partial \rho \mathbf{v}}{\partial t} + \nabla \cdot [\rho \mathbf{v} \otimes \mathbf{v} + P \mathbb{I}] = -\rho \nabla \phi - \sum_{g=1}^{N_g} \lambda_g \nabla E_g, \quad (2)$$

$$\begin{aligned} \frac{\partial E_{\text{tot}}}{\partial t} + \nabla \cdot [\mathbf{v}(E_{\text{tot}} + P)] &= -\rho \mathbf{v} \cdot \nabla \phi \\ &- \sum_{g=1}^{N_g} [\kappa_{Pg} \rho c (\Theta_g(T) - E_g) - \lambda_g \mathbf{v} \cdot \nabla E_g], \end{aligned} \quad (3)$$

$$\begin{aligned} \frac{\partial E_g}{\partial t} + \nabla \cdot [\mathbf{v} E_g] + \mathbb{P}_g : \nabla \mathbf{v} &= \nabla \cdot \left[\frac{c \lambda_g}{\rho \kappa_{Rg}} \nabla E_g \right] \\ &+ \kappa_{Pg} \rho c (\Theta_g(T) - E_g) + \nabla \mathbf{v} : \int_{\nu_{g-1/2}}^{\nu_{g+1/2}} \partial_\nu (v \mathbb{P}_\nu) d\nu, \end{aligned} \quad (4)$$

$$\nabla^2 \phi = 4\pi G \rho, \quad (5)$$

where ρ is the gas density, \mathbf{v} its velocity vector, P its thermal pressure, T its temperature, ϕ the gravitational potential, \mathbb{I} the identity operator, κ_{Pg} the Planck mean opacity, κ_{Rg} the Rosseland mean opacity, G the gravitational constant, c the speed of light, and λ_g the flux limiter. We note that N_g is the total number of radiative groups whose frequency borders are the $\nu_{g\pm 1/2}$. Θ_g is the energy carried by photons that have a Planck distribution of temperature T inside their given radiative group. E_{tot} is the total gas energy, which includes the kinetic and internal energy E :

$$E_{\text{tot}} = \frac{1}{2} \rho v^2 + E. \quad (6)$$

E_g (resp. \mathbb{P}_g) is the frequency-integrated radiative energy (resp. pressure tensor) inside each group:

$$E_g = \int_{\nu_{g-1/2}}^{\nu_{g+1/2}} E_\nu d\nu, \quad \mathbb{P}_g = \int_{\nu_{g-1/2}}^{\nu_{g+1/2}} \mathbb{P}_\nu d\nu. \quad (7)$$

The opacities are also computed in the same manner:

$$\kappa_{Rg} = \int_{\nu_{g-1/2}}^{\nu_{g+1/2}} \kappa_{R\nu} d\nu, \quad \kappa_{Pg} = \int_{\nu_{g-1/2}}^{\nu_{g+1/2}} \kappa_{P\nu} d\nu. \quad (8)$$

We define the total radiative energy E_r as the sum of the radiative energy inside each group:

$$E_r = \sum_{g=1}^{N_g} E_g. \quad (9)$$

Equation (1) is the continuity equation, Eq. (2) describes the conservation of momentum, Eq. (3) the conservation of energy, Eq. (4) the conservation of radiative energy, and Eq. (5) the Poisson equation for self-gravity.

The code uses the HLL Riemann solver to solve the hydro equations, and the radiative energy equations are solved using a time implicit solver with the following flux limiter (Minerbo 1978):

$$\lambda_g = \begin{cases} 2 / \left(3 + \sqrt{9 + 12R_g^2} \right), & \text{if } 0 \leq R_g \leq 3/2 \\ \left(1 + R_g + \sqrt{1 + 2R_g} \right)^{-1}, & \text{if } 3/2 < R_g \leq \infty \end{cases} \quad (10)$$

with $R_g = |\nabla E_g| / (\rho \kappa_R E_g)$. The radiative pressure tensor is given by:

$$\mathbb{P}_g = \left(\frac{1 - \chi_g}{2} \mathbb{I} + \frac{3\chi_g - 1}{2} \mathbf{n}_g \otimes \mathbf{n}_g \right) E_g, \quad (11)$$

where $\chi_g = \lambda_g + \lambda_g^2 R_g^2$ and $\mathbf{n}_g = \nabla E_g / |\nabla E_g|$. Under the optically thick limit, $R_g \rightarrow 0$ and $\lambda_g \rightarrow 1/3$ which causes \mathbb{P}_g to become isotropic. In the main body of this paper, we have used the gray approximation, meaning that there is a single group of photons (i.e., $N_g = 1$).

The equation of state used is the tabulated EOS of Saumon et al. (1995), which has been extended to lower densities by Vaytet et al. (2013). It describes the thermal properties of H_2 , H, H^+ , He, He^+ , and He^{2+} . The cloud has an initial mixture of 73% H and 27% He.

The gas and dust opacities were taken from Vaytet et al. (2013), who pieced together a table of opacities in the range of $10^{-19} \text{ g cm}^{-3} < \rho < 10^2 \text{ g cm}^{-3}$ and $5 \text{ K} < T < 10^7 \text{ K}$ from Semenov et al. (2003), Ferguson et al. (2005) and Badnell et al. (2005; see Fig. 2 of Vaytet et al. 2013). When temperatures are below 1500 K, the dust particles (which represent 1% of the mass content of the fluid) dominate the opacities and they are in thermal equilibrium with the gas. Once temperatures exceed 1500 K, the dust sublimates and the molecular gas opacities begin to dominate. Finally, when the temperatures exceed 3200 K, all molecules are dissociated and the atomic gas opacities dominate. The *Planck* and Rosseland mean opacity tables are computed within each frequency group according to the Delaunay triangulation process described in Vaytet et al. (2013). In gray radiative transfer simulations, there is only a single frequency group ($[10^5; 10^{19}] \text{ Hz}$) along which the entire opacities are integrated. The resulting opacity mesh is presented in Fig. 1, and the temperature-density distribution of the cells in our computational domain at the epoch of protostellar birth is overlaid in red. At low temperatures, the dust dominates the fluid's opacity; however, they are destroyed once temperatures exceed $\approx 1500 \text{ K}$ and the subsequent drop in κ_R is clearly visible in the figure. Once the gas transitions toward higher densities, the atomic gas opacities begin to rise and a new opacity peak appears.

Limiting ourselves to a RHD model is not without merit. Indeed, not only does this significantly reduce the computational costs of our simulations, it also has a physical justification. Current state-of-the-art papers involving nonideal MHD have consistently shown that the protostar is born with a weak magnetic

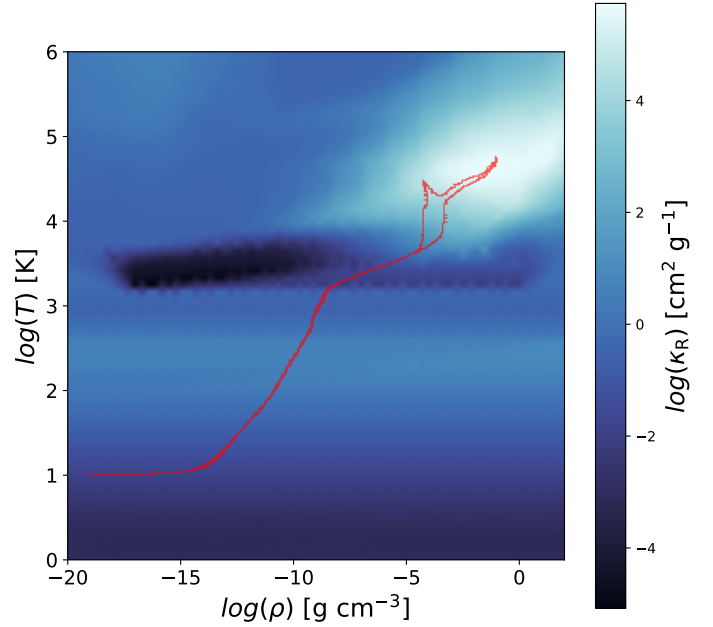


Fig. 1. Opacity mesh created for our gray radiative transfer approximation. The temperature-density distribution of all cells during the epoch of protostellar birth is overlaid in red.

field strength, thus placing the magnetic pressure orders of magnitude below the thermal pressure. One can thus omit magnetic fields when describing protostars prior to the beginning of a dynamo process.

2.2. Initial Conditions

Our initial conditions consists of a uniform density sphere of mass $M_0 = 1 M_\odot$, initial temperature $T_0 = 10 \text{ K}$, and a radius of $R_0 = 2.465 \times 10^3 \text{ AU}$. This molecular cloud core is 100 times denser than its surrounding environment, and its ratio of thermal to gravitational energies is

$$\alpha = \frac{5R_0 \kappa_B T_0}{2GM_0 \mu m_H} = 0.25, \quad (12)$$

where κ_B is Boltzmann's constant and m_H is the atomic mass constant. The mean molecular weight μ corresponds to 2.31 for our initial gas mixture.

As we have chosen to focus our attention on the formation and early evolution of the protostar, we have not included any motion in our initial conditions, be it in the form of coherent solid body rotation or any turbulent velocity vector field in the cloud core. This allows the ensuing gravitational collapse to form a spherical, central protostar in the absence of any disks. Hence, our computational resources are more devoted to the protostar, and we can integrate our simulations for longer timescales. In this respect, our study is equivalent to 1D calculations such as those of Larson (1969), Narita et al. (1970), Winkler & Newman (1980), Masunaga & Inutsuka (2000), Vaytet et al. (2013), Vaytet & Haugbølle (2017), Bhandare et al. (2018, 2020). The added benefit of carrying out these calculations in 3D is the ability to describe the turbulent motion within the second core, recently brought to light by the 2D study of Bhandare et al. (2020). As such, these initial conditions provide us with an ideal scenario to study the accretion shock and the interior structure of the protostar.

2.3. Refinement strategy

In order to resolve the interior of the protostar, an exceptionally high resolution is required. We continuously refine our AMR grid according to a modified Truelove criterion (Truelove et al. 1997):

$$\Delta x \leq \frac{\lambda_j^*}{N}, \quad (13)$$

where Δx is the cell length and $N = 20$. λ_j^* is the Jeans length computed at the cell's given density and at a temperature of 100 K:

$$\lambda_j^* = \begin{cases} \lambda_j \sqrt{\frac{100\text{K}}{T}} & \text{if } T > 100\text{ K} \\ \lambda_j & \text{otherwise} \end{cases} \quad (14)$$

where λ_j is the Jean's length. This allows the resolution to follow a length that varies in $\rho^{-1/2}$ independently of temperature once $T > 100$ K. The coarse grid has a resolution of 64^3 cells ($\ell_{\min} = 6$), and we allow 20 additional levels of refinement ($\ell_{\max} = 26$). This results in an effective spatial resolution of $\Delta x = 1.4 \times 10^{-4}$ AU at the maximum refinement level. Although some of the protostar's properties are not converged at this resolution (see Appendix B), we have nonetheless proceeded with it in order to circumvent the stringent time-stepping constraints.

Our refinement strategy provides us with $N \sqrt{\frac{T}{100\text{K}}}$ cells per actual Jeans length (until the maximum refinement level is reached), which throughout our simulation corresponds to $20\text{--}2 \times 10^3$ cells. In the protostar's central region, we have ≈ 60 cells per jeans length. This allows us to effectively resolve turbulent motions within the protostar.

Our simulation was run on two nodes, each containing 32 CPU cores. As reported in Vaytet et al. (2018), the load balancing performs poorly in RAMSES when simulating second gravitational collapses, as the majority of the computational load is contained in a small central region. As such, a smaller CPU workforce is the optimal choice as it reduces the MPI communications load. The simulation was run for a total of 2053.75 h, which corresponds to a usage of 131 440 CPU h. By using the Berthoud et al. (2020) estimate of 4.68 g hCPU^{-1} , the CO_2 equivalent carbon footprint of our simulation is ≈ 615 kg.

3. Results

3.1. Genesis

We first begin by describing the system at the epoch of protostellar birth. We define this moment as the instant a second accretion shock forms (i.e., a discontinuity in the radial velocity profile). In Fig. 2, we show plots displaying various physical profiles along radius and density. Panel e shows the temperature-density distribution of our cells. Here, the previously mentioned two step evolutionary sequence is clearly visible: the collapse begins isothermally, contracts adiabatically, and once the dissociation of H_2 begins, a second collapse occurs where $T \propto \rho^{1/10}$ ($\gamma_{\text{eff}} \approx 1.1$). The supersonic free-falling gas then collides with the protostellar surface which causes the shock heating observed after $\rho \sim 10^{-5} \text{ g cm}^{-3}$, and the gas begins a second phase of adiabatic contraction as the newly formed protostar continues accreting material. The temperatures inside the protostar reach upward of $\approx 8.5 \times 10^4$ K. This is a far-cry from the 10^6 K needed to fuse deuterium; the protostar must further contract and its core temperature needs to increase ten-fold in order to become a star and join the main sequence.

Panel a shows the radial velocity profile, where one can observe a prominent discontinuity at 6×10^{-3} AU ($\approx 1.3 R_\odot$), which marks the protostar's border. Another discontinuity, this time corresponding to the first Larson core border, is visible at 0.5 AU. The location of these shock fronts also correspond to steep density and temperature gradients in panels b and d. Both outside and inside the first core border, the density profile approaches $\rho \propto r^{-2}$ (dashed black line in panel b), which is characteristic of the collapse of an isothermal sphere (Larson 1969; Penston 1969). Just outside the second core border, the density profile closely approaches $\rho \propto r^{-1.5}$ (solid black line in panel b), which demonstrates that the accreted gas is free-falling into the newly formed protostar. Since $T \propto \rho^{\gamma_{\text{eff}}-1}$, we also see two differing temperature profiles in panel d; outside the first core border, the contraction occurs with $\gamma_{\text{eff}} = 7/5$, hence $T \propto r^{-0.8}$ (dashed black line). However, inside the first core the contraction occurs with $\gamma_{\text{eff}} \approx 1.1$. As a result, the temperature profile follows $T \propto r^{-0.2}$ (solid black line).

When the free-falling gas reaches the stellar surface, the supersonic collision heats it significantly, as it cannot dissipate its kinetic energy in the form of radiation in these extremely high optical depths (see Fig. 4b). This causes the temperature spike seen in panel d at the second core border, which exceeds the temperature in the protostar's outer layer. This exhibits the radiative nature of the protostar at birth; it mainly radiates the accretion energy it receives at the shock front which far outweighs the cooling flux that struggles to escape the opaque interior. Once inside the protostar, there is a significant amount of spread around $v_r = 0$, which shows that there are parcels of fluid that are both rising and falling, thus hinting at the presence of turbulent motions in the protostar's interior. Indeed, when visualizing the velocity vector field in Fig. 3, there is a significant amount of eddies visible downstream of the accretion shock.

In panel c, the radial entropy² profile is displayed. Here, we once again see two steep gradients corresponding to both core borders. Inside both cores, the entropy profile rises with the radius. This implies that the core is radiatively stable, and cannot generate any convection from its central regions³ (Stahler & Palla 2004). The nature of this turbulent motion will be studied in detail in Sect. 4.2. We subsequently also revisit the behavior of the entropy profile in Sect. 3.2.

In panel f, we display the sum of the enclosed gas and radiative energies E_{enc} as well as its constituent parts, namely radiative, kinetic, and internal energy, as a function of radius, and computed using

$$E_{\text{enc}}(r) = 4\pi \int_0^r (E_{\text{tot}} + E_r) r^2 dr. \quad (15)$$

Throughout the entire volume of our computational domain, the bulk of the system's energy resides under internal energy form, and kinetic energy is the second most prominent form. The majority of E_{enc} is within the protostar itself. By looking at the enclosed radiative energy curve, we can distinguish three plateaus. The first one, just outside the protostar's border, shows that the bulk of the radiative energy at $r < 0.1$ AU is located inside the protostar, and is a consequence of the weak radiative energy gradient outside the second core border (see Fig. 4a). This is also suggesting that very little radiation is escaping the protostar, thus hinting at the subcritical nature of the second core accretion shock (the radiative flux escaping the

² The entropy was obtained through an interpolation of the EOS table.

³ This is consistent with the 2D results of Bhandare et al. (2020).

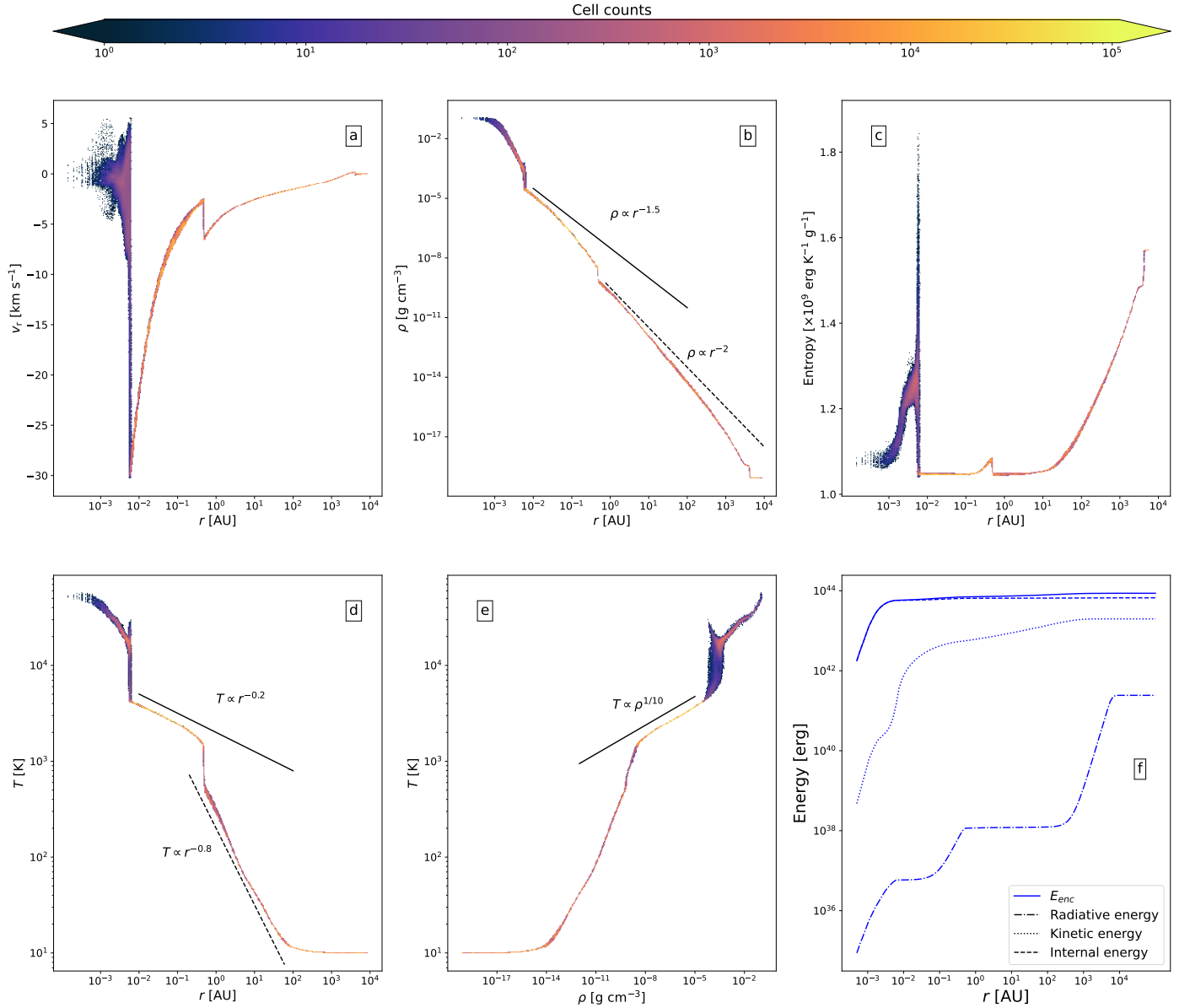


Fig. 2. Various sets of 2D histograms binning the cells in our computational domain (panels a–e) at the epoch of protostellar birth. Panels a–d represent respectively radial velocity, density, entropy, and temperature as a function of radius. The solid (resp. dashed) black line in panel b displays the expected density profile for a free-falling gas (resp. for the collapse of an isothermal sphere). The solid (resp. dotted) black line in panel d represents the expected temperature profile for the collapse of an isothermal sphere with $\gamma_{\text{eff}} = 1.1$ (resp. $\gamma_{\text{eff}} = 7/5$). Panel e displays temperature as a function of density, where the overlaid solid black line displays a contraction with $\gamma_{\text{eff}} = 1.1$. Panel f represents the sum of the enclosed gas and radiative energies at radius r (solid line, see Eq. (15)), along with its constituent parts, namely internal (dashed line), kinetic (dotted line), and radiative energies (dash-dotted line).

shock front is inferior to the incoming energy flux). The second plateau, located outside the first core border, is in fact not a real plateau; the enclosed radiative energy is indeed increasing. However there is far too little radiative energy outside the first core to lift the curve any further. Once $r > 10^2$ AU, the enclosed radiative energy curve increases once again, as the volume integral now includes the photons emitted by the isothermal phase of the contraction. Finally, the third plateau is simply caused by the fact that we have reached the boundaries of the simulation box, and no new cells are used to compute the volume integral.

We now turn to studying the radiative behavior of the simulation at the birth of the protostar. Figure 4 shows the specific radiative energy (panel a), and the opacity (black curve in panel b), averaged in radial bins and displayed as a function of

radius. The red curve in panel b shows the optical depth τ computed from the outer edge of the simulation box:

$$\tau = \int_r^{3R_0} \rho(r) \kappa_R(r) dr. \quad (16)$$

Panel c of this figure displays the luminosity $L(r)$, computed as:

$$L(r) = 4\pi r^2 c \frac{\lambda(r) \nabla E_r(r)}{\rho(r) \kappa_R(r)}. \quad (17)$$

Panel a shows us that the radiative energy is constant at large radii ($\frac{dE_r}{dr} = 0$). Since the photons being produced locally by the gas are streaming through an optically thin medium, E_r remains

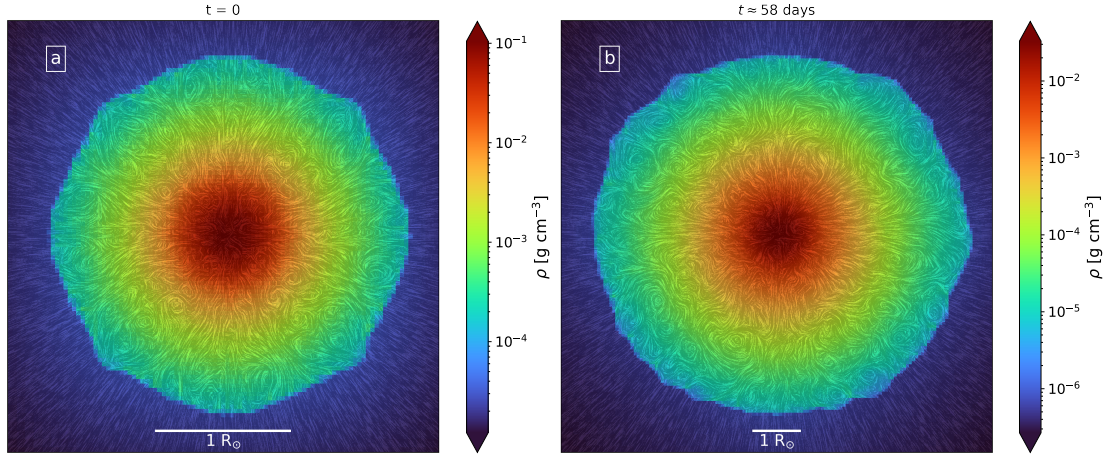


Fig. 3. Density slices through the center of the domain at the birth of the protostar ($t = 0$, panel a) and roughly 2 months later ($t \approx 59$ days, panel b). The swirly patterns are line integral convolution (LIC) visualizations of the velocity vector field, which display prominent eddies inside the newly formed protostar. Over the span of ≈ 2 months, the protostar has grown in radius by a factor ≈ 2.8 .

constant during this phase of isothermal contraction. Once the gas becomes optically thick to radiation, we witness a subsequent buildup in radiative energy. A sharp gradient, corresponding to the first core accretion shock, is then seen at 0.5 AU. It should be noted however that the first core accretion shock has already radiated a substantial amount of energy, which has then propagated outward. This is made possible by the supercritical nature of the first core accretion shock (Commerçon et al. 2011b; Vaytet et al. 2018). Inside the first core, the radiative energy gradient is not as steep as that of the adiabatic gas outside of it. Since $E_r \propto T^4$, we have $E_r \propto r^{-3.2}$ outside the first core ($\gamma_{\text{eff}} = 7/5$, gray dotted line), whereas $E_r \propto r^{-0.8}$ inside it ($\gamma_{\text{eff}} = 1.1$, gray dashed line). The temperatures found inside the first core exceed the dust sublimation temperature (≈ 1200 K), causing the drop in opacity seen in panel b. Once we reach the protostar, the high densities spike the atomic gas opacities, and the optical depth reaches a staggering 10^{15} . This causes the steep radiative energy gradient at the protostar's border ($\approx 6 \times 10^{-3}$ AU) and the subsequent buildup seen in its interior.

In the luminosity profile shown in panel c, we see a spike at the protostar's border. This is the second core accretion shock. Due to the temperature of the shock front, mainly Ultra-Violet photons are emitted at this radius, which are quickly reabsorbed by the optically thick gas upstream and reemitted in the infrared⁴. As such, the total luminosity exiting the protostellar surface should be measured just upstream of the shock front, which yields a value of $\approx 8 \times 10^{-7} L_{\odot}$. Curiously, the total luminosity becomes somewhat constant with the radius starting at 20 AU, which shows that the emanating radiative flux decreases as $F_{\text{rad}} \propto r^{-2}$. This means that the photosphere of the system is located at about this radius. The salient question one might ask here is how the system's behavior within the photosphere impacts the amount of flux escaping it, as that would allow us to link our current theoretical understanding of newly formed protostars with photometric observations. However, we have not been able to integrate our calculations long enough to witness any noticeable change in the radiative behavior of the photosphere.

3.2. Evolution of the protostar

We now turn to studying the evolution of the protostar over time. Due to our high resolution, the time stepping is very stringent. In addition, we have $\sim 3 \times 10^7$ cells inside the protostar's volume, which resulted in a very heavy computational load and our ability to integrate across long timescales was heavily impacted. Nevertheless, the results obtained provide us with valuable insights into the evolution of its physical properties and the radiative behavior of the accretion shock.

We thus begin by studying Fig. 5, which displays the evolution of various properties of the protostar. In order to compute these physical properties, we selected all cells whose thermal pressure support outweighs incoming ram pressure (see Appendix A). In addition, we leverage the complementary information available in Fig. 6, which displays various physical profiles, averaged in radial bins and displayed as a function of radius at different times.

In Fig. 5, panel a displays the enclosed mass inside the protostar. The protostar is born with a mass of $M_* \approx 4 \times 10^{-3} M_{\odot}$, which steadily grows over time. The mass accretion rate, displayed in panel d, is computed by integrating the mass flux on the protostar's surface:

$$\dot{M}_* = - \int_{S_*} \rho v_r dS, \quad (18)$$

where S_* is the protostar's surface. The mass accretion rate begins at a tremendous $0.2 M_{\odot} \text{ yr}^{-1}$, and quickly declines to $5.2 \times 10^{-3} M_{\odot} \text{ yr}^{-1}$ by the last snapshot of our simulation. The radius of the protostar is displayed in panel b. It is formed with a radius of $R_* \approx 1.3 R_{\odot}$, and it continuously increases over time. In view of the fact that it contains such a small mass, the large radii seen in panel b are intriguing. Indeed, panels a and b show that the protostar contains $\approx 1.7 \times 10^{-2} M_{\odot}$ in a radius of $9.5 R_{\odot}$ by the end of the simulation. This initial bloating phase has previously been reported in the literature (Larson 1969; Narita et al. 1970; Winkler & Newman 1980; Bhandare et al. 2020), and is caused by the radiative behavior of the shock front. As can be seen in Fig. 4b, the accretion shock has a very high optical depth, and its radiation is immediately absorbed by the gas just upstream, which is also optically thick. As a result, the protostar faces immense difficulty radiating away the kinetic energy of the gas it accretes, the majority of which is dumped into the internal energy budget of the protostar. This is more readily seen in

⁴ The multigroup simulation that we have run and presented in Appendix C permits us to better distinguish what photon frequencies are produced at all radii.

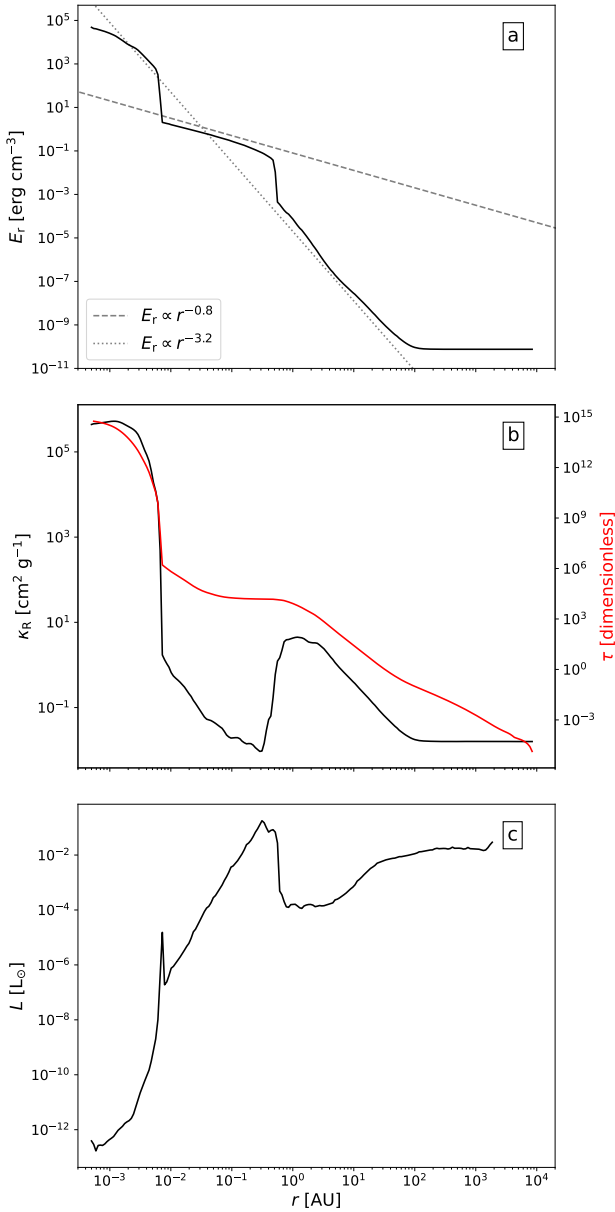


Fig. 4. Radiative energy (panel a), Rosseland mean opacity (black, panel b), optical depth (red, panel b), and luminosity (panel c), averaged in radial bins and displayed as a function of radius at the epoch of the protostar’s formation.

panel c of Fig. 5, which displays the surface integrated luminosity L_* (measured just upstream of the accretion shock) as well as the fraction f_{acc} of the accretion luminosity L_{acc} radiated away (blue curve of panel c). These two quantities are computed as

$$L_* = \int_{S_*} \frac{c\lambda\nabla E_r}{\rho\kappa_R} dS, \quad (19)$$

$$f_{\text{acc}} \approx \frac{L_*}{L_{\text{acc}}}, \quad (20)$$

where

$$L_{\text{acc}} = \frac{GM_*\dot{M}_*}{R_*}. \quad (21)$$

Equation (20) is only an approximation of the radiative efficiency of the shock front because L_* also contains the cooling flux ema-

nating from the protostar’s interior, although we expect the latter to be very small due to the optical depths such radiation has to travel through. All throughout the simulation, the protostar is extremely dim and it radiates only a minute fraction of the accretion luminosity. The continuous increase in protostellar luminosity is due to two reasons; the expanding radiative surface, and the decrease in shock density (see Fig. 5e), which reduces the optical depth of the accretion shock and facilitates the escape of radiation. Although the surface temperature of the protostar also decreases, its rate of decrease is not enough to reduce its luminosity output over time.

This accumulation of energy can also be seen in Fig. 6, which displays the evolution of various radial profiles over time. In panel e of this figure, one can see that the specific entropy of the gas downstream of the shock front is continuously increasing over time: the entire profile shifts upward as accretion progresses. However as the mass accretion rate decreases, the rate of increase in specific entropy also decreases. One can also see an increase in entropy in between the first and second core borders, caused by the radiation produced at the protostar’s shock front.

Another insight provided by this plot is the fact that the entropy continuously rises with the radius inside the protostar at all times during the simulation, meaning that it remains radiatively stable. Despite this, one can see a plateau develop just downstream of the second core shock front which is induced by the transport of heat in these regions. The mechanism behind this heat transport is the turbulent motion found within the protostar, which allows for a redistribution of energy throughout the protostar, and thus causes the entire entropy profile to shift upward. This becomes prominent over time as the effects of this turbulence begin to materialize (see Sect. 4.2 and the turbulence crossing time in Fig. 15c). As a consequence, the turbulent transport of energy becomes increasingly prominent over time in the protostar’s outer layers. Having carried out our simulation in 3D, our more complete description of turbulence has allowed this plateau to develop on much smaller timescales than in Bhandare et al. (2020)’s 2D simulations (see Appendix D). One can also distinguish a second plateau develop in the innermost regions. This secondary plateau is caused by the high degree of ionization in the central regions (see Fig. 8), which causes the fluid to transition to a lower entropy regime. The turbulent transport of heat within the protostar then causes this secondary plateau to develop. The mixing of entropy plays a crucial role in regulating the protostar’s radius. Indeed, as radiative cooling struggles to evacuate the immense amount of energy being accreted by the protostar, turbulence aids this process by redistributing heat in its outer regions, thus alleviating the bloating.

Curiously, panel b of Fig. 5 displays a sudden increase in protostellar radius at $t \approx 187$ days, which coincides with a sudden increase and subsequent drop in shock density and temperature. This corresponds to a free fall time of the first Larson core, and indeed the various radial profiles in Fig. 6 confirm that the first core is accreted by the protostar at this moment (see for instance the disappearance of the first core accretion shock in panel a or d). Although this causes an order of magnitude increase in protostellar luminosity, the radiative efficiency remains well below unity since the protostar is still deeply embedded in an optically thick cloud. Its radius must further increase to larger values before the accretion shock can properly evacuate its radiative energy into a less dense and optically thinner medium.

Figure 6 also informs us of the behavior of the gas upstream of the protostar’s shock front both prior to and after the

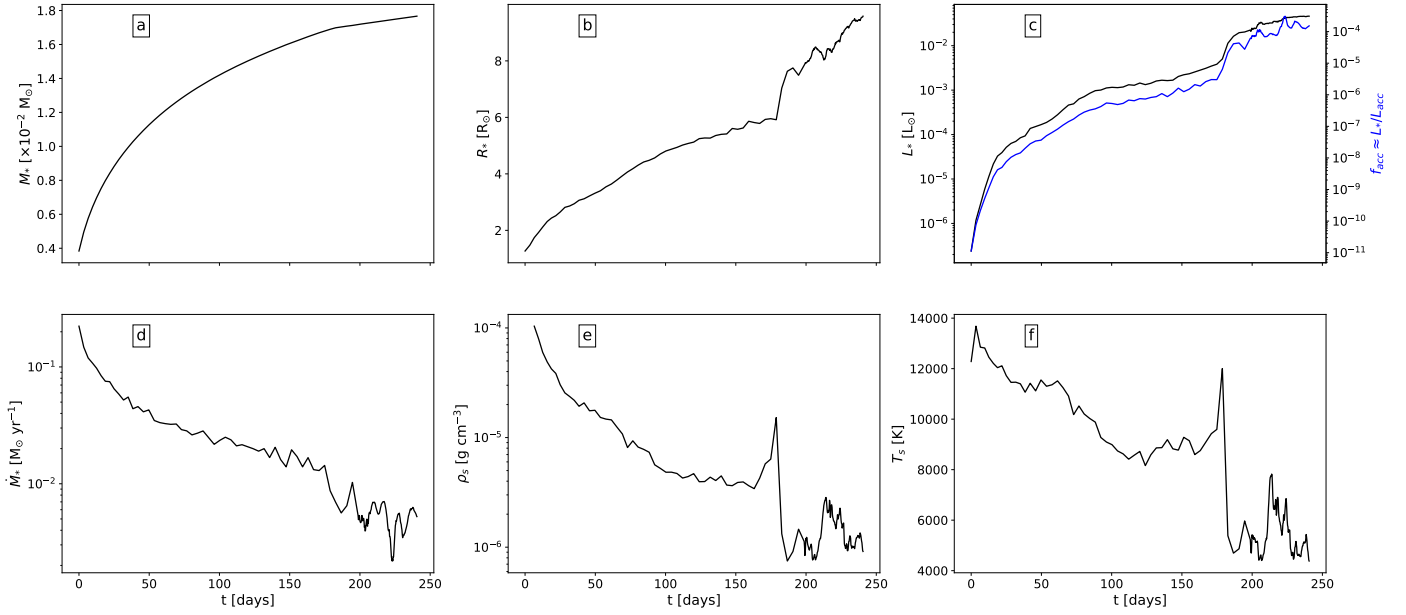


Fig. 5. Evolution of the physical properties of the protostar displayed as a function of time, where $t = 0$ marks the birth of the protostar. Panel a displays the protostar’s mass, panel b its radius, panel c (resp. panel d) its surface integrated luminosity (resp. mass accretion rate), panel e (resp. panel f) the average density (resp. temperature) at the shock front. The solid blue line in panel c represents the radiative efficiency of the protostar.

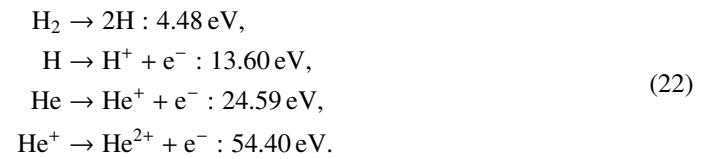
accretion of the first Larson core. As mentioned previously, the density profile in the inner regions of the first Larson core follows $\rho \propto r^{-1.5}$ (gray dashed line) and $\rho \propto r^{-2}$ in its outer layers. As seen in panel a of the figure, the boundary between these two profiles expands outward over time, such that the entire density structure inside the first Larson core shifts to $\rho \propto r^{-1.5}$. This behavior has previously been reported by Larson (1972), Shu (1977). The temperature profile follows $T \propto \rho^{\gamma_{\text{eff}}-1}$. Prior to the accretion of the first core, the H_2 molecules are undergoing the dissociation process, which places γ_{eff} at ≈ 1.1 . As a result, the temperature profile follows $T \propto r^{-0.15}$ (gray dashed line in panel b). Once the first core is accreted, the protostar directly accretes hot (and hence excited) H_2 molecules, whose γ_{eff} is $\approx 7/5$. As a result, the temperature profile now shifts to $T \propto r^{-0.6}$ (gray dotted line in panel b). We see the same behavior in the radiative energies; since $E_r \propto T^4$, we have $E_r \propto r^{-0.6}$ prior to the accretion of the first Larson core, and $E_r \propto r^{-2.4}$ afterwards.

Despite the nonlinear nature of the problem, it is our hope that a sub-grid model could be developed to properly describe the radiative feedback of the protostar unto its surrounding environment. To this end, we have displayed in Fig. 7 the protostar’s surface integrated luminosity, plotted against its radius. This has demonstrated a power-law relationship between the two, where $L_* \propto R_*^{5.7}$. The power-law fit was performed prior to the accretion of the first core (i.e., $R_* < 6 R_\odot$), as later times exhibit differing gas behaviors upstream of the accretion shock (Fig. 6), which in turn changes the exponent of the power-law. In addition, we do not have a sufficient number of data points to accurately describe $L_*(R_*)$ after the accretion of the first core. Although this result’s robustness needs further testing and investigation, it excitingly hints at the existence of an analytical model that can be found. Such a model will need to describe the temporal evolution of the gas behavior both upstream and downstream of the shock front, whereby one estimates the amount of radiative flux escaping the protostellar surface based on the local gas structure. We plan to

further explore this power-law relationship between L_* and R_* in the future.

3.3. Chemical composition

An important factor to consider following our discussion in Sect. 3.2 is the dissociation of molecular hydrogen and the ionization of atomic hydrogen and helium. These processes consume energy, which is supplied by accretion and thus must be considered when attempting to determine the energy budget, and hence the radius of the protostar. The energy consumed by these processes is:



Using the equation of state table, we can directly estimate the fractions of each of these species in our computational domain by interpolating their values. As such, we do not actually model their dynamics, but simply provide the expected amount of each species for a given cell. We thus display in Fig. 8 the mass fraction of each species X_i , averaged in radial bins where

$$\begin{aligned}
 X_{\text{H}_2} + X_{\text{H}} + X_{\text{H}^+} &= 1, \\
 X_{\text{He}} + X_{\text{He}^+} + X_{\text{He}^{2+}} &= 1.
 \end{aligned} \tag{23}$$

In panel a of this figure, we display these fractions at the epoch of the protostar’s formation. A steep gradient in the fraction of H_2 (red curves) is seen, which corresponds to the protostar’s accretion shock. Here, all remaining H_2 molecules are dissociated as a result of the shock heating, and only atomic hydrogen enters the protostar. The intense shock heating also begins ionizing the neutral hydrogen atoms (cyan curves), which happens in a much more gradual manner. However, the temperatures are not high enough to ionize the entirety of the atomic

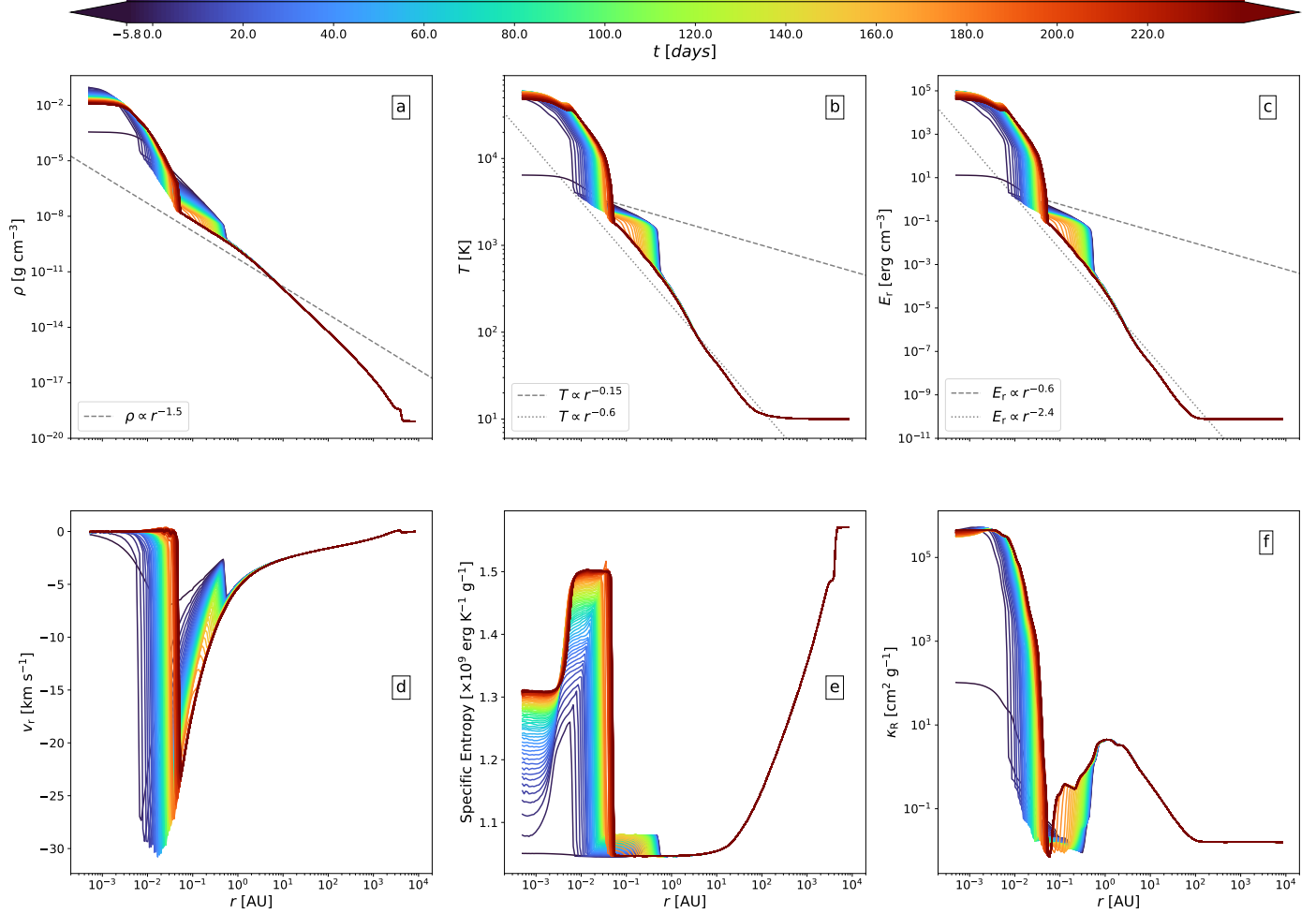


Fig. 6. Evolution of the density (panel a), temperature (panel b), radiative energy (panel c), radial velocity (panel d), specific entropy (panel e), and Rosseland mean opacity (panel f) profiles, averaged in radial bins and displayed as a function of radius for different times, where $t = 0$ marks the birth of the protostar. The last curves (dark red) on each panel correspond to $t \approx 241$ days. The dashed and dotted gray lines in panels a–c are power law curves representing the expected density, temperature, and radiative energy profiles both prior to and after the accretion of the first Larson core.

hydrogen reservoir, even in the central regions. We also see the onset of single (purple curves) and double (pink curves) He ionization just downstream of the accretion shock. The temperatures achieved in these regions cause a similar amount of He in first and second ionization states, although the curves begin to differ in the central regions. We see the same patterns ≈ 2 months later in panel b, although the accretion shock has moved outward and the total fraction of ionized H has increased, whereas the fraction of ionized He remains the same.

Using these fractions, we also compute the mass of each of these species and display them in Fig. 9 as a function of the protostar’s mass (M_* , analogous to time). Since almost no hydrogen is under molecular form inside the protostar, we have omitted displaying the mass this species represents in the figure. We see an almost linear increase of all species with M_* , although the slopes for each species differs. At about $M_* \approx 7.5 \times 10^{-3} M_\odot$, ionized Hydrogen becomes the dominant species inside the protostar in terms of mass, and by $M_* \approx 1.7 \times 10^{-2} M_\odot$, about $\approx 50\%$ of the protostar’s mass is under ionized form. However, the estimated amount of ionized material begins to decrease shortly afterward due to the decreasing density and temperature in the central core (see Figs. 6a,b). In any case, this figure shows us that the electrical conductivity of the protostar remains high following its birth.

By computing the total energy consumed by the dissociation and ionization processes, we find that they represent only $\approx 6\%$ of the total energy injected by accretion since the protostar’s birth. As such, the rest of the accretion energy is either dumped into the internal energy budget of the protostar or used to drive turbulent motions, which are eventually converted into thermal energy. We estimate the fraction of the accretion energy used to drive turbulence in Sect. 4.2.

4. Turbulent motion within the protostar

In this section, we aim to characterize the turbulence inside the protostar shown in Fig. 3 by describing it both quantitatively and qualitatively. We subsequently study how it evolves over time in our simulation.

4.1. Onset of turbulence

As stated previously, the rising entropy profile within the protostar suggests that this turbulence is not generated by a classical convective instability as postulated by Schwarzschild’s criterion, where the protostar would exhibit a transition from a radiative zone to a convective shell. Thus, another instability seems to be

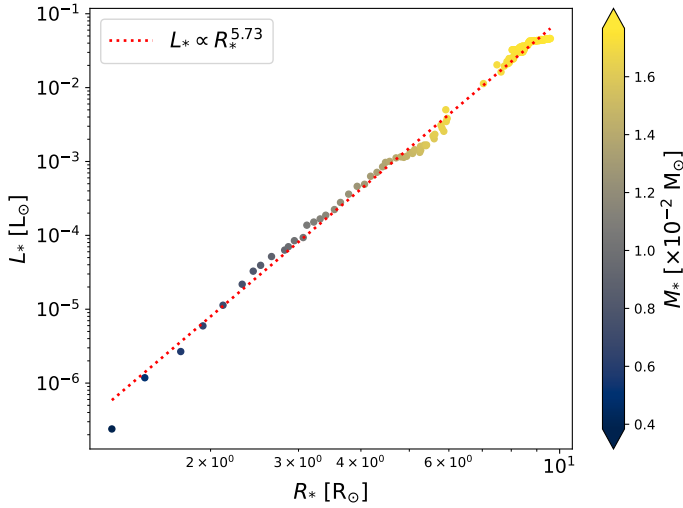


Fig. 7. Logarithmic scatter plot showing the protostellar luminosity as a function of radius (where each scatter point is color coded with the protostellar mass). A fit (red dotted line) reveals a power law relationship between L_* and R_* whose exponent is ≈ 5.7 .

at play here. Upon further investigation, we have discovered that the non-radial flow within the protostar has its origins during the hydrostatic bounce immediately following its formation.

Indeed, Fig. 10 shows the protostar at different critical moments during its birth. Panel a shows the protostar as the second core accretion shock begins to form. Here, minute deviations from a purely radial flow can be seen downstream of the shock front. These are due to our use of a Cartesian grid, which favors flow along the grid axis. Upon crossing the shock front, the upstream velocity dispersions are amplified by about an order of magnitude, which allows them to be seen in the streamlines. Nevertheless, the kinetic energy carried by the non-radial flow is well below that of the radial flow.

Several hours later, γ_{eff} reaches 4/3 in the central regions owing to the rising density and temperature, thus forming a hydrostatic equilibrium that halts any further inward flow. This causes a hydrostatic bounce (panel b), where fluid with $v_r > 0^5$ can be seen within the protostar. This bounce amplifies the non-radial flow within the protostar, although our grid geometry again seems to have an influence. Once the outgoing wave reaches the shock front, a physical instability seems to be triggered as strong vortical movement are produced within the protostar (panel c). Once the bounce has passed, these turbulent motions become sustained by accretion, as the supersonic radial flow of gas upstream of the accretion shock transfer's some of its momentum to the downstream gas, thus sustaining or amplifying any ortho-radial components in the downstream flow. This signals the onset of strong, stochastic turbulence within the protostar, as it becomes sustained through accretion. Indeed, Fig. 11 displays the kinetic energy power spectrum P_s within the protostar throughout the simulation (panel a), which exhibits the power-law relationship governing $P_s(\ell)$ and ℓ , where ℓ is the inverse of the wavenumber. The exponent (n) of this power-law obtained through a numerical fit is displayed in panel b; it hovers around 2. Although n drops during the accretion of the first core when $t \approx 180$ days, it returns to 2 afterwards. This implies that the turbulence within the protostar is being continuously maintained by accretion.

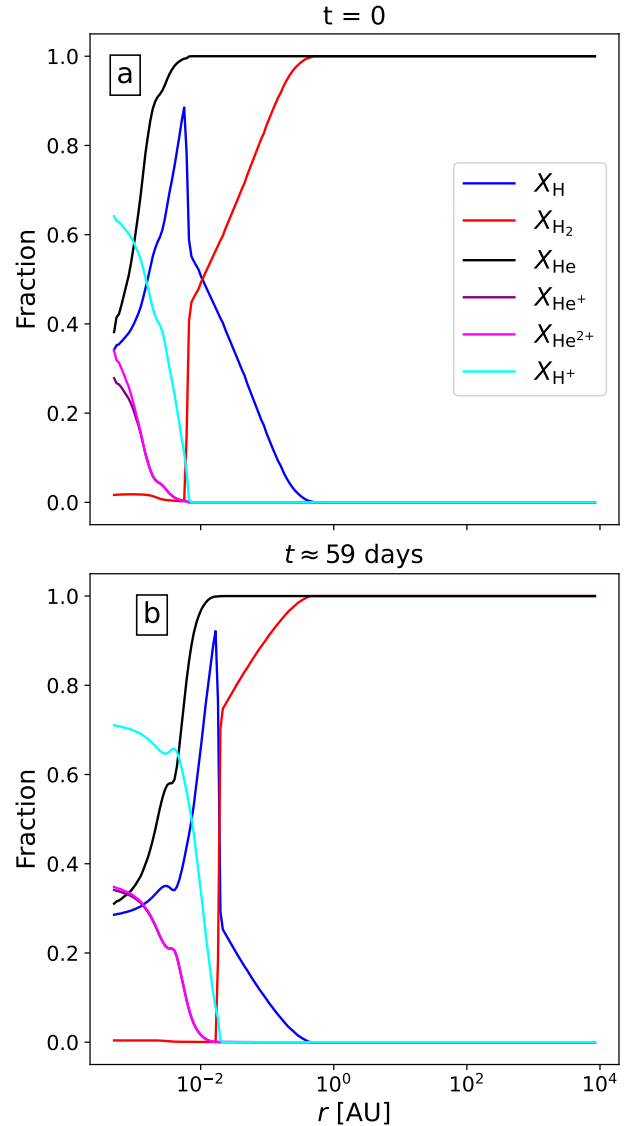


Fig. 8. Fraction of H_2 (red), H (blue), H^+ (cyan), He (black), He^+ (purple) and He^{2+} (pink), averaged in radial bins and displayed as a function of radius at the epoch of the protostar's formation (panel a) and ≈ 2 months later (panel b). See Eq. (23).

Another interesting observation provided by this figure is that the turbulence inside the protostar is not that expected of an incompressible fluid as postulated by Kolmogorov (1941), where $P_s(\ell) \propto \ell^{11/3}$, despite the fact that the velocity dispersions are subsonic and well below the local sound-speed (blue curve in Fig. 14). This is due to the heavily stratified nature of the protostellar interior, which hinders the inward motion of turbulent eddies.

In Fig. 12, we compare the ortho-radial kinetic energy $E_{v_{\phi}}$ with its radial counterpart E_{v_r} within the protostar. These two quantities are computed as:

$$E_{v_{\phi}} = 4\pi \int_0^{R_*} \rho r^2 (v_{\phi}^2 + v_{\theta}^2) dr, \quad E_{v_r} = 4\pi \int_0^{R_*} \rho r^2 v_r^2 dr. \quad (24)$$

Where v_{ϕ} and v_{θ} are respectively the azimuthal and meridional velocity. The curve suggests that the instability behind this turbulence causes an exponential growth of non-radial perturbations, before reaching a nonlinear phase where it stagnates. If

⁵ The outgoing wave is subsonic.

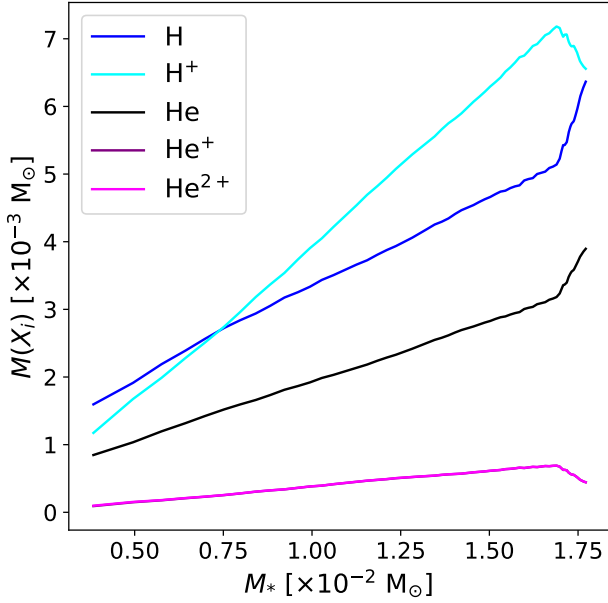


Fig. 9. Mass of H (blue), H⁺ (cyan), He (black), He⁺ (purple) and He²⁺ (pink) inside the protostar displayed as a function of protostellar mass. The purple and pink curves overlap very closely.

equipartition is achieved, one would expect $E_{v_{\theta,\phi}}/E_{v_r} \approx 2$; however, the figure shows that the ratio reaches ≈ 0.8 by $t \approx 30$ days and hovers around this value, meaning the flow within the protostar is mainly dominated by its radial component throughout the simulation.

In addition, although the entropy profiles averaged in radial bins in Fig. 5e show that the protostar is stable against convection, Fig. 13 shows that the turbulent motions can lead to local negative entropy gradients, where lower entropy fluid lies above higher entropy fluid. This causes weak convection to occur locally across all radii, and further contributes to the stochastic nature of the turbulence within the protostar.

We have seen this same pattern in higher resolution simulations; both $\ell_{\max} = 27$ and $\ell_{\max} = 28$ show the exact same onset of turbulence⁶. Through private communications with A. Bhandare, we have learned that a similar phenomena seems to occur in Bhandare et al. (2020)’s 2D simulations run on a polar grid. Indeed, their protostar is turbulent at birth despite its radiative stability (see their Fig. C.1), and this turbulence begins following the hydrostatic bounce.

When combining all of these elements together, we can conclude that although the seed for this turbulence has its origins in our grid geometry, the hydrostatic bounce and the subsequent amplification of turbulence caused by it and its interaction with the shock front are physical. We are still unsure as to what precise instability is at play here, but we have offered some evidence that could implicate the Standing Accretion Shock Instability (SASI, Blondin et al. 2003; Scheck et al. 2004; Foglizzo et al. 2007) in Appendix E.

In real astrophysical cases, the initial cloud core possesses both turbulent and rotational motion. If minuscule disturbances in the flow such as ours can provide the seed necessary to trigger turbulence within the protostar, then we predict that all protostars will be turbulent at birth.

⁶ We have presented the results of our $\ell_{\max} = 27$ in Appendix B; however, the time-stepping after second core formation in the $\ell_{\max} = 28$ was too stringent to produce any presentable results.

4.2. Accretion driven turbulence

Now that we have established that turbulent motion is created at protostellar-birth and later sustained by accretion, we proceed by providing a quantitative analysis of its behavior throughout our simulation. To this end, we begin with Fig. 14, which displays the velocity dispersions σ_v computed in radial bins as a function of radius (solid black line) at our last simulation snapshot. In this figure, the velocity dispersions upstream of the shock front are amplified by almost two orders of magnitude.

Once the matter has properly settled into the protostellar surface, the velocity dispersions scale with the radius following a power-law $\sigma_v \propto r^{9/10}$ (red fit in the figure). As the radius decreases, our ability to resolve these turbulent motions is hampered, since the number of cells in each radial bin decreases with decreasing volume. As a result, the scaling law is broken and the turbulence begins to dissipate through numerical diffusion. We would like to emphasize that the scaling law heavily depends on the internal structure of the protostar. As Fig. 6a has shown, the density profile (and hence the stratification) of the protostellar interior varies over time, which we have found is reflected in the scaling law between σ_v and r (the proportionality exponent between σ_v and r changes over time). Nevertheless, these turbulent motions carry a substantial amount of energy all throughout the protostar; the turbulent kinetic energy flux $\rho\sigma_v^3$ (dotted line) remains strong all throughout the interior.

Since we are dealing with accretion driven turbulence, a fraction of the incoming accretion energy is used to drive turbulent motions inside the protostar. In order to determine this fraction, we base our analysis on the analytical tools provided by Klessen & Hennebelle (2010), which provides an estimate of the amount of turbulence generated by accretion and lost through decay in astrophysical bodies. Consequently, we begin by defining these tools, namely the turbulent crossing time τ_d , the turbulence driving scale which we assume to be $2R_*$, and the mean 3-dimensional velocity dispersion $\langle\sigma_v\rangle$ inside the protostar (Klessen & Hennebelle 2010):

$$\tau_d \approx \frac{2R_*}{\langle\sigma_v\rangle}. \quad (25)$$

One can also compute the amount of turbulent kinetic energy inside the protostar through

$$E_{\text{turb}} = \frac{1}{2} M_* \langle\sigma_v\rangle^2, \quad (26)$$

where M_* is the protostar’s mass. Using this, we can estimate the loss of turbulent kinetic energy over time \dot{E}_{decay}

$$\dot{E}_{\text{decay}} \approx -\frac{E_{\text{turb}}}{\tau_d} = -\frac{1}{4} \frac{M_* \langle\sigma_v\rangle^3}{R_*}. \quad (27)$$

Thus, in order to sustain the turbulence observed inside our protostar, it needs to be continuously driven by the incoming accretion energy \dot{E}_{in}

$$\dot{E}_{\text{in}} = \frac{1}{2} M_* v_{\text{in}}^2, \quad (28)$$

where v_{in} is the infall velocity at the accretion shock. Finally, this allows us to compute the fraction of the accretion energy required to sustain the turbulence in the interior, which is characterized by the efficiency factor ϵ :

$$\epsilon = \left| \frac{\dot{E}_{\text{decay}}}{\dot{E}_{\text{in}}} \right|. \quad (29)$$

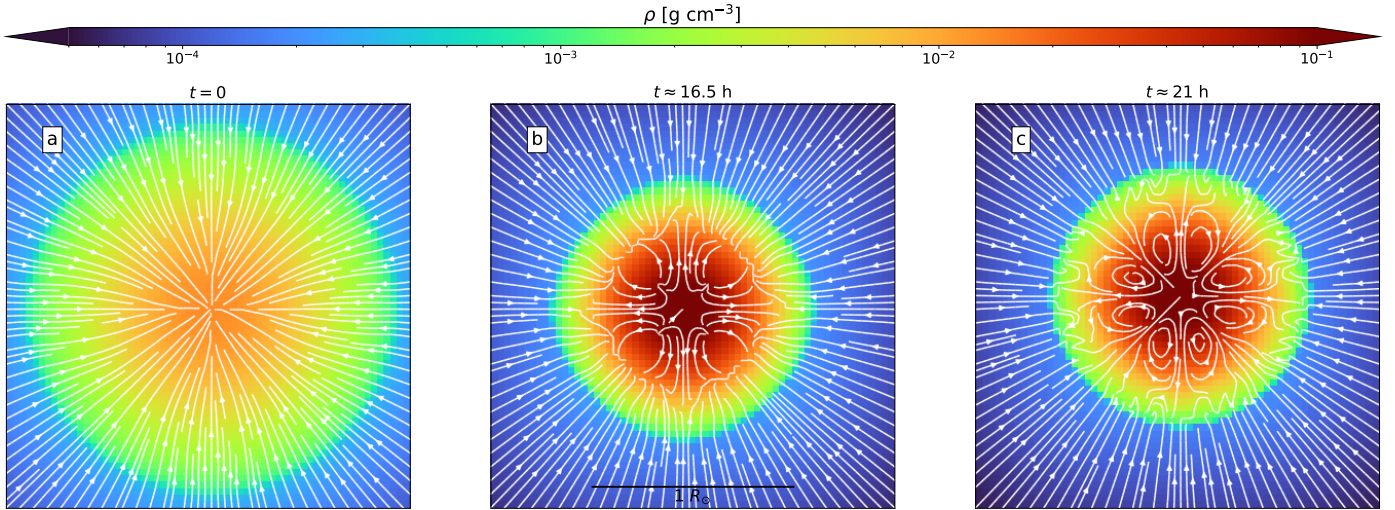


Fig. 10. Density slices through the center of the domain showing the onset of turbulence within the protostar. Streamlines of the velocity vector field are shown in white. Each panel represents a different time, with panel a showing the protostar during the formation of the accretion shock ($t = 0$), panel b after the onset of a hydro-dynamical rebound from the central region ($t \approx 16.5$ h), and panel c after the outgoing wave interacts with the shock front ($t \approx 21$ h). The scale bar in panel b applies to the other two panels.

If $\epsilon < 1$, then turbulence is sustained by accretion. In order to obtain $\langle \sigma_v \rangle$, we simply average the velocity dispersion inside the protostar by weighing it by mass. The mass weighing is done to ensure that the energy measurement is biased toward higher density gas.

In Fig. 15, we display $\langle \sigma_v \rangle$, \dot{E}_{in} , \dot{E}_{decay} and ϵ as a function of time. We have also displayed in panel c the turbulent crossing time (red line), which allows us to estimate the time required for the turbulence to dissipate from large eddies down to thermal energy. As the surface integrated mass accretion rate diminishes over time (see Fig. 5d), so too does the subsonic velocity dispersion inside the protostar. As a result, the accreted kinetic energy \dot{E}_{in} also reduces. The turbulence decay \dot{E}_{decay} also decreases over time. This is to be expected since the velocity dispersions decrease and the protostellar radius increases. Regardless, the turbulence decay \dot{E}_{decay} remains well below the injected accretion energy at all times; the efficiency factor peaks at $\approx 31\%$. This shows that the injected accretion energy is abundant enough to sustain the observed turbulence inside the protostar at any point during the simulation. However, since the turbulent driving scale increases as the protostar grows, so too does the spatial extent of the turbulent cascade process. This is more readily seen in Fig. 3, where larger eddies can be seen at the accretion shock as the protostar grows. This results in an increasing turbulent timescale, where the fraction of the injected accretion energy takes a more considerable amount of time to dissipate into thermal energy.

The ubiquitous turbulence found in the protostar raises the important question of how well it is described by our simulation. It is thus helpful to estimate the Reynolds number Re found within the protostar:

$$\text{Re} \sim \frac{2c_s R_*}{v_{\text{th}} \lambda_p}, \quad (30)$$

where c_s is the sound speed, λ_p the particle mean free path, and v_{th} the thermal speed of hydrogen atoms:

$$v_{\text{th}} = \sqrt{\frac{3k_B T}{m_H}}, \quad \lambda_p \sim 1/n\sigma, \quad (31)$$

where n is the number density of atoms with collision cross-section σ ($\approx 10^{-16}$ cm²). By our simple estimates, the Reynolds

number of the protostar's fluid should be $\sim 10^{14}$ at the surface ($c_s \sim 1$ km s⁻¹, $T \sim 10^3$ K, $n \sim 10^{18}$ cm⁻³) and $\sim 10^{17}$ in the central regions ($c_s \sim 10$ km s⁻¹, $T \sim 10^4$ K, $n \sim 10^{22}$ cm⁻³). These gargantuan Reynolds numbers mean that the characteristic scales by which viscosity effectively dissipates turbulence are orders of magnitude below our maximum spatial resolution. Indeed, such dissipation scales are on the order of the particle mean free path ($\sim [10^{-6} - 10^{-3}]$ cm), whereas our maximum spatial resolution is $\Delta x = 2.2 \times 10^9$ cm. As such, the turbulence is instead dissipated by our numerical diffusion, which means that our ability to describe this process is likely very impacted by our resolution. We have investigated the influence of our numerical resolution on the accretion driven turbulence in Appendix B and concluded that higher resolutions lead to stronger velocity dispersions in the protostar's interior, which in turn amplifies the turbulent transport of heat. For further inquiries on turbulence in star formation related processes, we invite the reader to see [McKee & Ostriker \(2007\)](#), [Hennebelle & Falgarone \(2012\)](#).

5. Discussions

5.1. The effects of initial conditions on the first and second Larson cores

A result which initially intrigued us is the size of the first Larson core in our simulation. Indeed, Fig. 2 shows a first core radius of 0.5 AU. However, Fig. 4 shows a photosphere located at a much larger radius of 20 AU. As such, the location at which the fluid transitions from an optically thin regime to an optically thick one does not coincide with that of the first core border. This is despite the fact that isothermality is broken at the location of this transition (Fig. 2d). Hence, the radius of our first core is smaller than that which is commonly reported in the literature (e.g., [Larson 1969](#); [Vaytet et al. 2013](#); [Vaytet & Haugbølle 2017](#); [Bhandare et al. 2018](#)). The small size of our first core can be attributed to our selection of the alpha value (Eq. (12)), which is smaller than those commonly adopted in the literature (> 0.5). For instance, [Vaytet et al. \(2013\)](#) compared the results of their simulations for different α values, and have found smaller first core radii for smaller α (see their Tables 1 and 2). This is

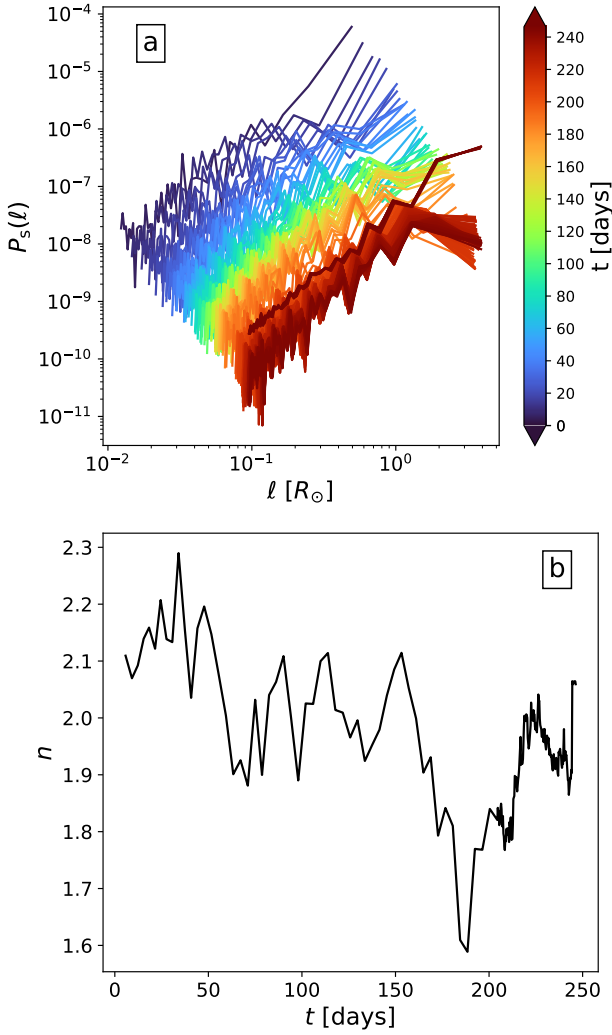


Fig. 11. A spectral analysis of the turbulence within the protostar. Panel a: Kinetic energy power spectrums as a function of characteristic scale ℓ of the gas within the protostar at different times, where $t = 0$ marks the epoch of protostellar formation. The last curve (dark red) corresponds to $t \approx 241$ days. Panel b: power-law fit of the curves in panel a, where $P_s(\ell) \propto \ell^n$.

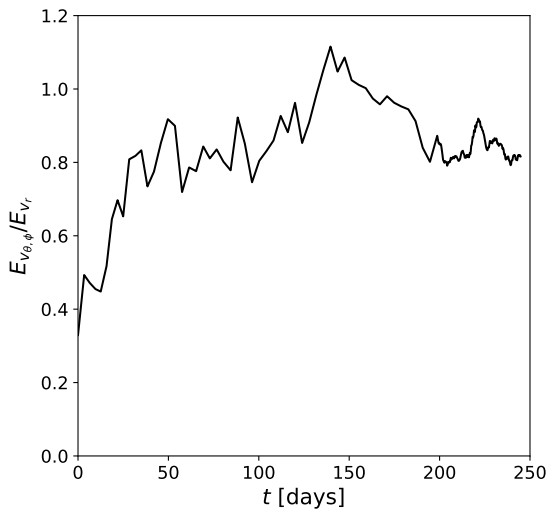


Fig. 12. Ratio of ortho-radial to radial kinetic energy inside the protostar (see Eq. (24)) as a function of time, where $t = 0$ marks the birth of the protostar.

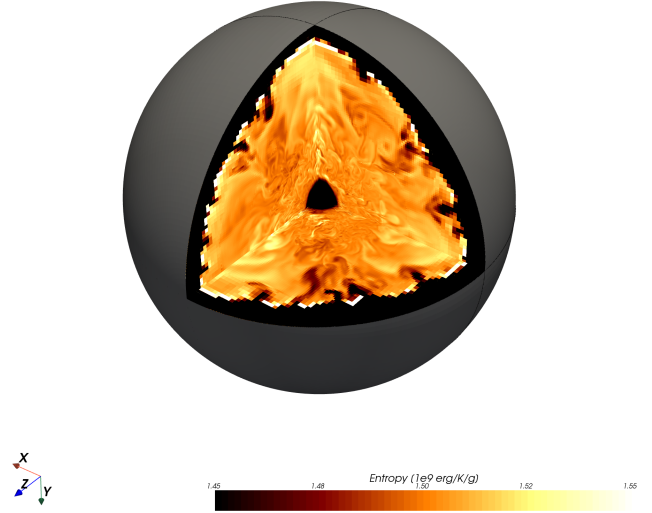


Fig. 13. Cross-sectional view of the protostar at our final simulation snapshot, showing the interior entropy. The colorbar has been artificially anchored for visualization purposes. The gray spherical outline is an artistic choice for better visualization and serves no physical meaning.

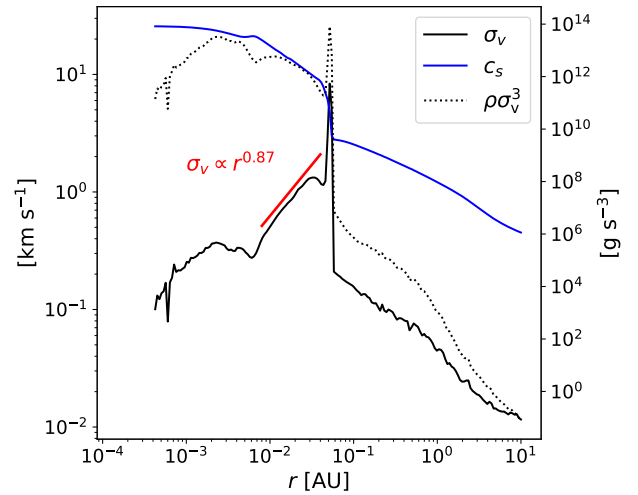


Fig. 14. Velocity dispersion computed in radial bins (black curve) and average local sound speed (blue curve), displayed as a function of radius at our last simulation snapshot ($t \approx 241$ days, where $t = 0$ marks the birth of the protostar). The red curve is a fit of the inertial range, whose exponent is $\approx 9/10$. The black dotted curve represents the turbulent energy flux (displayed in units of g s^{-3}).

due to the fact that smaller α values correspond to more violent gravitational collapses, where the high infall velocities and mass accretion rates lead to very strong ram pressure. As such, higher amounts of thermal pressure support are needed in order to attain a hydrostatic equilibrium in these configurations.

The value of α that we have adopted has however little bearing on the subsequent formation of the protostar. Indeed, the high mass accretion rates unto the protostar (which begin at $\sim 10^{-1} M_\odot \text{ yr}^{-1}$ and decline to $\sim 10^{-3} M_\odot \text{ yr}^{-1}$ by our last snapshot) have previously been reported by numerous papers independently of the initial conditions and physical model adopted (e.g., Vaytet et al. 2013; Tomida et al. 2013; Bate et al. 2014; Vaytet & Haugbølle 2017; Bhandare et al. 2020). The reason behind this is the first Larson core, which provides a momentary halt to accretion unto the central regions until temperatures

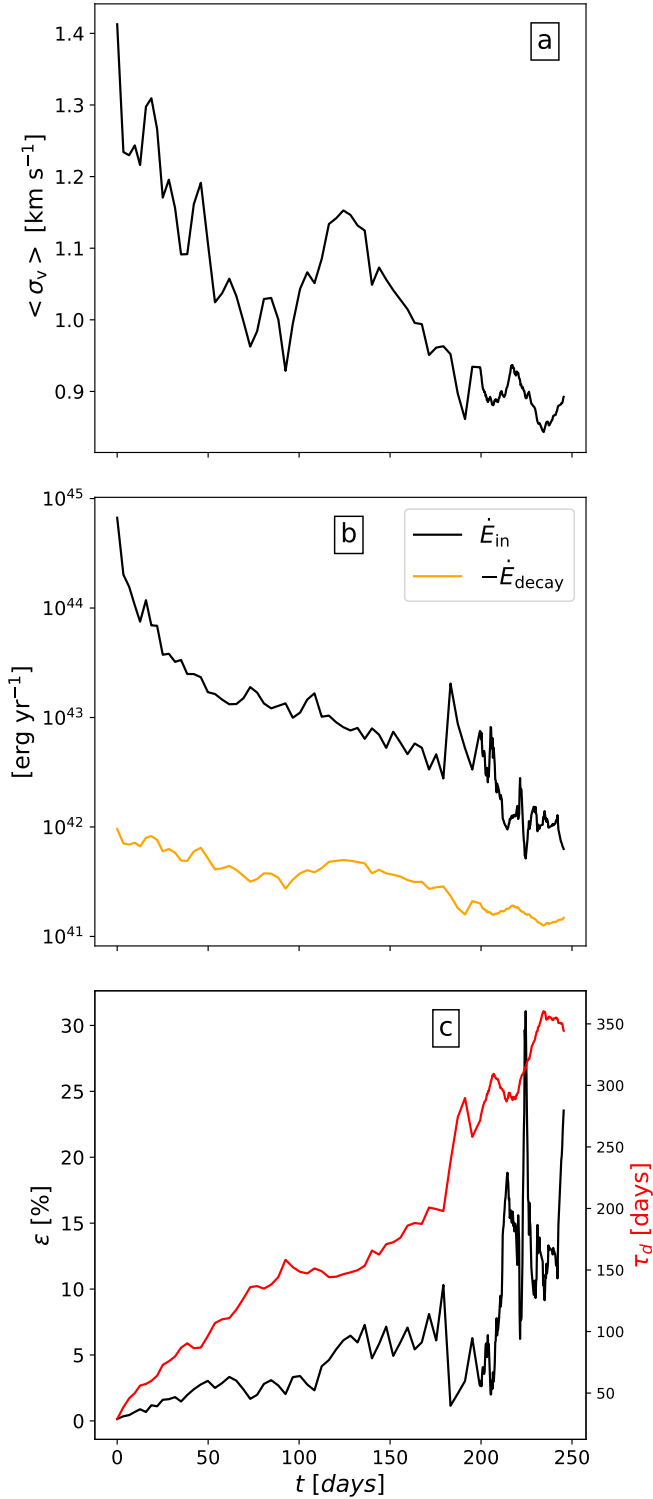


Fig. 15. Mass-weighted velocity dispersion inside the protostar (panel a), injected accretion energy alongside the turbulence decay (panel b), and efficiency factor (panel c) displayed as a function of time, where $t = 0$ marks the birth of the protostar. The red line in panel c corresponds to the turbulence crossing time (see Eq. (25)).

can exceed ≈ 2000 K, by which point the second collapse ensues. Since Larson (1969) has shown that the mass accretion rate asymptotically reaches $\sim c_s^3/G$, then one can expect $\dot{M}_* \sim 10^{-2} M_\odot \text{yr}^{-1}$, which explains the convergence seen in the literature.

5.2. The radiative behavior of the protostar

Figure 5 has shown us that the second core accretion shock remains subcritical throughout the simulation’s duration, and as a consequence the protostar’s radius swells dramatically over time. The most similar work in the literature to our study is that of Bhandare et al. (2020), which also exhibits a substantial increase of the protostar’s radius with mass. Since their study is two dimensional, they were able to integrate for much longer timescales (hundreds of years instead of our hundreds of days), and as such they were able to witness a contraction of the protostar in some of their simulations. This is explained by a reduction of the incoming mass accretion rate (i.e., a reduction in the incoming accretion energy), and an increased protostellar luminosity. They characterize this by comparing the Kelvin–Helmholtz timescale with the accretion timescale, which we have omitted from our study since the latter remains well below the former throughout our simulation⁷. Once the Kelvin–Helmholtz timescale drops below the accretion timescale (i.e., $f_{\text{acc}} > 1$), the protostar can evacuate its energy, which causes the contraction. However, this occurs once the protostars have expanded to very large radii (on the order of a few AU, with a strong dependence on the initial cloud mass), where the accretion shock has reached first core densities. Furthermore, they do not evolve the simulations long after the contraction, meaning that it is unknown if this contraction is maintained all the way to the formation of a solar-like object. Nevertheless, the subcritical nature of the second core accretion shock has been widely reported in the literature (Larson 1969; Winkler & Newman 1980; Vaytet et al. 2013, 2018; Bate et al. 2014; Bhandare et al. 2018, 2020). It has been settled that the radiative efficiency of protostars must be high during most of its main accretion phase, as that would allow them to form with reasonably small radii (Larson 1972; Appenzeller & Tscharnuter 1975; Winkler & Newman 1980; Stahler et al. 1980). Nevertheless, providing a quantitative estimate of the radiative efficiency of the second core accretion shock and how it varies over time remains of scientific interest. Indeed, many papers in the literature that are interested in larger spatial scales omit the expensive computations that we have performed; they set aside the protostar by replacing it with a sink particle, and prescribe its feedback effects using a sub-grid model (e.g., Urban et al. 2010; Vorobyov & Basu 2015; Hennebelle et al. 2020b, 2022). Thus, the radiative feedback of the protostar in these studies is $f_{\text{acc}} \times L_{\text{acc}}$, where f_{acc} is treated as a free parameter. The value of this parameter has been shown to have a significant effect on the resulting IMF (Hennebelle et al. 2020b). Our simulation shows that the radiative efficiency is extremely low immediately following its birth, and although it increases significantly over time, it remains well below the current values used in the literature. However, we expect it to reach unity once most of the envelope has been accreted, as that would significantly reduce the optical depth of the shock front. This would subsequently allow the protostar to contract by radiating away the large amount of energy it has accumulated.

5.3. The role of turbulence

Regardless of our simulation’s capacity in describing it, the existence of turbulent motion within the protostar from the moment of its inception is noteworthy, most notably for studies that aim

⁷ Our estimate of the radiative efficiency (Eq. (20)) is equivalent to the ratio of the accretion timescale to the Kelvin–Helmholtz timescale.

to model the formation of stellar magnetic fields. Indeed, as stated previously, since dissipative effects such as ambipolar diffusion and ohmic dissipation considerably reduce the magnetic field strength implanted in the protostar, a dynamo process is required in order to generate the magnetic fields observed in young stellar objects (~ 1 kG, [Johns-Kruhl et al. 2009](#)). In order to trigger such a dynamo process, convective motions are a prerequisite (e.g., [Durney et al. 1993](#); [Chabrier & Küker 2006](#)), and it is commonly believed that such motions arise once nuclear burning begins in the stellar core. Indeed, the onset of nuclear fusion reverses the entropy profile inside the star, such that the central core will possess a higher entropy than the outer layers. This is due to the fact that the colossal amounts of energy generated by fusion can not be transported through radiation alone, and thus convective motions begin. Since our study has shown that turbulent motion emerges at protostellar birth, we reiterate [Bhandare et al. \(2020\)](#)'s hypothesis that a dynamo process can begin far earlier than previously thought. Since such a process draws from the kinetic energy budget of the protostar, then it can also participate in regulating its radius.

5.4. Open questions

In our opinion, our results raise important questions that we hope will be addressed in the future. Firstly, the manner in which the radiative behavior of the protostar differs when one includes more realistic initial conditions, where turbulence or solid body rotation in the initial dense molecular cloud core provide the angular momentum budget necessary to form a disk, should be thoroughly investigated. Although [Bate et al. \(2014\)](#), [Vaytet et al. \(2018\)](#) have shown that the second core accretion shock remains strongly subcritical, [Vaytet et al. \(2018\)](#) have shown that the poles of the protostar radiate much more efficiently.

Secondly, the extent with which turbulence helps in regulating the swelling of the protostar should be analysed in depth. Our resolution study has shown that higher resolutions lead to stronger velocity dispersions; however, since it is extremely difficult to further increase the resolution, we suggest that 1D calculations that include turbulence through mixing length theory might offer better insights in this regard (e.g., [Larson 1969](#); [Palla & Stahler 1991](#)).

Finally, magnetic fields can help in regulating the radius of the protostar, and a quantitative study in this regard is desirable. Indeed, previous studies in the literature have shown that magnetic fields can generate outflows (e.g., [Machida et al. 2006, 2007](#); [Tomida et al. 2013](#); [Bate et al. 2014](#); [Tsukamoto et al. 2015](#); [Wurster et al. 2018](#); [Wurster & Lewis 2020a](#); see also [Mignon-Risse et al. 2021](#) for the high mass case). Such outflows can extract a significant amount of energy which would have otherwise been accreted by the protostar.

6. Conclusion

We have carried out a simulation modeling the collapse of a gravitationally unstable, uniform density sphere of mass $1 M_{\odot}$ to protostellar densities, using a 3D RHD description of the gas dynamics under the FLD approximation. The calculations describe the initial isothermal phase, the first adiabatic contraction, the second gravitational collapse triggered by the dissociation of H_2 , and the second adiabatic contraction. We follow the evolution of the resulting protostar for ≈ 247 days after its formation, which is longer than the first core free fall time of ≈ 187 days and hence we were able to witness the latter's accretion by the

protostar. Having placed a focus on the interior structure of the protostar, the simulation was carried out with the highest ever 3D resolution, which involved the use of 26 levels of refinement and $20-2 \times 10^3$ cells per jeans length. Our findings can be summarized as follows:

- (i) Following the formation of the protostar, its radius swells dramatically over time. This is due to the subcritical radiative nature of its shock front, which struggles to evacuate the immense amount of kinetic energy injected by accretion. The radiative efficiency of the protostar remains well below unity in the time-span that we have simulated, even after the accretion of the first core. However, as the protostar swells, the density (and hence the optical depth) of the accretion shock continuously decreases, which increases its radiative efficiency. We have revealed a power-law relationship between the luminosity just upstream of the shock front and the protostellar radius, a result which could aid in inferring the radiative behavior of the protostar across larger timescales once its robustness is established.
- (ii) Owing to our very high resolution, we were able to reproduce the findings of [Bhandare et al. \(2020\)](#)'s 2D simulations, where they have discovered that the protostar is turbulent from the moment of its inception despite its radiative stability. The turbulence is created during a hydrostatic bounce immediately following the birth of the protostar; it grows exponentially before reaching its non-linear phase, where it is then maintained by accretion. We have described this subsonic turbulence both quantitatively and qualitatively: a fraction ($< 31\%$) of the injected accretion energy is used to drive this turbulent motion, and the velocity dispersions show a power-law scaling with the radius. Since the protostar is heavily stratified, the behavior of this turbulence differs from the classical theory of [Kolmogorov \(1941\)](#). Due to the very high Reynolds numbers found in the protostar, our description of this turbulence is impacted by our numerical resolution. Our grid geometry also influences the behavior of the turbulence. Nevertheless, the heat transport it provides leads to significant entropy mixing and aids in regulating the protostellar swelling.
- (iii) We find that the protostar is not fully ionized at birth. However, as the protostar accretes material from its surroundings, the amount of mass within it under ionized form continuously increases over time. Hence, the electrical conductivity of the protostar increases over time. Additionally, we estimate that the dissociation of H_2 and the ionization of atomic hydrogen and helium represents only $\approx 6\%$ of the total energy injected by accretion. As such, the energy consumption of these processes plays an insignificant role in regulating the radius of the protostar. Nevertheless, we predict that the high electrical conductivity of the protostar, when combined with the turbulence in the interior, could lead to a dynamo process prior to the onset of deuterium burning. Since generating the stellar magnetic field comes at the expense of kinetic energy, this could also aid in regulating the swelling of the protostar's radius.
- (iv) For the first time, we have carried out during these calculations a frequency-dependent treatment of radiative transfer. The results, presented in [Appendix C](#), show no major differences to the gray approximation. This is in agreement with the 1D calculations of [Vaytet et al. \(2013\)](#).

Despite the short time-span of our simulation, we believe these results shed light on an otherwise poorly understood phase

of the stellar formation process. We are currently investigating how this evolutionary picture changes once we include angular momentum in the system (which leads to the formation of a circumstellar disk), the results of which will be presented in a follow-up paper.

Acknowledgements. We thank the anonymous referee for their useful comments that have improved the quality of this paper. This work has received funding from the French Agence Nationale de la Recherche (ANR) through the projects COSMHIC (ANR-20-CE31-0009), DISKBUILD (ANR-20-CE49-0006), and PROMETHEE (ANR-22-CE31-0020). We have also received funding from the European Research Council synergy grant ECOGAL (Grant: 855130). We thank Thierry Foglizzo and Anaëlle Maury for insightful discussions during the writing of this paper. We also thank Asmita Bhandare for providing access to the data of their [Bhandare et al. \(2020\)](#) paper. The simulations were carried out on the Alfvén super-computing cluster of the Commissariat à l'Énergie Atomique et aux énergies alternatives (CEA). Post-processing and data visualization was done using the open source [Osyris](#) package.

References

- Andre, P., Ward-Thompson, D., & Barsony, M. 1993, [ApJ](#), **406**, 122
- Appenzeller, I., & Tscharnuter, W. 1975, [A&A](#), **40**, 397
- Badnell, N. R., Bautista, M. A., Butler, K., et al. 2005, [MNRAS](#), **360**, 458
- Bate, M. R., Bonnell, I. A., & Price, N. M. 1995, [MNRAS](#), **277**, 362
- Bate, M. R., Tricco, T. S., & Price, D. J. 2014, [MNRAS](#), **437**, 77
- Berthoud, F., Bzeczniak, B., Gibelin, N., et al. 2020, [Estimation de l'empreinte carbone d'une heure.coeur de calcul](#), [Research report](#) (UGA – Université Grenoble Alpes; CNRS; INP Grenoble; INRIA)
- Bhandare, A., Kuiper, R., Henning, T., et al. 2018, [A&A](#), **618**, A95
- Bhandare, A., Kuiper, R., Henning, T., et al. 2020, [A&A](#), **638**, A86
- Bleuler, A., & Teyssier, R. 2014, [MNRAS](#), **445**, 4015
- Blondin, J. M., Mezzacappa, A., & DeMarino, C. 2003, [ApJ](#), **584**, 971
- Chabrier, G., & Küker, M. 2006, [A&A](#), **446**, 1027
- Commerçon, B., Teyssier, R., Audit, E., Hennebelle, P., & Chabrier, G. 2011a, [A&A](#), **529**, A35
- Commerçon, B., Audit, E., Chabrier, G., & Chièze, J. P. 2011b, [A&A](#), **530**, A13
- Commerçon, B., Debout, V., & Teyssier, R. 2014, [A&A](#), **563**, A11
- Dunham, M. M., Stutz, A. M., Allen, L. E., et al. 2014, in [Protostars and Planets VI](#), eds. H. Beuther, R. S. Klessen, C. P. Dullemond, & T. Henning, 195
- Durney, B. R., De Young, D. S., & Roxburgh, I. W. 1993, [Sol. Phys.](#), **145**, 207
- Ferguson, J. W., Alexander, D. R., Allard, F., et al. 2005, [ApJ](#), **623**, 585
- Foglizzo, T., Galletti, P., Scheck, L., & Janka, H. T. 2007, [ApJ](#), **654**, 1006
- González, M., Vaytet, N., Commerçon, B., & Masson, J. 2015, [A&A](#), **578**, A12
- Grudić, M. Y., Guszejnov, D., Offner, S. S. R., et al. 2022, [MNRAS](#), **512**, 216
- Hennebelle, P., & Falgarone, E. 2012, [A&ARv](#), **20**, 55
- Hennebelle, P., Commerçon, B., Lee, Y.-N., & Charnoz, S. 2020a, [A&A](#), **635**, A67
- Hennebelle, P., Commerçon, B., Lee, Y.-N., & Chabrier, G. 2020b, [ApJ](#), **904**, 194
- Hennebelle, P., Lebreuilly, U., Colman, T., et al. 2022, [A&A](#), **668**, A147
- Johns-Krull, C. M., Greene, T. P., Doppmann, G. W., & Covey, K. R. 2009, [ApJ](#), **700**, 1440
- Klessen, R. S., & Hennebelle, P. 2010, [A&A](#), **520**, A17
- Kolmogorov, A. 1941, [Dokl. Akad. Nauk SSSR](#), **30**, 301
- Larson, R. B. 1969, [MNRAS](#), **145**, 271
- Larson, R. B. 1972, [MNRAS](#), **157**, 121
- Lebreuilly, U., Hennebelle, P., Colman, T., et al. 2021, [ApJ](#), **917**, L10
- Machida, M. N., Inutsuka, S.-I., & Matsumoto, T. 2006, [ApJ](#), **647**, L151
- Machida, M. N., Inutsuka, S.-I., & Matsumoto, T. 2007, [ApJ](#), **670**, 1198
- Masunaga, H., & Inutsuka, S.-I. 2000, [ApJ](#), **531**, 350
- Maury, A. J., André, P., Testi, L., et al. 2019, [A&A](#), **621**, A76
- McKee, C. F., & Ostriker, E. C. 2007, [ARA&A](#), **45**, 565
- Mignon-Risse, R., González, M., & Commerçon, B. 2021, [A&A](#), **656**, A85
- Minerbo, G. N. 1978, [J. Quant. Spectr. Rad. Transf.](#), **20**, 541
- Narita, S., Nakano, T., & Hayashi, C. 1970, [Prog. Theor. Phys.](#), **43**, 942
- Palla, F., & Stahler, S. W. 1991, [ApJ](#), **375**, 288
- Penston, M. V. 1969, [MNRAS](#), **144**, 425
- Saumon, D., Chabrier, G., & van Horn, H. M. 1995, [ApJS](#), **99**, 713
- Scheck, L., Plewa, T., Janka, H. T., Kifonidis, K., & Müller, E. 2004, [Phys. Rev. Lett.](#), **92**, 011103
- Semenov, D., Henning, T., Helling, C., Ilgner, M., & Sedlmayr, E. 2003, [A&A](#), **410**, 611
- Shu, F. H. 1977, [ApJ](#), **214**, 488
- Stahler, S. W., & Palla, F. 2004, [The Formation of Stars](#) (Wiley-VCH)
- Stahler, S. W., Shu, F. H., & Taam, R. E. 1980, [ApJ](#), **241**, 637
- Teyssier, R. 2002, [A&A](#), **385**, 337
- Teyssier, R., & Commerçon, B. 2019, [Front. Astron. Space Sci.](#), **6**, 6
- Tomida, K., Machida, M. N., Saigo, K., Tomisaka, K., & Matsumoto, T. 2010, [ApJ](#), **725**, L239
- Tomida, K., Tomisaka, K., Matsumoto, T., et al. 2013, [ApJ](#), **763**, 6
- Tomida, K., Machida, M. N., Hosokawa, T., Sakurai, Y., & Lin, C. H. 2017, [ApJ](#), **835**, L11
- Truelove, J. K., Klein, R. I., McKee, C. F., et al. 1997, [ApJ](#), **489**, L179
- Tsukamoto, Y., Iwasaki, K., Okuzumi, S., Machida, M. N., & Inutsuka, S. 2015, [MNRAS](#), **452**, 278
- Urban, A., Martel, H., & Evans, N. J. II 2010, [ApJ](#), **710**, 1343
- Vaidya, B., Mignone, A., Bodo, G., & Massaglia, S. 2015, [A&A](#), **580**, A110
- Vaytet, N., & Haugbølle, T. 2017, [A&A](#), **598**, A116
- Vaytet, N., Chabrier, G., Audit, E., et al. 2013, [A&A](#), **557**, A90
- Vaytet, N., Commerçon, B., Masson, J., González, M., & Chabrier, G. 2018, [A&A](#), **615**, A5
- Vorobyov, E. I., & Basu, S. 2015, [ApJ](#), **805**, 115
- Winkler, K. H. A., & Newman, M. J. 1980, [ApJ](#), **236**, 201
- Wurster, J., & Lewis, B. T. 2020a, [MNRAS](#), **495**, 3807
- Wurster, J., & Lewis, B. T. 2020b, [MNRAS](#), **495**, 3795
- Wurster, J., Bate, M. R., & Price, D. J. 2018, [MNRAS](#), **481**, 2450
- Wurster, J., Bate, M. R., Price, D. J., & Bonnell, I. A. 2022, [MNRAS](#), **511**, 746

Appendix A: Defining the protostar in our simulation

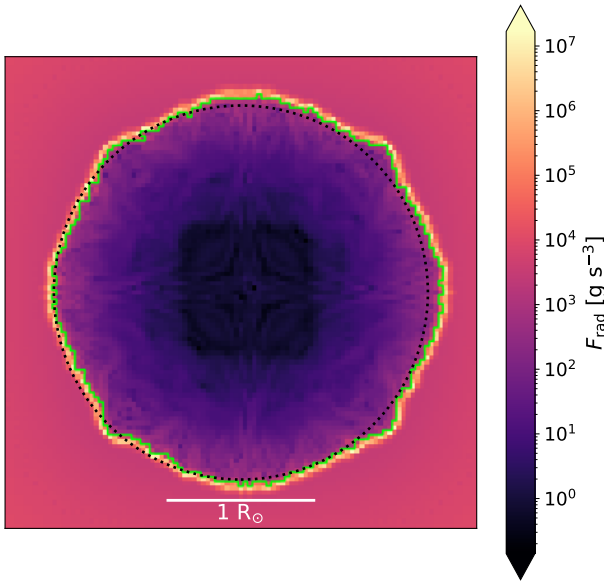


Fig. A.1. Illustration of our protostar definition criterion in a slice through the center of the domain at the epoch of protostellar formation. The colormap represents the local radiative flux, which prominently displays the second core accretion shock. The lime contour represents our $P \approx \rho v_r^2$ criterion for the protostellar surface, of which all cells within it are counted as among the protostar. The dotted black circle represents an angular average radius of the protostellar surface.

Herein, we present our definition of the protostar, namely the criterion by which we select cells that belong to it. Ideally, one would like to select all cells at and downstream of the accretion shock. For this, we have opted to adopt the criterion of Tomida et al. (2010), which selects all cells whose thermal pressure support outweighs ram pressure ($P > \rho v_r^2$). However, this criterion also selects cells belonging to the first core that are not currently undergoing a second gravitational collapse. As such, we have supplemented this criterion with a radius check, in which only cells at radii smaller than twice that of the 10^{-5} g cm $^{-3}$ density isocontour can be selected. In order to compute R_* , we simply average the radius of the $P \approx \rho v_r^2$ contour (i.e., the protostellar surface). The results of this criterion are presented in Fig. A.1, which displays satisfactory results as the $P \approx \rho v_r^2$ contour closely follows the accretion shock front.

Appendix B: Resolution study

As mentioned previously, simulating the stellar formation process requires a robust treatment of a multitude of physical processes. As such, each physical process requires an adequate spatial sampling in order to produce physical results. The most common approach in our field is a continuous refinement of the grid based on the local Jeans length as suggested by Truelove et al. (1997). This study suggested that the Jeans length be resolved with at least four cells; however, this is inadequate to describe a second gravitational collapse, as the huge dynamical range requires a more diligent approach to spatial refinement. In addition, the inclusion of magnetic fields, be they ideal or nonideal, as well as the incorporation of radiative transfer can add further strain on simulations, as this requires additional spatial sampling to describe the full range of magnetic

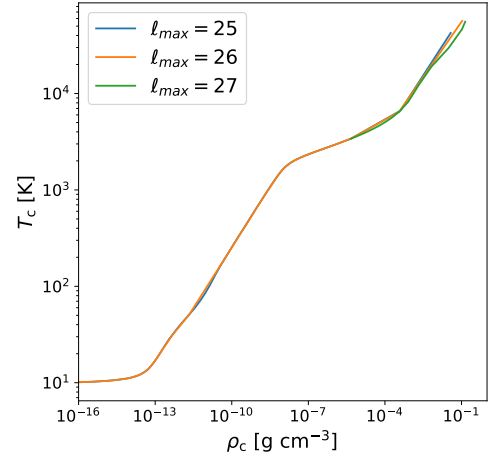


Fig. B.1. Central temperature plotted against central density prior to the first hydrodynamical bounce, for simulations with a maximum refinement level of 25 ($\Delta x = 2.93 \times 10^{-4}$ AU, blue curve), 26 ($\Delta x = 1.46 \times 10^{-4}$ AU, orange curve), and 27 ($\Delta x = 7.34 \times 10^{-5}$ AU, green curve).

resistivities and the dust and gas opacities (see the discussions in Vaytet & Haugbølle 2017; Vaytet et al. 2018; Wurster et al. 2022). As such, it is important to carry out thorough examinations of the effect of resolution to test the convergence of each simulation based on the physical processes included in it, as well as the initial conditions with which it is carried out.

To this end, we have carried out two additional lower and higher resolution simulations in which we vary the maximum refinement level; however, the number of cells per λ_J^* was maintained at 20 (see Eq. 13 and 14) as this has proven to be perfectly adequate. These two simulations possess a maximum refinement level ℓ_{\max} of 25 and 27, as opposed to the intermediate $\ell_{\max} = 26$ of the simulation presented in the main body of this paper. This respectively offers them a spatial resolution of $\Delta x = 2.93 \times 10^{-4}$ AU and $\Delta x = 7.34 \times 10^{-5}$ AU at the maximal refinement level, as opposed to $\Delta x = 1.46 \times 10^{-4}$ AU.

We thus show in Fig. B.1 the central temperature as a function of the central density prior to the first hydrodynamical bounce (i.e., the moment when the central density drops from one snapshot to the next). The figure shows that prior to the formation of the protostar, all three simulations have followed identical evolutionary paths. However, the maximum density reached differs; the lower resolution run with $\ell_{\max} = 25$ (blue curve) has attained 3.76×10^{-2} g cm $^{-3}$, the intermediate $\ell_{\max} = 26$ (orange curve) reached 1.05×10^{-1} g cm $^{-3}$, and the higher resolution $\ell_{\max} = 27$ (green curve) reached 1.39×10^{-1} g cm $^{-3}$. Thus, the central density achieved by the second gravitational collapse is resolution dependent; however, the intermediate resolution run achieved much closer results to the higher resolution run than to its lower resolution counterpart.

We now turn to Fig. B.2, which shows density slices through the center of the domain for all three simulations with their AMR refinement level contours. These slices are shown at a moment in time where all three protostars have reached similar masses. Unsurprisingly, the spherical morphology of the protostar is better described in the intermediate (panel b) and high (panel c) resolution runs. Furthermore, the additional refinement levels allow a better resolution of the shock front, which is crucial to properly describe the sharp protostellar border. We also note that the lower resolution run displays a much larger radius than its intermediate and higher resolution counterparts.

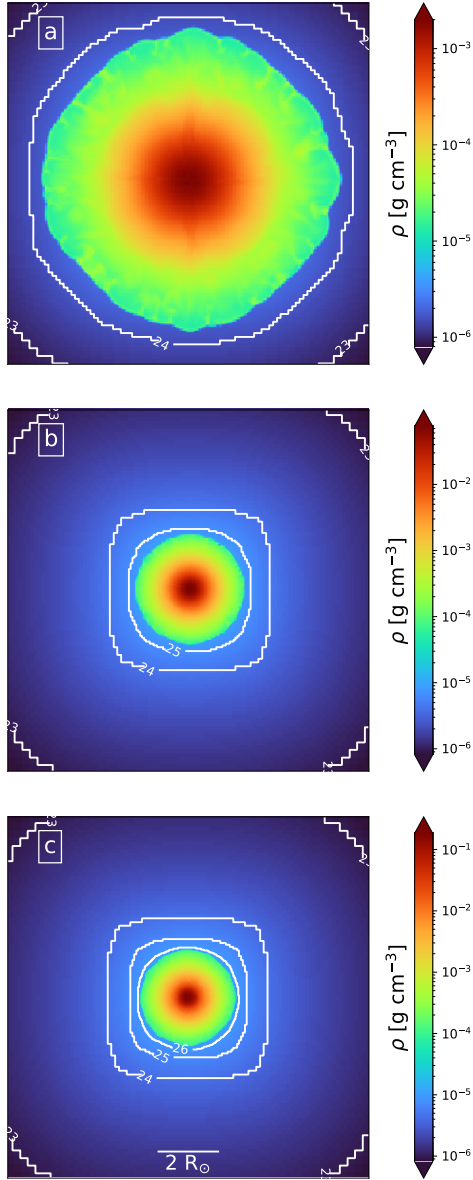


Fig. B.2. Density slices through the center of the domain for simulations with a maximum refinement level of 25 ($\Delta x = 2.93 \times 10^{-4}$ AU, panel a), 26 ($\Delta x = 1.46 \times 10^{-4}$ AU, panel b), and 27 ($\Delta x = 7.34 \times 10^{-5}$ AU, panel c). The scale bar in panel (c) applies to the other two panels. These slices are shown at a moment when all three protostars have reached similar masses ($5.9 \times 10^{-3} M_{\odot}$ for panel (a), $5.75 \times 10^{-3} M_{\odot}$ for panels (b) and (c)).

In Fig. B.3, we display the evolution of the radius (panel a) and masses (panel b) of the protostars. We note here that the higher resolution run (green curves) forms a smaller protostar, both in radius and in mass. In addition, it consistently shows smaller radii than the $\ell_{\max} = 25$ and 26 runs at similar masses. The radius of the protostar in the lower resolution simulation fluctuates wildly, as the interior is poorly resolved in this run. In addition, the protostar in this run shows a huge, spurious drop in mass by $t \approx 90$ days, which demonstrates that it is inadequate to describe its evolution. Since the radiative behavior of the accretion shock front is identical in all three runs (i.e., extremely subcritical), the smaller radius in the higher resolution run is explained by the more adequate description of turbulence it provides. Indeed, we show in panel (a) of Fig. B.4 the veloc-

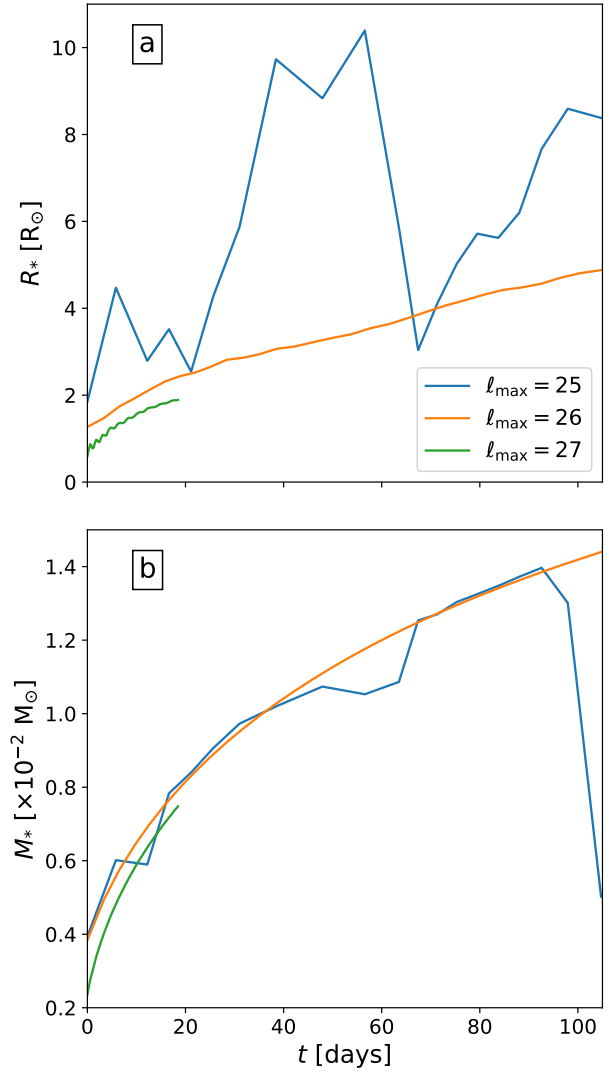


Fig. B.3. Radius (panel a) and mass (panel b) displayed as a function of time, where $t = 0$ marks the epoch of protostellar birth, for simulations with a maximum refinement level of 25 ($\Delta x = 2.93 \times 10^{-4}$ AU, blue curve), 26 ($\Delta x = 1.46 \times 10^{-4}$ AU, orange curve), and 27 ($\Delta x = 7.34 \times 10^{-5}$ AU, green curve).

ity dispersions computed in radial bins inside the protostar. The higher resolution run displays stronger velocity dispersions than the other two runs, which provides a better turbulent transport of heat. As a result, the plateau in the entropy profile is better developed here than in $\ell_{\max} = 25$ and 26 runs, which shows that the energy has been better redistributed. Hence, the radius of the protostar in the higher resolution run is consistently smaller.

Finally, we display in Fig. B.5 the ratio of ortho-radial to radial kinetic energies (see Eq. 24) of the protostars as a function of time. The temporal evolution here is similar for the $\ell_{\max} = 26$ and 27 runs, but the $\ell_{\max} = 25$ once again appears to be incapable of properly describing the turbulent motions within the protostar.

In summary, although this resolution study has shown that our simulations are not converged, the differences between the $\ell_{\max} = 26$ and $\ell_{\max} = 27$ runs are small enough for us to conclude that our results are sufficiently realistic for physical interpretations. When taking into account the stringent time-stepping involved in the $\ell_{\max} = 27$ run (which we could not integrate past a dozen days), we have concluded that $\ell_{\max} = 26$ is the optimal resolution choice.

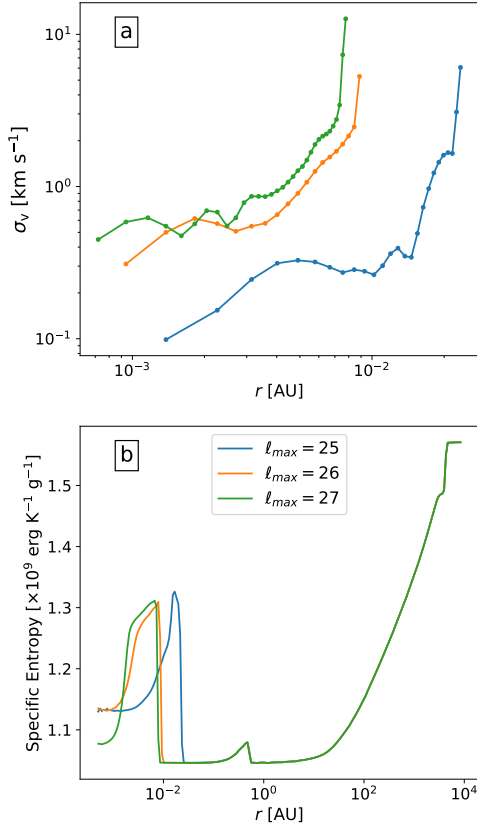


Fig. B.4. Velocity dispersion inside the protostar computed in radial bins (panel a) and average specific entropy (panel b), for simulations with a maximum refinement level of 25 ($\Delta x = 2.93 \times 10^{-4}$ AU, blue curves), 26 ($\Delta x = 1.46 \times 10^{-4}$ AU, orange curves), and 27 ($\Delta x = 7.34 \times 10^{-5}$ AU, green curves). These are shown at a moment in time where all three protostars have reached similar masses ($5.9 \times 10^{-3} M_{\odot}$ for $\ell_{\max} = 25$, $5.75 \times 10^{-3} M_{\odot}$ for $\ell_{\max} = 26$ and $\ell_{\max} = 27$).

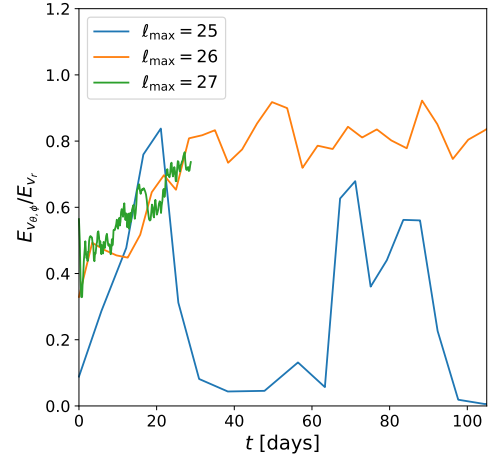


Fig. B.5. Kinetic energy of the ortho-radial flow compared to that of radial flow inside the protostar as a function of time, where $t = 0$ marks the birth of the protostar, for simulations with a maximum refinement level of 25 ($\Delta x = 2.93 \times 10^{-4}$ AU, blue curve), 26 ($\Delta x = 1.46 \times 10^{-4}$ AU, orange curve), and 27 ($\Delta x = 7.34 \times 10^{-5}$ AU, green curve).

Appendix C: Collapse with multigroup radiative transfer

In order to test the robustness of our simulation's results, which uses a gray approximation for its radiative transfer, we have conducted a second simulation with a multigroup description. It possesses the same initial conditions; however, we now split the $[10^5; 10^{19}$ Hz] frequency range into four distinctive groups. The results of the simulation are extremely similar to that of its gray counterpart, as previously reported by the 1D calculations in Vaytet et al. (2013).

Our choice of 4 groups was the result of significant memory constraints. Indeed, since our maximum refinement level is 26, this requires the allocation of around 1.5 TB of RAM memory, of which ≈ 915 GB are used by the AMR grid. Furthermore, such a memory cost meant that the 64 processing cores had to be spread across 4 times as many computing nodes, which increased the CPU communications burden. In addition to the heightened computational load, the added communications burden constrained our ability to integrate the simulation on longer timescales.

Since protostars form with temperatures $> 10^4$ K, most of the radiative energy is in the ultraviolet part of the electromagnetic spectrum. This energy is later absorbed by the surrounding gas and reemitted in the infrared. We thus chose to have both an infrared and an ultraviolet-visible group, with two other radiative groups bordering these two to avoid any energy omissions. The frequency borders of each group are presented in Table C.1, and the opacity meshes created for each of them using the previously mentioned Delaunay triangulation process are presented in Fig. C.1.

These meshes are very similar to the gray mesh (see Fig. 1); the dust destruction front and the subsequent atomic opacity peak are both clearly visible except for the X-ray mesh (panel d), where the destruction of the dust particles barely has a noticeable

effect. In addition, the X-ray mesh also contains a batch of triangles at $\log(T) \sim 3.5$, which is due to a lack of sampling points in the Vaytet et al. (2013) dataset. However, since this radiative group is the least prominent in terms of radiative energies, this will have a minor effect on our simulation.

The results of this multigroup simulation are displayed in Figures C.2 and C.3, where we compare it with its gray counterpart. Fig. C.2 shows the luminosity of each radiative group (computed using Eq. 17). We see that the total multigroup luminosity (lime dash-dotted line) and the gray luminosity (black dotted line) are very similar, albeit the location of the first core accretion shock differs slightly (0.5 and 0.6 AU). This is due to a slightly higher amount of enclosed radiative energy inside the first core for the multigroup run (in turn due to a higher opacity for UV-Visible photons), which causes its specific entropy to increase by virtue of radiative heating from the second core accretion shock.

Unsurprisingly, the UV-Visible group dominates the luminosity output of the protostar, whereas the IR group dominates everywhere else. At both first and second core shock fronts, the luminosity of each radiative group spikes, although the X-ray photons produced at these locations are quickly reprocessed by the other groups.

Finally, the evolution of the properties of the protostar formed in the multigroup run is compared to that of its gray counterpart in Fig. C.3. We find that the radii, luminosities and radiative efficiencies are extremely similar, although the mass differs slightly. As mentioned previously, the first core in the multigroup run has a slightly higher enclosed energy. This causes the mass accretion rate unto the second core to be lower. Despite the differing masses, the radii are very similar because of a similar amount of specific entropy.

This allows us to conclude that the multigroup description offers no major differences to its gray counterpart, a result which is in agreement with Vaytet et al. (2013).

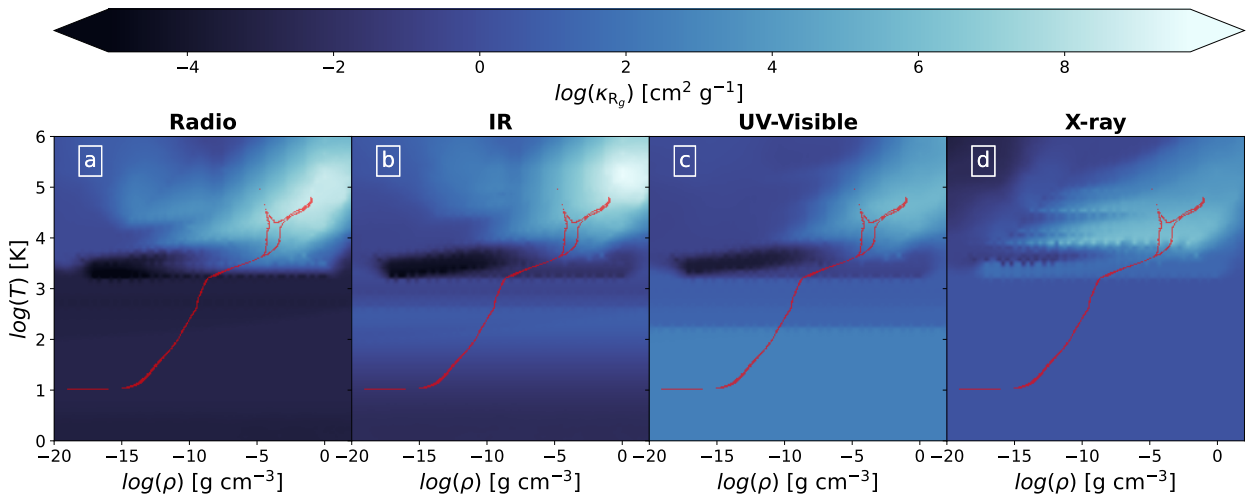
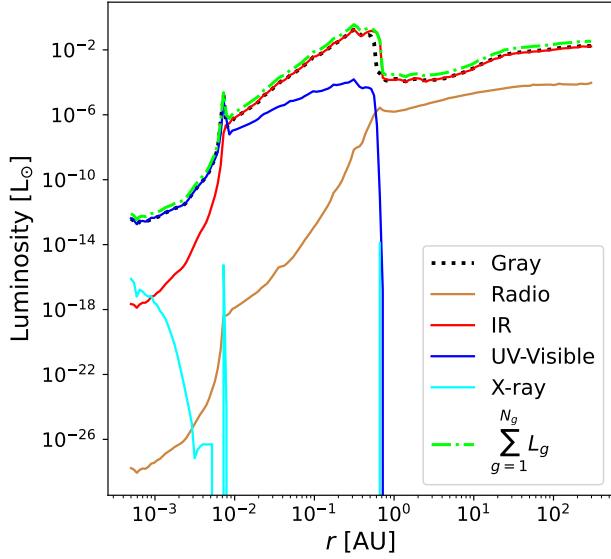
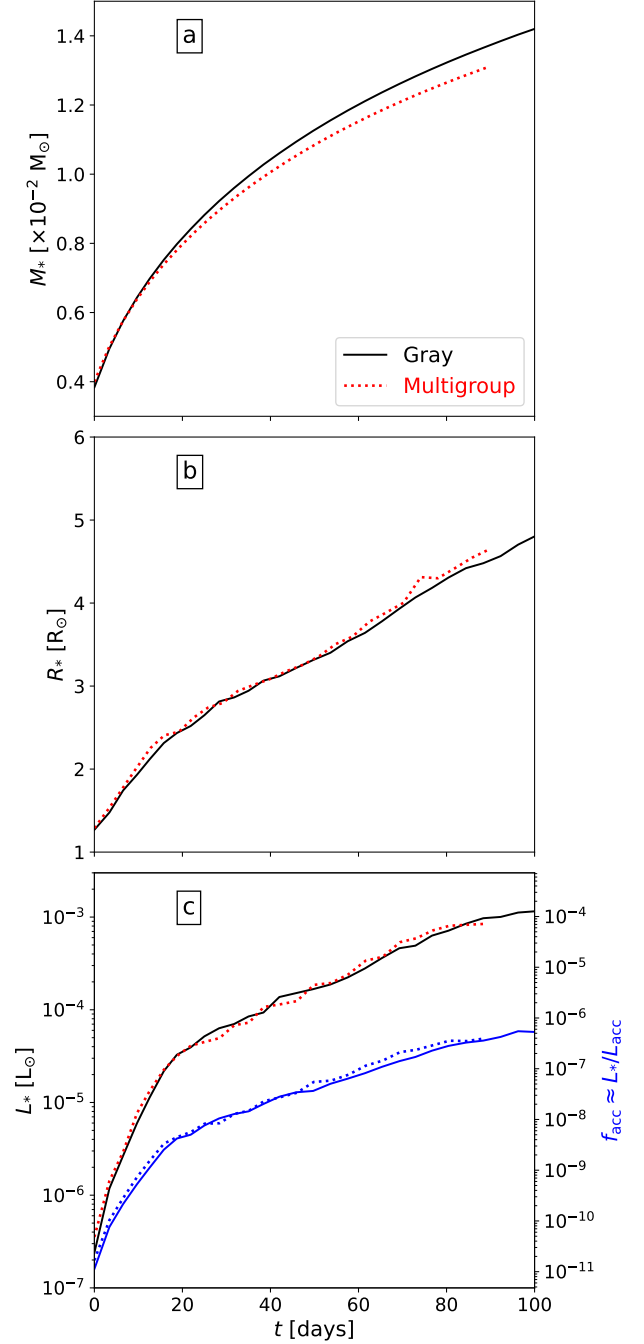


Fig. C.1. Rosseland mean opacity meshes created for each radiative group in our multigroup simulation (see Table C.1). The temperature-density distribution of all cells during the epoch of protostellar birth is overlaid in red.

Table C.1. Frequency and corresponding wavelength borders of the 4 radiative groups used in our multigroup simulation.

Radiative Group	$[\nu_1; \nu_2]$ (Hz)	$[\lambda_2; \lambda_1]$ (m)
1: Radio	$[10^5; 3 \times 10^{11}]$	$[3 \times 10^3; 10^{-4}]$
2: IR	$[3 \times 10^{11}; 4.287 \times 10^{14}]$	$[10^{-4}; 7 \times 10^{-7}]$
3: UV-Visible	$[4.287 \times 10^{14}; 3 \times 10^{16}]$	$[7 \times 10^{-7}; 10^{-8}]$
4: X-ray	$[3 \times 10^{16}; 10^{19}]$	$[10^{-8}; 3 \times 10^{-11}]$


Fig. C.2. Luminosity profiles displayed as a function of radius at the epoch of the protostar's birth for the gray radiative transfer simulation (dotted black line) and its multigroup counterpart (colored solid lines). The lime dash-dotted line is the total luminosity in the multigroup run.

Fig. C.3. Comparison of the protostellar mass (panel a), radius (panel b), and luminosity (panel c) between our gray radiative transfer simulation (solid black lines) and its multigroup counterpart (dotted red lines). The solid (resp. dotted) blue line in panel (c) represents the protostellar radiative efficiency in the gray (resp. multigroup) simulation.

Appendix D: Comparison with a 2D simulation

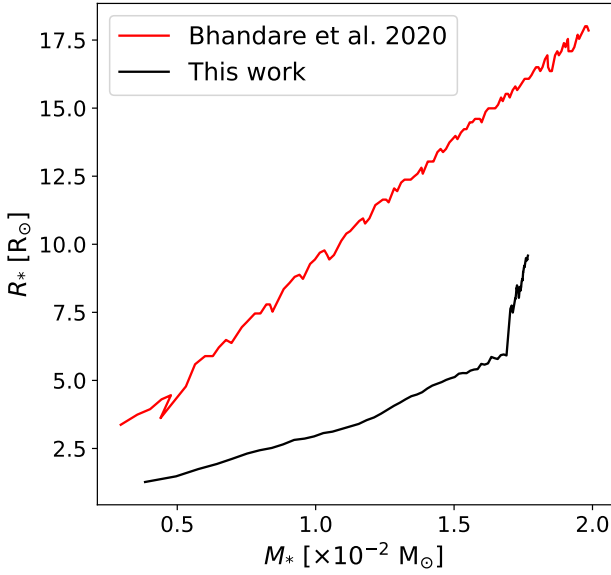


Fig. D.1. Radius of the protostar as a function of its mass: a comparison of the results of this paper (black curve) with those of [Bhandare et al. \(2020\)](#) (red curve).

Herein, we compare the results of our simulation with those of the $1 M_{\odot}$ 2D collapse calculations of [Bhandare et al. \(2020\)](#). Since their calculations are similar to ours, this will allow us to better assess what a three dimensional description of the gas motion offers. To this end, we begin by studying Fig. D.1, which shows the protostellar radius as a function of protostellar mass. We see that protostar is consistently more compact than in the 2D calculation; it possesses a smaller radius for a given mass. Since the radiative efficiency of the protostar is extremely low in both simulations, this cannot be explained by any of the protostars radiating away more energy than the other. We explain this difference in radii by comparing their radial entropy profiles in Fig. D.2: by the time the protostar reaches a mass of $\approx 1.76 \times 10^{-2} M_{\odot}$, the entropy plateau in the interior is achieved in our 3D simulation, whereas it has yet to form in the 2D counterpart. This allows us to conclude that the 3D description of the

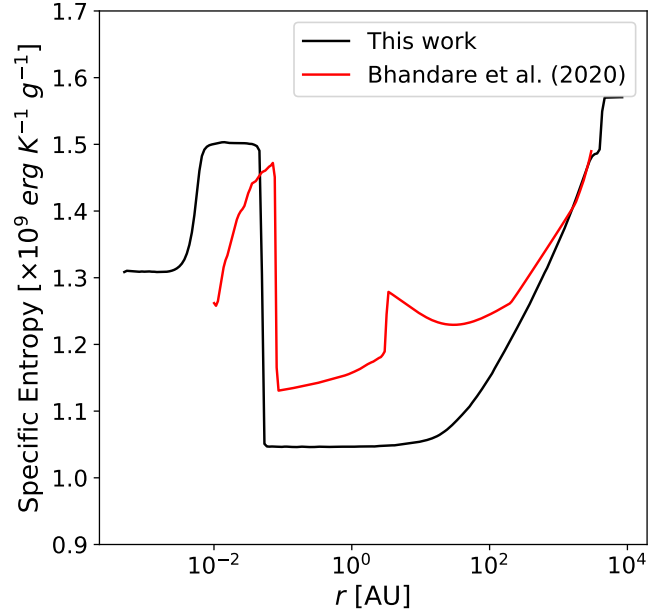


Fig. D.2. Comparison of the results of this paper (black curve) with those of [Bhandare et al. \(2020\)](#) (red curve). The curves display the specific entropy, averaged in radial bins and displayed as a function of radius, at a moment in time where both protostars have a mass of $\approx 1.76 \times 10^{-2} M_{\odot}$.

gas motion allows for more efficient entropy mixing, which regulates the radius of the protostar.

However, the entropy profile outside the second core is quite different in our two simulations. This can be explained by the different initial conditions. Indeed, [Bhandare et al. \(2020\)](#) have used a Bonnor-Ebert sphere as their initial conditions, whereas we have used a highly unstable uniform density sphere. This results in a shorter first core lifetime in our simulation, and it is accreted by the time our protostar has reached $\approx 1.76 M_{\odot}$. In addition to this, the equation of state table used in both simulations is different. This causes different behaviors in entropy, particularly inside the second Larson core since the [Saumon et al. \(1995\)](#) EOS takes into account the ionization of He, whereas the [Vaidya et al. \(2015\)](#) EOS used in [Bhandare et al. \(2020\)](#) does not.

Appendix E: Standing Accretion Shock Instability

Herein, we investigate whether or not the Standing Accretion Shock Instability (SASI, Blondin et al. 2003; Scheck et al. 2004; Foglizzo et al. 2007) could be the mechanism behind the onset of turbulence within our protostar. This instability is known to operate in core-collapse supernovae, where it causes them to appear aspherical. Recently, Bhandare et al. (2020) put forth the hypothesis that this instability could be at play in protostars, where it could cause oscillations of the accretion shock. SASI requires for feedback to occur between the central regions and the accretion shock. Although our physical environment heavily differs from that of a core-collapse supernova and we do not have a proto-neutron star downstream of our second core accretion shock, our protostar has a central region of highly dense, ionized gas that repulses inward flow. In this sense, the central regions of our protostar can communicate with the accretion shock through acoustic feedback. In the 2D study of Bhandare et al. (2020), the central regions ($r < 10^{-2}$ AU) were a part of a reflexive inner boundary, which can naturally provide feedback to the shock front.

In order to investigate whether this mechanism is responsible for the generation of turbulence in our protostar, we study our $\ell_{\max} = 27$ run presented in Appendix B due to its high spatial and temporal resolution. Indeed, this run presents oscillations of the protostellar radius possibly caused by SASI. To this end, we display in panel (a) of Fig. E.1 the amplitude of said oscillations, computed as $(R_* - \bar{R}_*)/\bar{R}_*$, where \bar{R}_* is the average radius of the protostar over a given period. Here, we can clearly see high amplitude, high frequency oscillations at protostellar birth; however, their amplitude and frequency reduces over time. This is more readily seen in the power spectrum of this curve (panel b), which shows a high energy peak corresponding to a period of ≈ 1.4 days, and a handful of lower energy low frequency peaks. These oscillation periods of the protostellar radius should be compared with the advection timescale t_{adv} , computed as (Foglizzo et al. 2007):

$$t_{\text{adv}} = \int_{R_{\nabla}}^{R_*} \frac{dr}{|v_r(r)|}, \quad (\text{E.1})$$

where R_{∇} is the radius where the gas has effectively settled following its crossing of the accretion shock (i.e., v_r has reached ≈ 0). Our estimate of t_{adv} has yielded ≈ 3 days, which is about twice as long as the oscillation period of the protostar. However, as the protostellar radius grows, so too does t_{adv} , which could explain why the frequency of oscillations is reducing over time.

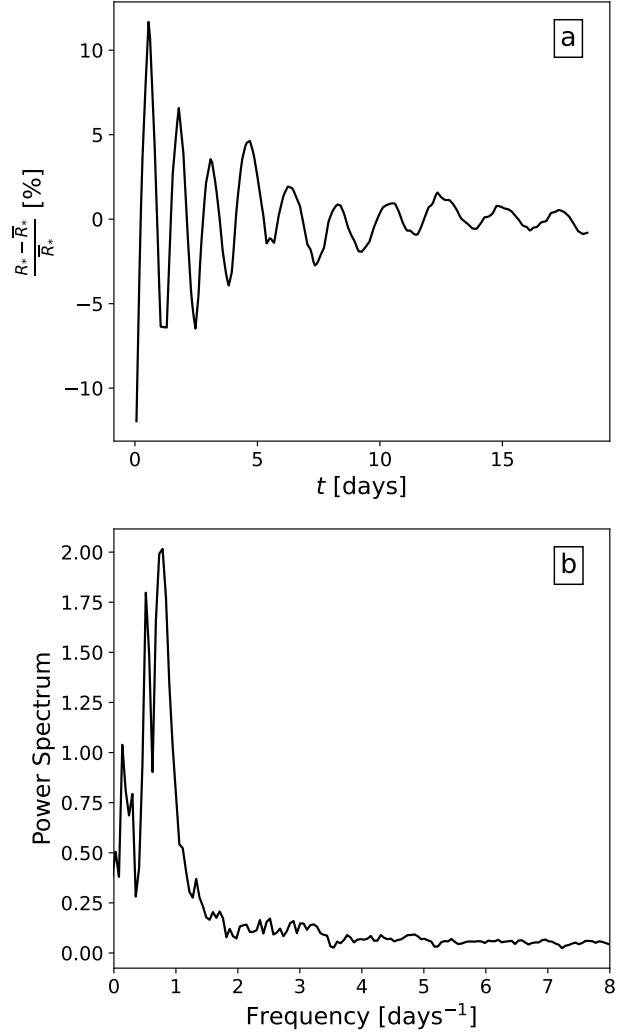


Fig. E.1. Amplitude of oscillations of the protostellar radius in the $\ell_{\max} = 27$ run (panel a), displayed as a function of time where $t = 0$ marks the birth of the protostar. Panel (b) displays the Fourier transform of the curve in panel (a).

Although these measurements do not allow us to conclude with certainty that SASI is operating in our protostar, they do indicate that we are in the regime where it is theoretically possible.

3.3 Paper II: Birth of circumstellar disks

In recent years, the main objective behind most efforts involved in studying the collapse of dense cores has not been the protostar itself, but rather, the circumstellar disk. The main idea being to produce a self-consistent model of the formation and evolution of said disk. However, doing so requires one to omit the protostar from simulations, as that would require a very stringent timestep that prohibits the study of the circumstellar disk across large enough timescales. As such, the inner-most regions relevant to protostellar and circumstellar disk formation (< 1 AU) are often omitted in favor of a sink particle, onto-which sub-grid physics are encoded. However, recent studies (Machida et al. 2014; Vorobyov et al. 2019; Hennebelle et al. 2020b) have shown that said sub-grid physics have a strong impact on the resulting properties of the circumstellar disk, be it during its formation or evolution. This implies that the star-disk interaction wrapped into the sub-grid model has to be self-consistently modeled, and calls for a concerted effort in which the protostar and circumstellar disk are jointly studied.


After the publication of my first paper, I shifted my focus from the protostar to circumstellar disks. Although the spherically symmetrical calculation has delivered valuable insights on the interior structure of the protostar and the radiative behavior of its accretion shock, it provide us with an incomplete description of the birth of protostars as it does not account for angular momentum. In order to do so, we decided to introduce an initially turbulent velocity vector field in the dense core. This is to account for the fact that molecular clouds are highly turbulent structures (Larson 1981; Miville-Deschênes et al. 2017) whose large scale turbulent motions cascade down to the scale of dense cores. Although a survey of velocity dispersions inside these structures is currently lacking in the literature, case-studies have so far shown subsonic measurements (Bergin & Tafalla 2007; Gaudel et al. 2020), and so we have chosen to include at most transonic turbulence in our initial conditions.

Studying the star-disk interaction, as well as the radiative behavior of the protostar in these conditions, had never been done before in the literature. The main reason behind this being the stringent timestepping constraints that forced theorists to prematurely stop their calculations as soon as the second Larson core had formed. During this project, I ran a multitude of simulations with a variety of initial conditions in which the initial amount of angular momentum in the dense core varied. In order to alleviate timestepping constraints, while maintaining the extremely high resolution and stringent refinement criterion required to study both the nascent protostar and its circumstellar disk, we decided to omit magnetic fields from these calculations. This has a physical justification; all non-ideal MHD simulations having reached the second collapse stage in the literature report that magnetic fields are diffused by Ohmic dissipation and ambipolar diffusion to the point where thermal pressure support vastly outweighs magnetic pressure in high density gas ($\rho > 10^{-11}$ g cm $^{-3}$). As such, one may describe the early evolution of the protostar to a reasonably high degree of fidelity without magnetic fields, although one must keep in mind that the behavior at lower densities is heavily affected by them.

Despite the absence of magnetic fields, each simulation required months of CPU wall

time and at least 100 000 CPU hours in total. This brute-force approach allowed us to describe the combined birth of the protostar and its circumstellar disk with unprecedented detail. The paper below, published in *Astronomy & Astrophysics*, presents its findings.

Formation of low-mass protostars and their circumstellar disks[★]

A. Ahmad¹, M. González¹, P. Hennebelle², and B. Commerçon³

¹ Université Paris Cité, Université Paris-Saclay, CEA, CNRS, AIM, 91191 Gif-sur-Yvette, France
e-mail: adnan.ali.ahmad1998@gmail.com

² Université Paris-Saclay, Université Paris Cité, CEA, CNRS, AIM, 91191 Gif-sur-Yvette, France

³ Univ. Lyon, Ens de Lyon, Univ. Lyon 1, CNRS, Centre de Recherche Astrophysique de Lyon UMR5574, 69007 Lyon, France

Received 25 January 2024 / Accepted 21 April 2024

ABSTRACT

Context. Understanding circumstellar disks is of prime importance in astrophysics; however, their birth process remains poorly constrained due to observational and numerical challenges. Recent numerical works have shown that the small-scale physics, often wrapped into a sub-grid model, play a crucial role in disk formation and evolution. This calls for a combined approach in which both the protostar and circumstellar disk are studied in concert.

Aims. We aim to elucidate the small-scale physics and constrain sub-grid parameters commonly chosen in the literature by resolving the star-disk interaction.

Methods. We carried out a set of very high resolution 3D radiative-hydrodynamics simulations that self-consistently describe the collapse of a turbulent, dense molecular cloud core to stellar densities. We studied the birth of the protostar, the circumstellar disk, and its early evolution (<6 yr after protostellar formation).

Results. Following the second gravitational collapse, the nascent protostar quickly reaches breakup velocity and sheds its surface material, thus forming a hot ($\sim 10^3$ K), dense, and highly flared circumstellar disk. The protostar is embedded within the disk such that material can flow without crossing any shock fronts. The circumstellar disk mass quickly exceeds that of the protostar, and its kinematics are dominated by self-gravity. Accretion onto the disk is highly anisotropic, and accretion onto the protostar mainly occurs through material that slides on the disk surface. The polar mass flux is negligible in comparison. The radiative behavior also displays a strong anisotropy, as the polar accretion shock was shown to be supercritical, whereas its equatorial counterpart is subcritical. We also find a remarkable convergence of our results with respect to initial conditions.

Conclusions. These results reveal the structure and kinematics in the smallest spatial scales relevant to protostellar and circumstellar disk evolution. They can be used to describe accretion onto regions commonly described by sub-grid models in simulations studying larger-scale physics.

Key words. stars: early-type – stars: evolution – stars: formation – stars: low-mass – stars: pre-main sequence – stars: protostars

1. Introduction

Circumstellar disks form as a result of the conservation of angular momentum during the collapse of gravitationally unstable pre-stellar cloud cores. Understanding the formation of these disks and their subsequent evolution is of fundamental importance in astrophysics, as they are the birthplace of planets. This task is, however, heavily impeded by numerous challenges in observing star-forming regions, as the dense infalling envelope obscures the nascent disk during the class 0 phase. As such, most observational constraints come from more evolved class I and II disks. From a theoretical standpoint, the prohibitive time-stepping constraints in numerical simulations has made it nearly impossible to self-consistently describe the evolution of a newly formed circumstellar disk over a sufficiently large timescale in order to compare it with observations. To circumvent these constraints, theorists have abandoned the description of the innermost regions (<1 AU) and instead use sink particles (Bate et al. 1995; Bleuler & Teyssier 2014) onto which sub-grid physics are encoded. These particles interact with the surrounding gas through self-gravity and accretion as well as through radiative and mechanical feedback effects such as out-

flows and stellar winds. The parameters of these particles, such as their effective radius and accretion thresholds, have largely been chosen on the grounds of educated guesswork. Although necessary to study the global evolution of the disk, reducing the inner regions (which contain the protostar) to a sub-grid model can produce nonphysical results, especially when much of the actual sub-grid physics that have been encoded remain poorly constrained.

In this respect, Machida et al. (2014) investigated the effects of sink parameters on the formation of circumstellar disks. They found that the choice of the sink radius and its accretion threshold can, in conjunction with the physical model employed, dictate the formation and evolution of a circumstellar disk. Vorobyov et al. (2019) led a similar study but focused on the mass transport rate from the sink cell to the protostellar surface. They found that simulations with a slower mass transport rate would form more massive disks and that the accretion rate onto the protostar displayed more episodic behavior.

Finally, Hennebelle et al. (2020a) studied the influence of the sink accretion threshold on the global evolution of the disk. They found that while the mass contained within the sink is insensitive to this parameter, the disk radius and mass exhibit a strong sensitivity to it. Indeed, they found that the disk mass increases significantly at higher accretion thresholds.

[★] Movies are available at <https://www.aanda.org>

From these empirical studies, it has become clear that a deeper understanding of the disk's inner boundary is a necessary endeavor to pursue in order to understand the global disk evolution. Of course, this is not the only field of application of sink particles. Much larger scale simulations that seek to provide a protoplanetary disk or stellar population synthesis by modeling the collapse of an entire molecular cloud, such as those of [Bate \(2012, 2018\)](#), [Hennebelle et al. \(2020b\)](#), [Lebreuilly et al. \(2021, 2024a,b\)](#), [Grudić et al. \(2022\)](#), also rely on sink particles for their inclusion of small-scale physics. This also applies to simulations studying the high-mass regime (e.g., [Krumholz et al. 2009](#); [Kuiper et al. 2010](#); [Mignon-Risse et al. 2021a,b, 2023](#); [Commerçon et al. 2022](#); [Oliva & Kuiper 2023](#)). However, understanding the inner boundaries of circumstellar disks requires a self-consistent description of the inner regions in which one must model the formation of the protostar following a second gravitational collapse triggered by the dissociation of H_2 molecules and its subsequent interaction with the disk. Although [Larson \(1969\)](#) had pioneered second collapse calculations in spherical symmetry, the field has since developed ever more robust codes to tackle the problem in the three dimensions necessary to describe the formation of a circumstellar disk while including ever more complex physics such as radiative transfer (e.g., [Whitehouse & Bate 2006](#); [Bate 2010, 2011](#); [Ahmad et al. 2023](#)) and magnetic fields under the ideal and non-ideal approximations ([Machida et al. 2006, 2007, 2008, 2011](#); [Machida & Matsumoto 2011](#); [Tomida et al. 2013, 2015](#); [Bate et al. 2014](#); [Tsukamoto et al. 2015](#); [Wurster et al. 2018, 2021, 2022](#); [Vaytet et al. 2018](#); [Machida & Basu 2019](#); [Wurster & Lewis 2020](#)). Although the latest studies struggle to integrate across large timescales due to stringent time-stepping constraints, an important result they've shown is that the higher density gas ($\rho > 10^{-10} \text{ g cm}^{-3}$) is poorly magnetized due to magnetic resistivities, thus placing the magnetic pressure orders of magnitude below the thermal pressure. As such, in addition to greatly alleviating numerical constraints, omitting magnetic fields allows one to describe the inner sub-AU region with reasonably high fidelity prior to the birth of a stellar magnetic field through a dynamo process. Additionally, these studies have not studied in depth the interaction between the nascent protostar and its surrounding disk, mostly due to the prohibitive time-stepping. Nevertheless, they have offered valuable insight regarding the system's structure following the second collapse phase. Indeed, they seem to indicate that the inner regions are characterized by a density plateau in the innermost region ($< 10^{-2}$ AU), which then transitions toward a power-law distribution ([Saigo et al. 2008](#); [Machida & Matsumoto 2011](#); [Tsukamoto et al. 2015](#); [Vaytet et al. 2018](#)).

In this paper, we investigate the inner boundaries of newly formed circumstellar disks using high resolution 3D radiation-hydrodynamics (RHD) calculations of the collapse of a dense molecular cloud core to protostellar densities under the gray flux limited diffusion approximation (FLD). To this end, we modeled the collapse of the pre-stellar core, the formation of a first hydrostatic Larson core, the second gravitational collapse triggered by the dissociation of H_2 molecules, and the subsequent early evolution of the inner regions. Particular attention was given to the interaction between the nascent protostar and the disk and how such a process evolves over time.

2. Model

We carried out our simulations using the RAMSES ([Teyssier 2002](#)) adaptive mesh refinement (AMR) code and the same setup

employed in [Ahmad et al. \(2023\)](#) but with a notable difference being the presence of angular momentum in the system through the inclusion of an initially turbulent velocity vector field parameterized by a turbulent mach number M_a . [Commerçon et al. \(2011, 2014\)](#) and [González et al. \(2015\)](#) implemented FLD in the code. We used the equation of state of [Saumon et al. \(1995\)](#) and the opacity tables of [Semenov et al. \(2003\)](#), [Ferguson et al. \(2005\)](#), and [Badnell et al. \(2005\)](#), which were pieced together by [Vaytet et al. \(2013\)](#). The initial conditions consist of a uniform density sphere of mass $M_0 = 1 M_\odot$, initial temperature $T_0 = 10$ K, and a radius of $R_0 = 2.465 \times 10^3$ AU, thus yielding a ratio of thermal to gravitational energy of $\alpha = 0.25$. We present four runs in the main body of this paper where the initial amount of turbulence varies: $M_a = 0.2$ for run G1, 0.4 for G2, 0.8 for G3, and 1 for G4. Although M_a varies, the turbulent seed does not. This means that run G4 has five times as much initial angular momentum as G1. For comparative purposes, we also ran two additional simulations, labeled G5 and G6. The simulation of G5 possesses the same parameters as run G2 but also includes solid body rotation in the initial cloud core, whose ratio of rotational to gravitational energy is $\beta_{\text{rot}} = 10^{-2}$. Run G6 also contains the same parameters as G2, but it has a higher α of 0.5.

We used the same refinement strategy as in [Ahmad et al. \(2023\)](#); however, since angular momentum is present in the system, the simulations do not require a resolution as stringent as their spherically symmetrical counterpart, as the properties of the protostar, such as its central density and radius, are easier to resolve. Thus, we lowered the maximum refinement level ℓ_{max} to 25 in order to alleviate our time-stepping constraints, thus yielding a spatial resolution of $\Delta x = 2.9 \times 10^{-4}$ AU at the finest level (the coarse grid is 64^3 cells, with $\ell_{\text{min}} = 6$). Nevertheless, the stringent refinement criterion yielded some of the best-resolved disks in the literature. Indeed, the circumstellar disks in our simulations have $[95 - 2.7 \times 10^3]$ cells per Jeans length, with $\sim 10^7$ cells within their volume.

3. Results

Our simulations cover the initial isothermal contraction of the cloud, the birth of the first Larson core, the second gravitational collapse, and the subsequent evolution of the star-disk system. The physics at large scales (i.e., from the cloud core to the first Larson core) have been thoroughly discussed in the literature, and as such, they are only briefly covered in our paper. Below, we focus our study on the behavior of the system in the innermost regions that contain the protostar.

3.1. The dynamical range

Herein, we illustrate the full dynamical range covered by all of our simulations using run G4 as an example. To this end, we display in [Fig. 1](#) column densities at various scales (panels a–d), and slices through the center of the domain displaying density (panels e–f), radiative flux (panels g–h), and temperature (panels i–j). Panel a displays the column density at the scale of the dense molecular cloud core. Here, a filamentary structure of size $\approx 10^3$ AU formed by gravo-turbulence can be seen ([Tsukamoto & Machida 2013](#)), and within this structure a first Larson core is born. In this run, the first core lifetime is significantly extended thanks to ample angular momentum, which reduces the mass accretion rate onto it. As such, a disk was able

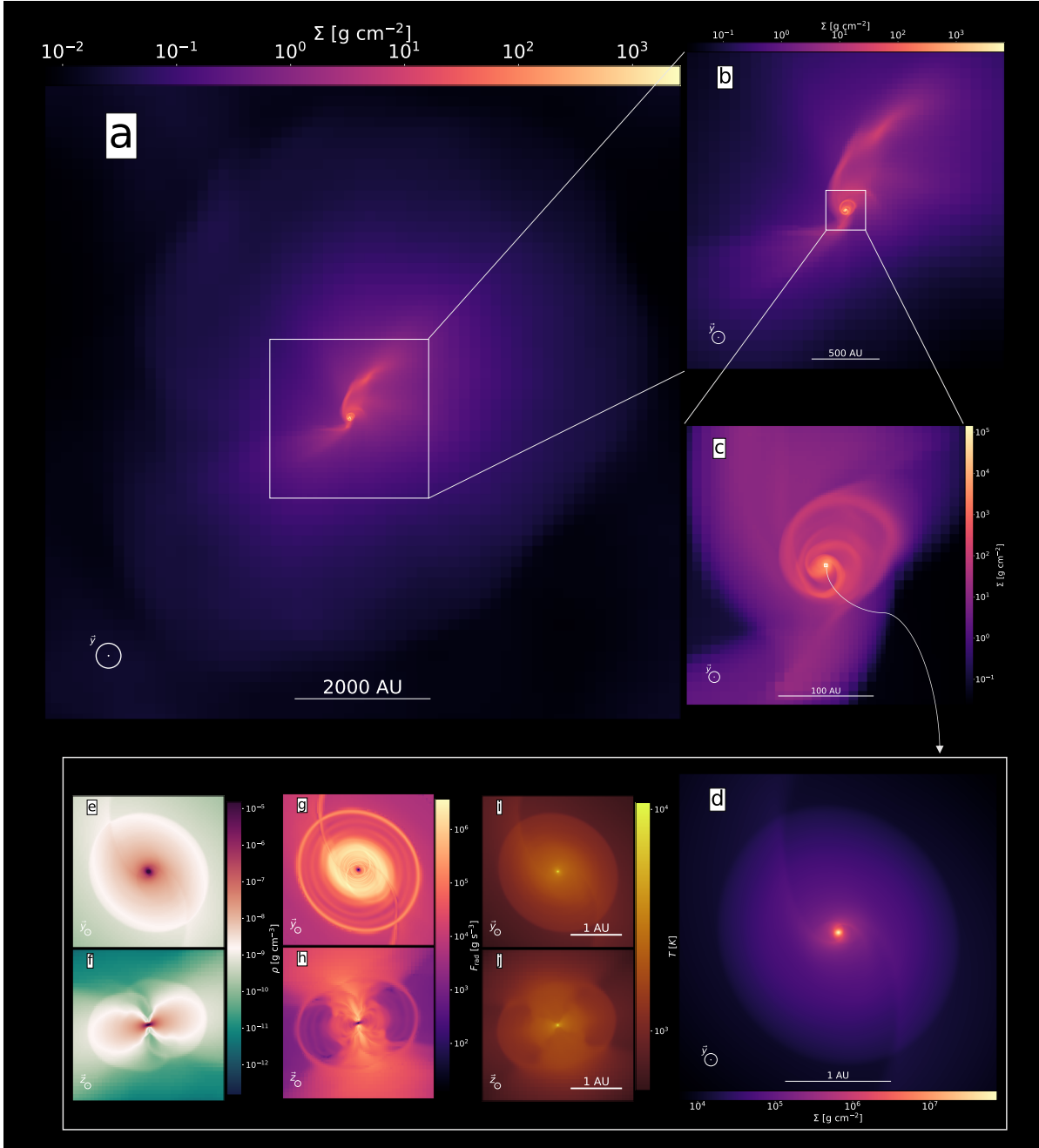


Fig. 1. Visualization of the entire dynamical range covered in our simulations. The figure displays data taken from the final snapshot of run G4. Panels a–d show the projected gas column density along the y direction across multiple scales, ranging from $\approx 9.35 \times 10^3$ AU in panel a to 3 AU in panel d. Panels e–j are slices through the center of the domain along the y direction for panels e, g, and i, and along the z direction for panels f, h, and j. These display density (panels e and f), radiative flux (panels g and h), and temperature (panels i and j). The color bars in panels e and f are centered on the density of the inner disk’s shock front ($\approx 1.5 \times 10^{-9}$ g cm $^{-3}$ at this snapshot).

to form around it¹, as seen in panel c. Within this disk, the second collapse takes place and gives birth to the protostar and the circumstellar disk, as seen in the lower panels.

3.2. Protostellar breakup

We begin by describing the structure of the system shortly after the onset of the second gravitational collapse using Fig. 2. We

¹ In the case of runs G1 and G2, no disk was formed at these scales prior to the onset of the second collapse. This is discussed further in Sect. 3.5.

use data from run G6 as an example, although the evolutionary sequence displayed here applies to all other runs as well. The top row of this figure (panels a–d) displays the local radiative flux, an excellent tracer of shock fronts. It is computed as

$$F_{\text{rad}} = -\frac{c\lambda\nabla E_r}{\rho\kappa_R}, \quad (1)$$

where c is the speed of light, λ the Minerbo (1978) flux limiter, E_r the radiative energy, ρ the gas density, and κ_R the Rosseland mean opacity. At a shock front, kinetic energy is converted into radiation and as such it is accompanied by an increase in

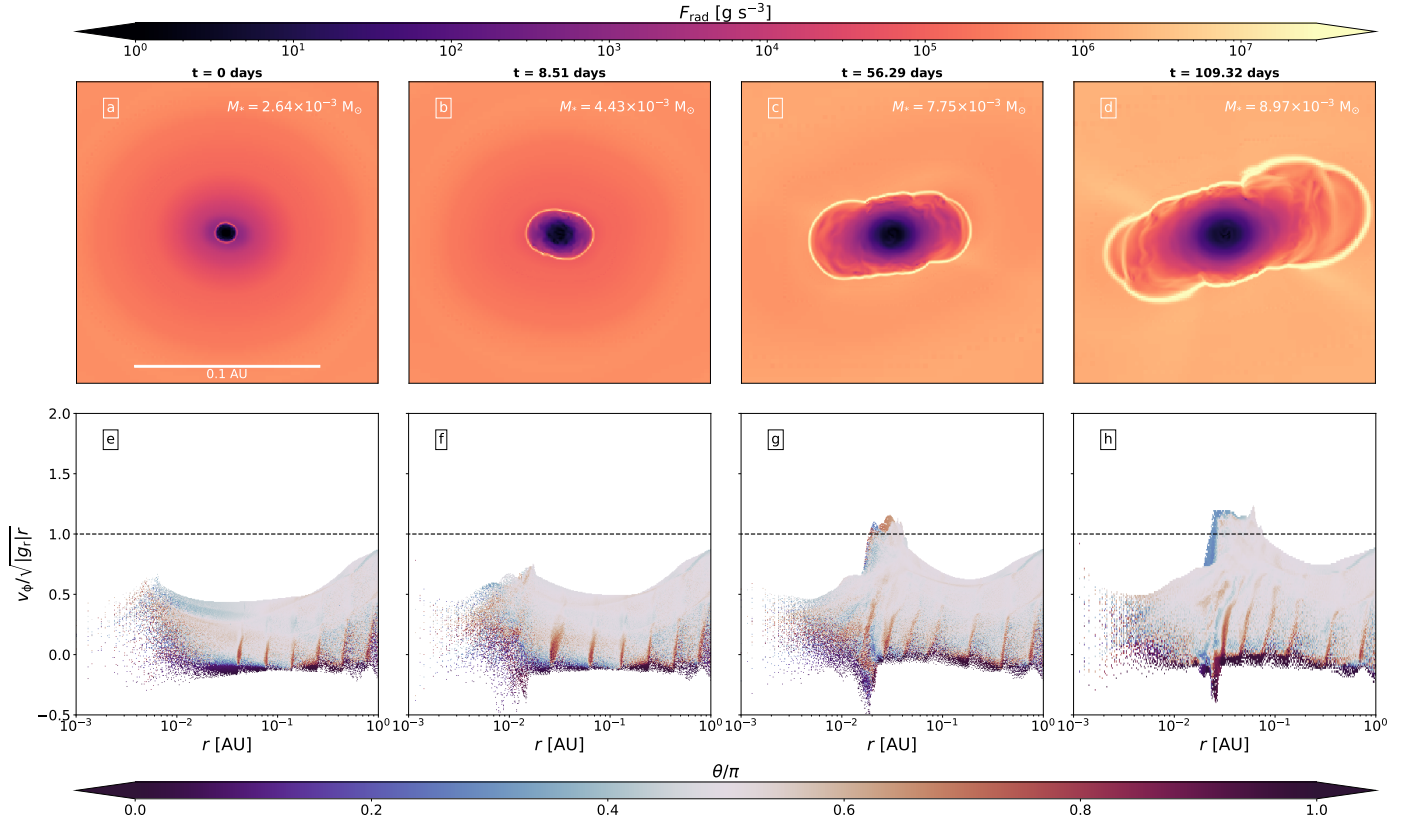


Fig. 2. Demonstration of the breakup of the protostar due to excess angular momentum. The data is taken from run G6. Each column represents a different time, where $t = 0$ marks the birth of the protostar. Panels a–d are slices along the z direction through the center of the domain that display the local radiative flux emanating from the cells (see Eq. (1)). The scale bar in panel a applies to panels b–d as well. The mass of the protostar at each snapshot is displayed in the top-right corners of panels a–d. Panels e–h display 2D histograms binning all the cells in our computational domain, which show the distribution of azimuthal velocities divided by $\sqrt{g_r r}$ with respect to radius. The color code in the histograms represents the co-latitude θ divided by π , where $\theta/\pi = 0.5$ corresponds to the equator and $\theta/\pi = 1$ (respectively 0) corresponds to the south (respectively north) pole. The dotted black lines in panels e–h display $v_\phi/v_{\text{crit}} = 1$ (see Eq. (2)). An animated version of this plot is available [online](#).

radiative flux. Hence, this quantity prominently displays accretion shocks and spiral waves.

The bottom row of the figure (panels e–h) displays the azimuthal velocity² distribution of all cells in our computational domain with respect to radius, which we have divided by the critical velocity beyond which the centrifugal force exceeds the radial component of the gravitational force:

$$v_{\text{crit}} = \sqrt{|g_r| r}, \quad (2)$$

where

$$g_r = -\frac{\partial \phi}{\partial r}. \quad (3)$$

Here, ϕ is the gravitational potential obtained through the Poisson equation.

Once the gas has completed its dissociation of H_2 molecules and ample thermal pressure support is gathered, the second Larson core (i.e., the protostar) is formed. At birth (first column), the protostar is a thermally supported spherical object, and its azimuthal velocities are well below v_{crit} . A mere eight and a half days later (second column), the protostar has nearly doubled in mass, and an equatorial bulge is now visible in panel b. This is due to the fact that as the protostar accretes, it is also accumulating angular momentum. Nevertheless, it is still rotating below

² v_ϕ was computed along the angular momentum vector of the gas within 0.5 AU.

v_{crit} . A month later (third column), the outer shells of the protostar finally exceed v_{crit} , after which material spreads outward and transitions to a differential rotation profile in which the centrifugal force is now the main counterbalance to gravity. The sustained accretion ensures a constant flow of material within the protostar exceeding v_{crit} .

3.3. An embedded protostar

The expulsion of material by the protostellar surface will naturally lead to the formation of a circumstellar disk. Here, we study how such a disk grows and evolves while analyzing the accretion mechanism onto the protostar and the disk. To this end, we studied Fig. 3, which displays density slices through the center of the computational domain for run G1 at different times. The velocity streamlines are color coded with the local radial mass-flux $-\rho v_r$, where red colors denote inward transport of material, blue colors denote outward transport, and white signifies very little transport. The evolutionary sequence displayed here applies to all other runs.

Panels a and f display the system once temperatures exceed 2000 K and the dissociation of H_2 is triggered, where the gas spirals inward almost isotropically. The central region accumulates material quickly, and once ample thermal pressure support is gathered, the protostar forms. We display in panels b and g the structure of the system once the protostar reaches breakup velocity. As the protostar’s surface begins expelling

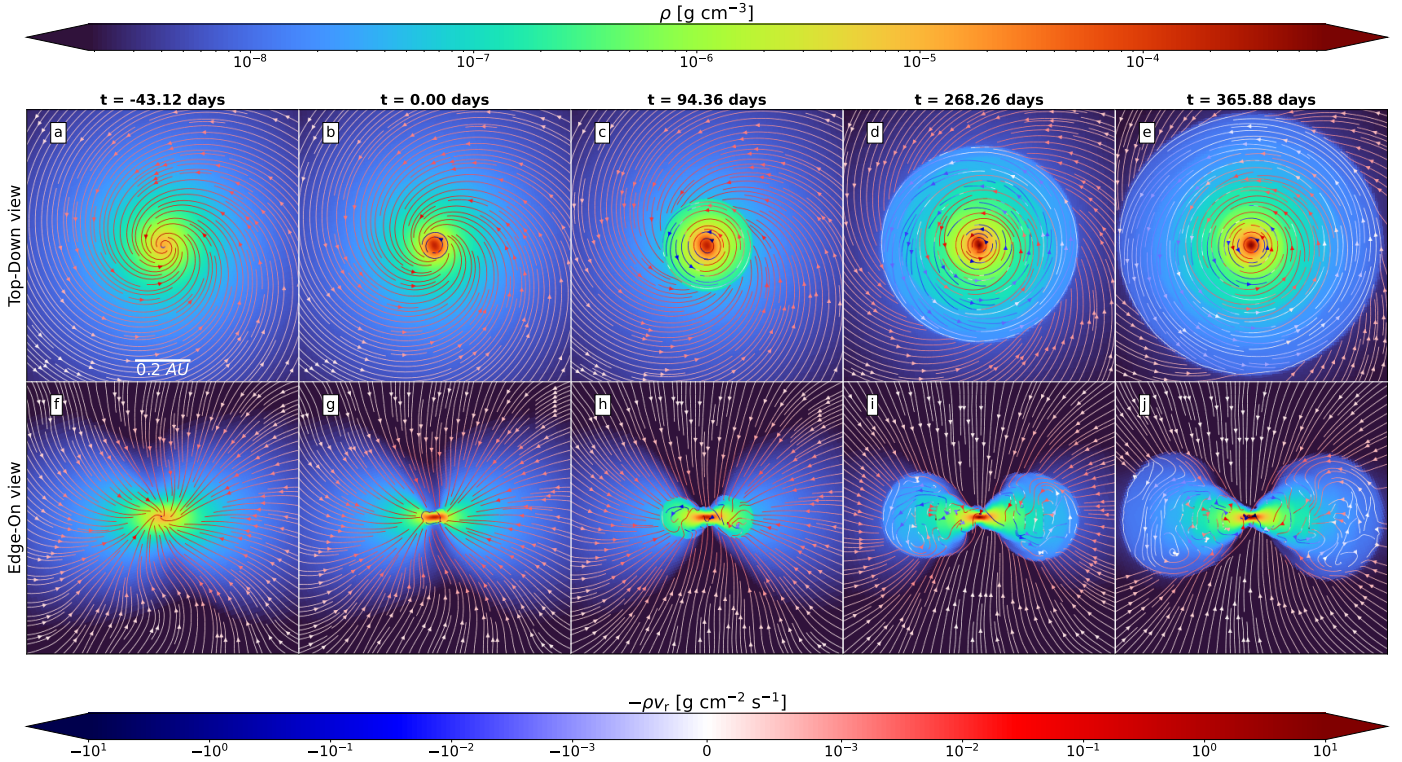


Fig. 3. Top-down (top row, panels a–e) and edge-on (bottom row, panels f–j) slices through the center of the domain of run G1 displaying density and velocity streamlines. The color coding in the velocity streamlines displays the local radial mass flux $-\rho v_r$. Each column displays a different epoch, where $t = 0$ (panels b and g) corresponds to the moment of protostellar breakup. The scale bar in panel a applies to all other panels. An animated version of this plot is available [online](#).

material, a disk immediately forms afterward, and as time progresses, an increasing amount of material collides with the disk instead of the protostar, thus causing the former to grow significantly over time. Hereafter, we refer to this newly formed circumstellar disk as the inner disk (in accordance with the terminology of Machida & Matsumoto 2011). In panel d, we observed the development of spiral waves, which seem to have subsided into near-circular waves in panel e.³ We note that during this phase, the accretion timescale of the disk ($\dot{M}_d/\dot{M}_d \sim 10^{-2} M_\odot/10^{-2} M_\odot \text{ yr}^{-1} = 1 \text{ yr}$) is shorter than its dynamical timescale ($2\pi R_d/v_\phi \sim 2\pi \times 1 \text{ AU}/3 \text{ km s}^{-1} \approx 10 \text{ yr}$). This means that any angular momentum redistribution process within the inner disk occurs on longer timescales than accretion. Thus, accretion is the dominant process behind the expansion of the disk.

We now turn to studying the accretion process with the aid of the streamlines in Figs. 3 and 4, which displays the radial mass flux in slices through the center of the domain. In addition, we display unbroken velocity vector field streamlines in Fig. 5 at a curated moment. Although the polar regions initially bring a large amount of material to the central protostar, the polar reservoir of gas is quickly depleted and by $t \approx 268$ days (fourth columns and onward of Figs. 3 and 4), very little mass is accreted through the poles. Indeed, most of the material landing at the protostellar surface is sliding on the inner disk’s surface, as its velocity component normal to the disk surface is not strong enough to break through the shock front. We note, however, that some material landing on the disk surface can sometimes break through the shock front and is then transported into the inner disk, as can be seen in panel b of Fig. 5. The previously men-

tioned spiral waves can be seen transporting material radially in panels d and e. This is more apparent in Fig. 6, which displays the radial mass flux averaged in radial bins and measured separately for both the upper layers of the disk and its main body for all our runs. One can see that in all runs and across all radii, the upper layers of the disk have a strictly positive radial mass flux, whereas the main body shows alternating inflows and outflows of material.

What is most visually striking from the edge-on views is the vertical extent of the disk: it is substantially flared, giving it the shape of a torus. This is more so apparent in the 3D rendering of the system displayed in Fig. 7. The inner disk’s surface (rendered in blue) completely engulfs the protostar (rendered in green). Figure 7 also displays the 3D velocity streamlines, which show that the material accreted through the poles carries with it angular momentum as the gas is spiraling inward. The cross-sectional slices in the figure display the radiative flux, which reveals shock fronts and spiral waves. Interestingly, there does not seem to be any shock fronts separating the protostar from the inner disk (barring the spiral waves). This means that the accretion shock envelopes both the protostar and the inner disk, and the two act as a continuous fluid system. As such, differentiating the protostar and the inner disk is rather difficult, but the rotational profiles seem to indicate that the protostar is in solid body rotation and the inner disk exhibits differential rotation.⁴ All other runs have displayed an identical structure of the inner disk.

³ The gravitational stability of the inner disk is discussed in Sect. 3.6.

⁴ See Appendix A for an overview of how each object was defined.

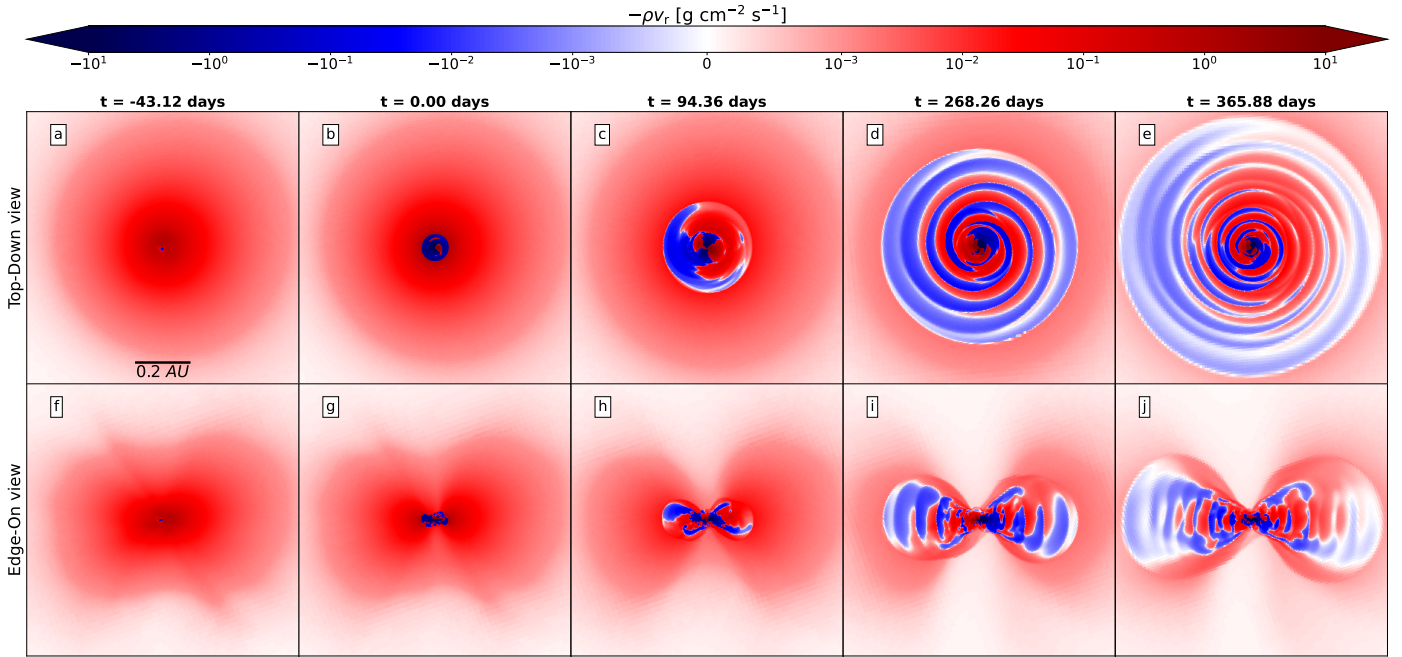


Fig. 4. Same as Fig. 3 but displaying only the local radial mass flux $-\rho v_r$ in order to better demonstrate how accretion occurs in the star and inner disk system. An animated version of this plot is available [online](#).

3.4. A convergent structure

We display in Figs. 8 and 9 the radiative flux in slices through the center of the domain for runs G1–G6 at a moment in time where the inner disk has reached a radius of ≈ 0.5 AU. We note the almost identical structure of the inner disk in all runs: it is toroidal and highly flared. We also note that run G3 (panels c and q) displays a strong eccentricity, as the outer disk that formed around the first Larson core in this run was already highly eccentric prior to the second collapse.

In the top-down slices (panels a–d), we notice ripples in radiative flux. These are spiral waves which have relaxed into nearly circular perturbations. We note that runs G1 and G2 have stronger spirals waves (i.e., the radiative flux emanating from them is stronger) due to their higher mass. (For a more in-depth analysis of these spiral waves, see Sect. 3.6).

An interesting observation from panels e–h of Fig. 8 is the prominence of the radiative flux along the poles. Indeed, the polar region is much less dense than the equator, which causes the radiative flux to escape much more easily along this direction. This also causes the gas to heat up in the polar direction⁵.

3.5. Evolution

Having ascertained the structure of the system in the innermost regions following the second gravitational collapse, we follow the temporal evolution of the inner disk with the aid of Fig. 10. The properties of the inner disk once it has reached a radius of 1 AU are of particular interest, as that is the most commonly chosen sink radius.

First, we point out the different evolutionary history of each simulation in panel a. This figure displays the maximum density in our computational domain as a function of time since the birth of the first core. The moment in which each curve exhibits a sharp rise in central density corresponds to the onset of the sec-

ond gravitational collapse. Here, we observed clearly that simulations with higher initial amounts of angular momentum have a delayed onset of second collapse, as the additional centrifugal support significantly extends the first core’s lifetime by reducing its mass accretion rate. In runs G3, G4, G5, and G6, the first core lifetime is long enough for it to have a disk built around it such that the inner disk forms within a disk (Machida & Matsumoto 2011). Despite the differing evolutionary histories, the resulting properties of the inner disk, displayed in panels b, c, e, and f, show remarkable similarity. Indeed the temporal evolution of the inner disk equatorial radius R_d (panel f), shows very little spread. The specific angular momentum of the inner disks, displayed in panel e, also exhibit striking similarity. This shows that the amount of specific angular momentum in the inner disk is independent of the initial amount of angular momentum in the parent cloud core, a result that is in agreement with Wurster & Lewis (2020)’s non ideal MHD and hydro simulations. Furthermore, the entirety of the angular momentum budget of the first core is found within the inner disk and protostar after it is accreted.

The curves in panel c display the inner disk’s mass (M_d), which exhibit the same evolutionary trend and $M_d(1 \text{ AU}) \in [1.634 \times 10^{-2}; 2.755 \times 10^{-2}] M_\odot$. The mass of the protostar (panel d), although very similar in runs G1–G4, has runs G5–G6 as outliers since M_* is about $\gtrsim 40\%$ larger in these runs. Interestingly, M_* also seems to be decreasing in most runs, meaning that the protostar is shedding its mass to the disk due to excess angular momentum. The notable exception is run G1, in which the protostar’s mass is increasing due to strong gravitational torques.

Finally, we turn our attention to panel b, which displays the density of the inner disk’s equatorial shock front (ρ_s). We measure this quantity along the equator since that is the region where most of the incoming mass flux lands on the inner disk (as shown in Fig. 3). As such, this quantity is an equivalent to the accretion threshold used in sink particles (n_{acc}). We report $\rho_s(1 \text{ AU}) \in [5.35 \times 10^{-10}; 2 \times 10^{-9}] \text{ g cm}^{-3}$. The most commonly adopted accretion threshold in the literature is $1.66 \times 10^{-11} \text{ g cm}^{-3}$ ($n_{\text{acc}} = 10^{13} \text{ cm}^{-3}$). We thus suggest higher values of n_{acc} when possible

⁵ The radiative behavior of the system is studied in Sect. 5.

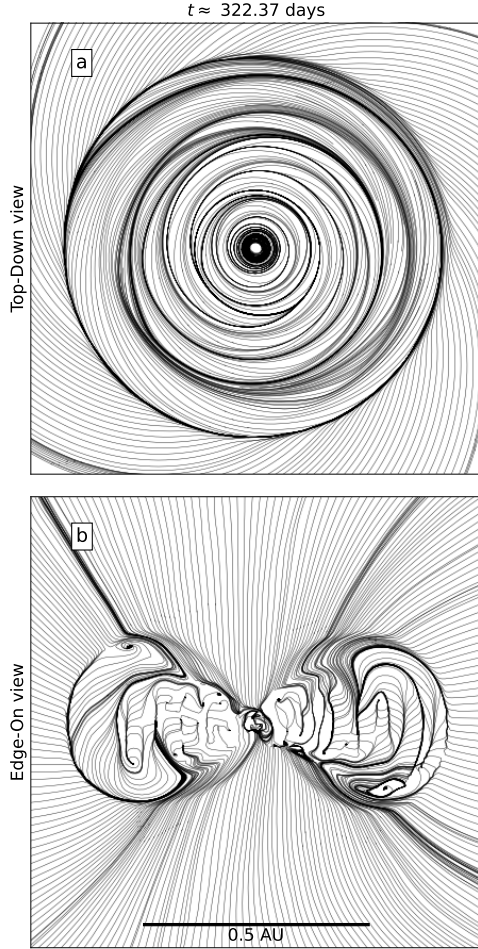


Fig. 5. Unbroken velocity vector field streamlines of run G1 at $t \approx 322$ days after the birth of the inner disk illustrating the dynamics of accretion onto the disk and protostar in a top-down (panel a) and edge-on (panel b) view. The scale bar in panel b applies to panel a as well. An animated version of these streamlines, made using windmap (<https://github.com/rougier/windmap>) is available [online](#).

for studies employing sink particles whose radius is 1 AU. However, we acknowledge that this can significantly increase the numerical cost of simulations, and thus might be too constraining for certain studies, particularly those that aim for very long temporal evolution.

The reason for such a convergence in the inner disk properties is the first core itself. As discussed in [Ahmad et al. \(2023\)](#), this hydrostatic object halts any inward accretion until temperatures can exceed the H_2 dissociation temperature of 2000 K, after which the second collapse ensues. As such, the mass accretion rate asymptotically reaches c_s^3/G ($\sim 10^{-2} M_\odot \text{yr}^{-1}$, [Larson 1969](#); [Penston 1969](#)) independently of initial conditions, provided that a first core forms. The small spread we observed in [Fig. 10](#) is the result of our turbulent initial conditions, as no discernible trend can be inferred from their differences. We expect the large-scale initial conditions to play a more significant role later on when the entirety of the first Larson core is accreted and that mass accretion rates onto the innermost regions are dictated by transport processes within the disk and by the infall of material onto said disk.

We note that in the case where an outer disk exists prior to the onset of a second collapse, the inner disk will simply merge with it ([Machida & Matsumoto 2011](#)). This was the case for runs

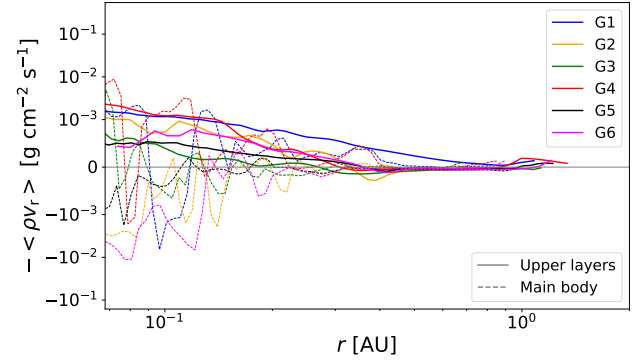


Fig. 6. Average radial mass flux measured in radial bins for runs G1 (blue), G2 (orange), G3 (green), G4 (red), G5 (black), and G6 (magenta) at a moment in time where the inner disk has reached ≈ 1 AU in radius. Only cells belonging to the inner disk were considered (see [Appendix A](#) for information on how the inner disk was defined). The solid lines represent measurements made on the upper layers of the disk, whereas the dashed lines represent measurements made in its main body.

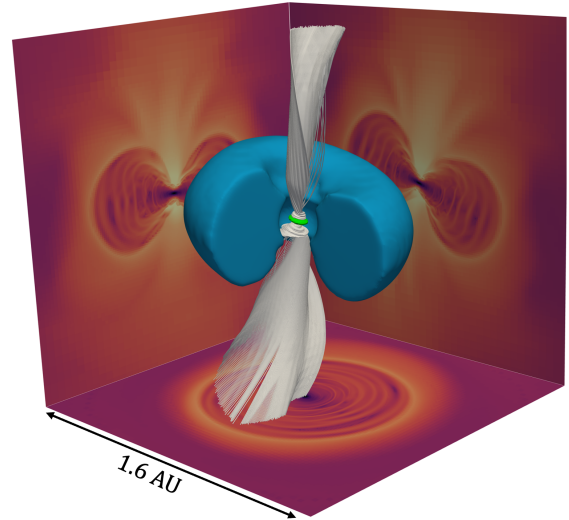


Fig. 7. Three-dimensional view of the inner disk and protostar at a moment in time when the former has reached ≈ 0.5 AU in radius. The blue structure is the surface of the inner disk. The inner $r < 0.1$ AU region has been cut out in order to reveal the flow onto the protostar (rendered in green). The white curves are velocity vector field streamlines launched along the poles to reveal polar accretion. The bottom, left, and right panels are cross sections through the center of the domain displaying the radiative flux. The visualized volume is $1.6 \times 1.6 \times 1.6 \text{ AU}^3$. An animated version of this plot is available [online](#).

G3, G4 and G5. The first core lifetime in runs G1 and G2 was not long enough for it to gather enough material around it to form a disk.

3.6. Gravitational stability of the inner disk

The existence of such a massive circumstellar disk naturally begs the question of whether it will undergo fragmentation or not. In order to determine the gravitational stability of the inner disk, we use the classical Toomre Q parameter ([Toomre 1964](#)):

$$Q = \frac{\omega c_s}{\pi G \Sigma}, \quad (4)$$

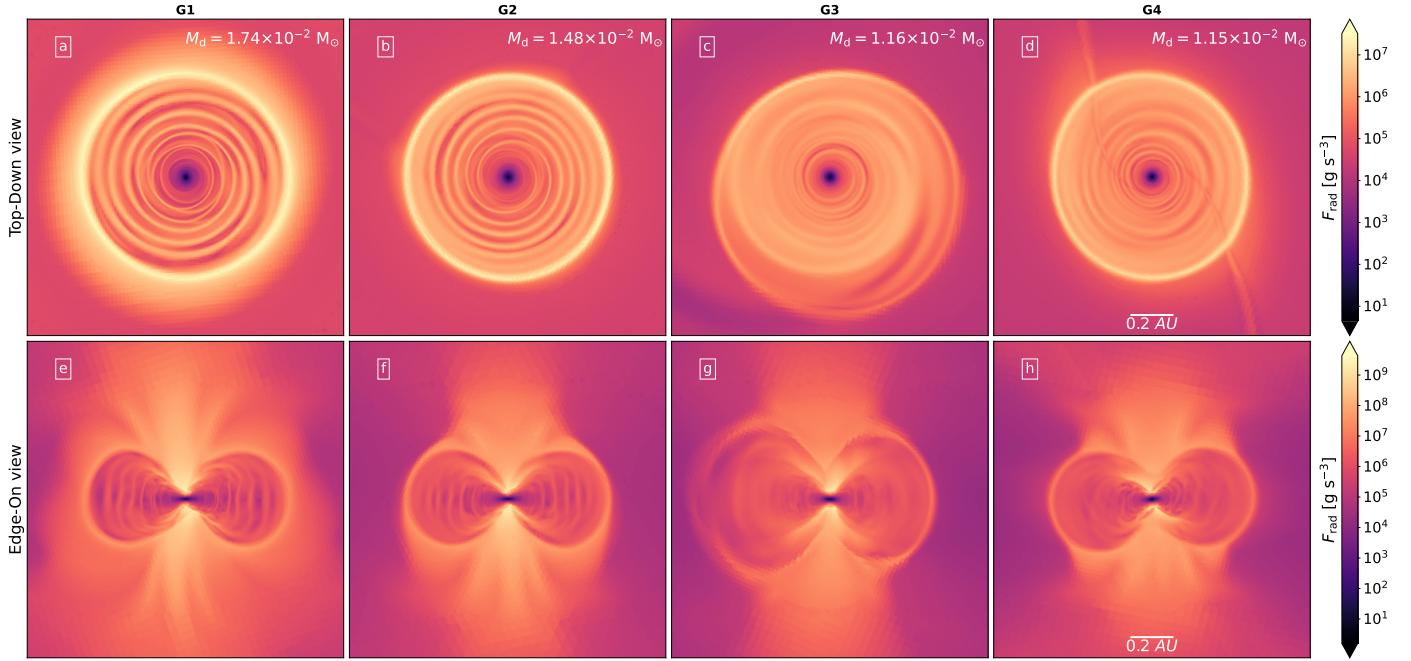


Fig. 8. Slices through the center of the domain for runs G1, G2, G3, and G4 (respectively first, second, third, and fourth columns) showing the local radiative flux in a top-down (top row, panels a–d) and edge-on (bottom row, panels e–h) view. The slices illustrate the structure of the accretion shock as well as the presence of spirals in the inner disk (see Eq. (1)). The scale bar in panels d and h apply to all other panels as well. The slices are shown at a moment in time where the inner disks have reached a radius of ≈ 0.5 AU. The mass of each inner disk is displayed in the top-right corners of panels a–d.

where c_s is the gas sound speed, Σ its surface density, and ω its epicyclic frequency, defined as

$$\omega^2 = \frac{1}{r^3} \frac{\partial(r^4 \Omega^2)}{\partial r}, \quad (5)$$

where Ω is the angular velocity of the gas. This parameter represents the ratio of the outward pointing forces on the gas, namely the centrifugal and pressure gradient forces, to the inward pointing gravitational force. If $Q < 1$, the disk is unstable and a fragmentation is likely. We measure the sound speed and the angular velocity by averaging along the vertical axis of the inner disk.

We display the real part of Q in top-down slices through the center of the domain for run G1 in Fig. 11 at curated moments. In panel a, we display the circumstellar disk at its birth, just after the protostar exceeded breakup velocity and began shedding its mass. This results in a ring of gas surrounding the protostar, whose Q value is above unity. In panel b, we display the system just prior to the onset of the first large amplitude spiral wave. Here, the Q parameter remains above unity in the innermost regions of the disk; however, an hourglass-shaped region has $Q < 1$ at slightly larger radii. The ratio of inner disk mass to protostellar mass has also increased by a factor ≈ 7 . In panel c, a coherent two-armed spiral wave is launched from the center, and it grows radially as it is sheared apart by differential rotation when propagating outward. Finally, panels d and e show that these spiral waves relax into nearly circular ripples as a result of the increase in temperature. The Q values in panels b–e hovers around unity throughout the disk, meaning that the disk remains marginally stable against gravitational instabilities despite its high mass relative to that of the protostar. This is due to its very high temperature.

A recent numerical study by [Brucy & Hennebelle \(2021\)](#) has shown that the fragmentation barrier of disks is quite blurry; it is better described by a probabilistic approach and said probabili-

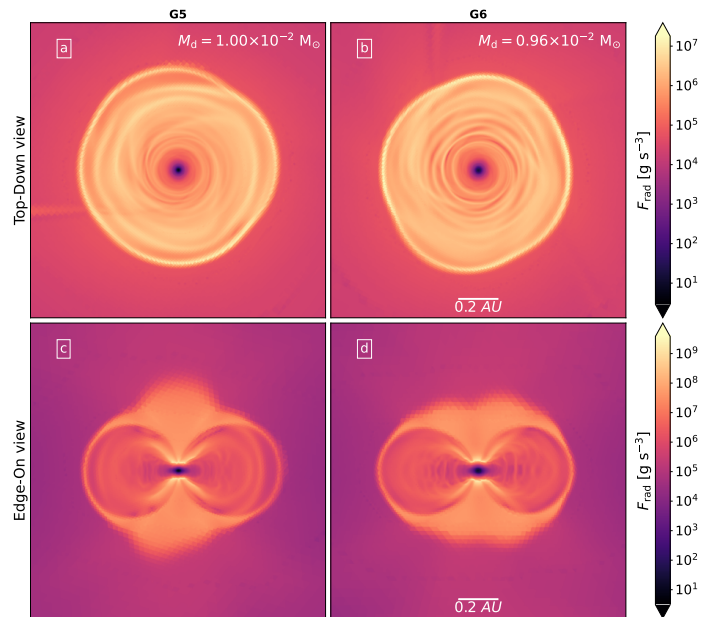


Fig. 9. Same as Fig. 8 but for runs G5 and G6 (respectively first and second columns).

ties strongly depend on how efficiently the disk is able to cool. As such, the fragmentation of the disk is also set by the cooling criterion. In our case, the inner disk is still strongly accreting, and a considerable amount of accretion energy is absorbed by the disk, particularly along the optically thick equator (this is shown in Sect. 5). This ensures that the inner disk remains hot and thus mostly stable against fragmentation despite its very high mass relative to the protostar. The primary regulator of the inner disk

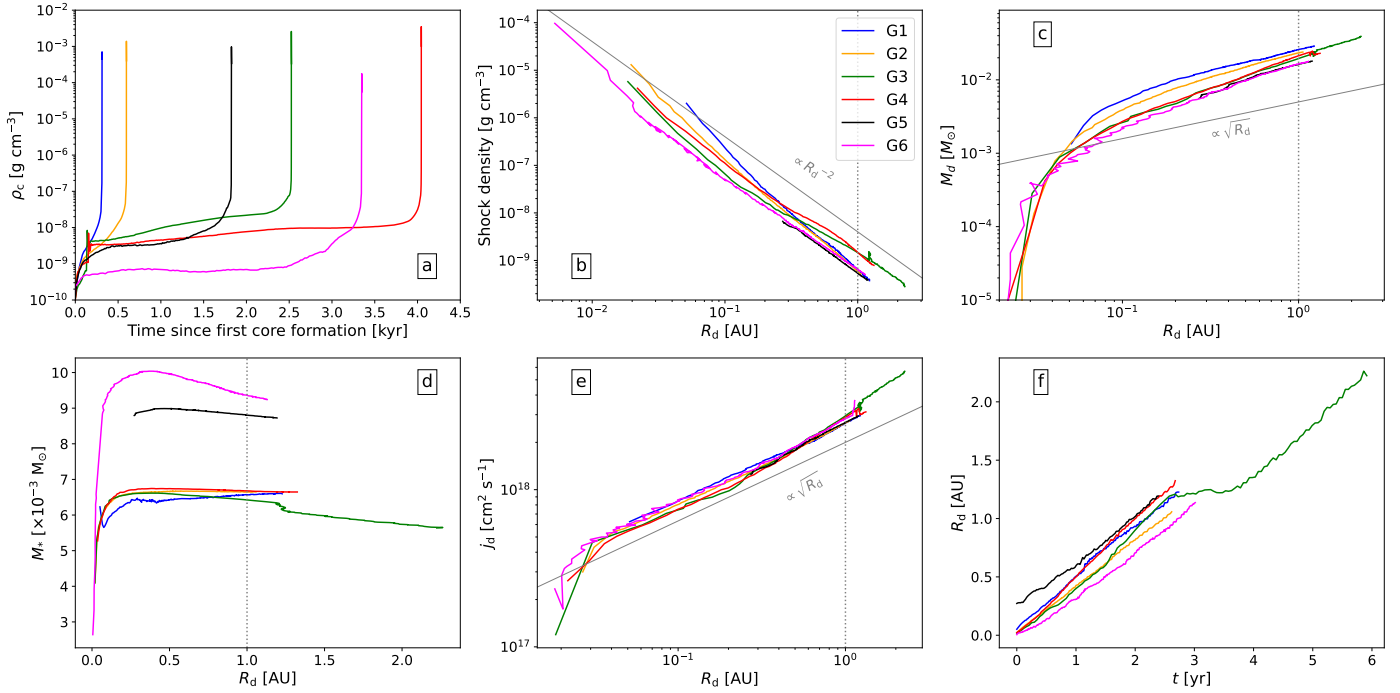


Fig. 10. Temporal analysis of the inner disk in all our runs. Blue is for G1, orange for G2, green for G3, red for G4, black for G5, and magenta for G6. Panel a provides the context in which the inner disk is born by displaying the central density's evolution since the formation of the first Larson core (defined as the moment where $\rho_c > 10^{-10} \text{ g cm}^{-3}$). Panels b–e respectively display as a function of the inner disk's equatorial radius R_d (analogous to time) the density of the inner disk's equatorial shock front, the mass of the inner disk, the protostellar mass, and the specific angular momentum of the inner disk. Panel f displays the evolution of the inner disk radius with respect to time, where $t = 0$ marks the moment of birth of the inner disk. The gray dotted line in panels b–e marks $R_d = 1 \text{ AU}$. (For information on how the inner disk was defined, see Appendix A).

temperature during this phase is the endothermic dissociation of H_2 , which places γ_{eff} at ≈ 1.1 .

4. Gas structure and kinematics

Herein, we provide a more quantitative analysis of the structure and kinematics of the inner disk with the aid of Fig. 12. Panels a–e of this figure display various quantities azimuthally averaged in radial bins in the equatorial region, where the equator was defined as the region in which $\theta/\pi \in [0.45; 0.55]$, where θ is the co-latitude. The curves are shown at a moment in time in which the inner disk has reached a radius of $\approx 1 \text{ AU}$.

Panel a displays the equatorial density curve, which exhibits a plateau in the innermost regions ($r < 10^{-2} \text{ AU}$) and a power law tail⁶. This behavior has been described by all previous 3D studies in the literature that employ either pure hydro or non-ideal MHD. This density structure, as well as the radial velocity curves displayed in panel b, suggest that no discontinuity in the flow separates the protostar from the inner disk. The only way for us to differentiate the two is by studying the rotational behavior of the system: we observed an object in solid body rotation in the inner-most regions ($j \propto r^2$, panel d) and a transition to a differential rotation profile (panel c).

4.1. Deviations from Keplerian rotation

We observed a significant deviation from Keplerian rotation ($v_\phi \propto r^{-0.5}$) in the inner disk. Indeed, it seems that $v_\phi \propto r^{-0.3}$.

⁶ We note that the disk in which the protostar was born in run G6 had fragmented prior to second collapse, and three first Larson cores exist within it. This causes the density spikes seen at larger radii.

In order to explain such a difference, one must start by analyzing the balance equation between the centrifugal, pressure, and gravitational forces (Pringle 1981; Lodato 2007):

$$\frac{v_\phi^2}{r} = \frac{1}{\rho} \frac{\partial P}{\partial r} - g_r, \quad (6)$$

where P is the thermal pressure. By assuming a radial density profile where $\rho \propto r^{-\beta}$ and radial isothermality ($\partial c_s^2 / \partial r \approx 0$), we may write

$$v_\phi^2 \approx -g_r r - \beta c_s^2, \quad (7)$$

where c_s is the gas sound speed. We may approximate g_r from the column density profile of the inner disk:

$$g_r \approx -\frac{GM_{\text{enc}}(r)}{r^2}, \quad (8)$$

where G is the gravitational constant and

$$M_{\text{enc}}(r) = M_* + 2\pi \int_{R_*}^r \Sigma(r') r' dr'. \quad (9)$$

Here, Σ is the disk's surface density. We note that this is merely an analytical estimate of g_r , which is different from the true potential computed in Eq. (3). Now let us assume a column density profile of $\Sigma \propto r^{-\xi}$. This means that the $g_r r$ term in Eq. (7) scales with $r^{-\xi+1}$, whereas the βc_s^2 term scales with $r^{-\beta(\gamma-1)}$ ($T \propto \rho^{\gamma-1}$). From Fig. 12, we can write $\xi \approx 3/2$ and $\beta \approx 3$. Additionally, $\gamma \approx 1.1$ in the inner disk (panel e of Fig. 12). Thus, $g_r r \propto r^{-0.5}$ and $\beta c_s^2 \propto r^{-0.3}$. This means that we may expect stronger deviations from Keplerian velocity at larger radii in the inner disk. At $R_d = 1 \text{ AU}$, we have $M_d \sim 10^{-2} M_\odot$

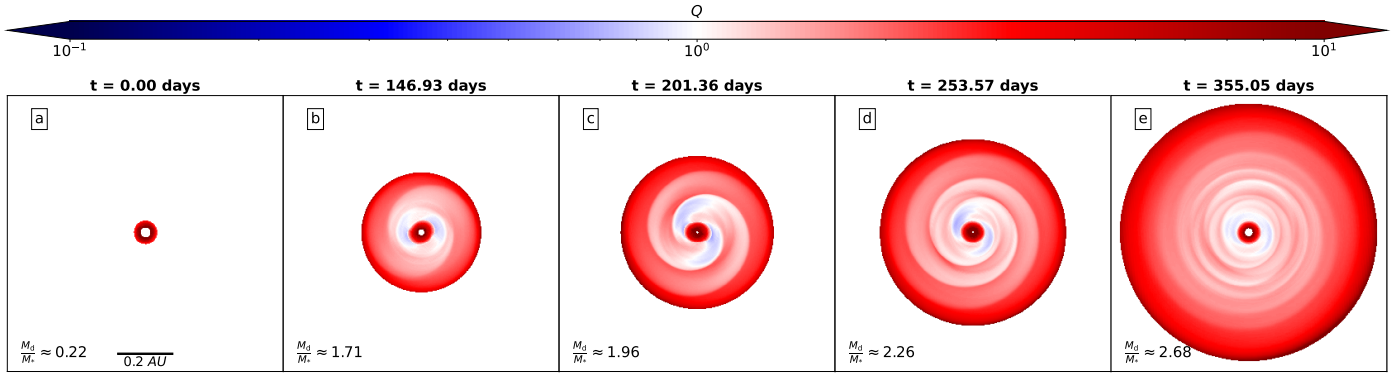


Fig. 11. Top-down slices through the center of the domain of run G1 displaying the real part of the Toomre Q parameter (see Eq. (4)) at different times. Here, $t = 0$ (panel a) corresponds to the moment of birth of the inner disk. Only cells belonging to the inner disk were used in the calculation of Q . The ratio of the inner disk mass to protostellar mass is displayed on the bottom left of each panel. The scale bar in panel a applies to all other panels. An animated version of this plot is available [online](#).

and $c_s \sim 1 \text{ km s}^{-1}$. As such, $\sqrt{1 + \beta c_s^2/g_r r} \approx 0.8$, and we thus expect the deviation from Keplerian rotation to be of the order of $(v_\phi - v_K)/v_K \approx -20\%$ (where $v_K = \sqrt{GM_{\text{enc}}/r}$). Panel g of Fig. 12 shows us that these are reasonable approximations.

Note that what we call “Keplerian” rotation in the present paper is different from its commonly adopted meaning in the literature. Indeed, the literature defines the Keplerian velocity as $v_{K,\text{lit}} = \sqrt{GM_*/r}$; however, as the disk’s mass exceeds that of the protostar by up to a factor of seven, the measured deviations from $v_{K,\text{lit}}$ would be $\sim 100\%$.

4.2. Analytical description of the inner disk structure

Herein, we set out to provide an analytical description of the structure of the inner disk, which is rather exotic by virtue of its very high mass relative to that of the protostar, as well as its very high temperature. This is not meant to be a full analytical development, but rather, one that seeks to deepen our understanding of the structure witnessed in our simulations. Namely, we seek to understand why $\Sigma \propto r^{-3/2}$, and in turn provide an analytical prediction of n_{acc} . To do so, we use as our starting point the important result shown in Sect. 3.6, namely that $Q \approx 1$ throughout most of the inner disk. This allowed us to link the sound speed c_s and the disk’s column density profile Σ through

$$c_s \approx \frac{\pi G \Sigma}{\Omega}. \quad (10)$$

We can write the following power-law descriptions of these two quantities

$$\Sigma = \Sigma_0 \left(\frac{r}{R_*} \right)^{-\xi}, \quad (11)$$

$$c_s = c_{s0} \left(\frac{r}{R_*} \right)^{-\beta(\gamma-1)/2}, \quad (12)$$

where we have made use of the fact that $\rho \propto r^{-\beta}$. We note that Ω is constrained by Σ through the equation

$$\Omega \approx \sqrt{\frac{G}{r^3} \left(M_* + 2\pi \int_{R_*}^r \Sigma r' dr' \right)}. \quad (13)$$

This allowed us to write

$$\Sigma_0 \approx \frac{c_{s0}}{\pi G} \sqrt{\frac{GM_*}{R_*^3}}. \quad (14)$$

To describe Σ , one must thus first obtain the boundary values at $r = R_*$ and $r = 1 \text{ AU}$. Since Σ and c_s are linked through Eq. (10), this is equivalent to finding the boundary values of c_s . Our simulations indicate $\beta \approx 3$, and $\gamma \approx 1.1$ in the inner disk. Hence, $c_s \propto r^{-0.15}$. This allowed us to write

$$\log \left(\frac{c_{s0}}{c_s} \right) = \frac{\beta(\gamma-1)}{2} \log \left(\frac{r}{R_*} \right) = 0.15 \times \log \left(\frac{r}{R_*} \right). \quad (15)$$

Since $R_* \sim 10^{-2} \text{ AU}$,

$$c_{s0} = 10^{0.3} \times c_s(1 \text{ AU}) \approx 2 \times c_s(1 \text{ AU}). \quad (16)$$

This means that when traveling from the protostellar surface to $r = 1 \text{ AU}$, c_s reduces by a factor of approximately two. The temperature of the inner disk is $\sim 10^3 \text{ K}$, hence $c_s(1 \text{ AU}) \sim 1 \text{ km s}^{-1}$ and $c_{s0} \sim 2 \text{ km s}^{-1}$. By using Eq. (10), we can link this boundary condition to ξ :

$$\left(\frac{c_s}{c_{s0}} \right)^2 = \left(\frac{r}{R_*} \right)^{3-2\xi} \frac{M_*}{M_{\text{enc}}}, \quad (17)$$

$$\Rightarrow \left(\frac{c_s}{c_{s0}} \right)^2 = \left(\frac{r}{R_*} \right)^{3-2\xi} \frac{M_*}{M_* + 2\pi \frac{\Sigma_0}{R_*^\xi (-\xi+2)} (r^{-\xi+2} - R_*^{-\xi+2})}. \quad (18)$$

Numerically solving Eq. (18) for ξ such that $(c_s/c_{s0})^2 \approx 1/4$ yields $\xi \approx 1.38$ (with $M_* \sim 10^{-3} M_\odot$), which is close to the value witnessed in most of our runs ($\approx 3/2$, panel h of Fig. 12).

Once we had a description of both Σ and c_s , we could describe the density profile with the aim of predicting n_{acc} as

$$\rho = \frac{\Sigma}{2h}, \quad (19)$$

where h is the disk scale height:

$$h = \frac{c_s}{\Omega}. \quad (20)$$

Thus, this analytical framework provides $\rho(1 \text{ AU}) \approx 5.37 \times 10^{-10} \text{ g cm}^{-3}$ ($n_{\text{acc}} \approx 3.23 \times 10^{14} \text{ cm}^{-3}$, when considering a mean molecular weight of one). This result is within the bounds provided by the simulations ($[5.35 \times 10^{-10}; 2 \times 10^{-9}] \text{ g cm}^{-3}$), and thus we consider it to be satisfactory.

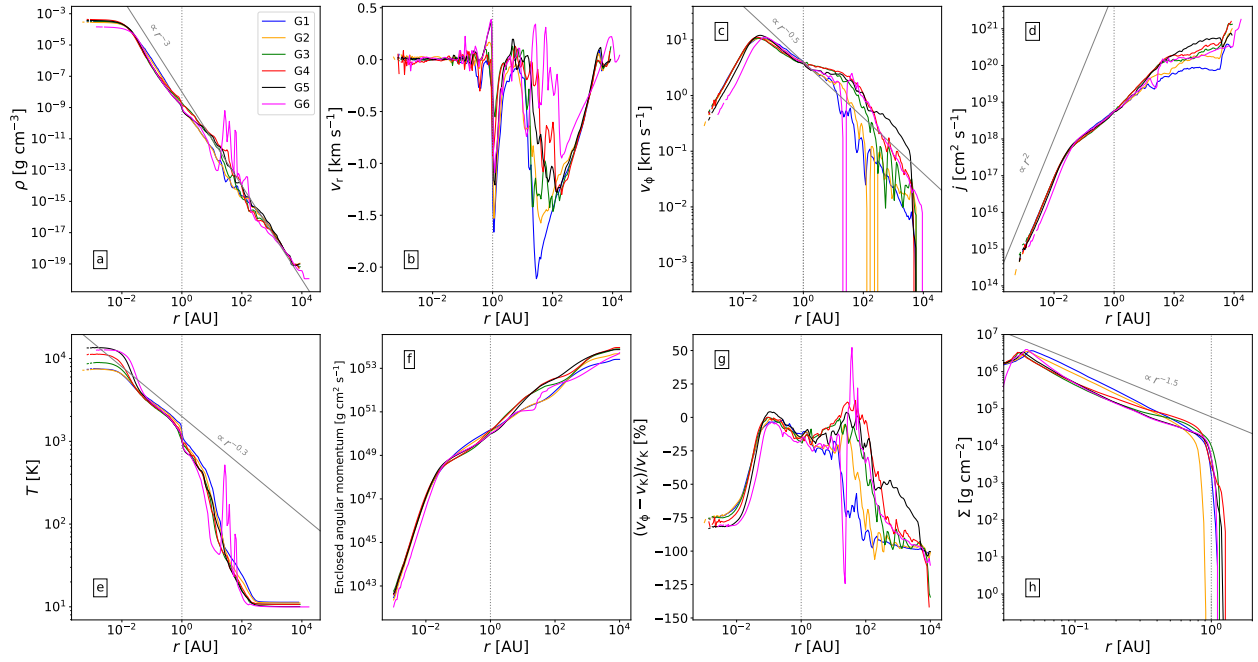


Fig. 12. Studying the structure and kinematics of the gas in our simulations. Panels a–e display a set of azimuthally averaged quantities along the equatorial regions with respect to radius, where the equator was defined as the region where $\theta/\pi \in [0.45; 0.55]$ at a moment in time where the inner disk has reached ≈ 1 AU in radius. Panel a displays the density, panel b shows the radial velocity, panel c presents the azimuthal velocity, panel d shows the specific angular momentum, and panel e presents the temperature. Panel f displays the enclosed angular momentum, and panel g displays the deviation from Keplerian rotation along the disk midplane. Panel h displays the column density profile of the inner disk, where non-disk cells were masked.

4.3. Radial transport within the inner disk

Once we had an analytical framework with which we could describe the inner disk, it was of interest to quantify the transport of material within it. More specifically, we wished to describe the transport processes using a simple alpha-disk model (Shakura & Sunyaev 1973) and compare it with the measured values within our simulations. A common approach in this regard is to measure the stress tensors induced by turbulent fluctuations and the self-gravity of the disk, respectively α_R and α_{grav} (e.g., Lodato & Rice 2004; Brucy & Hennebelle 2021; Lee et al. 2021). However, in our case, we found these measurements difficult to interpret, as the disk is awash with eccentric motions (Lovascio et al., in prep.), turbulent eddies, spiral waves, and erratically infalling material (see for example Fig. 5), which resulted in unreliable values of α_R and α_{grav} . Instead, we opted for a simpler approach in which we attempted to fit an approximate analytical description of the transport within the inner disk with the measured values of our simulations. The mass accretion rate at any given radius in our simulations can be obtained using

$$\dot{M}_s(r) = -2\pi r \Sigma \langle v_r \rangle, \quad (21)$$

where $\langle v_r \rangle$ is the vertically averaged radial velocity. We note that the majority of the inward transport of material occurs in the upper layers of the disk, as seen in Fig. 6. Along the midplane, material tends to spread outward, causing negative mass accretion rates. As such, when performing the vertical average of v_r , we weighed v_r in two different ways:

$$\langle v_r \rangle_z = \frac{1}{z_{\text{max}} - z_{\text{min}}} \int_{z_{\text{min}}}^{z_{\text{max}}} v_r dz, \quad (22)$$

$$\langle v_r \rangle_\rho = \frac{1}{\Sigma} \int_{z_{\text{min}}}^{z_{\text{max}}} \rho v_r dz, \quad (23)$$

where z_{min} and z_{max} are respectively the minimal and maximal heights of the disk at a given radius and azimuth. $\langle v_r \rangle_z$ will thus be biased by the infall in the upper layers of the disk, whereas $\langle v_r \rangle_\rho$ will be biased by the dense midplane.

The analytical estimate of the mass accretion rate is (Shakura & Sunyaev 1973; Pringle 1981)

$$\dot{M}(r) = 3\pi\nu\Sigma, \quad (24)$$

where ν is the effective viscosity of the inner disk

$$\nu = \frac{\alpha_{\text{sh}} c_s^2}{\Omega}. \quad (25)$$

Here, α_{sh} is the Shakura & Sunyaev (1973) alpha which dictates the vigour of radial mass transport. Using the equations developed in the previous section, we may write Eq. (24) as

$$\dot{M}(r) = 3\alpha_{\text{sh}} \frac{c_{s0}^3}{G} \left(\frac{r}{R_*} \right)^{-\beta(\gamma-1)-\xi+3/2} \sqrt{\frac{M_*}{M_{\text{enc}}}}, \quad (26)$$

$$\Rightarrow \dot{M}(r) = 3\alpha_{\text{sh}} \frac{c_{s0}^3}{G} \left(\frac{r}{R_*} \right)^{-\beta(\gamma-1)-\xi+3/2} \times \sqrt{\frac{M_*}{M_* + 2\pi \frac{\Sigma_0}{R_*^{-\xi(-\xi+2)}} (r^{-\xi+2} - R_*^{-\xi+2})}}. \quad (27)$$

We may obtain an estimate of the α_{sh} parameter in Eq. (26) with the aid of Fig. 13, which displays the mass accretion rate in our simulations computed using Eq. (21) at a moment in time when the inner disk radius has reached ≈ 1 AU. We measure \dot{M}_s using both $\langle v_r \rangle_z$ (panel a) and $\langle v_r \rangle_\rho$ (panel b). Using average stellar parameters reported in the figure caption, we over-plot Eq. (26) (solid gray lines). The figure shows that the vigour of inward transport varies across all radii, and in the case of runs G2-6, the

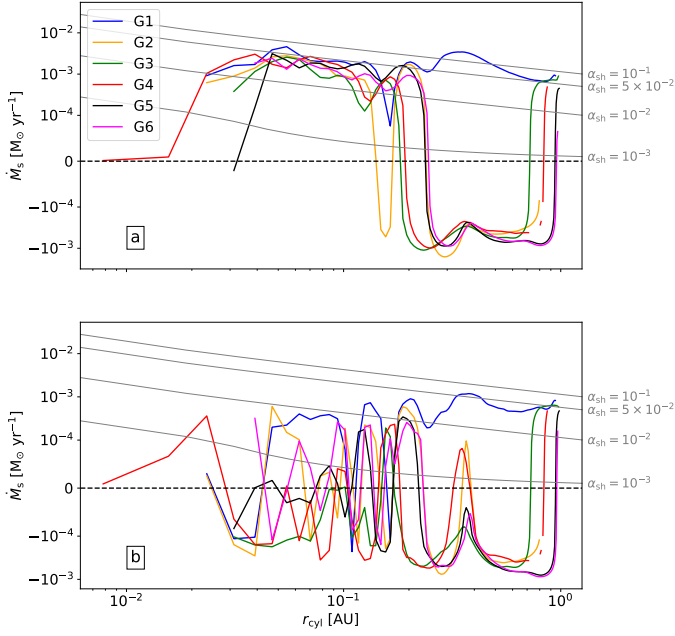


Fig. 13. Radial mass accretion rate within the inner disk for all runs (solid colored lines) as a function of cylindrical radius and computed using Eq. (21) at a moment in time when R_d has reached ≈ 1 AU. Only cells belonging to the inner disk were used in the computation of \dot{M}_s . Panel a displays the measurements of \dot{M}_s made using $\langle v_r \rangle_z$ (Eq. (22)), whereas panel b displays the same measurements made using $\langle v_r \rangle_p$ (Eq. (23)). The solid gray lines are analytical estimates of radial transport computed using Eq. (26), with $\alpha_{\text{sh}} = 10^{-1}$ (top), 5×10^{-2} (middle), and 10^{-2} (bottom). The other parameters for the solid gray lines are $M_* \approx 7 \times 10^{-3} M_\odot$; $R_* \approx 3 \times 10^{-2}$ AU; $c_{s0} \approx 5 \text{ km s}^{-1}$; $\beta \approx 3$; $\xi \approx 3/2$, and $\gamma \approx 1.1$.

outer layers ($r > 0.2$ AU) of the inner disk have negative mass accretion rates, meaning that material is mostly spreading outward. In panel b, we saw that the transport of material in the main body of the inner disk fluctuates wildly. Furthermore, any inward transport in this region consistently has lower mass accretion rates than in the upper layers of the disk (panel a). Indeed, the upper layers of the disk have a mass accretion rate that can be approximated by Eq. (26) with $\alpha_{\text{sh}} \sim 5 \times 10^{-2}$.

We note, however, that \dot{M}_s varies not only in space but also in time, and so the value of α_{sh} reported here is not valid throughout the entirety of the class 0 phase. Indeed, once most of the remnants of the first Larson core are accreted, and that the mass accretion rate onto the star-disk system significantly reduces, this will inevitably cause a decrease in α_{sh} , as \dot{M}_s is mainly dominated by the infall and will thus drop by several orders of magnitude. We would thus have a disk whose angular momentum transport is very weak, with $\alpha_{\text{sh}} \sim [10^{-5}; 10^{-3}]$, but whose mass is significantly higher than that of the protostar. In addition, panel d of Fig. 10 shows that despite the inward transport of material within the inner disk, the protostellar mass is decreasing in most runs as a result of excess angular momentum. This allowed us to conclude that although the inner disk can be described by the physics of alpha disks, such a description is a first-order approximation whose results are not entirely reliable.

5. Radiative behavior

Although the protostar has not reached the temperatures required for fusion yet ($> 10^6$ K), it will dominate the radiative output of

the system by virtue of its high temperature and its accretion luminosity. A quantitative analysis of said radiative behavior is seldom provided in the literature, and it is the purpose of this section.

To this end, we first begin by providing a qualitative overview of the radiative behavior of the system at medium (i.e., 10^2 AU) scales. As discussed previously, the structure of the accretion shock is rather complex, as it envelopes both the protostar and the inner disk. Nevertheless, the polar accretion shock, as seen in the bottom rows of Figs. 8 and 9, produces the majority of the radiative flux. In addition, the density cavity along the poles allows said radiation to escape much more easily than along the optically thick equator. This is reflected in Fig. 14, which displays the radiative flux emanating from each cell in edge-on slices across the center of our domain at curated moments for run G5. The protostar is born embedded within a disk that formed around the first Larson core (panel a). As time progresses, the radiation produced at the protostellar accretion shock escapes and brightens the polar regions significantly (panels b–d). However, the equatorial regions remain dark as the radiative flux struggles to pierce through the highly opaque disk. As such, the disk is almost unaffected by the protostar’s radiation.

We now turn to providing a quantitative analysis of the radiative behavior of the protostar and inner disk. To do so, as in Vaytet et al. (2018), Bhandare et al. (2020), and Ahmad et al. (2023), we compare two quantities: the radiative flux just upstream of the accretion shock (F_{rad} , see Eq. (1)), and the incoming accretion energy flux. However, since the shock front’s structure is complex, we measure these quantities in only four directions: north-south along the poles, and east-west along the equator (see panel a of Fig. 15):

$$F_{\text{acc,pol}} \approx -\rho v_r \frac{GM_{\text{enc}}(R_*)}{R_*} - E v_r - P v_r - \frac{\rho v_r^3}{2}, \quad (28)$$

$$F_{\text{acc,eq}} \approx -\rho v_r \frac{GM_{\text{enc}}(R_d)}{R_d} - E v_r - P v_r - \frac{\rho v_r^3}{2}, \quad (29)$$

where R_* (resp. R_d) is the protostellar (resp. inner disk) radius, E the gas internal energy, P its thermal pressure, and

$$M_{\text{enc}}(r) = 4\pi \int_0^r \rho r'^2 dr'. \quad (30)$$

This allowed us to define the radiative efficiency as

$$f_{\text{acc,pol}} \approx \frac{F_{\text{rad,pol}}}{F_{\text{acc,pol}}}, \quad (31)$$

$$f_{\text{acc,eq}} \approx \frac{F_{\text{rad,eq}}}{F_{\text{acc,eq}}}. \quad (32)$$

These are approximate measurements of the radiative efficiency of the accretion shock because the radiative flux also contains the cooling flux emanating from the protostellar interior, although the later remains smaller than that produced at the accretion shock because of the low temperature of the protostar ($\sim 10^4$ K) prior to deuterium burning.

We display in panels b and c of Fig. 15 the resulting measurements of $f_{\text{acc,pol}}$ and $f_{\text{acc,eq}}$ obtained through ray-tracing. A schematic drawing displaying the location at which each quantity was measured is presented in panel a. In contrast to spherically symmetrical calculations, the radiative efficiency of the accretion shock displays a strong anisotropy: the polar accretion

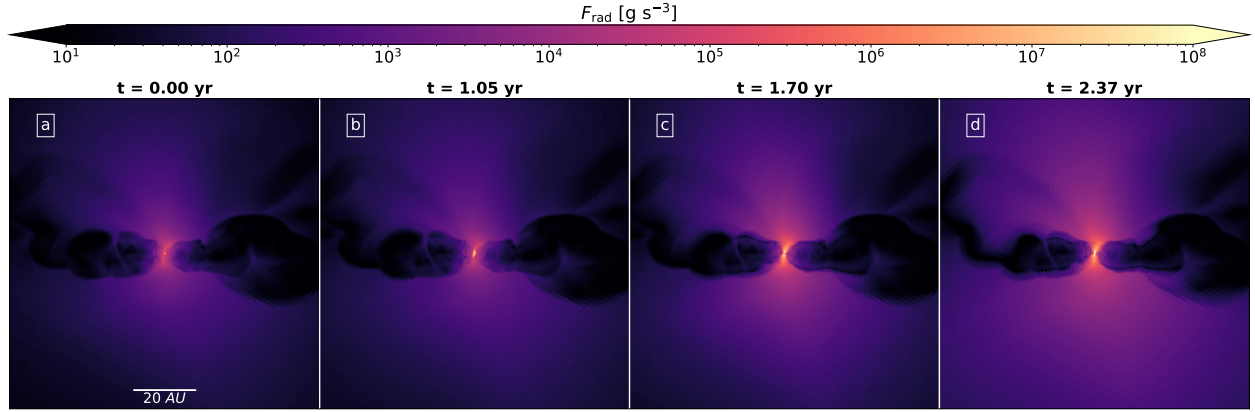


Fig. 14. Edge-on slices through the center of the domain displaying the local radiative flux at different times (see Eq. (1)). Here, $t = 0$ (panel a) corresponds to the moment of protostellar birth. The data is taken from run G5. The scale bar in panel a applies to all other panels. An animated version of this plot is available [online](#).

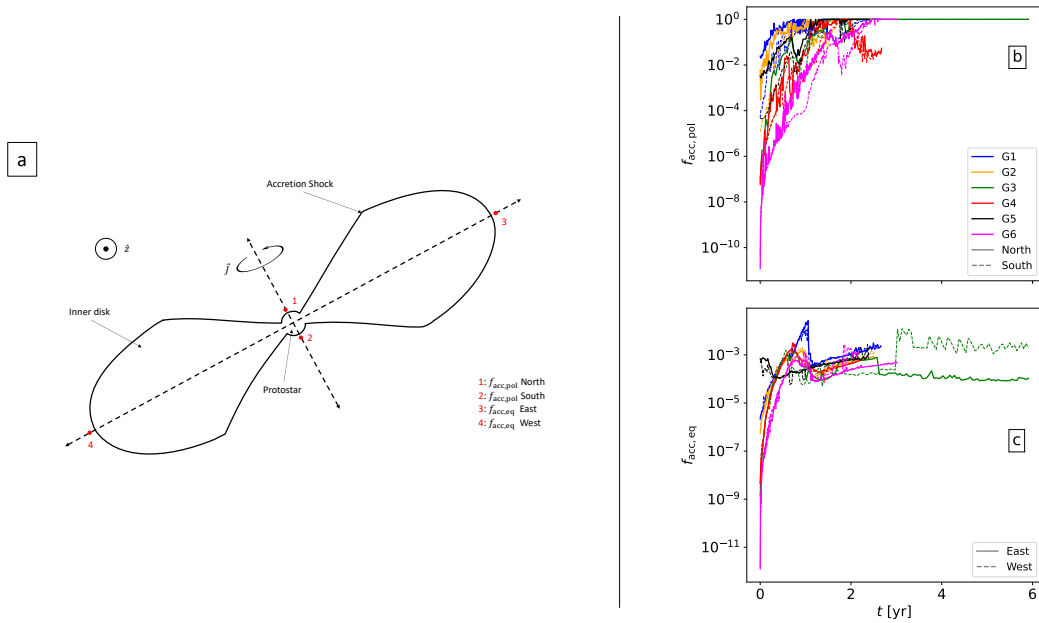


Fig. 15. Quantitative analysis of the radiative behavior of the accretion shock. Panel a is a schematic representation of the star and inner disk system, where the solid line is the location of the accretion shock that envelopes both the protostar and the disk. The dashed lines represent four rays launched from the center of the system along which the location of the accretion shock is found and its radiative efficiency measured just upstream from it (numbered red dots). The resulting measurements are presented in panels b and c. North and South (respectively solid and dashed lines in panel b and East and West (respectively solid and dashed lines in panel c) are shown for all simulations. These display the polar and equatorial radiative efficiencies (respectively $f_{\text{acc,pol}}$ and $f_{\text{acc,eq}}$; see Eqs. (31) and (32)).

shock (panel b) is much more efficient than its equatorial counterpart (panel c). Indeed, the polar shock front reaches supercriticality ($f_{\text{acc,pol}} = 1$) in less than 2.5 years for most runs, whereas $f_{\text{acc,eq}} < 1$ throughout all simulations. This is due to the polar density cavity that allows the accretion shock to shine into an optically thin medium, whereas the equatorial accretion shock remains optically thick due to the remnants of the first Larson core and the presence of an extended outer disk around it.

The drop in $f_{\text{acc,eq}}$ seen in most runs (e.g., at $t \approx 1.2$ yr for run G1) is due to the equatorial shock front expanding out of the opacity gap, a region where temperatures are high enough to sublimate dust (see Fig. 1 of Ahmad et al. 2023). This causes the shock front to shine into a region of higher opacity, which in turn reduces its luminosity. Eccentric inner disks can also cause an east-west anisotropy, as is most apparent in run G3. In contrast,

we witness very minor anisotropies when comparing north-south radiative efficiencies.

The low radiative efficiency of the equatorial shock front has an important consequence on the structure of the inner disk: as it accretes, the majority of the accretion energy is dumped into its thermal budget, thus causing it to maintain a high temperature and to swell along the vertical extent.

6. Discussions

6.1. The star-disk structure

In the common star formation paradigm, the protostar is often seen as a standalone object wholly separate from the circumstellar disk due to an accretion shock separating the two. Our results

show that such a boundary does not exist: the transition from the protostar to the inner disk is a smooth one, and the two act as a continuous fluid system. This means that until either torque mechanisms transport sufficient material inward, or a protostellar magnetosphere arises, the protostar and the inner disk will continue to behave as a continuous fluid system.

Unfortunately, obtaining observational constraints on the structure of the system in such a young and deeply embedded object is very difficult, but two recent studies by [Laos et al. \(2021\)](#) and [Le Gouellec et al. \(2024\)](#) seem to be offering hints on the accretion mechanism during the class 0 phase. Whereas [Laos et al. \(2021\)](#) argues for magnetospheric accretion similarly to class I objects by basing their arguments on the similar shapes of the Bry line profiles, [Le Gouellec et al. \(2024\)](#) additionally analyzed the velocity profiles of these lines which exhibited clear differences. Based on this result, they concluded that the accretion mechanism in class 0 sources must be of a different nature. Additionally, they report very vigorous accretion unto the central regions. These observations are an indirect probe of the structure of the system following the second collapse. If a stellar magnetosphere cannot be inferred from them, then we argue that a structure similar to that described in this paper may be present.

6.2. Toward an eventual fragmentation

Although our analysis of the gravitational stability of the inner disk indicates that it is currently marginally stable against gravitational instabilities, it is also in a transient state in which it maintains an incredibly high temperature through accretion. This is by virtue of the low radiative efficiency of the inner disk's shock front. The protostar, as shown in Sect. 5, contributes almost nothing to heating the inner disk because it is currently embedded within it and the majority of its radiative flux escapes along the poles. One can imagine that such a disk will inevitably cool down once accretion subsides, and thus would be much more prone to fragmentation. The high mass budget of the inner disk also indicates that such fragmentations can occur multiple times, and thus lead to the formation of multiple star systems, or perhaps of Jupiter-like planets in close proximity to the central star.

6.3. Caveats

Although the radiative-hydro approximation is valid for the timescales described here, this obviously cannot be the case on longer timescales, as the stellar magnetic field will undoubtedly increase once a dynamo process begins. Furthermore, the hot, dense, and highly turbulent inner disk may also generate a dynamo process ([Balbus & Hawley 1991](#); [Wardle 1999](#); [Lesur et al. 2014](#); [Riols & Latter 2019](#); [Deng et al. 2020](#)). The onset of strong magnetic fields will bring about outflows and jets, as well as induce strong magnetic torques that can transport material inward and also reduce the rotation rate of the protostar to observed values in more evolved systems ($\sim 10\%$ of breakup velocity, [Hartmann & Stauffer 1989](#); [Herbst et al. 2007](#)). These will likely heavily influence the evolution of the system in the innermost regions. Nevertheless, the simulation presented in [Machida & Basu \(2019\)](#) was integrated for 2000 years after protostellar birth with non-ideal MHD, and their results seem to indicate that $\rho_s(1 \text{ AU}) \sim 10^{-9} \text{ g cm}^{-3}$ (see their Fig. 13). Their protostar also seems to progressively separate from the inner disk (see panels m–p of their Fig. 5 and v_r in their Fig. 11), likely

as a result of magnetic torques. Although state of the art non-ideal MHD simulations indicate that thermal pressure support far outweighs its magnetic counterpart in circumstellar disks (e.g., [Machida et al. 2010](#); [Vaytet et al. 2018](#); [Machida & Basu 2019](#); [Lee et al. 2021](#)), magnetic torques likely outweigh turbulent viscosity or gravitational torques (as quantified by [Machida & Basu 2019](#)).

In addition, although we notice relatively little spread in our results, more exhaustive constraints on the inner boundaries of circumstellar disks can be obtained by exploring a more varied range of M_0 , α , and β_{rot} . This was not done due to computational constraints, as the simulations are expensive to run at such high resolution (each run used at least 100 000 CPU hours in total).

6.4. Consequences on global disk evolution scenarios

As a result of the high values of n_{acc} hereby reported, the mass of circumstellar disks in numerical simulations may have been underestimated by about an order of magnitude ([Hennebelle et al. 2020a](#)). This appears to be inconsistent with observations of class 0 disks, which report lower disk masses of $\sim 10^{-2} M_{\odot}$ ([Tobin et al. 2020](#)). We note, however, that a recent study by [Tung et al. \(2024\)](#) has found that class 0 disk masses are routinely underestimated with current observational techniques. Nevertheless, the results indicate that the disk is very massive at birth, and naturally one must question how such a disk might evolve over time.

As such, we put forward two speculative evolutionary scenarios that we believe to be possible. The first scenario rests on the previously discussed fragmentation of the disk; as accretion subsides and the disk cools, it will become more prone to gravitational instabilities. Should the inner disk fragment, a significant amount of angular momentum could be extracted from the system.

Another scenario would rest on the strength of magnetic fields in the inner disk. Perhaps the results of current state of the art papers that report high thermal to magnetic pressure ratios are overestimating the strength of magnetic resistivities in the gas whose density exceeds first Larson core densities ($\rho > 10^{-13} \text{ g cm}^{-3}$), and thus would be underestimating the magnetic field strength within the protostar's and inner disk's precursor. This is in light of new studies ([Lebreuilly et al. 2023](#); [Kawasaki & Machida 2023](#); [Tsukamoto et al. 2023](#); [Vallucci-Goy et al., in prep.](#)) that cast doubt on the validity of the MRN ([Mathis-Rumple-Nordsiek](#), [Mathis et al. 1977](#)) dust size distribution used in said state of the art papers. In the case where the resistivities inside the first Larson core are overestimated, we would expect stronger coupling within the gas prior to hydrogen ionization. Although the ratio of thermal to magnetic pressure is still expected to greatly exceed unity within the inner disk, this would undoubtedly increase the strength of magnetic torques and cause a more central distribution of material, in which the protostar quickly exceeds the inner disk's mass and separates itself from it. However, simulations employing MRN resistivities create disk radii in broad agreement with observational surveys ([Maury et al. 2019](#); [Tobin et al. 2020](#)), in which the magnetic field truncates the disk radius at $\sim 10^1 \text{ AU}$. Perhaps the disk radii can serve as a lower bound on magnetic resistivities for low density gas, whereas the strength of magnetic fields in young stellar objects ($\sim 10^3 \text{ G}$, [Durney et al. 1993](#); [Chabrier & Küker 2006](#)) can serve as an upper bound on resistivities within the first Larson core.

6.5. Comparison with previous works

We now turn to comparing our results with previous calculations in the literature that have resolved the birth of the protostar and the inner disk structure described in this paper. Due to the very stringent time-stepping, only a handful of such studies exist. To our knowledge, the first report of the existence of a swollen disk-like structure around the second core is that of [Bate \(1998\)](#), who carried out their calculations using the SPH numerical method under the barotropic approximation. [Saigo et al. \(2008\)](#) later confirmed the existence of such a structure with their own barotropic calculations, this time using a nested-grid code. Although these papers do not have enough details presented for us to quantitatively compare our results, the description they provide of the structure of the second core and its surroundings seem to be qualitatively similar to ours. Following these two studies, [Machida & Matsumoto \(2011\)](#) led a detailed study of the inner disk under the barotropic approximation in which they include magnetic fields with ohmic dissipation, where they found qualitatively similar results to the hydro case. Notably, they report an inner disk mass of $\sim 10^{-2} M_{\odot}$, and a protostellar mass of $\sim 10^{-3} M_{\odot}$, in accordance with our results.

More recent studies include those of [Wurster et al. \(2018, 2022\)](#), [Vaytet et al. \(2018\)](#), [Machida & Basu \(2019\)](#), [Wurster & Lewis \(2020\)](#). The simulations presented in [Vaytet et al. \(2018\)](#) were also run with the RAMSES code while including magnetic fields. They reported the existence of a circumstellar disk around the protostar when including magnetic resistivities. They also reported that they could not resolve the shock front separating the protostar from the inner disk, but as we have demonstrated in this paper, such a shock front does not exist. The mass of the disk reported in their paper is $\sim 10^{-4} M_{\odot}$, which is to be expected given their short simulation time following protostellar birth (24 days) that results from stringent time-stepping.

As stated previously, [Machida & Basu \(2019\)](#) have also studied the inner disk, in which they were able to follow the calculations for a period of 2000 years following protostellar birth. Their results seem to indicate similar ratios of protostellar to disk mass than our paper, and the structure of their inner disk also seems to be similar to ours despite the presence of a magnetically launched outflow and a high velocity jet.

Finally, [Wurster et al. \(2018, 2021, 2022\)](#), [Wurster & Lewis \(2020\)](#) ran these calculations using SPH and all non-ideal MHD effects: ohmic dissipation, ambipolar diffusion, and the hall effect. They found the same disk structure following the second collapse phase. In contrast to [Machida & Basu \(2019\)](#), they report no high velocity jets and argue that magnetically launched outflows are circumstantial and depend on the initial turbulent velocity vector field, as well as the non-ideal effects at play. The only way in which we may quantitatively compare our results to theirs is through the protostellar mass, which seems to be $\sim 10^{-3} M_{\odot}$. The inner disk mass was not measured in these papers.

In summary, the circumstellar disk structure described in this paper is routinely found in previous papers simulating the second collapse in 3D. Although the quantitative details of the properties of said disk may differ due to different numerical methods and physical setups, it is guaranteed to be recovered in simulations that possess sufficient amounts of angular momentum in the first core. As such, the only simulations that do not recover it are those that make use of the ideal MHD approximation, which extracts too much angular momentum from the system and prevents the protostar from ever reaching breakup velocity.

7. Conclusion

We have carried out a set of high resolution 3D RHD simulations that self-consistently model the collapse of a $1 M_{\odot}$ dense molecular cloud core to stellar densities with the goal of studying the innermost (< 1 AU) regions. Our results are summarized as follows:

- (i) Following the second gravitational collapse, the protostar is formed through hydrostatic balance. Through accretion, the protostar accumulates angular momentum and reaches breakup velocity, after which it sheds some of its mass to form a hot, dense, and highly turbulent circumstellar disk, which we call the inner disk. The protostar is embedded within this disk, and no shock front separates the two. As accretion continues, the disk completely engulfs the protostar and spreads outward due to a combination of excess angular momentum and accretion. The disk mass exceeds that of the protostar by a factor of approximately seven, which means that the majority of the mass following the second collapse resides in the disk and its self-gravity dominates, with notable contributions from thermal pressure on its dynamics. In the case where an outer disk exists prior to the second collapse, this circumstellar disk forms within it, and the two merge after the inner disk spreads to sufficiently large radii.
- (ii) Despite the differing evolutionary histories at larger spatial scales, the star-disk structure formed after the onset of the second collapse is identical, with a small spread caused by the turbulent initial conditions. This is due to the formation of the first Larson core in all our simulations, a hydrostatic object that ensures that the second collapse occurs in approximately similar conditions.
- (iii) Accretion onto the protostar mainly occurs through material that slides on the disk's surface, as polar accretion has a low-mass flux in comparison. Along the equator, material spreads outward due to excess angular momentum. Accretion onto the inner disk is highly anisotropic.
- (iv) The radiative emissions of the star-disk system are anisotropic. The radiative efficiency of the accretion shock is supercritical along the poles, whereas the inner disk's equatorial shock front is subcritical and on the order of 10^{-3} .
- (v) The density of the inner disk's shock front at 1 AU (the most commonly used sink radius) is in the range of $[5.35 \times 10^{-10}; 2 \times 10^{-9}] \text{ g cm}^{-3}$, which is about an order of magnitude higher than the commonly used sink accretion threshold of $1.66 \times 10^{-11} \text{ g cm}^{-3}$. Thus, we suggest higher accretion thresholds for studies employing sink particles whenever possible. We note, however, that our results correspond to very early times and may not be applicable throughout the entirety of the class 0 phase.
- (vi) In order to physically decouple the protostar from its disk and reduce its rotation rate to observed values, torque mechanisms need to transport a sufficient amount of angular momentum outward. Magnetic fields are likely to play this role.

These results reveal the structure and kinematics of the innermost regions of circumstellar disks, which are often omitted from simulations due to computational constraints. Although our results are valid for the timescales described here (< 6 years following protostellar birth), we expect magnetic fields to play a more significant role later on, particularly in creating powerful torques that transport material toward the protostar.

Acknowledgements. This work has received funding from the French Agence Nationale de la Recherche (ANR) through the projects COSMHIC (ANR-20-CE31-0009), DISKBUILD (ANR-20-CE49-0006), and PROMETHEE (ANR-22-CE31-0020). We have also received funding from the European Research Council synergy grant ECOGAL (Grant: 855130). We thank Ugo Lebreuilly, Anaëlle Maury, and Thierry Foglizzo for insightful discussions during the writing of this paper. The simulations were carried out on the Alfvén super-computing cluster of the Commissariat à l'Énergie Atomique et aux énergies alternatives (CEA). Post-processing and data visualization was done using the open source Osyris (<https://github.com/osyris-project/osyris>) package. 3D visualizations were done using the open-source PyVista (<https://docs.pyvista.org/version/stable/>) package (Sullivan & Kaszynski 2019).

References

- Ahmad, A., González, M., Hennebelle, P., & Commerçon, B. 2023, *A&A*, **680**, A23
- Badnell, N. R., Bautista, M. A., Butler, K., et al. 2005, *MNRAS*, **360**, 458
- Balbus, S. A., & Hawley, J. F. 1991, *ApJ*, **376**, 214
- Bate, M. R. 1998, *ApJ*, **508**, 508
- Bate, M. R. 2010, *MNRAS*, **404**, L79
- Bate, M. R. 2011, *MNRAS*, **417**, 2036
- Bate, M. R. 2012, *MNRAS*, **419**, 3115
- Bate, M. R. 2018, *MNRAS*, **475**, 5618
- Bate, M. R., Bonnell, I. A., & Price, N. M. 1995, *MNRAS*, **277**, 362
- Bate, M. R., Tricco, T. S., & Price, D. J. 2014, *MNRAS*, **437**, 77
- Bhandare, A., Kuiper, R., Henning, T., et al. 2020, *A&A*, **638**, A86
- Bleuler, A., & Teyssier, R. 2014, *MNRAS*, **445**, 4015
- Brucy, N., & Hennebelle, P. 2021, *MNRAS*, **503**, 4192
- Chabrier, G., & Küker, M. 2006, *A&A*, **446**, 1027
- Commerçon, B., Teyssier, R., Audit, E., Hennebelle, P., & Chabrier, G. 2011, *A&A*, **529**, A35
- Commerçon, B., Debout, V., & Teyssier, R. 2014, *A&A*, **563**, A11
- Commerçon, B., González, M., Mignon-Risse, R., Hennebelle, P., & Vaytet, N. 2022, *A&A*, **658**, A52
- Deng, H., Mayer, L., & Latter, H. 2020, *ApJ*, **891**, 154
- Durney, B. R., De Young, D. S., & Roxburgh, I. W. 1993, *Sol. Phys.*, **145**, 207
- Ferguson, J. W., Alexander, D. R., Allard, F., et al. 2005, *ApJ*, **623**, 585
- González, M., Vaytet, N., Commerçon, B., & Masson, J. 2015, *A&A*, **578**, A12
- Grudić, M. Y., Guszejnov, D., Offner, S. S. R., et al. 2022, *MNRAS*, **512**, 216
- Hartmann, L., & Stauffer, J. R. 1989, *AJ*, **97**, 873
- Hennebelle, P., Commerçon, B., Lee, Y.-N., & Charnoz, S. 2020a, *A&A*, **635**, A67
- Hennebelle, P., Commerçon, B., Lee, Y.-N., & Chabrier, G. 2020b, *ApJ*, **904**, 194
- Herbst, W., Eisloffel, J., Mundt, R., & Scholz, A. 2007, in *Protostars and Planets V*, eds. B. Reipurth, D. Jewitt, & K. Keil, 297
- Joos, M., Hennebelle, P., & Ciardi, A. 2012, *A&A*, **543**, A128
- Kawasaki, Y., & Machida, M. N. 2023, *MNRAS*, **522**, 3679
- Krumholz, M. R., Klein, R. I., McKee, C. F., Offner, S. S. R., & Cunningham, A. J. 2009, *Science*, **323**, 754
- Kuiper, R., Klahr, H., Beuther, H., & Henning, T. 2010, *ApJ*, **722**, 1556
- Laos, S., Greene, T. P., Najita, J. R., & Stassun, K. G. 2021, *ApJ*, **921**, 110
- Larson, R. B. 1969, *MNRAS*, **145**, 271
- Lebreuilly, U., Hennebelle, P., Colman, T., et al. 2021, *ApJ*, **917**, L10
- Lebreuilly, U., Vallucci-Goy, V., Guillet, V., Lombart, M., & Marchand, P. 2023, *MNRAS*, **518**, 3326
- Lebreuilly, U., Hennebelle, P., Maury, A., et al. 2024a, *A&A*, **683**, A13
- Lebreuilly, U., Hennebelle, P., Colman, T., et al. 2024b, *A&A*, **682**, A30
- Lee, Y.-N., Charnoz, S., & Hennebelle, P. 2021, *A&A*, **648**, A101
- Le Gouellec, V. J. M., Greene, T. P., Hillenbrand, L. A., & Yates, Z. 2024, *ApJ*, **966**, 91
- Lesur, G., Kunz, M. W., & Fromang, S. 2014, *A&A*, **566**, A56
- Lodato, G. 2007, *Nuovo Cimento Rivista Serie*, **30**, 293
- Lodato, G., & Rice, W. K. M. 2004, *MNRAS*, **351**, 630
- Machida, M. N., & Basu, S. 2019, *ApJ*, **876**, 149
- Machida, M. N., & Matsumoto, T. 2011, *MNRAS*, **413**, 2767
- Machida, M. N., Inutsuka, S.-I., & Matsumoto, T. 2006, *ApJ*, **647**, L151
- Machida, M. N., Inutsuka, S.-I., & Matsumoto, T. 2007, *ApJ*, **670**, 1198
- Machida, M. N., Inutsuka, S.-I., & Matsumoto, T. 2008, *ApJ*, **676**, 1088
- Machida, M. N., Inutsuka, S.-I., & Matsumoto, T. 2010, *ApJ*, **724**, 1006
- Machida, M. N., Inutsuka, S.-I., & Matsumoto, T. 2011, *PASJ*, **63**, 555
- Machida, M. N., Inutsuka, S.-I., & Matsumoto, T. 2014, *MNRAS*, **438**, 2278
- Mathis, J. S., Ruml, W., & Nordsieck, K. H. 1977, *ApJ*, **217**, 425
- Maury, A. J., André, P., Testi, L., et al. 2019, *A&A*, **621**, A76
- Mignon-Risse, R., González, M., & Commerçon, B. 2021a, *A&A*, **656**, A85
- Mignon-Risse, R., González, M., Commerçon, B., & Rosdahl, J. 2021b, *A&A*, **652**, A69
- Mignon-Risse, R., González, M., & Commerçon, B. 2023, *A&A*, **673**, A134
- Minerbo, G. N. 1978, *J. Quant. Spectr. Radiat. Transf.*, **20**, 541
- Oliva, A., & Kuiper, R. 2023, *A&A*, **669**, A80
- Penston, M. V. 1969, *MNRAS*, **144**, 425
- Pringle, J. E. 1981, *ARA&A*, **19**, 137
- Riols, A., & Latter, H. 2019, *MNRAS*, **482**, 3989
- Saigo, K., Tomisaka, K., & Matsumoto, T. 2008, *ApJ*, **674**, 997
- Saumon, D., Chabrier, G., & van Horn, H. M. 1995, *ApJS*, **99**, 713
- Semenov, D., Henning, T., Helling, C., Ilgner, M., & Sedlmayr, E. 2003, *A&A*, **410**, 611
- Shakura, N. I., & Sunyaev, R. A. 1973, *A&A*, **24**, 337
- Sullivan, C., & Kaszynski, A. 2019, *J. Open Source Softw.*, **4**, 1450
- Teyssier, R. 2002, *A&A*, **385**, 337
- Tobin, J. J., Sheehan, P. D., Megeath, S. T., et al. 2020, *ApJ*, **890**, 130
- Tomida, K., Tomisaka, K., Matsumoto, T., et al. 2013, *ApJ*, **763**, 6
- Tomida, K., Okuzumi, S., & Machida, M. N. 2015, *ApJ*, **801**, 117
- Toomre, A. 1964, *ApJ*, **139**, 1217
- Tsukamoto, Y., & Machida, M. N. 2013, *MNRAS*, **428**, 1321
- Tsukamoto, Y., Iwasaki, K., Okuzumi, S., Machida, M. N., & Inutsuka, S. 2015, *MNRAS*, **452**, 278
- Tsukamoto, Y., Machida, M. N., & Inutsuka, S.-I. 2023, *PASJ*, **75**, 835
- Tung, N.-D., Testi, L., Lebreuilly, U., et al. 2024, *A&A*, **684**, A36
- Vaytet, N., Chabrier, G., Audit, E., et al. 2013, *A&A*, **557**, A90
- Vaytet, N., Commerçon, B., Masson, J., González, M., & Chabrier, G. 2018, *A&A*, **615**, A5
- Vorobyov, E. I., Skliarevskii, A. M., Elbakyan, V. G., et al. 2019, *A&A*, **627**, A154
- Wardle, M. 1999, *MNRAS*, **307**, 849
- Whitehouse, S. C., & Bate, M. R. 2006, *MNRAS*, **367**, 32
- Wurster, J., & Lewis, B. T. 2020, *MNRAS*, **495**, 3807
- Wurster, J., Bate, M. R., & Price, D. J. 2018, *MNRAS*, **481**, 2450
- Wurster, J., Bate, M. R., & Bonnell, I. A. 2021, *MNRAS*, **507**, 2354
- Wurster, J., Bate, M. R., Price, D. J., & Bonnell, I. A. 2022, *MNRAS*, **511**, 746

Appendix A: Defining the protostar and inner disk in our simulations

The definition of the protostar in our simulations is rather semantic, as it is not a separate object from the inner disk. We use the same criterion as Vaytet et al. (2018) for defining the protostar: it is simply the gas whose density is above $10^{-5} \text{ g cm}^{-3}$. We note that in Vaytet et al. (2018), the authors mention that they do not have enough resolution to resolve the protostellar accretion shock separating it from the circumstellar disk, although as we have shown in Sect. 3.2, such a discontinuity does not exist.

In order to define the inner disk, none of the criteria currently used in the literature were adequate in our case, mostly due to our use of turbulent initial conditions. Additionally, in some simulations, the second collapse occurred within a larger-scale disk,

which further complicated our disk selection criterion. Inspired by Joos et al. (2012), we used the following criterion:

$$\begin{cases} P > \rho v_r^2, & \text{Thermal support against radial infall} \\ \rho v_\phi^2 > P, & \text{Centrifugal support exceeds pressure} \\ \rho_s < \rho < 10^{-5} \text{ g cm}^{-3}, & \text{Density threshold} \end{cases}$$

where ρ_s is the density of the inner disk's equatorial shock front, obtained at each snapshot through ray-tracing. This criterion ensures that no cells currently undergoing the second gravitational collapse phase are selected and that sufficient angular momentum is present in the gas to qualify as a disk. The third item in this criterion states that $\rho < 10^{-5} \text{ g cm}^{-3}$, but this is again an arbitrary choice to separate the protostar from its circumstellar disk.

3.4 MHD simulations

Following our results in the previous paper, we pondered on their universality. Indeed, these simulations leveraged the results of previous state of the art papers to omit magnetic fields and push the calculations much further in time. The most significant results found were the breakup of the protostar and the subsequent rapid radial spreading of the newly-formed circumstellar disk, whose resulting properties may differ under the influence of a magnetic field. Furthermore, although there exists a number of papers reporting on the magnetic field properties of newly-formed protostars, the vast majority of these use idealized setups in which solid body rotation is assumed and a magnetic field threads the dense cloud core. In addition, these calculations are often stopped soon after protostellar birth, and little is reported on the structure of the magnetic field in protostars. With this in mind, during the last year of my PhD, I ran a set of MHD simulations reaching the second collapse stage, however, due to the numerical cost of these simulations, they were not as exhaustive and have a much shorter horizon of predictability than the RHD runs presented in the previous sections. Nevertheless, these simulations have yielded interesting results pertaining to the problems tackled during this thesis, namely the angular momentum problem and the magnetic flux problem.

3.4.1 Context

In recent years, the role of magnetic fields in star formation has garnered a significant amount of interest. Aided by advances in far-infrared and submillimeter (e.g., ALMA, NOEMA, VLA) instruments capable of measuring linearly polarized dust emissions, magnetic fields have been observed in dense cloud cores (Kirk et al. 2006; Jones et al. 2015; Kandori et al. 2018; Myers & Basu 2021) where they exhibit supercriticality (i.e., the mass-to-flux ratio is above unity) and a typical field strength of $\sim 10^{-5}$ G. Furthermore, using Zeeman line splitting techniques (Crutcher & Kemball 2019), they have also been observed in young stellar objects with values of $\sim 10^3$ G (Johns-Krull 2007; Johns-Krull et al. 2009; Yang & Johns-Krull 2011; Flores et al. 2024). Should the magnetic field be perfectly coupled to the fluid during the collapse of the dense core (i.e., the ideal MHD approximation), flux freezing implies that the resulting protostar would have a magnetic field strength of $\sim 10^6$ G, far in excess of observed values. Therefore, a considerable amount of magnetic flux is lost by the time the protostar becomes visible. This problem is known as the *magnetic flux problem*, which has so far eluded a concise answer. Current observational surveys of magnetic fields of young stellar objects, although limited in sample size, have so far failed to find any correlation between magnetic field strength and stellar age, however they report a decreasing magnetic flux over time. This favors the fossil field hypothesis, meaning that the measured magnetic fields in these evolved sources are carried over from their inception in the second Larson core. Ultimately, solving this problem requires a detailed model of the evolution of the protostellar magnetic field as the protostar transitions from the class 0 to the class I phase, accounting for prestellar evolution and describing the magnetic field's evolution using dynamo theory, however such a model is yet to be developed and little is reported on the subject in the literature. In the absence of any such model,

the fossil field hypothesis remains favored and this may provide a constraint on star formation simulations, as they must be able to form a protostar whose magnetic field has a strength of $\sim 10^3$ G.

A similar and closely linked issue to this is the *angular momentum problem*, which states that should angular momentum be conserved during the collapse of the dense core, stars would rotate far above their breakup velocity and circumstellar disks would be an order of magnitude larger than their observed sizes ($\sim 10^1$ AU, [Maury et al. 2019](#); [Tobin et al. 2020](#)). Once again, the ideal MHD approximation fails to conform to observational data as it produces magnetic braking that is efficient enough to extract all angular momentum from the dense core (i.e., the *magnetic braking catastrophe*, [Matsumoto & Tomisaka 2004](#); [Hennebelle & Teyssier 2008](#); [Hennebelle & Fromang 2008](#); [Mellon & Li 2008](#)). It is now widely admitted that resistive processes, mainly ambipolar diffusion, are responsible for breaking the ideal MHD limit towards higher density gas and reducing the magnetic braking efficiency to the point where a disk may form and reach sizes comparable to observations (e.g., [Masson et al. 2016](#); [Hennebelle et al. 2016](#); [Vaytet et al. 2018](#); [Machida & Basu 2019](#); [Wurster & Lewis 2020a,b](#)). In addition to this, resistive MHD simulations report a converged magnetic field strength of ~ 0.1 G in the first Larson core (primarily due to ambipolar diffusion), which allows for the second Larson core to form with a magnetic field strength of $\sim 10^3$ G (e.g., [Vaytet et al. 2018](#); [Machida & Basu 2019](#); [Wurster et al. 2022](#)).

In order to account for resistive processes, one must use a detailed chemical network that describes the abundance of charged species. In addition, one must also make an assumption on the dust grain size and density distribution in order to determine the surface area available for chemical reactions ([Marchand et al. 2016](#); [Zhao et al. 2020](#)), and to account for the fact that the dust particles themselves may be the main charge carriers. In this regard, the Matthis-Rumple-Nordsiek distribution ([Mathis et al. 1977](#)) is most often used, as it is mostly valid for dust particles in the interstellar medium, however, recent studies having undertaken the effort of re-evaluating the MRN distribution during the collapse of dense cores have called into question its validity ([Lebreuilly et al. 2023](#); [Kawasaki & Machida 2023](#); [Tsukamoto et al. 2023a](#); [Vallucci-Goy et al. 2024](#)). Most notably, these studies reveal an absence of small grains toward gas densities close to first Larson core values ($\sim 10^{-13}$ g cm $^{-3}$), which in turn causes a stark drop in Ohmic resistivity, to the point where it is no longer a viable dissipative process at densities of the first Larson core and higher. The Hall effect, even within the MRN framework, remains the most poorly constrained resistive effect. Studies accounting for it report drastically different evolutionary scenarios for protoplanetary disks (e.g., [Tsukamoto et al. 2015a](#); [Wurster & Lewis 2020a](#); [Wurster et al. 2022](#)), however the computed resistivities are too uncertain to draw any conclusions on the subject. The only resistive effect whose role and behavior during the protostellar collapse can be inferred with reasonable confidence is ambipolar diffusion, whose reduction in magnetic braking efficiency allows for the formation of disks whose sizes are in broad agreement with class 0 disk size surveys.

Finally, it has recently become clear that subgrid models used in protostellar collapse calculations in order to alleviate timestepping constraints produce results that are very

sensitive to their parameters (Machida et al. 2014; Vorobyov et al. 2019; Hennebelle et al. 2020b). This requires one to study the innermost sub-au region of circumstellar disks, which entails second-collapse calculations resolving both the protostar and the newly-formed circumstellar disk. A number of said calculations exist in the literature (e.g., Vaytet et al. 2018; Machida & Basu 2019; Wurster & Lewis 2020b; Wurster et al. 2022). However, the majority of these use idealized setups in which solid-body rotation is assumed and turbulence is absent in the initial dense cloud core. This absence of turbulence allows the magnetic field to maintain a coherence which amplifies its effects, be it magnetic braking or the launching of outflows and jets. In addition, with the exception of Wurster & Lewis (2020b); Wurster et al. (2022); Machida & Basu (2019), these calculations are often stopped soon after protostellar birth owing to timestepping constraints. Nevertheless, they found that the resulting protostar and circumstellar disk are thermally supported bodies, where thermal pressure gradient forces vastly outweigh their magnetic counterparts. In this regard, Ahmad et al. (2024) led a study in which the RHD approximation was used and found that the nascent protostar quickly reaches breakup speeds, by which point a circumstellar disk forms around it and expands outward. This occurs regardless of the initial conditions of the parent dense core. Machida & Matsumoto (2011) and Bhandare et al. (2024) similarly report the existence of this disk surrounding the protostar (hereafter called the inner disk or circumstellar disk).

In the present study, we continue our work in Ahmad et al. (2024) by including the effects of magnetic fields in our calculations, both under the ideal and non-ideal MHD approximation, while accounting for radiative transfer using the Flux Limited Diffusion (FLD) approximation. Our goals are to describe the birth and early evolution of the protostar and the circumstellar disk surrounding it. In light of the aforementioned recent studies around dust size distribution during protostellar collapses that report a stark drop in Ohmic resistivities, we have chosen to ignore Ohmic dissipation in our non-ideal MHD simulation, and only ambipolar diffusion is accounted for. We follow the collapse of a dense cloud core to stellar densities, and describe the initially isothermal phase of the collapse, the formation of the first Larson core and its subsequent adiabatic contraction, the second collapse following the dissociation of H_2 molecules, the birth of the protostar, and subsequently push the calculations as far as possible in time. In our pursuit of describing the smallest spatial scales relevant to protostellar and circumstellar disk birth, we have obtained the best resolved protostars and circumstellar disk in the MHD literature. Particular attention is given to the structure of the magnetic field within the nascent protostar, as well as within the circumstellar disk. The evolution of the nascent circumstellar disk is also compared to its hydro counterpart in order to better ascertain the effects of magnetic fields on the system. Our results, reported below, carry multiple implications for the angular momentum and the magnetic flux problem. In addition, they offer constraints on subgrid parameters used in disk evolution studies.

3.4.2 Numerical setup

We have used the same setup as in [Ahmad et al. \(2024\)](#), with the same refinement strategy. It consists of a uniform density dense cloud core of radius $R_0 = 2.465 \times 10^3$ AU, mass $M_0 = 1 M_\odot$ and temperature 10 K, equivalent to an initial ratio of thermal to gravitational energy of 0.25. Angular momentum is present through the inclusion of a turbulent velocity vector field parameterized by the turbulent Mach number \mathcal{M} , which we have set to 0.4. Radiative transfer is accounted for under FLD approximation. A uniform magnetic field threads the dense cloud core along the z axis, and its strength is parameterized by the mass-to-flux ratio which we have set to 4. This corresponds to an initial magnetic field strength of $\sim 10^{-5}$ G in the dense cloud core, and an Alfvénic Mach number of $\mathcal{M}_a \approx 0.12$. This setup is identical to that of run G2 in [Ahmad et al. \(2024\)](#), with the only difference being the presence of magnetic fields.

Two simulations will be presented in this section; one under the ideal MHD approximation (hereafter IMHD) and one in which we have accounted for ambipolar diffusion (hereafter NIMHD). These two simulations use the same refinement strategy, however run IMHD has a maximum refinement level of $\ell_{\max} = 26$ (the coarsest level is at $\ell_{\min} = 6$) whereas run NIMHD has $\ell_{\max} = 25$. As we will see later-on, this is because run IMHD forms a much more compact protostar, whose properties require a finer spatial resolution to describe. This means that at the finest refinement level, run IMHD and NIMHD respectively have a spatial resolution of $\Delta x_{\text{IMHD}} = 1.4 \times 10^{-4}$ AU and $\Delta x_{\text{NIMHD}} = 2.9 \times 10^{-4}$ AU.

Zoom-out

Owing to very stringent time-stepping constraints, run NIMHD requires approximately two days of CPU wall time in order to integrate ≈ 40 hours. This is because the timestep at the finest level reaches a mere minute, and the poor load balancing causes most cells to be handled by a few CPUs. As the protostar and circumstellar disk grow and expand over time, this problem is aggravated as a considerable number of cells are created to describe the newly formed structures. In order to alleviate the timestepping constraints, we have also run a simulation branched out of run NIMHD nearly 0.4 years after protostellar birth, in which the maximum refinement level was reduced from $\ell_{\max} = 25$ to $\ell_{\max} = 24$. This allowed us to push the simulation considerably further out in time,³ which is particularly useful to study the expansion of the newly-formed circumstellar disk. This run, labeled "NIMHD_LR", is discussed in [Sec. 3.4.6](#).

3.4.3 Large scale structures

We first begin by describing the system at the scale of the dense core itself ($\sim 10^3$ AU), with the goal of providing the contextual environment in which the protostar is born. To this end, we compare runs IMHD and NIMHD in [Fig. 3.3](#) at our final simulation

³The $\ell_{\max} = 25$ simulation ran for ≈ 0.55 years after protostellar birth, whereas the $\ell_{\max} = 24$ simulation ran from ≈ 0.44 years to ≈ 1.57 years.

snapshots (respectively ≈ 23.25 and ≈ 23.39 kyr after simulation start), which displays the column density (first row), the optical depth τ computed along the line of sight (second row), and the maximum temperature along the line of sight (third row). τ is computed as

$$\tau = \int_{z_{\min}}^{z_{\max}} \rho \kappa_{\text{R}} dz , \quad (3.9)$$

where ρ is the gas density and κ_{R} the Rosseland mean opacity.

The column density maps show a filamentary structure of size $\sim 10^2$ AU forming in both runs. This structure is formed by gravo-turbulence (Tsukamoto & Machida 2013), however it appears much thinner in these calculations than their RHD counterparts in Ahmad et al. (2024). This is due to magnetic braking, which extracts a significant amount of angular momentum from the gas and thus prevents it from spreading out as much. Since ambipolar diffusion begins acting at higher densities ($\sim 10^{-14}$ g cm $^{-3}$), the two runs yield identical column density maps outside the filament, however in the case of run NIMHD it has fragmented into two distinct dense cores (Fiege & Pudritz 2000). The existence of a secondary bound fragment within the filament is owing to an extended first core lifetime. Indeed, the first core survived ≈ 100 years longer in run NIMHD owing to a reduced mass accretion rate onto it, which is in turn due to less efficient magnetic braking. In this time span, the filament fragmented in run NIMHD, whereas the stringent timestepping following the second collapse froze the simulation at larger scales in run IMHD, and no bound fragment is witnessed at its final simulation snapshot.

Despite the very similar structure, the two runs have differing optical depth maps (panels c and d). Indeed, run NIMHD has a more spatially extended optically thick region (lime-colored contours) than run IMHD. This is due to the differing temperatures found within the cloud core, as ambipolar diffusion significantly heats-up the gas (panel f). The increase in temperature at these densities manifests itself as an increase in opacity (see figure 1 of Ahmad et al. 2023). This serves to show that the two models should produce distinct emission maps that may be discriminated against with current observational instruments.

We now turn to studying the collapse in quantitative terms using Fig. 3.4. Panel (a) of this figure displays the maximum density of the simulation as a function of time since first core formation (defined as the moment where $\rho_{\max} > 10^{-10}$ g cm $^{-3}$). The steep rise in ρ_{\max} in this figure corresponds to the second collapse (i.e., protostellar birth). We see here that the two runs display different first core lifetimes, with run NIMHD entering the second collapse phase nearly 200 years later. This is in contrast to Vaytet et al. (2018)'s results, who reported a longer first core lifetime in their ideal MHD simulation due to the interchange instability reducing mass accretion rates onto it. This discrepancy between our results is due to our use of turbulent initial conditions, which although does not prevent the emergence of the interchange instability in run IMHD (panel a of Fig. 3.3), still reduces its efficiency. The first core in run NIMHD survived for a total of ≈ 250 years, which is about half as much as the hydrodynamical run presented in Ahmad et al. (2024). Its extended lifetime in comparison to run IMHD is due to the reduced magnetic braking efficiency, which allows for angular momentum to reduce mass accretion rates onto the first core. The maximum density

reached post-second collapse in run IMHD is $\sim 10^{-1} \text{ g cm}^{-3}$, and $\sim 10^{-3} \text{ g cm}^{-3}$ in run NIMHD.

During the collapse, flux freezing causes the magnetic field strength to increase with increasing density (with $B \propto \rho^{2/3}$). This causes the maximum magnetic field strength (B_{max}) in run IMHD, shown in panel (b), to continuously increase over time (with increasing central density), with small drops in magnetic field strength being caused by turbulent reconnection. In run NIMHD however, the magnetic field strength displays a plateau at $\sim 10^{-1} \text{ G}$, owing to ambipolar diffusion. Once the second collapse occurs, flux freezing (which is recovered in run NIMHD following dust sublimation and the ionization of atomic gas species) once again causes a strong increase in magnetic field strength, which reaches $\sim 10^5 \text{ G}$ in run IMHD and $\sim 10^3 \text{ G}$ in run NIMHD. We also notice in both runs that the magnetic field strength measured at the location of maximum density (B_{central} , dotted lines) is a factor ≈ 2 below B_{max} . Following the second gravitational collapse (panel c), the maximum magnetic field strength reaches $\approx 3 \times 10^5 \text{ G}$ in run IMHD, and $\approx 10^4 \text{ G}$ in run NIMHD. Soon after protostellar birth, the maximum field strength in run IMHD continuously decreases to $\sim 5 \times 10^4 \text{ G}$, and in the case of run NIMHD, it decreases to $\sim 6 \times 10^3 \text{ G}$ and plateaus around this value. We see the same trend in B_{central} , which fails to coincide with B_{max} following the second collapse, and whose discrepancy with it seems to worsen over time. We show later in [Sec. 3.4.5](#) that the drop in magnetic field strength in run IMHD is mostly due to an outward advection of magnetic flux. The discrepancy between B_{max} and B_{central} has been reported in previous papers in the literature, most notably [Wurster & Lewis \(2020b\)](#); [Wurster et al. \(2022\)](#). They also report a reduction in B_{max} shortly following protostellar birth. Our results confirm their findings, however the cells containing ρ_{max} and B_{max} are separated by a very small distance ($\sim 10^{-2} \text{ AU}$) in our simulations, and we do not report the existence of a "magnetic wall" on which magnetic flux is accumulated as they do.

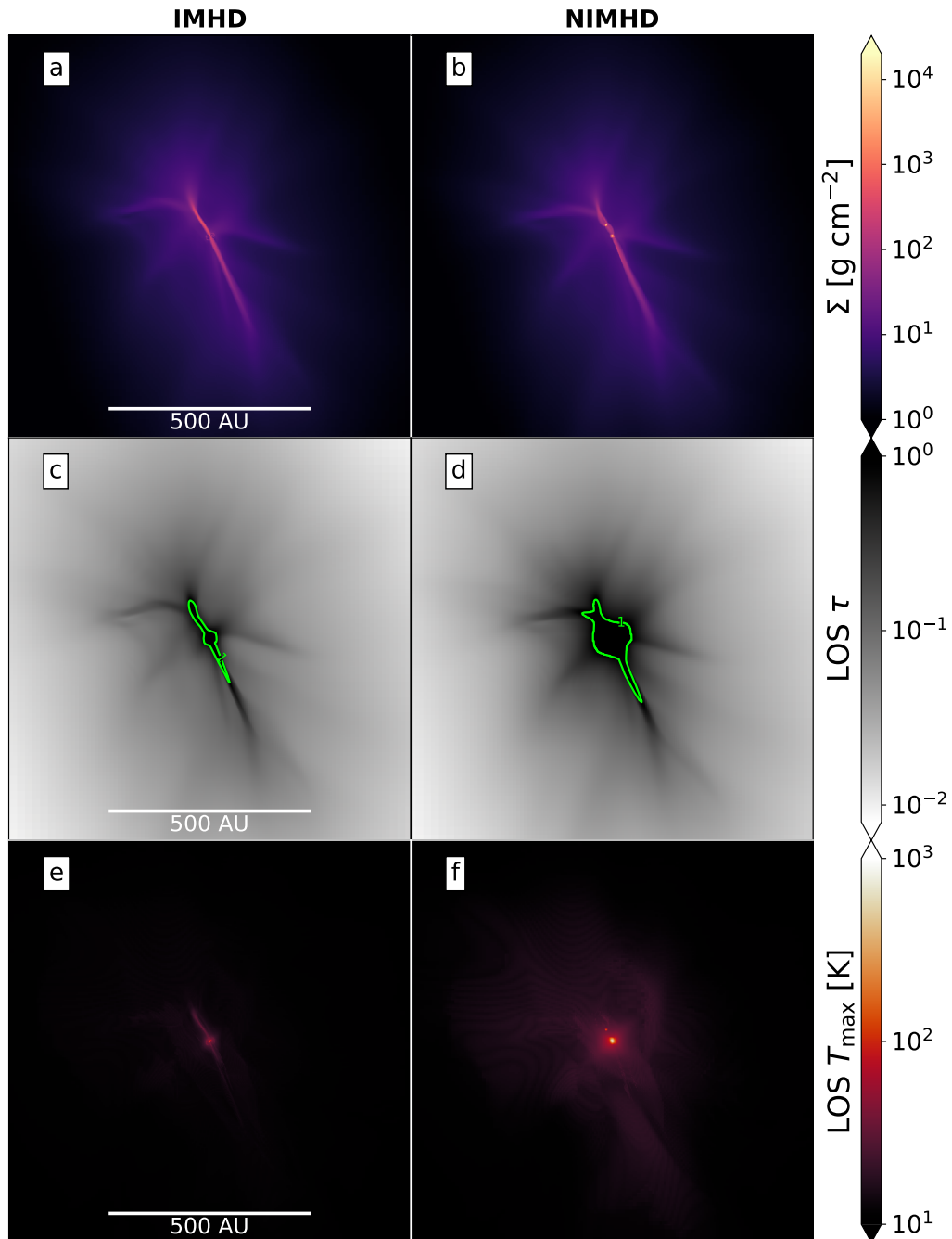


Figure 3.3: A comparison of runs IMHD (first column) and NIMHD (second column) at the scale of the dense cloud core itself. The snapshots are taken respectively at $t \approx 23.25$ and $t \approx 23.39$ kyr following the collapse of the dense core. The first row displays column density (panels a and b), the second row displays the optical depth computed along the line of sight (panels c and d), and the last row displays the maximum temperature along the line of sight (panels e and f). All maps are projections along the z axis. The lime-colored contour in panels (c) and (d) represent an optical depth of unity. The scale bars in the first column apply to the second column as well.

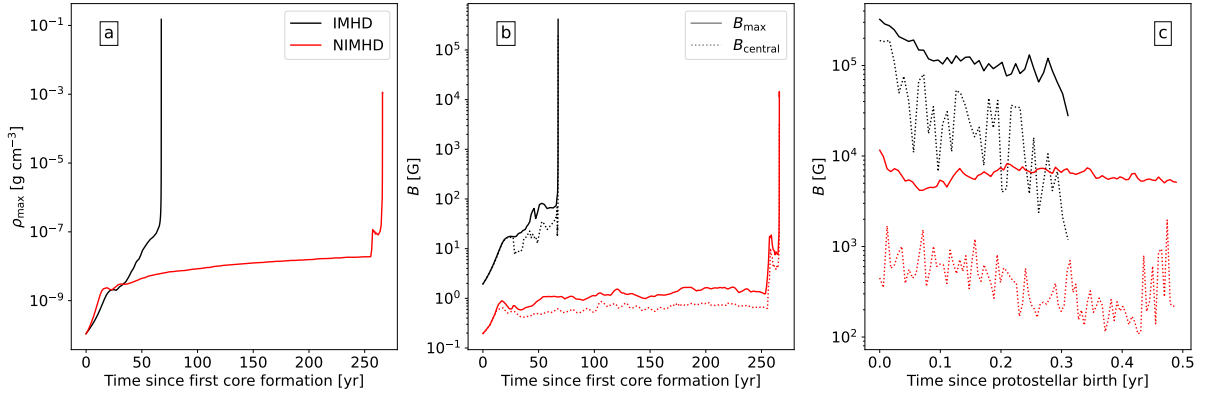


Figure 3.4: A quantitative comparison of the collapse between run IMHD (black) and run NIMHD (red). Panel (a) displays the evolution of the maximum density since the formation of the first Larson core, which we define as the time where a density of $\approx 10^{-10}$ g cm $^{-3}$ is achieved. Panel (b) and (c) display the magnetic field strength evolution as a function of time since first core formation and since protostellar birth (defined as the moment a density of $\approx 10^{-5}$ g cm $^{-3}$ is reached), where the solid lines represent the maximum magnetic field strength and the dotted lines represent the field’s strength measured at the location of maximum density.

3.4.4 The second collapse

Qualitative result of the second collapse

We now turn to the main focus of our study; the structure of the system following the second gravitational collapse. To this end, we first begin by studying the qualitative structure of the system with the aid of density, temperature, radiative flux, and radial velocity slices displayed in figures 3.6 and 3.7. The slices are projected along the angular momentum vector of the gas within 0.2 AU for run NIMHD, and in the case of run IMHD, along the z axis since there is virtually no angular momentum left in the gas owing to the efficiency of magnetic braking.

The differences between the resulting protostars are stark. The first row displays the system at protostellar birth, which we define as our $t = 0$. The protostar in run IMHD is more compact than run NIMHD, displaying higher densities and temperatures owing to the lack of centrifugal support against gravity. This causes it to form at a radius of $\approx 0.97 R_{\odot}$, whereas in run NIMHD, the centrifugal support flattens the protostar considerably and extends its radius to $\approx 4.8 R_{\odot}$. In the weeks following the formation of the protostar in run IMHD (panels b-e and l-o of Figs. Fig. 3.6 and Fig. 3.7), its size grows considerably as it accretes material from its surroundings. This is due to the subcritical nature of its accretion shock, which struggles to radiate the incoming accretion energy (see Ahmad et al. 2023). In addition, filamentary structures protruding from the stellar surface can be seen growing in spatial extent as time progresses. These are in fact current sheets akin to coronal mass loops, which appear as filaments when visualized in slices. Additionally, an approximately spherical shell of material

surrounds the protostar, which is most apparent in the density and radiative flux slices of Fig. 3.6 and Fig. 3.7. This corresponds to a region of strong magnetic pressure, which supports the gas against gravity and hence drives the radial velocities down to ≈ 0 . Notably, we report no high-velocity jets or outflows surrounding the protostar in this run. This is likely due to our use of turbulent initial conditions, which was shown to significantly disrupt these processes by Wurster & Lewis (2020b).

In the case of run NIMHD, an entirely different evolutionary sequence is witnessed. As time progresses, a disk-like structure surrounding the protostar is formed. This is due to the latter’s accumulation of angular momentum, after-which it reaches breakup velocity and material is advected outward. This result confirms the findings of Ahmad et al. (2024), in which no magnetic fields were present. As the disk grows in size and in mass, it exhibits spiral waves which form as a result of gravitational instabilities. These spiral waves carry a significant amount of angular momentum outward and cause increased mass accretion rates onto the protostar.

These figures show the importance of including ambipolar diffusion in our calculations, as they permit enough angular momentum to survive and hence avert the magnetic braking catastrophe.

Defining the protostar and circumstellar disk

Since the two runs yield drastically different qualitative properties, one must have robust definitions for both the protostar and the circumstellar disk before proceeding to any quantitative comparison. In the case of run IMHD, the protostar is a thermally supported body, however, simply finding the cells in which thermal pressure support is attained as is done in Ahmad et al. (2023) is inadequate, as the current sheets protruding from the stellar surface also satisfy this definition. As such, we have decided to define the protostar as being all cells in which at least 90% of H_2 molecules are dissociated (i.e., $X_{\text{H}_2} < 10^{-1}$, where X_{H_2} is the fraction of hydrogen under molecular form).

In the case of run NIMHD, the presence of centrifugal support drastically changes the structure of the protostar, which flattens along the equator. Further complicating things, the transition from thermal pressure support to mainly centrifugal support against gravity is smooth, and no shock front separates the protostar from its circumstellar disk (Ahmad et al. 2024). As a result, we adopt the same arbitrary definition for the protostar as in Vaytet et al. (2018); Ahmad et al. (2024), namely, that it is the gas whose density exceeds $10^{-5} \text{ g cm}^{-3}$. To illustrate why these two criteria were used, we display in Fig. 3.5 their results when applied to both simulations. The criterion defining the protostar as being $X_{\text{H}_2} < 10^{-1}$ is displayed in the first row, where we see that it recovers the stellar surface in run IMHD but fails to do so in run NIMHD. On the other hand, the second criterion stating that the star is defined as $\rho > 10^{-5} \text{ g cm}^{-3}$ and displayed in the second row, shows that it selects extended current sheets protruding from the stellar surface in run IMHD but recovers a centrifugally flattened surface in run NIMHD.

The circumstellar disk is defined as in Ahmad et al. (2024); it is the centrifugally

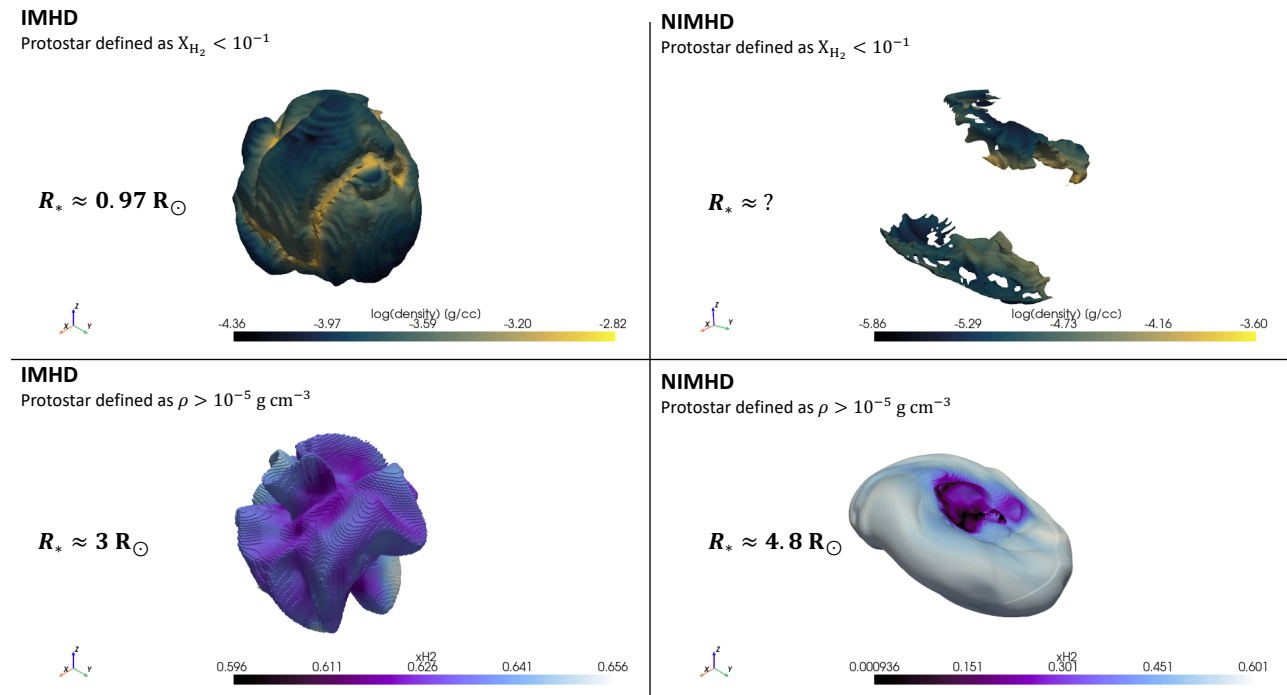


Figure 3.5: A 3D illustration of the two criteria used to define the protostar, as applied in run IMHD (first columns) and run NIMHD (second columns). The first row displays an isocontour of $X_{\text{H}_2} \approx 10^{-1}$, whereas second row displays an isocontour of $\rho \approx 10^{-5} \text{ g cm}^{-3}$. The colorbar in the first (resp. second) row displays the gas density (resp. X_{H_2}) in the extracted surface.

supported gas whose thermal pressure support exceeds incoming ram pressure, and whose density exceeds the density of the shock front (which is in turn determined through ray-tracing).

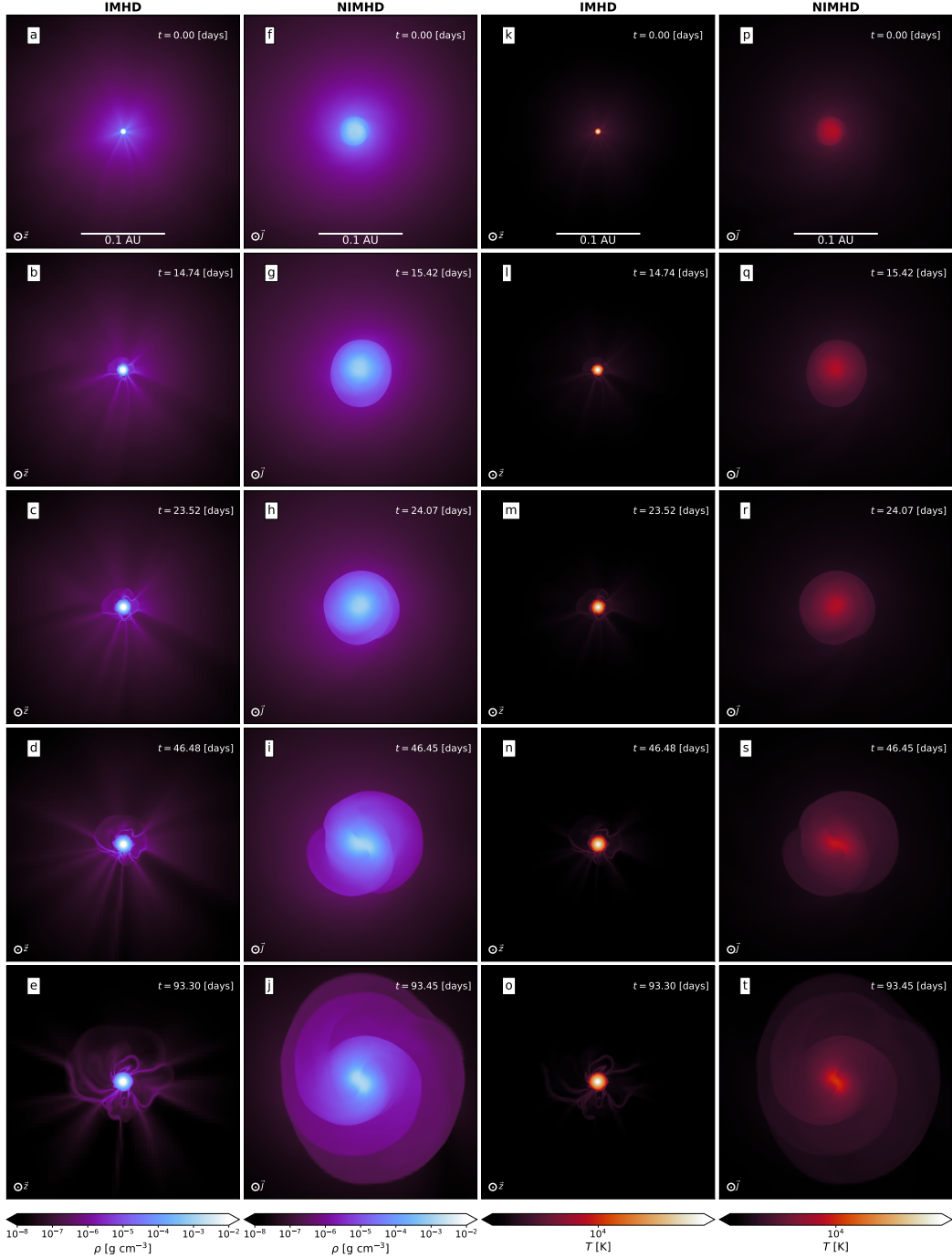


Figure 3.6: A set of slices showing the evolution of the density (first two columns) and temperature (last two columns) for run IMHD (first and third column, panels a-e and k-o) and run NIMHD (second and fourth column, panels f-j and p-t). Each row represents a different time, where $t = 0$ corresponds to the moment of protostellar birth. For comparative purposes, the slices are shown at similar times, and the timestamp is written in the top right corner of each panel. The slices are done in the z direction for run IMHD, and along the angular momentum vector for run NIMHD. The scale bars in the first row apply to all other rows as well.

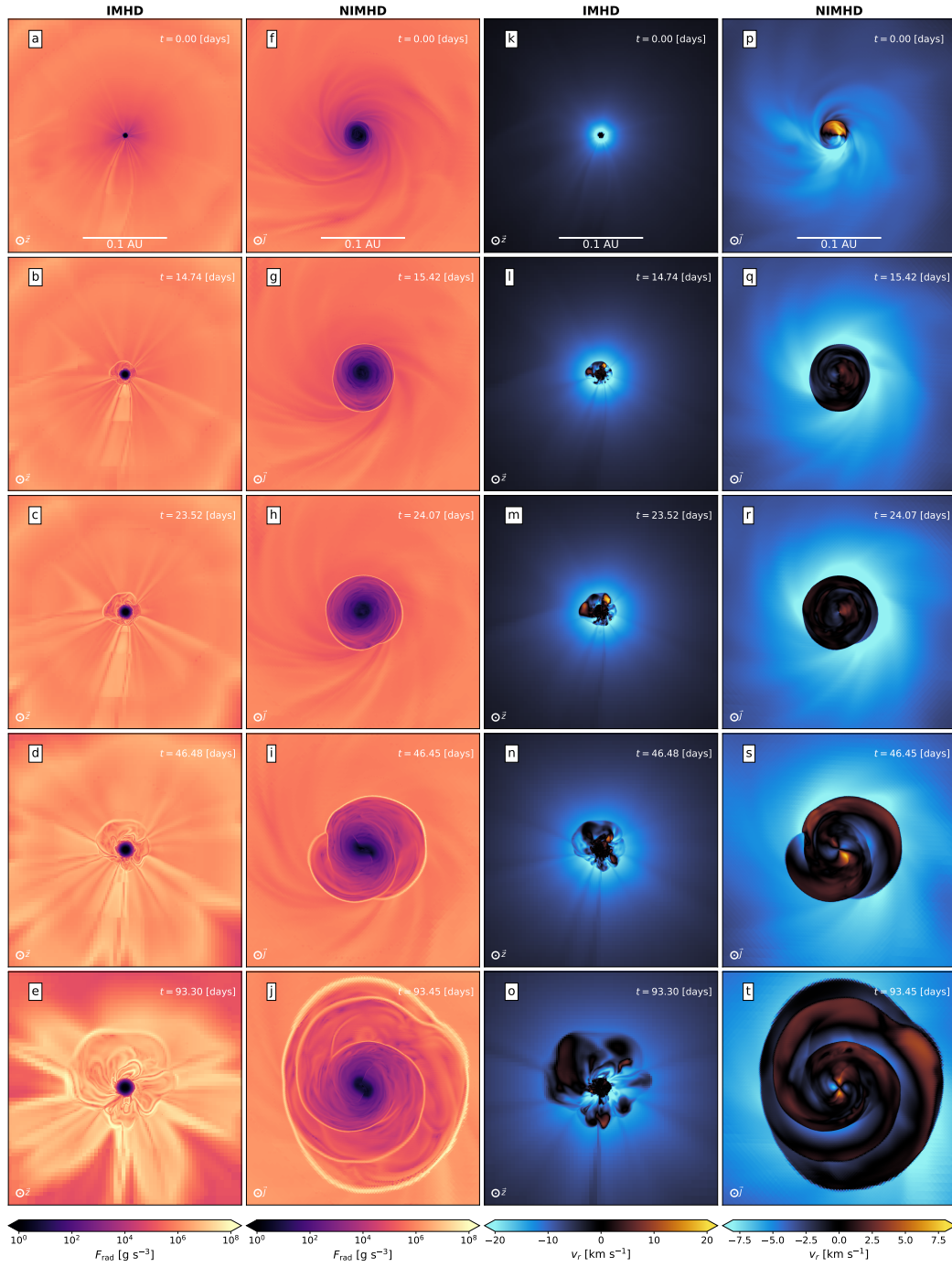


Figure 3.7: Same as Fig. 3.6, but this time showing the radiative flux (first two columns) and radial velocity (last two columns).

Gas structure and kinematics

We now turn to providing a more quantitative comparison between run IMHD and run NIMHD. To this end, we display in [Fig. 3.8](#) and [Fig. 3.9](#) averages of various physical quantities. In the case of run NIMHD, since the structure we witness is a flattened disk-like structure, these quantities are averaged azimuthally in cylindrical bins in which only cells in the midplane region are selected. The midplane is defined as the region in which $z \in [-2.5; 2.5] \times 10^{-2}$ AU, where the z component is computed along the angular momentum axis of the gas within 0.1 AU. In the case of run IMHD, the measurements are done using the spherical coordinate system since the protostar and the distribution of material around it possess a spherical morphology.

We begin by studying the structure of run IMHD ([Fig. 3.8](#)). The density profile at protostellar birth, displayed in panel (a) (solid line), shows that the central region of the protostar reaches $\sim 10^{-1}$ g cm $^{-3}$.⁴ Nearly 117 days later (dotted line), this value drops to $\sim 10^{-3}$ g cm $^{-3}$. In both snapshots, a power-law tail follows the central density peak. The sharp discontinuity in the radial velocity profile (panel d) displays the location of the accretion shock, which is $\approx 4 \times 10^{-3}$ AU ($\approx 0.86 R_{\odot}$) and subsequently moves outward as the protostar expands. The azimuthal velocity curves, shown in panel (e), display the efficiency of magnetic braking in this simulation: nearly no angular momentum survived, as v_{ϕ} alternates between positive and negative values and is mostly a noisy measurement. In panel (c), the specific entropy of the gas⁵ is shown. Here, as in [Ahmad et al. \(2023\)](#), we see that $ds/dr > 0$ throughout the protostellar interior, meaning that the protostar is radiatively stable against convective instabilities. However, as accretion still drives turbulence within the protostellar interior ([Bhandare et al. 2020](#); [Ahmad et al. 2023](#)), the entropy profile at our final snapshot is flattened as a result of the mechanical transport of energy. The entropy profile has also been lifted upwards as a result of the accretion of energy. These results are very similar to the spherically symmetrical RHD run presented in [Ahmad et al. \(2023\)](#), which again illustrates how efficient magnetic braking is in this run.

In [Fig. 3.9](#) however, we witness very different results for run NIMHD. Firstly, the density reached in the central regions is two orders of magnitude lower and at $\sim 10^{-3}$ g cm $^{-3}$, a value close to the hydro runs presented in [Ahmad et al. \(2024\)](#). Unlike in run IMHD however, no hydrostatic bounce occurs and the maximum density remains constant as time progresses. The temperature shown in panel (b) is also an order of magnitude lower than in run IMHD, and sits close to 5×10^3 K, however this increases to 7×10^3 K nearly 191 days later, meaning that the protostar is heating up as it accretes material. The cylindrical radial velocity v_{cyl} , displayed in panel (d), shows that the protostellar accretion shock is formed at 2×10^{-2} AU ($\approx 4.3 R_{\odot}$), which is nearly five times larger than in run IMHD. This midplane shock front expands outward to 2×10^{-1} AU at our final snapshot. We emphasize that it is no longer the protostellar accretion shock that is displayed by the discontinuity in v_{cyl} , but rather, that

⁴This value was shown to be unconverged in [Ahmad et al. \(2023\)](#), albeit not by a lot and the resolution is such that its numerical outcomes are reliable enough for physical interpretation.

⁵The specific entropy is obtained through an interpolation of the equation of state table.

of the newly-formed circumstellar disk in which the protostar is embedded. In panel (e), we display the azimuthal velocity curves. Here, we see very clearly that rotational motion exists, as $v_\phi > 0$ throughout the radii displayed in the figure. Furthermore, these curves show that the central regions are in solid body rotation, whereas the circumstellar disk exhibits differential rotation. At $t \approx 190$ days, the disk displays a fully Keplerian ($v_K = \sqrt{GM_*/r}$) rotation profile (dashed red curve).

Finally, we display in panel (c) the specific entropy of the gas. As in run IMHD, the protostar is radiatively stable against convective motion. However, at our final simulation snapshot, we see that it is no longer the case as there exists a region in which $ds/dr < 0$. This is likely caused by the prominent spiral waves in the star disk system, and will further contribute to creating strong turbulent motion that act as effective viscosity and extract angular momentum from the gas, thus driving accretion in the midplane regions.

This analysis once again shows the stark differences of both runs; whereas the almost entirely complete absence of angular momentum in run IMHD owing to magnetic braking causes the second collapse to form structures more akin to those produced in spherically symmetrical calculations, the inclusion of ambipolar diffusion allows a considerable amount of angular momentum to survive and hence form a rotationally supported disk surrounding the protostar. In this sense, run NIMHD is more related to hydrodynamical runs than to run IMHD, and thus should be quantitatively and qualitatively compared as such.

3.4.5 Magnetic field structure

In this section, we describe the structure and morphology of the magnetic field within and in the close vicinity of the protostar. To this end, we display in Fig. 3.10 and Fig. 3.11 slices showing the magnetic field strength and plasma β ($= 8\pi P/B^2$). In Fig. 3.10, the slices are shown in a top-down (panels a-e and k-o) and edge-on (panels f-j and p-t) view, whereas the absence of rotation in run IMHD renders any such double-visualization useless, and we may visualize these quantities along the z axis only. We will also leverage the information available in Fig. 3.8 and Fig. 3.9.

The magnetic field streamlines of run NIMHD are displayed in panels (a-j) of Fig. 3.10. In the top-down view (panels a-e), we see the magnetic field lines being dragged by the nascent protostar. At the temperature-density regime displayed here, the ideal MHD limit is recovered as all dust grains are sublimated and ambipolar diffusion is no longer at play. In addition, the plasma β values displayed in the last two rows indicates that thermal pressure support far outweighs magnetic pressure support, meaning that it is the fluid that dictates the behavior of the magnetic field. As such, the rotation of the newly-formed protostar and circumstellar disk causes a significant build-up of the toroidal component of the magnetic field, as the lines are twisted and tangled to an extreme degree by the violent second collapse. Along the disk midplane, there also seems to be a significant amount of turbulent magnetic eddies, which appear most prominent at later times. These are likely formed as a result of the emergence of spiral

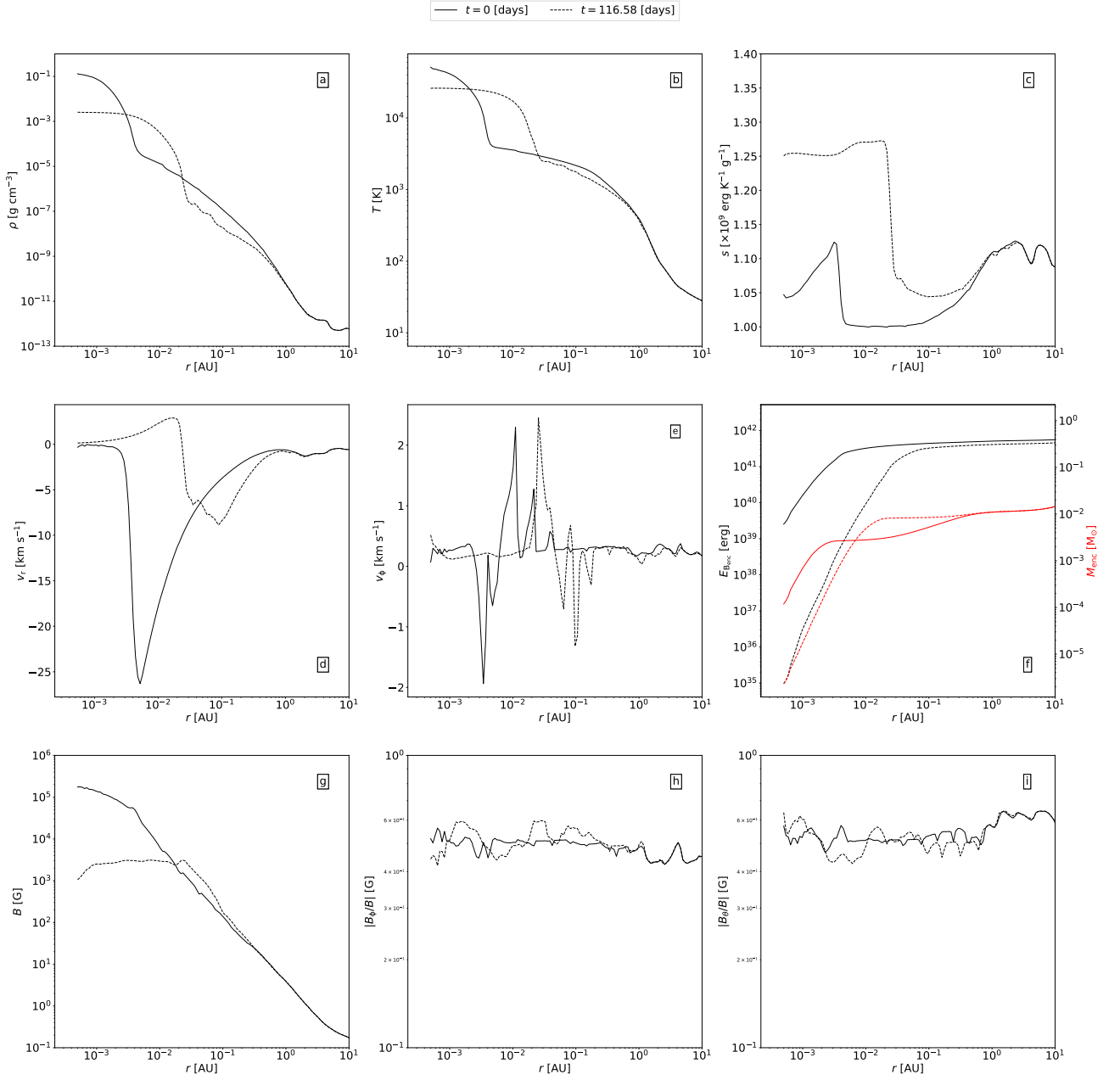


Figure 3.8: A set of measurements of various physical properties of run IMHD at protostellar birth ($t = 0$, solid lines) and $t \approx 117$ days later (dotted lines). These are averages in spherical bins, and show the gas density (panel a), temperature (panel b), entropy (panel c), radial and azimuthal velocity (panels d and e), magnetic field intensity (panel g), and the azimuthal and meridional components of the magnetic field, normalized by its magnitude (panels h and i). Panel (f) displays the enclosed magnetic energy (black lines) and the enclosed mass (red lines) as a function of spherical radius.

waves (see Figs. 3.6 and 3.7), which create significant turbulent motion within the disk. In essence, the turbulent eddies show that the magnetic field is at places confined within a tube-like structure which crosses the disk midplane, and hence showcases a

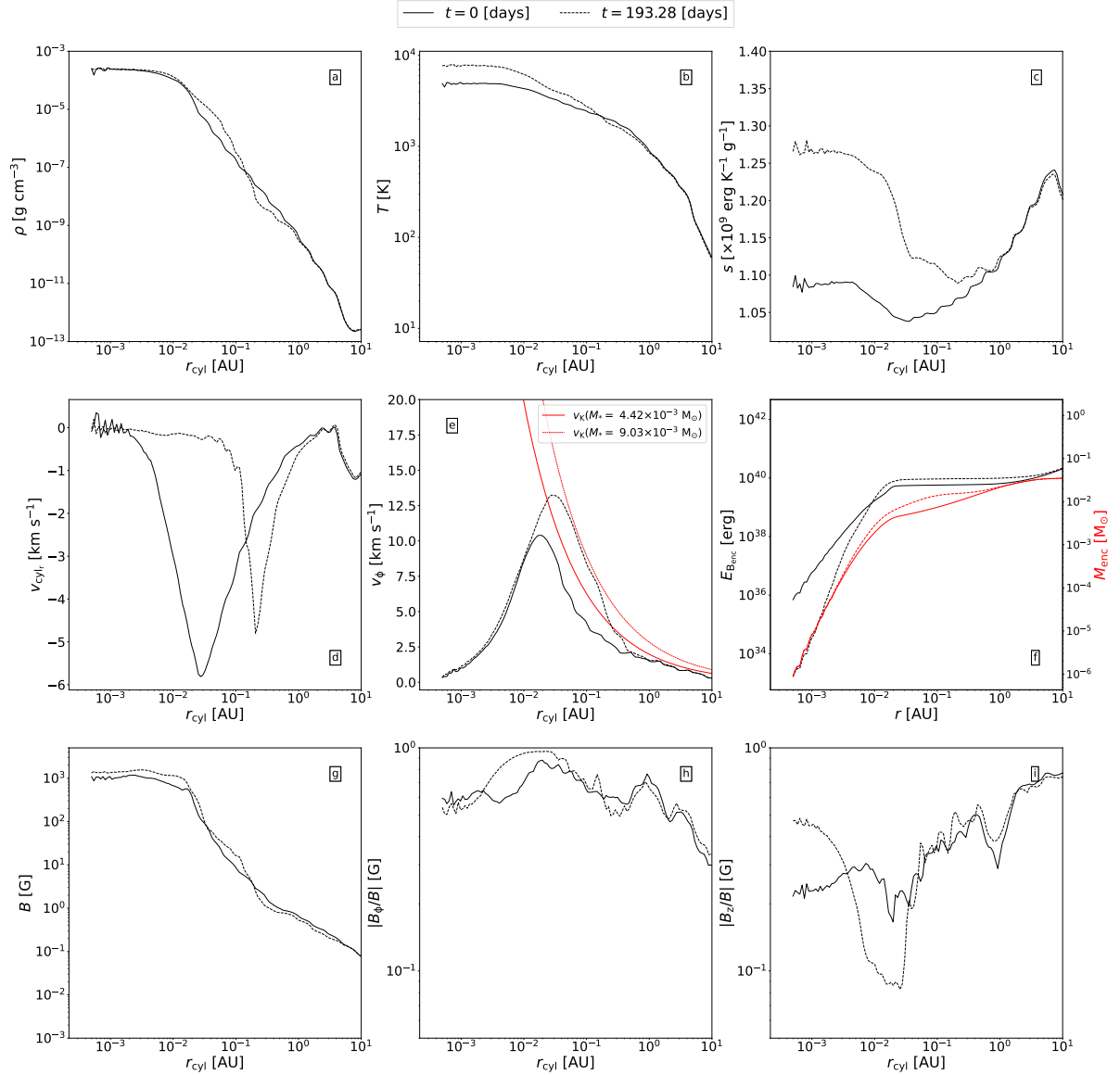


Figure 3.9: A set of measurements of various physical properties of run NIMHD. These were done in cylindrical radial bins, in which only cells belonging to the midplane, defined as $z \in [-2.5; 2.5] \times 10^{-2}$ AU, were used. Solid lines are measurements done at $t = 0$ (corresponding to the moment of protostellar birth), and dotted lines are measurements done ≈ 190 days later. Panel (a), (b), and (c) display respectively the gas density, temperature, and specific entropy. Panels (d) and (e) display the gas' (cylindrical) radial and azimuthal velocity. The red curves in panel (e) display the Keplerian velocity computed with the protostar's mass at a given snapshot. Panels (g), (h), and (i) display the magnetic field strength, its toroidal component, and its vertical component. The toroidal and vertical components are normalized by the total magnetic field strength. Panel (f) displays the enclosed magnetic energy (black lines) and the enclosed mass (red lines) as a function of spherical radius.

significant poloidal component within the disk. We also note the spiral structure of the magnetic field intensity within the star-disk system. In [Wurster et al. \(2022\)](#), it is claimed that the Hall effect is responsible for the creation of this spiral structure, however our results show here that the Hall effect is not necessary to form it.

Interestingly, in the edge-on view of panels (h-j), we see what appears to be a dipolar field in the western half of the star-disk system, where magnetic field streamlines originating from the southern pole of the protostar loop back into its northern pole, however we are unsure as to why the feature appears only in the western half.⁶ Outside the star-disk system, the magnetic field lines are mostly vertical and they thread the two bodies, showcasing the poloidal nature of the magnetic field in these regions. The plasma β decreases in the polar regions over time due to the depletion of material in these regions as the second collapse proceeds ([Ahmad et al. 2024](#)), which in turn causes a reduction in thermal pressure support. The disk's surface also appears to have a plasma $\beta \approx 1$, and the velocity vector field streamlines indicate that a considerable amount of material is advected toward the protostar from the upper layers of the disk, as reported previously in the MHD run of [Lee et al. \(2021\)](#) and the hydro runs of [Ahmad et al. \(2024\)](#). Despite this, we see no outflow or high velocity jet developing, as the velocity vector field streamlines in panels (p-t) are pointing towards the protostar, thus indicating infall. Any such outflows are likely to occur at much later times, when the polar reservoir of gas is significantly depleted and the plasma β in these regions drop to very small values. This once again confirms the results of [Wurster & Lewis \(2020b\)](#), which found that turbulence in the initial dense cloud core significantly delays the onset of jets and outflows. This is likely due to the absence of coherent magnetic field lines, which significantly hinders the onset of jets and outflows.

With regards to the spatial distribution of the magnetic field within the star-disk system, we unsurprisingly see that the central region containing the protostar has the strongest field strength, reaching $\approx 5 \times 10^3$ G. In accordance with [Wurster et al. \(2022\)](#) higher resolution runs, we witness spiral structures in magnetic field strength throughout the star-disk system.

In panels (h) and (i) of [Fig. 3.9](#), quantitative measurements of B_ϕ and B_z are provided. The cylindrical radial velocity displayed in panel (d) allows one to locate the accretion shock, which manifests itself as a strong discontinuity.⁷ Firstly, at $t = 0$, the toroidal component is the dominant one within the protostar. However, at $t \approx 191$ days, the poloidal component is significantly built up and it becomes stronger than its toroidal counterpart. At larger radii (i.e., within the circumstellar disk), the opposite occurs: we see a build-up of the toroidal component of the magnetic field whereas the poloidal component is significantly reduced. In panel (f), the black lines display the enclosed magnetic energy within the (spherical) radius r , which is computed as:

$$E_{B_{\text{enc}}} = \frac{1}{2} \int_0^r B^2 r^2 dr . \quad (3.10)$$

We see that the innermost regions of the system lose magnetic energy over time. In these regions, the gas recovers the ideal MHD limit and flux freezing holds, with

⁶We believe this feature is likely transient, as it is not as evident at later times.

⁷The asymmetrical distribution of matter in the equatorial regions caused by the disk's eccentricity dilutes the azimuthal average and causes v_{cyl} to diffuse.

$B \propto \rho^{2/3}$. Since the density within said regions remains somewhat constant, their loss of magnetic energy is due to an outward advection of material, as the protostar exceeds breakup velocity and begins shedding its surface material (Ahmad et al. 2024).

We now turn to describing the magnetic field structure of run IMHD (Fig. 3.11). Here, at $t = 0$ (panels a and f), we see an extreme pinching of the magnetic field lines as a result of the second gravitational collapse. In addition, the field lines outside the protostar (lime contour) are almost entirely radial, with virtually no toroidal component present. However, as in Ahmad et al. (2023), we find strong turbulent motion within the protostar.⁸ This causes all magnetic field components within the protostar to reach a similar strength, a fact that is particularly evident in panels (h) and (i) of Fig. 3.8. Surrounding the protostar, we once again witness the spherical structure described earlier. Here, we see that this structure displays stronger magnetic field strengths than its surroundings, thus driving the plasma β down to considerably lower values. This allows the gas to reach considerably higher values of magnetic pressure, which creates a secondary shock front upstream of the protostellar shock front (the velocity vector field streamlines are shown in panels f-j). In doing so, this structure acts as a sort of "cocoon" for the protostar. We also see in this figure that the current sheets protruding from the protostellar surface have a plasma $\beta \approx 1$, and the gas seems to be dragged along them toward the protostar.

Figure 3.8 offers some insight regarding the nature of the "cocoon". Panel (a) of this figure displays the radial density profile, which exhibits a drop of approximately two orders of magnitude in the central regions following a hydrostatic bounce (Ahmad et al. 2023). This in turn causes a drop in B (panel g), however we also notice a region of increased magnetic field strength outside the protostellar surface, hinting at an outward advection of magnetic flux. This is more evident in panel (f), where the black lines display $E_{B_{\text{enc}}}$. Here, at $t = 0$, we see that the region containing most of the enclosed mass (i.e., the region in which M_{enc} ceases to increase) coincides with the region containing most of the enclosed magnetic energy. However, this is no longer the case at $t \approx 117$ days, showing that magnetic energy was advected outwards. The small discrepancy in $E_{B_{\text{enc}}}$ seen at $r = 1$ AU between the two snapshots is caused by turbulent reconnection, which destroys magnetic flux.

One final result we would like to report is in regards to the slices shown in panels (f-j) of Fig. 3.11, displaying the plasma β of the gas. In Vaytet et al. (2018), it is reported that the protostar formed under the ideal MHD approximation is a magnetically supported object. However, we show here that all gas downstream of the protostellar accretion shock (lime contour) has a plasma $\beta \approx 1$ or $\gg 1$. This means that the protostar is an entirely thermally supported body. In addition, we have overlaid on these slices the velocity vector field streamlines, which show that no outflow or jet is being launched by the protostar. This is to be expected given the immensely unstructured nature of the magnetic field in this run, which exhibits no coherent toroidal component.

⁸This is better seen in later times displayed in the figure.

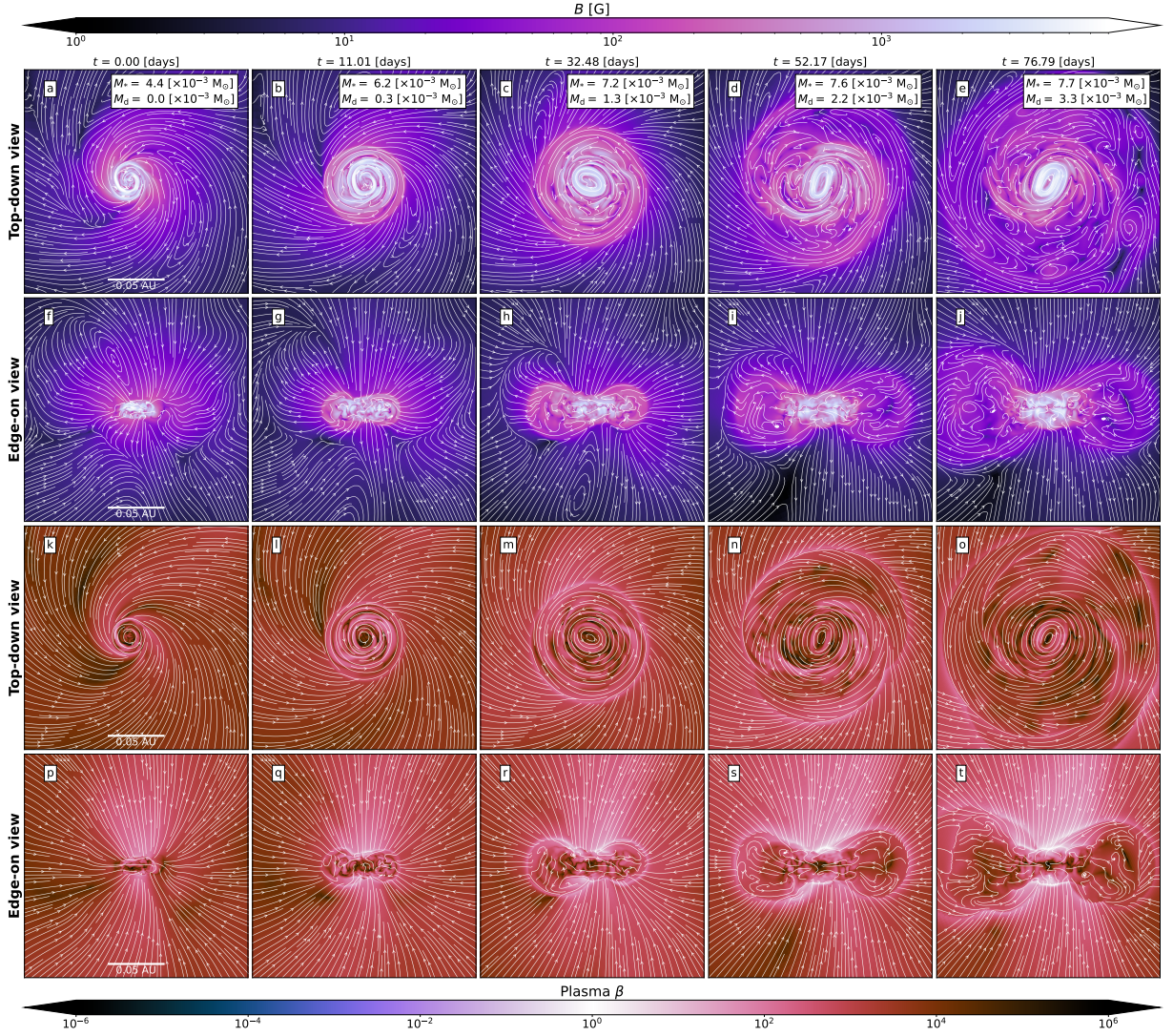


Figure 3.10: The magnetic field of run NIMHD: a set of slices displaying the magnetic field strength (top two rows) and plasma β (bottom two rows) in a top-down (first and third rows) and edge-on (second and fourth rows) view. The white curves in the first two rows (panels a-j) are magnetic field streamlines, whereas in the last two rows (panels k-t) they are velocity vector field streamlines. Each column represents a different time, where $t = 0$ corresponds to the moment of protostellar birth. The mass of the protostar and its circumstellar disk is displayed in the top right corner of panels a-e. The scale bars in the first column apply to all other columns as well.

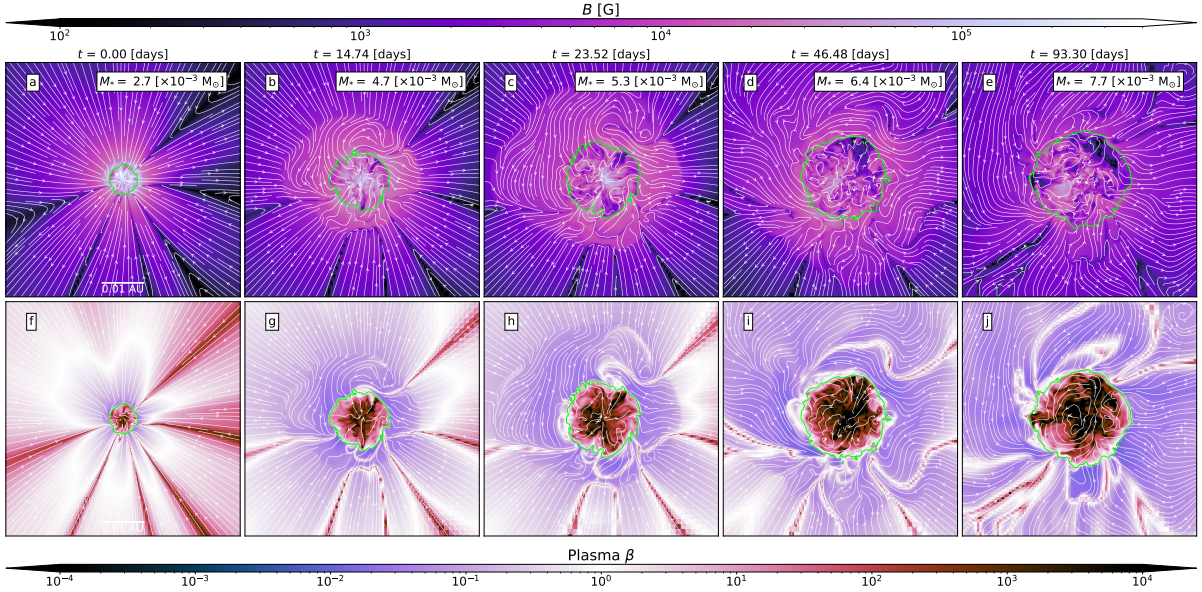


Figure 3.11: Same as Fig. 3.10, but for run IMHD. Since there is virtually no rotation in this run, the slices are done along the z axis only. The lime-colored contour designates the stellar surface.

3.4.6 Disk expansion: comparison with the hydro case

We now turn to providing a quantitative description of the evolution of the circumstellar disk over time. Since its structure appears to be qualitatively similar to the hydro case (a large and highly flared disk), we will compare it to that obtained in run G2 of Ahmad et al. (2024), whose initial conditions and numerical setup are the same (notwithstanding the absence of magnetic fields). In addition, since Fig. 3.10 has shown that the plasma $\beta \gg 1$ within the disk, we expect a similar evolution to the hydro case but with a notable increase in torquing owing to the strong magnetic field strength. To this end, we display in Fig. 3.12 the mass, radius, specific angular momentum, and density at the equatorial shock front of the circumstellar disk in run NIMHD (black curves) and in the hydro run of Ahmad et al. (2024) (orange curves, hereafter run HD). We also leverage the information provided in Fig. 3.13, which displays the column density maps of runs NIMHD and HD (resp. panels a and b) and their corresponding radial profiles (panel c). The velocity profiles are shown in panel d.

Additionally, since it is of interest to advance the simulation in time, we have branched run NIMHD at ≈ 0.4 years following protostellar birth and run a parallel simulation with a reduced $\ell_{\max} = 24$, which significantly alleviates the computational cost of the simulation. The properties of the disk in this run, labeled "NIMHD_LR", are shown in the green curves of Fig. 3.12. The overlap between the black and green curves shows that its results are realistic enough for physical interpretations.

We first begin by studying the temporal evolution of the disk's radius with respect

to time (panel e). We note the fact that although the evolution in the initial 0.3 years are identical in the HD and NIMHD runs, they later diverge as run NIMHD exhibits a slower disk growth in time owing to strong torque mechanisms. Nevertheless, the plot displaying disk's mass with respect to its radius (panel b) shows that the HD and NIMHD runs exhibit a similar evolutionary trend, although run NIMHD's curves appears more oscillatory than that of run HD. These oscillations are caused by strong spiral waves within the disk in run NIMHD, which carry a significant amount of material inwards and in doing so, also reduce the mass of the disk when compared to run HD. Indeed, at a given disk radius, run NIMHD displays a smaller mass than run HD. These spiral waves are likely caused by magnetic torques, which reduce the gas's centrifugal support against gravity, and they warp the disk, as can prominently be seen in panel (a) of Fig. 3.13. Indeed, when measuring the mass-weighted mean magnetic field strength within a radius of 10 AU, the toroidal component outweighs all others by an order of magnitude (≈ 270 G, compared to ≈ 60 G for the cylindrical radial component and ≈ 25 G for the vertical field). This means that the magnetic field is mostly parallel to the disk midplane, which has been shown to cause prominent spiral waves to develop (Joos et al. 2012; Li et al. 2013; Hennebelle et al. 2020a). In contrast, the hydro disk (panel b) remains circular. This causes higher column densities in the outer regions of the disk in run HD than in run NIMHD (panel c). Finally, the higher protostellar mass causes faster rotation in the innermost regions of the disk in run NIMHD (panel d), and its velocity profile closely approaches the Keplerian profile (dashed line), whereas in run HD the velocity profile is super-Keplerian owing to the disk's self-gravity.

The prominence of magnetic braking is further displayed in panel (c) of Fig. 3.12, which shows the protostellar mass as a function of disk radius. Here, we see that although run HD quickly reaches a plateau in disk mass, run NIMHD shows a rapidly growing protostar. Note that the specific angular momentum of the disk, shown in panel (d), is the same in both runs and scales as $\sqrt{R_d}$.⁹ In panel (f), we show the specific angular momentum of the gas within 1 AU, computed both outside of the disk (dotted lines) and within it (solid and dashed lines). This figure shows that the disk in run NIMHD is accreting from a reservoir of gas containing a smaller amount of angular momentum than run HD, which shows that magnetic braking occurred before the gas was accreted onto the disk.

The reduced mass of the disk in run NIMHD when compared to run HD also manifests itself in a reduced disk density. More specifically, when measuring the density at the disk's equatorial shock front, we see that it is consistently lower than in run HD. Although we could not integrate the calculations to the point where the disk reaches the commonly used sink accretion radius of 1 AU, the current trend seen (and extended by run NIMHD_LR) seems to indicate that the equatorial shock density in our MHD simulations will be lower than in the hydro case.

⁹This scaling is a consequence of the disk's Keplerian velocity profile.

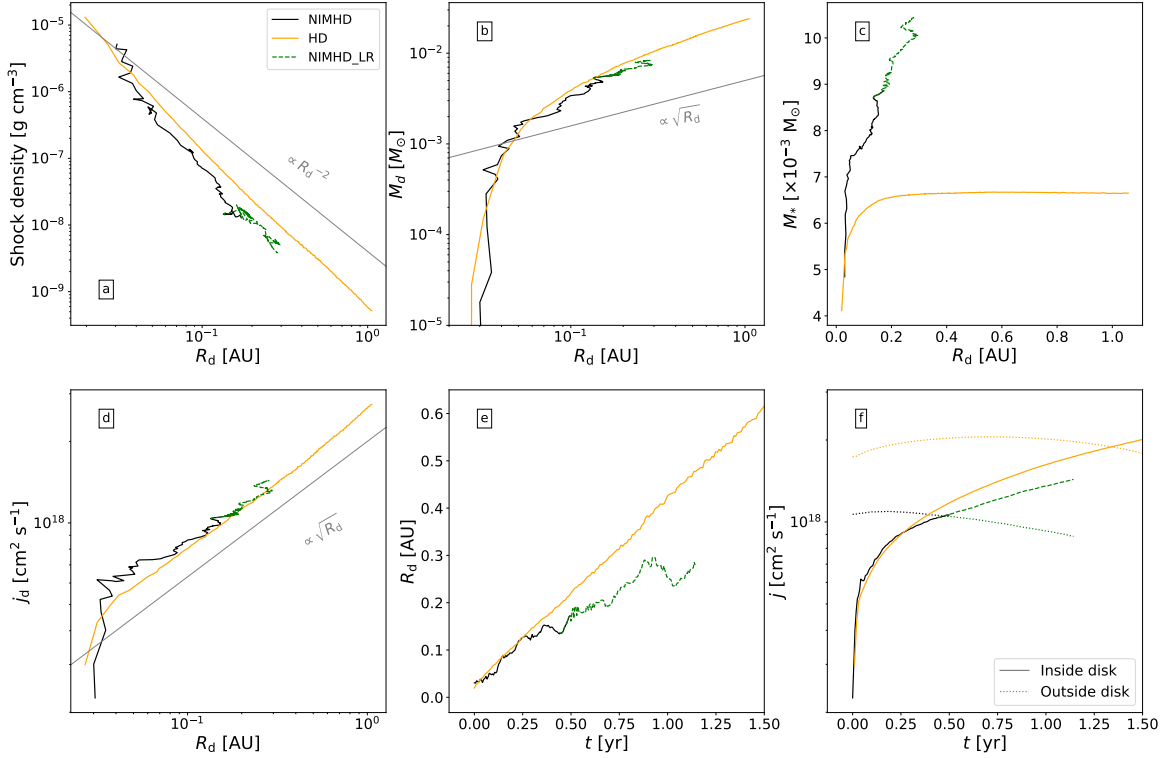


Figure 3.12: Temporal evolution of the circumstellar disk of run NIMHD (black curves), compared with its hydro counterpart (orange curves). The green curves are a zoom-out branched from run NIMHD and run at a lower resolution with $\ell_{\max} = 24$ (see Sec. 3.4.2). Panels (a), (b), (c), and (d) display as a function of the disk’s equatorial radius R_d respectively the density measured at the disk’s equatorial shock front, the mass of the disk, the mass of the protostar, and the disk’s specific angular momentum. Panel (e) displays R_d as a function of time, where $t = 0$ marks the moment of birth of the disk. Panel (f) displays the specific angular momentum of the gas within 1 AU found inside the disk (solid and dashed lines) and outside the disk (dotted lines) as a function of time since the birth of the disk.

3.4.7 Discussions

The results presented here, most notably those of run NIMHD, are noteworthy for a number of outstanding issues in stellar formation theory. We discuss their implications in this wider context below.

The angular momentum problem

In Ahmad et al. (2024), we reported on the birth of the circumstellar disk as a result of the breakup of the protostar and the subsequent vigorous radial expansion of the disk in time. Run NIMHD has confirmed that such a phenomenon is reproduced even in the presence of magnetic fields, provided that magnetic resistivities are accounted

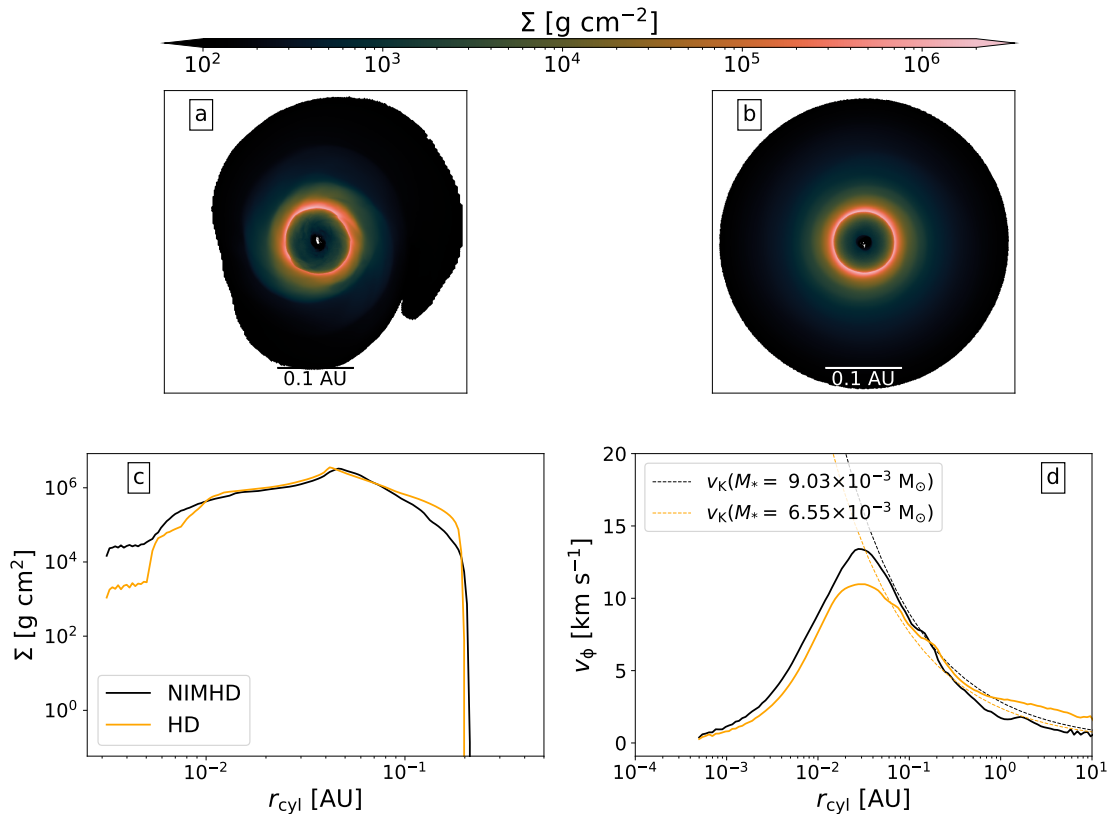


Figure 3.13: A structural and kinematic comparison between run NIMHD and HD (resp. black and orange curves in panels c and d). Panel (a) displays column density maps for run NIMHD at our final simulation snapshot, which is ≈ 190 days after protostellar birth. Panel (b) displays the equivalent map for run HD, at a moment in time where its radius is comparable to that of run NIMHD (≈ 0.2 AU). Only cells belonging to the disk were used in the making of these maps. The second row displays the radial profiles of column density (panel c) and azimuthal velocity (panel d). The dashed lines in panel (d) display the Keplerian velocity computed with the protostar’s mass.

for. In the literature, Machida & Matsumoto (2011); Vaytet et al. (2018); Machida & Basu (2019); Bhandare et al. (2024) have also reported on the birth of a circumstellar disk that rapidly expands to larger radii. What these simulations seem to show is that a paradigm shift is required in our understanding of the angular momentum problem. Indeed, long has it been implicitly implied in stellar formation theory that angular momentum must be lost *during* the collapse so as to prevent the protostar from ever reaching breakup velocity (Bodenheimer 1995). What our comparison between run IMHD and NIMHD shows is that should angular momentum transport by magnetic fields be so efficient so as to prevent the protostar from ever reaching breakup velocity, then no circumstellar disk forms: it is the very fact that the protostar achieves rotational breakup that allows for circumstellar disks to form in our simulations. As such, whatever angular momentum transport process is responsible for spinning down the protostar to the $\sim 10 - 15\%$ of breakup velocity as is observed in YSOs (Rebull et al.

2004; Herbst et al. 2007) is acting on longer timescales than the free-fall time of the cloud.

The magnetic flux problem

As mentioned previously, YSOs are consistently found to have \sim kG magnetic field strengths, with the earliest measurements being those of class I sources. Since the current observational data points towards a fossil field hypothesis, this value serves as a constraint for second collapse calculations, as they must implant a kG field strength in the protostar. Our results, and those of Vaytet et al. (2018); Machida & Basu (2019); Wurster et al. (2022), show that such a value may be achieved and maintained following the second collapse. The uncertainty here lies in the short horizon of predictability of second collapse calculations, as they must be able to simulate $\sim 10^5$ years following protostellar birth in order to make an adequate comparison with observations. As such, in order to advance the field, better constraints on magnetic field strengths both at dense core scales through the measurement of linearly polarized dust emissions, or at much smaller scales through Zeeman broadening, are required in class 0 sources. However, these measurements are immensely difficult to undertake owing to the optical depths involved.

In the meantime, a significant amount of theoretical modeling is required in order to describe the evolution of the protostellar magnetic field in conjunction with pre-stellar evolution models, however simplified such models are. Numerically costly simulations such as those presented in this thesis are immensely helpful in obtaining the initial properties and structure of the protostar, however their short horizon of predictability precludes them from definitively solving the magnetic flux problem.

The missing mass problem

Current observational surveys of class 0/I disks estimate their masses to be $\sim 10^{-3} - 10^{-2} M_{\odot}$ (e.g., Tobin et al. 2020), which appears to be an order of magnitude lower than those predicted by theoretical studies ($\sim 10^{-2} - 10^{-1} M_{\odot}$, e.g., Machida & Matsumoto 2011; Tsukamoto et al. 2015b,a; Tomida et al. 2015; Masson et al. 2016; Lee et al. 2021, see the discussions in Tsukamoto et al. 2023a). Notwithstanding the uncertainties involved in current observational methods (Tung et al. 2024), this discrepancy has been dubbed the "missing mass problem". It has also been shown that current subgrid models aiming to emulate the sub-AU regions by replacing them with a sink particle show a strong sensitivity to the parameters chosen in said model. In Hennebelle et al. (2020b), the sink accretion threshold was shown to particularly affect the disk mass, with lower accretion thresholds leading to lower disk masses. The results of Ahmad et al. (2024) seemed to show that the sink accretion threshold used in most simulations is a factor ≈ 40 lower than it should be, thus exacerbating the missing mass problem as that would mean that disks are in reality much more massive in simulations. Although the disk in run NIMHD has not reached the commonly chosen sink accretion radius of 1 AU yet, an extrapolation of the trend it shows would lead to an accretion threshold

that is an order of magnitude lower than that in the hydro run of [Ahmad et al. \(2024\)](#). This is owing to magnetic torques that significantly increase the protostellar mass in comparison to hydro runs, and thus leads to a disk with lower density. As such, we cautiously conclude that omitting magnetic fields produces a disk density at 1 AU that is too computationally expensive to be emulated in sub-grid models, despite the fact that the plasma β of the gas is well above unity in the magnetized runs. A more thorough understanding of the disk properties thus not only requires one to study the nascent protostar and disk in concert, but also requires better constraints on dust resistivities that dictate the amount of angular momentum inherited by the disk.

In any case, this issue highlights the need for better comparisons between observations and theoretical models, as [Tung et al. \(2024\)](#) has shown that current observational estimates of disk masses are inadequate and fail to predict the current sizes when compared to simulations.

The importance of adequate dust resistivity tables

An important uncertainty in our current understanding of sub-AU regions is the dust resistivity used. The MRN dust size distribution is increasingly called into question by studies that account for dust coagulation and fragmentation during protostellar collapses ([Lebreuilly et al. 2023](#); [Kawasaki & Machida 2023](#); [Tsukamoto et al. 2023a](#); [Vallucci-Goy et al. 2024](#); [Bhandare et al. 2024](#)). Our simulations are undertaken under the assumption that Ohmic resistivity is, as predicted by dust-size distribution studies, negligible. This leads to stronger magnetic fields within the first Larson core, which in turn increases the magnetic field intensity in the nascent protostar and circumstellar disk. As a result, magnetic torques drive considerably more material towards the protostar, thus leading to a reduced disk density.

As such, the properties of the newly-formed circumstellar disk are highly sensitive to the dust resistivities that dictate the magnetic field intensity inherited from larger spatial scales. A better understanding of the sub-AU regions is predicated upon accurate dust resistivity tables, which requires a better understanding of the dust size distribution. This will ultimately be achieved by longer wavelength observations of star-forming regions in order to probe optically thin dust emissions, as well as by advances in our theoretical modelling of dust growth and fragmentation during protostellar collapses.

3.4.8 Conclusion

In the present study, we have undertaken radiative MHD simulations describing the collapse of a turbulent and gravitationally unstable dense cloud core of $1 M_{\odot}$ to stellar densities, both under the ideal MHD approximation and under the non-ideal approximation in which we have accounted for ambipolar diffusion. Our stringent refinement criterion, as well as high spatial resolution, allowed us to describe the nascent protostar and circumstellar disk with unprecedented resolution. We push the calculations as far as possible in time following protostellar birth in order to study the nascent disk's expansion, reaching ≈ 0.5 years in our high resolution run and ≈ 1.2 years in our lower

resolution run. Our results may be summarized as follows:

- (i) In accordance with previous results in the literature, the ideal MHD approximation leads to very efficient magnetic braking which prevents the formation of a circumstellar disk (i.e., the magnetic braking catastrophe). The results of the second gravitational collapse in this run is a central, spherical accumulation of material that leads to the birth of a spherical protostar, with current sheets protruding from the stellar surface. The properties of the nascent protostar are similar to those obtained in spherically symmetrical hydrodynamical runs such as [Ahmad et al. \(2023\)](#). The protostar also exhibits strong turbulent motion.
- (ii) When accounting for ambipolar diffusion, the efficacy of magnetic braking is significantly reduced toward higher density gas, which allows the nascent protostar to reach breakup velocity and shed its surface material to form a circumstellar disk around it. The protostar is embedded within its circumstellar disk, whose birth and early evolution is qualitatively similar to the RHD runs presented in [Ahmad et al. \(2024\)](#), as the plasma β within the disk far exceeds unity. The nascent disk vigorously expands in the radial direction. This result carries implications for the angular momentum problem, as we show that the protostar must achieve breakup velocity in order to form a circumstellar disk. As such, angular momentum transport processes must spin-down the protostar on considerably longer timescales than the free-fall time of the dense cloud core.
- (iii) The magnetic field implanted in the protostar at birth has a strength of $\sim 10^5$ G in the ideal MHD run, which then continuously reduces to $\sim 10^4$ G as the simulation progresses. In the non-ideal MHD run, the implanted field has a strength of $\sim 10^3$ G which is maintained throughout the simulations duration. Since current observational surveys of magnetic fields in YSOs favor the fossil field hypothesis, this puts the non-ideal MHD simulation in agreement with them.
- (iv) The structure of the magnetic field in both runs is, as expected, vastly different. In the ideal MHD run, the magnetic field lines are tangled by the turbulent motion within the protostar, and the azimuthal and meridional components (B_ϕ and B_θ) reach similar strengths. In addition, we see a magnetically supported structure resembling a cocoon upstream of the accretion shock. In the non-ideal MHD run, the magnetic field is mostly toroidal (B_ϕ), although a notable poloidal component (B_z) threads the star-disk system. Within the protostar, the poloidal component is significantly built-up over time.
- (v) Owing to our use of turbulent initial conditions, the magnetic field mostly loses its coherence and we see no outflows or jets in both runs. In the non-ideal MHD run however, the plasma β in the polar regions upstream of the protostellar accretion shock is continuously being reduced. Coupled with the fact that a poloidal component is being built-up in the protostar, this may lead to the launching of an outflow at later times.
- (vi) When comparing the nascent disk in the non-ideal MHD run to its hydro counterpart (from [Ahmad et al. 2024](#)), we note a reduced disk density. This is caused

by the presence of strong magnetic and gravitational torques within the disk, which transport a significant amount of material towards the protostar. This also causes the protostar to become more massive than in the hydro case. The reduced disk density in turn causes a reduced density at the disk's equatorial shock front, which is an important measure for studies of global disk evolution that leverage sink particles to advance the simulations in time. The trends seen in our simulations indicate that the shock front's density at 1 AU in the magnetized case is an order of magnitude lower than that reported in the hydro runs of [Ahmad et al. \(2024\)](#). As such, we cautiously conclude that current subgrid models used in the literature are valid.

Although we may learn a lot from expensive simulations like the ones presented in this study, it is important to note that their horizon of predictability is rather short and their results may not be applicable throughout the entirety of the class 0 phase. The importance of magnetic fields in dictating the transport of material within the circumstellar disk also highlights the need for better constraints on the dust-size distribution, which requires significant observational and theoretical efforts.

3.5 Miscellaneous results

Herein, we present miscellaneous results obtained during the thesis that, although are interesting, do not warrant a publication on their own.

3.5.1 Merger of First Larson cores

Thanks to our use of adaptive mesh refinement when simulating the collapse of turbulent dense cloud cores, we could resolve the formation of multiple first Larson cores that had formed as a result of the fragmentation of a gravo-turbulent filament, or through gravitational instabilities in circumstellar disks. Some of these first Larson cores would then merge together. To our knowledge, no paper in the literature reports on this, and so we would like to present it in this manuscript.

To this end, we display in [Fig. 3.14](#) a merger of two first Larson cores which formed within the same gravo-turbulent filament. This run was a radiative MHD simulation in which ambipolar diffusion is accounted for. It possesses the same numerical setup as run NIMHD presented in [Sec. 3.4](#), but with a turbulent Mach number of $\mathcal{M} = 1$ instead of 0.4.

The top row of the figure displays the column density of the gas, which shows two first Larson cores that appear spherical in morphology. These two bodies approach each other as they travel within their host filament over a few dozen years, and they begin their merger in panel (b). In panels (c-e), we see a notable increase in rotational velocity as the first Larson core that resulted from the merger appears significantly more flattened than its progenitor cores. As a result of the increase in rotational velocity, the magnetic field lines are dragged along by the gas, which builds up a significant toroidal component. As a result of this, we witness in panels (i) and (j) the onset of a low velocity outflow ($\approx 2 \text{ km s}^{-1}$). Events like these allow for the first Larson core to accumulate material faster than by simply accreting the surrounding gas, and hence would lead to a faster second gravitational collapse.

3.5.2 Multigroup simulations

In appendix C of [Ahmad et al. \(2023\)](#), a simulation accounting for multigroup radiative transfer was carried out. The simulation accounted for 4 radiative groups: radio, infrared, ultra-violet/visible, and X-rays (see table C.1 of [Ahmad et al. 2023](#) for the frequency ranges of each group).

The simulation, carried out in spherical symmetry, failed to yield any meaningful physical differences to its gray counterpart, and its added computational cost was deemed unworthy given the similarities. However, the simulations presented in [Ahmad et al. \(2024\)](#) show that the structure and behavior of the radiative shock front changes significantly when a disk forms around the second Larson core. As such, I carried out a similar multigroup simulation accounting for angular momentum in the initial dense core, with the goal of studying the radiative behavior of the star-disk system using a

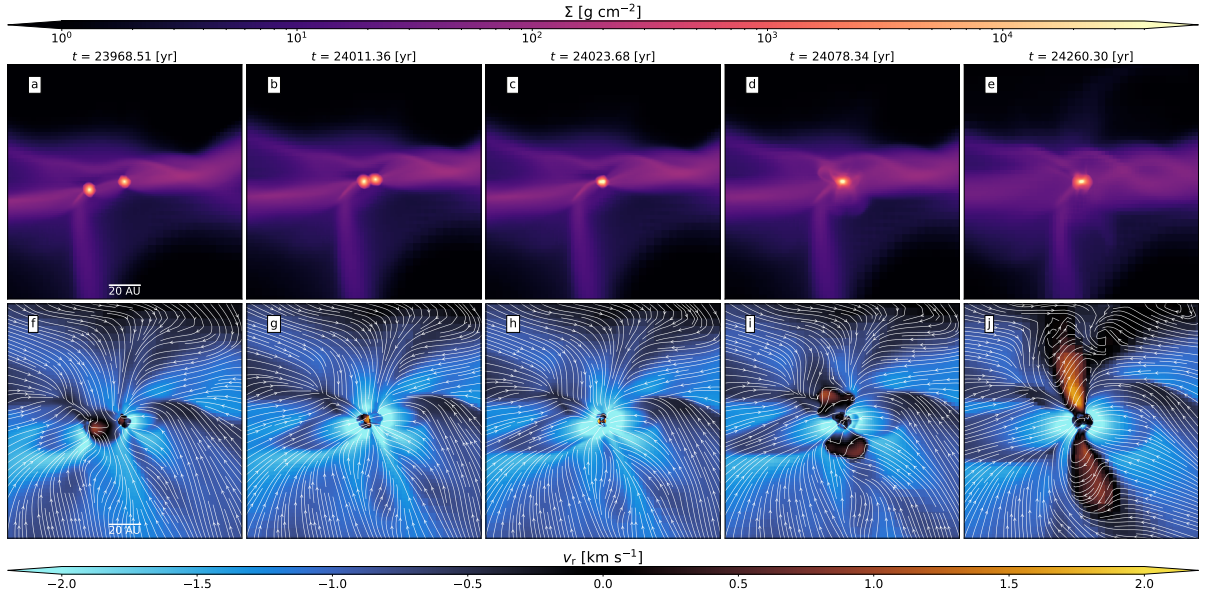


Figure 3.14: A merger of two first Larson cores within a gravo-turbulent filament. Each column represents a different time, where $t = 0$ corresponds to the beginning of the simulation. The first row (panels a-e) displays the gas column density. The second row (panels f-j) displays a radial velocity slice across the center of the scene, with velocity vector field streamlines displayed in white.

more realistic radiative transfer description. This simulation had the same setup as the gray FLD run G2 of [Ahmad et al. \(2024\)](#), with the only difference being the number of radiative groups described.

The resulting disk properties as compared to the gray run are presented in [Fig. 3.15](#), which shows the mass-radius relationship of the circumstellar disk. The figure shows that the multigroup run once again fails to yield any meaningful differences to its gray counterpart. The reasons for this can be seen in [Fig. 3.16](#), which shows that the radiative energies of the star-disk system are completely dominated by the infrared group. The UV/visible group, although producing photons at protostellar scales, has its radiation quickly reabsorbed by the gas and re-emitted at infrared wavelengths. Most UV/visible photons escape along the polar density cavity, where they are re-processed in the infrared. As such, the multigroup run yields slight differences in radiative energy to its gray counterpart along the polar regions (see panels f and h of [Fig. 3.16](#)), but not within the disk owing to the high optical depths involved.

To conclude on this experiment, we have shown that the multigroup run’s added computational burden is not justified given its similarities to the gray run.

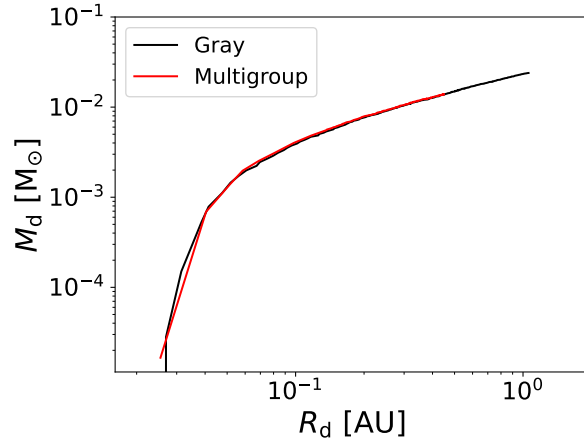


Figure 3.15: The mass-radius of the circumstellar disk: a comparison between a gray simulation (black line) and a multigroup run (red line).

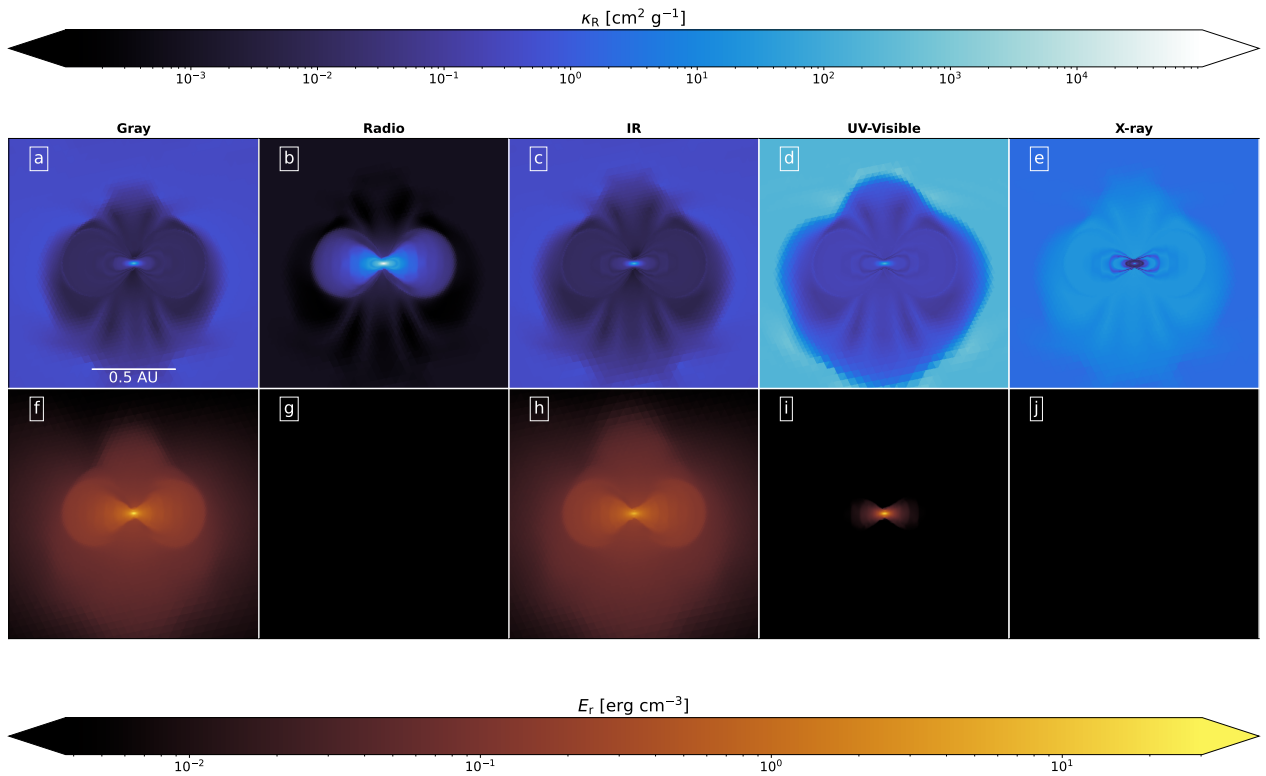


Figure 3.16: Slices across the center of the computational domain, displaying the Rosseland mean opacities (top row) and radiative energies (bottom row) for the multigroup run (second column and onward) and the gray run (first column). The slices are shown at a moment in time where both runs have a similar disk radius of ≈ 0.45 AU.

Chapter 4

Conclusion and Perspectives

During the past three years, I had the opportunity to carry out state-of-the-art research in which I simulated the birth and early evolution of stars and circumstellar disks. This was made possible by decades of algorithmic and code development in `RAMSES`, which allowed for the inclusion of multiple highly non-linear physical processes to be included in our calculations. In addition, observational breakthroughs in the field have allowed astronomers to lift the veil on the physical processes behind the genesis of stars and circumstellar disks, thus furthering our understanding of the progenitors of planetary systems. Despite being mired in the heavy numerical cost of the simulations, these were pushed beyond many previous studies in the literature, both in terms of effective spatial resolution and in physical timescales described, allowing me to study the nascent structures in the simulations with unprecedented detail.

Having been immersed in a field of research in which rapid progress is being made, I was able to place my work in a detailed scientific context, and links between a number of physical scales and processes could be drawn. In [chapter 1](#), some outstanding issues of star formation pertaining to the work done during this thesis are presented. The goal of the thesis was to provide a rigorous analysis of the second gravitational collapse, a critical step in the collapse of a dense cloud core that leads to the formation of a protostar.

In [chapter 2](#), the theoretical background required to model the birth of stars, as well as the numerical techniques used in our `RAMSES` simulations are presented. In addition to these, I share some of the expertise I've gathered in analysing the simulation's results, both in terms of performative boosts through parallelization, and in terms of data visualization techniques that greatly aid in extracting a physical interpretation of the simulation's results. The latter proved particularly useful during my thesis, and some common 3D visualization and 3D printing techniques are presented.

In [chapter 3](#), the results of my simulations are presented. These have so far led to two publications in the *Astronomy & Astrophysics* journal during my thesis, with a third one in preparation. The first publication studies the nascent protostar in spherical symmetry using radiative hydrodynamics (RHD), and the second paper studies the collapse while including angular momentum in the initial dense cloud core. This

led to the formation of circumstellar disks shortly following protostellar birth, and the two object’s interaction and joint evolution was studied in detail. Finally, a suite of simulations including magnetic fields, both under the ideal and non-ideal MHD approximation, are presented in this chapter. These led to significantly different gas dynamics than in the hydrodynamical runs.

Below, I summarize the main insights offered by my work on some of star formation’s outstanding issues. Some perspectives of future works are also presented.

4.1 The insights gained by second collapse calculations

On the protostar itself

The main benefit of simulating the second collapse is the fact that one may self-consistently model the birth of the protostar itself. Our first publication simulated the collapse of a dense core in spherical symmetry, thus leading to the birth of a protostar which we studied in-depth. The protostar is formed through hydrostatic equilibrium once ample thermal pressure support is built following the resumption of adiabatic heating when most H_2 molecules are dissociated.

By virtue of our very high resolution (20 – 2000 cells per Jeans length), we have discovered an instability in the first hours of protostellar birth: as the gas is in the process of establishing a hydrostatic equilibrium following the completion of H_2 dissociation, small perturbation in the flow are exponentially amplified, leading to strong turbulent motion within the protostar that is then sustained by accretion. This confirms a previous finding by [Bhandare et al. \(2020\)](#), who reported that the protostar is turbulent at birth despite its radiative stability. The turbulent transport of material within the protostellar interior leads to very efficient entropy mixing, which drives the entropy gradient to zero, thus allowing said interior to be modelled by a polytrope. This result goes against the common paradigm in which the onset of turbulent motion within the protostar coincides with deuterium ignition.

On the luminosity problem

Following the birth of the protostar, its radius swells owing to the subcritical nature of its shock front; the immense optical depths upstream of the accretion shock prohibit the protostar from radiating away the gargantuan amounts of kinetic energy it is accreting (the mass accretion rate is $\sim 10^{-1} M_\odot$). This results in the addition of significant amounts of high entropy content to the protostellar interior (i.e., *hot accretion*), thus causing the increase in radius. The strong turbulent motion within the protostar aids in regulating its swelling. Although the radiative efficiency of the protostar is initially well below unity, as accretion progresses, the density upstream of the shock front reduces, which allows for an increasing amount of radiation to escape. In our second paper, which accounts for angular momentum in the initial dense core, material gathers in a disk, which creates a density cavity along the polar regions. This cavity enables

the protostar to shine into an optically thin medium, thus allowing its shock front to reach supercriticality in ~ 2 years and radiate away the vast majority of the incoming accretion energy. Owing to the physical analysis of the shock front in our simulations, the ad-hoc assumption of radiative supercriticality used in pre-stellar evolution models to conform their predictions to observations, has now been proven to be true.

On the formation of circumstellar disks and the angular momentum problem

In our simulations accounting for angular momentum in the initial dense cloud core, we find that the protostar reaches breakup velocity in a matter of months. This means that the centrifugal force along the equatorial regions exceeds the radial component of gravity, thus causing material to be advected outward due to excess angular momentum. Thus, a smooth transition from mainly thermally to centrifugally supported gas is witnessed, and a circumstellar disk is formed as a result. The accretion shock envelops both the protostar and the disk, and the two act as a continuous fluid system. As the nascent protostar and disk accrete material from their surroundings, the former vigorously spreads radially. The disk's temperature, compounded by the subcritical nature of its accretion shock, causes it to flare-up significantly along the vertical extent, and it completely engulfs the protostar in volume. This occurs independently of the initial conditions at larger spatial scales, with a small spread caused by the turbulent initial conditions.

When accounting for magnetic fields in our calculations, drastically different results are obtained, depending on whether the ideal or non-ideal MHD approximation is used. In the former, magnetic braking is efficient to such an extent that almost no angular momentum remains in the gas at higher densities. This prevents the protostar from ever reaching breakup speeds, and thus no circumstellar disk forms. On the other hand, when ambipolar diffusion is included in our calculations, the efficiency of magnetic braking is reduced and breakup velocities are achieved following protostellar birth, similarly to our hydrodynamical runs. This allows a circumstellar disk to form, however its properties are slightly different than in our RHD runs. Indeed, although the thermal to magnetic pressure ratio far exceeds unity in the disk, magnetic torques carry a significant amount of material inward, thus leading to a more massive protostar. In the RHD runs, the mass of the disk exceeds that of the protostar up to seven-fold, whereas it is comparable to it in our MHD runs. In both cases, the disk's self-gravity has a significant influence on its dynamics.

On larger scales, we find that an outer, more extended disk of radius ~ 10 AU may form around the first Larson core. The existence of this disk prior to the second collapse mainly depends on the first core's lifetime, which is very sensitive to the physics at play, as well as to the initial angular momentum budget of the dense core. For instance, in our RHD runs, increasing the strength of the initial turbulent velocity vector field yielded more extended first core lifetimes, which lead to the formation of disks around the latter. When including magnetic fields, angular momentum is efficiently extracted from low density gas, and no outer disk formed. Following the second collapse, the circumstellar disk that formed as a result of protostellar breakup quickly expands in radius and merges with the more extended outer disk should the latter exist.

On the magnetic flux problem

Current observational surveys of magnetic field intensities in young stellar objects, although lackluster in sample size, report a mean value of ~ 1 kG and favor the fossil field hypothesis of the origin of magnetic fields in stars. This means that the latter is carried over from protostellar birth, and thus second collapse calculations can provide insights on how such an implantation occurs. Under the ideal MHD approximation, the magnetic field implanted in the protostar has a strength of $\sim 10^5$ G and shows a decreasing trend thereafter, owing to an outward advection of material, and to turbulent reconnection caused by the strong turbulent motion within the protostar.

However, in the simulation in which we include ambipolar diffusion, the implanted field has a strength of $\sim 10^3$ G that is thereafter maintained. In order to implant such a field in the protostar, the magnetic flux within the dense core is diffused by ambipolar diffusion to a value of ~ 0.1 G within the first Larson core. After the second collapse, the ideal MHD limit is recovered as all dust particles are sublimated and the gas begins to ionize, and half the mass content of the protostar is shown to be under ionized form. A field strength of ~ 0.1 G within the first core also seems to be in agreement with paleomagnetic measurements of solar system meteorites, water maser observations in protostellar jets, and in broad agreement with observational surveys of disk sizes.

On jets and outflows

The use of turbulent initial conditions in our MHD runs greatly reduced the coherence of the initial magnetic field threading the dense core. Although an interchange instability developed in the ideal MHD run which caused material to move outward in the radial direction, this was not the case in the non-ideal run. On stellar scales, we report no jets or outflows in both the ideal and non-ideal runs, however in the latter simulation the plasma β of the gas is continuously reducing over time in the polar regions. As a strong poloidal component is simultaneously being built-up, this could in the future lead to launching of a jet. Turbulence in the initial dense core thus has a delaying effect on the launching of jets and outflows.

On the importance of adequate dust resistivities

Our non-ideal MHD simulation has shown the importance of including ambipolar diffusion in the calculations. Should the latter not be included, the protostar would be devoid of a circumstellar disk as it never reaches breakup velocity, and it would have a magnetic field strength far in excess of what is observed in YSOs.

In addition to this, the properties of the nascent disk in our MHD runs are affected by the efficient torque mechanisms the magnetic field provides. These transport a considerable amount of material towards the protostar, which in turn reduce the disk's density. This result has repercussions on larger scale simulations that wish to simulate much longer timescales, as they omit the inner-most sub-AU region in favor of a sink particle that accretes material from its surroundings with a given accretion threshold.

Currently, when measuring what said accretion threshold should be, we find an order of magnitude difference between the RHD and MHD runs, thus emphasizing the need for adequate dust resistivities, as they dictate the magnetic field strength inherited by the structures formed following the second collapse and by extension, the disk density.

4.2 Perspectives

Throughout this thesis, exciting results were obtained that pushed the boundaries of our understanding of stars and circumstellar disks. Each new simulation offered insights on certain physical processes and phenomena, but new questions always rose. Below, I summarize the work that can be done as a follow-up to this thesis.

Unravelling the origin of magnetic fields in stars

In addition to needing a better understanding of dust resistivities, and by extension the dust size distribution, understanding the origins of magnetic fields in stars will require a collaborative effort in which knowledge from pre-main sequence stellar evolution, dynamo theory, and stellar formation theory are combined. This will allow us to form a cohesive theory modelling the implantation of a magnetic field in the protostar, and how the former behaves during the latter's subsequent evolution towards the main sequence.

From the point of view of second collapse calculations, detailed constraints on the magnetic field intensity and structure according to the initial conditions of the collapse can be provided, in addition to the interior structure of the protostar following its birth. These can then be used by a pre-main sequence evolutionary model to describe the evolution of the interior structure of the protostar, and direct numerical simulations can then be applied to discern whether the protostar is conducive to dynamo action. However, the magnetic field inherited by the protostar at birth strongly depends on the coupling of the field to the gas during the collapse. Knowledge of the strength of this field is predicated upon a detailed knowledge of dust grains, and at the scale of dense cores, variations in dust emissivities are observed (Maury et al. 2022). Large millimeter interferometers such as NOEMA and ALMA are currently being used to produce more detailed observations of dust emissions, and their observations may aid in obtaining better constraints on the dust properties in star-forming regions. In the meantime, simulations with non-MRN dust resistivities may be run with the goal of performing a parameter space exploration, and their results may be used to infer the possible range of magnetic field strengths implanted in the protostar.

Simulating longer timescales

The main drawback of second collapse calculations is the short horizon of predictability they provide. Indeed, owing to a combination of stringent timestepping constraints and poor load-balancing, the simulations can only describe the first few years following the

birth of the protostar. In order to significantly increase the simulated physical time, sub-grid models such as the use of a sink particle need to be used. However, finding the correct parameters, namely the accretion threshold and the radiative efficiency, not to mention any mechanical feedback effects from the protostar such as jets, needs a careful calibration to self-consistent simulations.

In this respect, it would also be useful to use a different, more modern code to carry out the simulations. Graphical Processor Units (GPUs) have become increasingly available, and the computing power they offer can be leveraged to gain performance boosts. As such, a number of MHD AMR codes are now developed on hybrid frameworks, capable of running on both GPUs and CPUs, such as **Dyablo** that is currently in development at CEA. In addition, a stripped-down version of RAMSES, aptly called **mini-RAMSES**, is currently in development. Its main difference to the main code is the manner in which communications are handled; load balancing occurs much more frequently, with significant gains in performance for setups possessing a large ℓ_{\max} . A second collapse calculation using this code might be of interest.

Predicting disk properties using machine learning: the ORACLE project

Due to the challenges associated with observing class 0 and I disks embedded in optically thick star-forming cores, current observational techniques fail to recover the correct disk mass when measuring dust continuum emissions (Tung et al. 2024). In order to better link observations with theoretical models, I had the idea to build a database of synthetic observations of disks, extracted from nearly ~ 100 TB of simulation data available at CEA. This would allow me to train a convolutional neural network on a dataset containing $\sim 10^5$ synthetic observations after adequate data-augmentation techniques (e.g., different points of view and different ages) are applied, which may then infer the disk mass from observational data.

The simulations at CEA have a wide variety of initial conditions, physical setups, and numerical resolutions, thus allowing me to create a varied dataset on which to train the neural network. Once a disk is found and extracted in a simulation, a radiative transfer tool (such as RADMC-3D for instance) may be applied to obtain an intensity map, and an instrument simulator (such as CASA) may then produce the full synthetic observation.

Ultimately, the goal would be to make such a dataset available to the wider astronomical community using the **Galactica** service.

Appendix A

Useful code snippets

Snippet 1: Extracting a uniform grid from a simulation subdomain using Osyris

```
1 from tqdm import tqdm
2 import os
3 dx = .1*osyris.units("au")
4 resolution = min(256,
5     ↪ int(dx.to("au").magnitude/data["amr"]["dx"].min().to("au").values))
6 grid_res = (resolution, resolution, resolution)
7 dz = dx # extent to be covered in z axis by volume stack
8 scalar = "density"
9 unit = "g/cm^3"
10 data["hydro"][scalar] = data["hydro"][scalar].to(unit)
11 # computing z coordinates for the stack
12 z_coord =
13     ↪ osyris.Array(values=np.linspace((center.z-dz/2).to("au").values,
14         (center.z+dz/2).to("au").values, grid_res[-1]), unit="au")
15 # proceed to data gathering
16 volume_stack = []
17 for i in tqdm(range(grid_res[-1]), ascii=True, desc="Creating volume
18     ↪ stack for scalar field '{}'.format(scalar)):
19     # first select new image center
20     new_xc = center.x; new_yc = center.y; new_zc = z_coord[i]
21     new_im_center = osyris.Vector(x=new_xc.to("au").values,
22         y=new_yc.to("au").values,
23         z=new_zc.to("au").values,
24         unit="au")
25     plane = osyris.map({"data":data["hydro"][scalar]},
26         origin=new_im_center, dx=dx, direction="z",
27         ↪ resolution=grid_res[0], plot=False)
28     volume_stack.append(plane.layers[0]['data'].data)
29 # scalar fields get stacked on first axis
30 np.save(dump_path, np.stack(volume_stack, axis=0))
```


Snippet 2: Extracting a uniform grid from a simulation subdomain using Osyris. Application to a vector field

```

1 dx = .1*osyris.units("au")
2 resolution = min(256*2,
  ↪ int(dx.to("au").magnitude/data["amr"]["dx"].min().to("au").values))
3 # grid resolution in (x,y,z)
4 grid_res = (resolution, resolution, resolution)
5 dz = dx # extent to be covered in z axis by volume stack
6 field = "B_field"
7 units = "G"
8
9 # computing z coordinates for the stack
10 z_coord =
  ↪ osyris.Array(values=np.linspace((center.z-dz/2).to("au").values,
11                               (center.z+dz/2).to("au").values, grid_res[-1]),
12              unit="au")
13
14 fields = ["x", "y", "z"]
15 volume_stack = []
16 for i,u in enumerate(fields):
17     vs = []
18     data["hydro"]["{}_{}".format(field, u)] =
  ↪ getattr(data["hydro"][field], u).to(units)
19     for i in tqdm(range(grid_res[-1]), ascii=True, desc="Creating
  ↪ volume stack for vector field '{} ({}
  ↪ component)".format(field, u)):
20         # first select new image center
21         new_xc = center.x; new_yc = center.y; new_zc = z_coord[i]
22         new_im_center = osyris.Vector(x=new_xc.to("au").values,
23                                     y=new_yc.to("au").values,
24                                     z=new_zc.to("au").values,
25                                     unit="au")
26
27         plane = osyris.map({"data":data["hydro"]["{}_{}".format(field,
  ↪ u]}},
28                           origin=new_im_center, dx=dx, direction="z",
  ↪ resolution=grid_res[0], plot=False)
29         vs.append(plane.layers[0]['data'].data)
30     volume_stack.append(vs)
31 # vector fields get stacked on the last axis.
32 np.save(dump_path, np.stack(volume_stack, axis=-1))

```

Snippet 3: Loading a scalar field onto a Pyvista uniform grid

```

1 import pyvista as pv
2 stack = np.load(path)
3 xmin = -100; xmax = 100;
4 ymin = -100; ymax = 100;
5 zmin = -100; zmax = 100;
6 dx = (xmax-xmin)/stack.shape[0]
7 dy = (ymax-ymin)/stack.shape[1]
8 dz = (zmax-zmin)/stack.shape[2]
9 # Create the grid on which PyVista can deposit the data
10 grid = pv.ImageData()
11 grid.dimensions = stack.shape
12 grid.origin = [xmin, ymin, zmin]
13 grid.spacing = [dx, dy, dz]
14 grid.point_data['scalar'] = stack.flatten(order='C')

```

Snippet 4: Loading a vector field onto a Pyvista uniform grid

```

1 vec = np.load(path)
2 vx = vec[..., 0]
3 vy = vec[..., 1]
4 vz = vec[..., 2]
5 vectors = np.column_stack((vx.ravel(), vy.ravel(), vz.ravel()))
6 # Create the grid on which PyVista can deposit the data
7 grid = pv.ImageData()
8 grid.dimensions = stack.shape
9 grid.origin = [xmin, ymin, zmin]
10 grid.spacing = [dx, dy, dz]
11 grid[field_name] = vectors
12 grid[field_name+" (norm)"] = np.linalg.norm(vectors, axis=1)

```

Snippet 5: Volume render of a scalar field with interactive opacity using Pyvista

```

1 def update_opacity_distance(val):
2     vr.GetProperty().SetScalarOpacityUnitDistance(val)
3     return
4
5 p = pv.Plotter()
6 vr = p.add_volume(grid, scalars="scalar", cmap="magma", clim=[-4, -1],
7     opacity="linear", mapper="gpu",
8     opacity_unit_distance=grid.length / 25,
9     shade=True, scalar_bar_args={"interactive":True})
10 f = lambda val: vr.GetProperty().SetScalarOpacityUnitDistance(val)
11 p.add_slider_widget(rng=[0, grid.length/4],
12     ↪ callback=update_opacity_distance, title="Opacity Distance")
13 p.show_grid()

```

Snippet 6: Static streamline placement using Pyvista

```

1 grid_vertices = [ # starting point coordinates
2                 [(xmax,ymin,zmax), (xmin,ymax,zmin)], # diagonal
3                 [(xmax,ymin,zmin), (xmin,ymax,zmax)], # diagonal
4                 [(xmax,ymax,zmin), (xmin,ymin,zmax)], # diagonal
5                 [(xmin,ymin,zmin), (xmax,ymax,zmax)], # diagonal
6                 [(0,0,zmin), (0,0,zmax)], # cross sectional
7                 [(xmin,0,0), (xmax,0,0)], # cross sectional
8                 [(0,ymin,0), (0,ymax,0)], # cross sectional
9                 ]
10 nstream_packets = [i for i in range(len(grid_vertices))]
11
12 for i in nstream_packets:
13     stream, src = grid.streamlines(field_name, return_source=True,
14     ↪ n_points=500, pointa=grid_vertices[i][0],
15     ↪ pointb=grid_vertices[i][1], progress_bar=True,
16     ↪ integration_direction="both")
17     stream_list.append(stream)
18
19 p = pv.Plotter()
20 for stream in stream_list:
21     strm1 = stream.tube(radius=0.0015)
22     plotter.add_mesh(strm1, color="w")
23
24 p.show()

```

Snippet 7: Interactive streamline placement using Pyvista

```

1 def simulate(pointa, pointb):
2     streamlines = grid.streamlines(field_name,
3     ↪ n_points=300, max_steps=500, pointa=pointa, pointb=pointb,
4     ↪ integration_direction='both', terminal_speed=0, max_time=20
5     )
6     p.add_mesh(streamlines, name='streamlines', line_width=2,
7     ↪ render_lines_as_tubes=True, cmap='turbo', scalars=field_name+"
8     ↪ (norm)")
9
10 p = pv.Plotter()
11 p.add_line_widget(callback=simulate, use_vertices=True)
12 p.show()

```

Snippet 8: Iso-contouring using Pyvista

```

1 contours = grid.contour(np.arange(rhomin, rhomax+1, .5))
2 smooth_contour = contours.smooth(n_iter=2000, progress_bar=True)
3 p = pv.Plotter()
4 p.add_mesh(smooth_contour, opacity=.4, clim=[rhomin, rhomax], cmap="viridis")
5 p.show()

```

Snippet 9: ROI render using Pyvista

```
1 rho = np.load(path+"rho.npy")
2 pos = np.load(path+"pos.npy")
3 c = # numpy boolean array
4 points = np.transpose([pos[0][c],pos[1][c],pos[2][c]])
5 cloud = pv.PolyData(points)
6 cloud['log(rho) [g/cm^3]'] = np.log10(rho[c])
7 p = pv.Plotter()
8 p.add_mesh(cloud, cmap="magma", clim=None, opacity="linear")
9 p.show()
```


Bibliography

- Ahmad, A., González, M., Hennebelle, P., & Commerçon, B. 2023, *A&A*, **680**, [A23](#)
- Ahmad, A. A., González, M., Hennebelle, P., & Commerçon, B. 2024, *arXiv e-prints*, [arXiv:2404.14496](#)
- Allen, A., Li, Z.-Y., & Shu, F. H. 2003, *ApJ*, **599**, [363](#)
- Andersson, B. G., Lazarian, A., & Vaillancourt, J. E. 2015, *ARA&A*, **53**, [501](#)
- André, P. 2002, in *EAS Publications Series*, Vol. 3, *EAS Publications Series*, ed. J. Bouvier & J.-P. Zahn, [1–38](#)
- Andre, P., Ward-Thompson, D., & Barsony, M. 1993, *ApJ*, **406**, [122](#)
- Appenzeller, I. & Tscharnuter, W. 1975, *A&A*, **40**, [397](#)
- Arce, H. G., Shepherd, D., Gueth, F., et al. 2007, in *Protostars and Planets V*, ed. B. Reipurth, D. Jewitt, & K. Keil, [245](#)
- Armitage, P. J. 2011, *ARA&A*, **49**, [195](#)
- Audard, M., Ábrahám, P., Dunham, M. M., et al. 2014, in *Protostars and Planets VI*, ed. H. Beuther, R. S. Klessen, C. P. Dullemond, & T. Henning, [387–410](#)
- Badnell, N. R., Bautista, M. A., Butler, K., et al. 2005, *MNRAS*, **360**, [458](#)
- Balbus, S. A. & Hawley, J. F. 1991, *ApJ*, **376**, [214](#)
- Banerjee, R. & Pudritz, R. E. 2006, *ApJ*, **641**, [949](#)
- Baraffe, I., Chabrier, G., & Gallardo, J. 2009, *ApJL*, **702**, [L27](#)
- Baraffe, I., Elbakyan, V. G., Vorobyov, E. I., & Chabrier, G. 2017, *A&A*, **597**, [A19](#)
- Baraffe, I., Vorobyov, E., & Chabrier, G. 2012, *ApJ*, **756**, [118](#)
- Bate, M. R. 1998, *The Astrophysical Journal*, **508**, [508](#)
- Bate, M. R. 2010, *MNRAS*, **404**, [L79](#)
- Bate, M. R. 2011, *MNRAS*, **417**, [2036](#)

-
- Bate, M. R., Tricco, T. S., & Price, D. J. 2014, *MNRAS*, **437**, 77
- Beichman, C. A., Myers, P. C., Emerson, J. P., et al. 1986, *ApJ*, **307**, 337
- Bergin, E. A. & Tafalla, M. 2007, *ARA&A*, **45**, 339
- Bhandare, A., Commerçon, B., Laibe, G., et al. 2024, *arXiv e-prints*, [arXiv:2404.09257](https://arxiv.org/abs/2404.09257)
- Bhandare, A., Kuiper, R., Henning, T., et al. 2020, *A&A*, **638**, A86
- Bhandare, A., Kuiper, R., Henning, T., et al. 2018, *A&A*, **618**, A95
- Blandford, R. D. & Payne, D. G. 1982, *MNRAS*, **199**, 883
- Bodenheimer, P. 1995, *ARA&A*, **33**, 199
- Boss, A. P. 1989, *ApJ*, **345**, 554
- Braiding, C. R. & Wardle, M. 2012, *MNRAS*, **427**, 3188
- Brucy, N. & Hennebelle, P. 2021, *MNRAS*, **503**, 4192
- Chabanier, S., Bournaud, F., Dubois, Y., et al. 2020, *MNRAS*, **495**, 1825
- Chabrier, G., Baraffe, I., Allard, F., & Hauschildt, P. 2000, *ApJ*, **542**, 464
- Chabrier, G. & Küker, M. 2006, *A&A*, **446**, 1027
- Chevance, M., Krumholz, M. R., McLeod, A. F., et al. 2023, in *Astronomical Society of the Pacific Conference Series*, Vol. 534, *Protostars and Planets VII*, ed. S. Inutsuka, Y. Aikawa, T. Muto, K. Tomida, & M. Tamura, **1**
- Chieze, J. P. 1987, *A&A*, **171**, 225
- Colman, T., Brucy, N., Girichidis, P., et al. 2024, *arXiv e-prints*, [arXiv:2403.00512](https://arxiv.org/abs/2403.00512)
- Commerçon, B., Debout, V., & Teyssier, R. 2014, *A&A*, **563**, A11
- Commerçon, B., Teyssier, R., Audit, E., Hennebelle, P., & Chabrier, G. 2011, *A&A*, **529**, A35
- Commerçon, B. 2009, *Formation d'étoile : étude de l'effondrement des coeurs prestellaires*, 1 vol. (164 f.), thèse de doctorat dirigée par Chabrier, Gilles et Audit, Edouard Physique Lyon, École normale supérieure (sciences) 2009
- Cowling, T. G. 1945, *Proceedings of the Royal Society of London Series A*, **183**, 453
- Crutcher, R. M. 2012, *ARA&A*, **50**, 29
- Crutcher, R. M. & Kembball, A. J. 2019, *Frontiers in Astronomy and Space Sciences*, **6**, 66
- Dapp, W. B. & Basu, S. 2010, *A&A*, **521**, L56

-
- Dapp, W. B., Basu, S., & Kunz, M. W. 2012, [A&A](#), **541**, [A35](#)
- Dobler, W., Stix, M., & Brandenburg, A. 2006, [ApJ](#), **638**, [336](#)
- Donati, J. F., Bouvier, J., Alencar, S. H., et al. 2019, [MNRAS](#), **483**, [L1](#)
- Dunham, M. M., Allen, L. E., Evans, Neal J., I., et al. 2015, [ApJS](#), **220**, [11](#)
- Dunham, M. M., Stutz, A. M., Allen, L. E., et al. 2014, in *Protostars and Planets VI*, ed. H. Beuther, R. S. Klessen, C. P. Dullemond, & T. Henning, [195–218](#)
- Durney, B. R., De Young, D. S., & Roxburgh, I. W. 1993, [Solar Physics](#), **145**, [207](#)
- Evans, C. R. & Hawley, J. F. 1988, [ApJ](#), **332**, [659](#)
- Evans, Neal J., I., Dunham, M. M., Jørgensen, J. K., et al. 2009, [ApJS](#), **181**, [321](#)
- Ferguson, J. W., Alexander, D. R., Allard, F., et al. 2005, [ApJ](#), **623**, [585](#)
- Fiege, J. D. & Pudritz, R. E. 2000, [MNRAS](#), **311**, [105](#)
- Fischer, W. J., Hillenbrand, L. A., Herczeg, G. J., et al. 2023, in *Astronomical Society of the Pacific Conference Series*, Vol. 534, *Protostars and Planets VII*, ed. S. Inutsuka, Y. Aikawa, T. Muto, K. Tomida, & M. Tamura, [355](#)
- Fischer, W. J., Megeath, S. T., Furlan, E., et al. 2017, [ApJ](#), **840**, [69](#)
- Flores, C., Connelley, M. S., Reipurth, B., & Boogert, A. 2019, [ApJ](#), **882**, [75](#)
- Flores, C., Connelley, M. S., Reipurth, B., Boogert, A., & Doppmann, G. 2024, [arXiv e-prints](#), [arXiv:2405.12451](#)
- Flores, C., Connelley, M. S., Reipurth, B., & Duchêne, G. 2022, [ApJ](#), **925**, [21](#)
- Frisch, U. 1995, *Turbulence. The legacy of A.N. Kolmogorov*
- Fromang, S., Hennebelle, P., & Teyssier, R. 2006, [A&A](#), **457**, [371](#)
- Galli, D., Lizano, S., Shu, F. H., & Allen, A. 2006, [ApJ](#), **647**, [374](#)
- Gaudel, M., Maury, A. J., Belloche, A., et al. 2020, [A&A](#), **637**, [A92](#)
- Godunov, S. K. & Bohachevsky, I. 1959, *Matematičeskij sbornik*, **47(89)**, [47\(89\)](#)
- González, M., Stehlé, C., Audit, E., et al. 2006, [Laser and Particle Beams](#), **24**, [535](#)
- González, M., Vaytet, N., Commerçon, B., & Masson, J. 2015, [A&A](#), **578**, [A12](#)
- Goodman, A. A., Benson, P. J., Fuller, G. A., & Myers, P. C. 1993, [ApJ](#), **406**, [528](#)
- Gray, W. J., McKee, C. F., & Klein, R. I. 2018, [MNRAS](#), **473**, [2124](#)
- Haisch, Karl E., J., Lada, E. A., & Lada, C. J. 2001, [ApJL](#), **553**, [L153](#)
- Harten, A. 1983, [Journal of Computational Physics](#), **49**, [357](#)

-
- Hartigan, P., Frank, A., Foster, J. M., et al. 2011, *ApJ*, **736**, 29
- Hayashi, C. 1961, *Publications of the ASJ*, **13**, 450
- Hennebelle, P. & Ciardi, A. 2009, *A&A*, **506**, L29
- Hennebelle, P., Commerçon, B., Chabrier, G., & Marchand, P. 2016, *ApJL*, **830**, L8
- Hennebelle, P., Commerçon, B., Lee, Y.-N., & Chabrier, G. 2020a, *ApJ*, **904**, 194
- Hennebelle, P., Commerçon, B., Lee, Y.-N., & Charnoz, S. 2020b, *A&A*, **635**, A67
- Hennebelle, P. & Falgarone, E. 2012, *A&AR*, **20**, 55
- Hennebelle, P. & Fromang, S. 2008, *A&A*, **477**, 9
- Hennebelle, P. & Inutsuka, S.-i. 2019, *Frontiers in Astronomy and Space Sciences*, **6**, 5
- Hennebelle, P. & Teyssier, R. 2008, *A&A*, **477**, 25
- Herbst, W., Eislöffel, J., Mundt, R., & Scholz, A. 2007, in *Protostars and Planets V*, ed. B. Reipurth, D. Jewitt, & K. Keil, 297
- Hosokawa, T. & Omukai, K. 2009, *ApJ*, **691**, 823
- Hueso, R. & Guillot, T. 2005, *A&A*, **442**, 703
- Hull, C. L. H., Plambeck, R. L., Bolatto, A. D., et al. 2013, *ApJ*, **768**, 159
- Jeans, J. H. 1902, *Philosophical Transactions of the Royal Society of London Series A*, **199**, 1
- Johns-Krull, C. M. 2007, *ApJ*, **664**, 975
- Johns-Krull, C. M., Greene, T. P., Doppmann, G. W., & Covey, K. R. 2009, *ApJ*, **700**, 1440
- Johns-Krull, C. M. & Valenti, J. A. 1996, *ApJL*, **459**, L95
- Jones, T. J., Bagley, M., Krejny, M., Andersson, B. G., & Bastien, P. 2015, *AJ*, **149**, 31
- Joos, M., Hennebelle, P., & Ciardi, A. 2012, *A&A*, **543**, A128
- Joos, M., Hennebelle, P., Ciardi, A., & Fromang, S. 2013, *A&A*, **554**, A17
- Kandori, R., Tamura, M., Nagata, T., et al. 2018, *ApJ*, **857**, 100
- Kaviraj, S., Laigle, C., Kimm, T., et al. 2017, *MNRAS*, **467**, 4739
- Kawasaki, Y. & Machida, M. N. 2023, *MNRAS*, **522**, 3679
- Kenyon, S. J., Hartmann, L. W., Strom, K. M., & Strom, S. E. 1990, *AJ*, **99**, 869
- Khokhlov, A. 1998, *Journal of Computational Physics*, **143**, 519

-
- Kirk, J. M., Ward-Thompson, D., & Crutcher, R. M. 2006, *MNRAS*, **369**, 1445
- Klose, S. 1986, *Astrophysics and Space Sciences*, **128**, 135
- Kolmogorov, A. 1941, *Akademiia Nauk SSSR Doklady*, **30**, 301
- Könyves, V., André, P., Men'shchikov, A., et al. 2015, *A&A*, **584**, A91
- Krumholz, M. R., Crutcher, R. M., & Hull, C. L. H. 2013, *ApJL*, **767**, L11
- Kuiper, R., Klahr, H., Beuther, H., & Henning, T. 2010, *ApJ*, **722**, 1556
- Kuiper, R., Klahr, H., Beuther, H., & Henning, T. 2011, *ApJ*, **732**, 20
- Lada, C. J. 1987, in *Star Forming Regions*, ed. M. Peimbert & J. Jugaku, Vol. 115, **1**
- Lada, C. J. & Wilking, B. A. 1984, *ApJ*, **287**, 610
- Larson, R. B. 1969, *MNRAS*, **145**, 271
- Larson, R. B. 1972, *MNRAS*, **157**, 121
- Larson, R. B. 1981, *MNRAS*, **194**, 809
- Lavail, A., Kochukhov, O., Hussain, G. A. J., et al. 2017, *A&A*, **608**, A77
- Lazarian, A. 2007, *Journal of Quantitative Spectroscopy and Radiative Transfer*, **106**, 225
- Lazarian, A. & Vishniac, E. T. 1999, *ApJ*, **517**, 700
- Lebreuilly. 2020
- Lebreuilly, U., Commerçon, B., & Laibe, G. 2020, *A&A*, **641**, A112
- Lebreuilly, U., Hennebelle, P., Colman, T., et al. 2021, *ApJL*, **917**, L10
- Lebreuilly, U., Hennebelle, P., Maury, A., et al. 2024, *A&A*, **683**, A13
- Lebreuilly, U., Vallucci-Goy, V., Guillet, V., Lombart, M., & Marchand, P. 2023, *MNRAS*, **518**, 3326
- Ledoux, P. 1947, *ApJ*, **105**, 305
- Lee, Y.-N., Charnoz, S., & Hennebelle, P. 2021, *A&A*, **648**, A101
- Lesur, G., Flock, M., Ercolano, B., et al. 2023, in *Astronomical Society of the Pacific Conference Series*, Vol. 534, *Protostars and Planets VII*, ed. S. Inutsuka, Y. Aikawa, T. Muto, K. Tomida, & M. Tamura, **465**
- Levermore, C. D. 1984, *Journal of Quantitative Spectroscopy and Radiative Transfer*, **31**, 149
- Li, Z.-Y., Krasnopolsky, R., & Shang, H. 2013, *ApJ*, **774**, 82

-
- Lodato, G. 2007, *Nuovo Cimento Rivista Serie*, **30**, 293
- Lodato, G. & Rice, W. K. M. 2004, *MNRAS*, **351**, 630
- López-Valdivia, R., Sokal, K. R., Mace, G. N., et al. 2021, *ApJ*, **921**, 53
- Lovelace, R. V. E., Li, H., Koldoba, A. V., Ustyugova, G. V., & Romanova, M. M. 2002, *ApJ*, **572**, 445
- Lynden-Bell, D. 1996, *MNRAS*, **279**, 389
- Lynden-Bell, D. & Pringle, J. E. 1974, *MNRAS*, **168**, 603
- Mac Low, M.-M., Klessen, R. S., Burkert, A., & Smith, M. D. 1998, *Physical Review Letters*, **80**, 2754
- Machida, M. N. & Basu, S. 2019, *ApJ*, **876**, 149
- Machida, M. N., Inutsuka, S.-i., & Matsumoto, T. 2006, *ApJL*, **647**, L151
- Machida, M. N., Inutsuka, S.-i., & Matsumoto, T. 2007, *ApJ*, **670**, 1198
- Machida, M. N., Inutsuka, S.-i., & Matsumoto, T. 2008, *ApJ*, **676**, 1088
- Machida, M. N., Inutsuka, S.-I., & Matsumoto, T. 2011, *Publications of the ASJ*, **63**, 555
- Machida, M. N., Inutsuka, S.-i., & Matsumoto, T. 2014, *MNRAS*, **438**, 2278
- Machida, M. N. & Matsumoto, T. 2011, *MNRAS*, **413**, 2767
- Madura, T. I. 2017, *Publications of the Astronomical Society of the Pacific*, **129**, 058011
- Marchand, P., Masson, J., Chabrier, G., et al. 2016, *A&A*, **592**, A18
- Marchand, P., Tomida, K., Commerçon, B., & Chabrier, G. 2019, *A&A*, **631**, A66
- Masson, J., Chabrier, G., Hennebelle, P., Vaytet, N., & Commerçon, B. 2016, *A&A*, **587**, A32
- Masunaga, H. & Inutsuka, S.-i. 2000, *ApJ*, **531**, 350
- Mathis, J. S., Rumpl, W., & Nordsieck, K. H. 1977, *ApJ*, **217**, 425
- Matsumoto, T. & Tomisaka, K. 2004, *ApJ*, **616**, 266
- Maury, A., Hennebelle, P., & Girart, J. M. 2022, *Frontiers in Astronomy and Space Sciences*, **9**, 949223
- Maury, A. J., André, P., Testi, L., et al. 2019, *A&A*, **621**, A76
- McKee, C. F. 1999, in NATO Advanced Study Institute (ASI) Series C, Vol. 540, The Origin of Stars and Planetary Systems, ed. C. J. Lada & N. D. Kylafis, 29

-
- Mellon, R. R. & Li, Z.-Y. 2008, *ApJ*, **681**, 1356
- Mignon-Risse, R., González, M., & Commerçon, B. 2021, *A&A*, **656**, A85
- Mihalas, D. & Mihalas, B. W. 1984, Foundations of radiation hydrodynamics
- Minerbo, G. N. 1978, *Journal of Quantitative Spectroscopy and Radiative Transfer*, **20**, 541
- Miville-Deschênes, M.-A., Murray, N., & Lee, E. J. 2017, *The Astrophysical Journal*, **834**, 834
- Moscadelli, L., Oliva, A., Surcis, G., et al. 2023, *A&A*, **680**, A107
- Moss, D. 2003, *A&A*, **403**, 693
- Mouschovias, T. C. 1985, *A&A*, **142**, 41
- Mouschovias, T. C. & Spitzer, L., J. 1976, *ApJ*, **210**, 326
- Myers, P. C. & Basu, S. 2021, *ApJ*, **917**, 35
- Narita, S., Nakano, T., & Hayashi, C. 1970, *Progress of Theoretical Physics*, **43**, 942
- Norman, M. L., Wilson, J. R., & Barton, R. T. 1980, *ApJ*, **239**, 968
- Offner, S. S. R. & McKee, C. F. 2011, *ApJ*, **736**, 53
- Ohtani, T., Kimura, S. S., Tsuribe, T., & Vorobyov, E. I. 2014, *Publications of the ASJ*, **66**, 112
- Ouyed, R. & Pudritz, R. E. 1997, *ApJ*, **482**, 712
- Paczynski, B. 1978, *Acta Astronomica*, **28**, 91
- Padoan, P., Haugbølle, T., & Nordlund, Å. 2014, *ApJ*, **797**, 32
- Padoan, P. & Nordlund, Å. 1999, *ApJ*, **526**, 279
- Padovani, M., Galli, D., & Glassgold, A. E. 2009, *A&A*, **501**, 619
- Padovani, M., Hennebelle, P., Marcowith, A., & Ferrière, K. 2015, *A&A*, **582**, L13
- Padovani, M., Marcowith, A., Hennebelle, P., & Ferrière, K. 2016, *A&A*, **590**, A8
- Palla, F. & Stahler, S. W. 1991, *ApJ*, **375**, 288
- Palla, F. & Stahler, S. W. 1993, *ApJ*, **418**, 414
- Pineda, J. E., Sipilä, O., Segura-Cox, D. M., et al. 2024, *A&A*, **686**, A162
- Price, D. J. & Bate, M. R. 2007, *MNRAS*, **377**, 77
- Ray, T. P. & Ferreira, J. 2021, *New Astronomy Review*, **93**, 101615

-
- Rebull, L. M., Wolff, S. C., & Strom, S. E. 2004, *AJ*, **127**, 1029
- Robinson, R. D., J. 1980, *ApJ*, **239**, 961
- Roe, P. L. 1986, *Annual Review of Fluid Mechanics*, **18**, 337
- Saigo, K., Tomisaka, K., & Matsumoto, T. 2008, *ApJ*, **674**, 997
- Santos-Lima, R., de Gouveia Dal Pino, E. M., & Lazarian, A. 2012, *ApJ*, **747**, 21
- Saumon, D., Chabrier, G., & van Horn, H. M. 1995, *ApJS*, **99**, 713
- Schneider, N., Bontemps, S., Simon, R., et al. 2011, *A&A*, **529**, A1
- Schönke, J. & Tscharnuter, W. M. 2011, *A&A*, **526**, A139
- Schwarzschild, K. 1906, Nachrichten von der Königlichen Gesellschaft der Wissenschaften zu Göttingen. Math.-phys. Klasse, **195**, 41
- Scoville, N. Z., Yun, M. S., Clemens, D. P., Sanders, D. B., & Waller, W. H. 1987, *ApJS*, **63**, 821
- Seifried, D., Banerjee, R., Pudritz, R. E., & Klessen, R. S. 2012, *MNRAS*, **423**, L40
- Semenov, D., Henning, T., Helling, C., Ilgner, M., & Sedlmayr, E. 2003, *A&A*, **410**, 611
- Shakura, N. I. & Sunyaev, R. A. 1973, *A&A*, **24**, 337
- Shu, F. H. 1977, *ApJ*, **214**, 488
- Sokal, K. R., Johns-Krull, C. M., Mace, G. N., et al. 2020, *ApJ*, **888**, 116
- Solomon, P. M., Rivolo, A. R., Barrett, J., & Yahil, A. 1987, *ApJ*, **319**, 730
- Spitzer, Lyman, J. & Tomasko, M. G. 1968, *ApJ*, **152**, 971
- Spruit, H. C. 2013, *arXiv e-prints*, [arXiv:1301.5572](https://arxiv.org/abs/1301.5572)
- Stahler, S. W. 1983, *ApJ*, **274**, 822
- Stahler, S. W. & Palla, F. 2004, *The Formation of Stars*
- Stahler, S. W., Shu, F. H., & Taam, R. E. 1980, *ApJ*, **241**, 637
- Stamatellos, D., Hubber, D. A., & Whitworth, A. P. 2007, *MNRAS*, **382**, L30
- Stamer, T. & Inutsuka, S.-i. 2018, *ApJ*, **869**, 179
- Sullivan, C. & Kaszynski, A. 2019, *The Journal of Open Source Software*, **4**, 1450
- Tayler, R. J. 1987, *MNRAS*, **227**, 553
- Teysier, R. 2002, *A&A*, **385**, 337

-
- Teyssier, R., Chapon, D., & Bournaud, F. 2010, [ApJL](#), **720**, L149
- Teyssier, R. & Commerçon, B. 2019, [Frontiers in Astronomy and Space Sciences](#), **6**, 6
- Tobin, J. J., Sheehan, P. D., Megeath, S. T., et al. 2020, [ApJ](#), **890**, 130
- Tomida, K., Okuzumi, S., & Machida, M. N. 2015, [ApJ](#), **801**, 117
- Tomida, K., Tomisaka, K., Matsumoto, T., et al. 2013, [ApJ](#), **763**, 6
- Tomisaka, K. 2002, [ApJ](#), **575**, 306
- Toomre, A. 1964, [ApJ](#), **139**, 1217
- Tscharnuter, W. M. 1987, [A&A](#), **188**, 55
- Tscharnuter, W. M., Schönke, J., Gail, H. P., Tieloff, M., & Lüttjohann, E. 2009, [A&A](#), **504**, 109
- Tsukamoto, Y., Iwasaki, K., Okuzumi, S., Machida, M. N., & Inutsuka, S. 2015a, [ApJL](#), **810**, L26
- Tsukamoto, Y., Iwasaki, K., Okuzumi, S., Machida, M. N., & Inutsuka, S. 2015b, [MNRAS](#), **452**, 278
- Tsukamoto, Y. & Machida, M. N. 2013, [MNRAS](#), **428**, 1321
- Tsukamoto, Y., Machida, M. N., & Inutsuka, S.-i. 2023a, [Publications of the ASJ](#), **75**, 835
- Tsukamoto, Y., Maury, A., Commerçon, B., et al. 2023b, in *Astronomical Society of the Pacific Conference Series*, Vol. 534, *Protostars and Planets VII*, ed. S. Inutsuka, Y. Aikawa, T. Muto, K. Tomida, & M. Tamura, 317
- Tsukamoto, Y., Okuzumi, S., Iwasaki, K., Machida, M. N., & Inutsuka, S. 2018, [ApJ](#), **868**, 22
- Tung, N.-D., Testi, L., Lebreuilly, U., et al. 2024, [arXiv e-prints](#), [arXiv:2401.12142](#)
- Umebayashi, T. & Nakano, T. 1990, [MNRAS](#), **243**, 103
- Vallucci-Goy, V., Lebreuilly, U., & Hennebelle, P. 2024, [arXiv e-prints](#), [arXiv:2406.00124](#)
- van der Vorst, H. & Melissen, J. 1990, [IEEE Transactions on Magnetics](#), **26**, 26
- van Leer, B. 1974, [Journal of Computational Physics](#), **14**, 361
- Vaytet, N., Chabrier, G., Audit, E., et al. 2013, [A&A](#), **557**, A90
- Vaytet, N., Commerçon, B., Masson, J., González, M., & Chabrier, G. 2018, [A&A](#), **615**, A5
- Vaytet, N. & Haugbølle, T. 2017, [A&A](#), **598**, A116

-
- Vaytet, N., Tomida, K., & Chabrier, G. 2014, *A&A*, **563**, A85
- Verliat, A., Hennebelle, P., Maury, A. J., & Gaudel, M. 2020, *A&A*, **635**, A130
- Vorobyov, E. I. & Basu, S. 2010, *ApJ*, **719**, 1896
- Vorobyov, E. I. & Basu, S. 2015, *ApJ*, **805**, 115
- Vorobyov, E. I., Skliarevskii, A. M., Elbakyan, V. G., et al. 2019, *A&A*, **627**, A154
- Weiss, B. P., Bai, X.-N., & Fu, R. R. 2021, *Science Advances*, **7**, eaba5967
- Whitehouse, S. C. & Bate, M. R. 2006, *MNRAS*, **367**, 32
- Williams, J. P. & Cieza, L. A. 2011, *ARA&A*, **49**, 67
- Wilson, R. W., Jefferts, K. B., & Penzias, A. A. 1970, *ApJL*, **161**, L43
- Winkler, K. H. A. & Newman, M. J. 1980, *ApJ*, **236**, 201
- Wurster, J., Bate, M. R., & Bonnell, I. A. 2021, *MNRAS*, **507**, 2354
- Wurster, J., Bate, M. R., & Price, D. J. 2018, *MNRAS*, **481**, 2450
- Wurster, J., Bate, M. R., Price, D. J., & Bonnell, I. A. 2022, *MNRAS*, **511**, 746
- Wurster, J. & Lewis, B. T. 2020a, *MNRAS*, **495**, 3795
- Wurster, J. & Lewis, B. T. 2020b, *MNRAS*, **495**, 3807
- Wurster, J., Price, D. J., & Bate, M. R. 2016, *MNRAS*, **457**, 1037
- Xu, W. & Kunz, M. W. 2021, *MNRAS*, **502**, 4911
- Yang, H. & Johns-Krull, C. M. 2011, *ApJ*, **729**, 83
- Yang, H., Johns-Krull, C. M., & Valenti, J. A. 2005, *ApJ*, **635**, 466
- Yang, H., Johns-Krull, C. M., & Valenti, J. A. 2008, *AJ*, **136**, 2286
- Yorke, H. W. & Sonnhalter, C. 2002, *ApJ*, **569**, 846
- Zhao, B., Caselli, P., Li, Z.-Y., & Krasnopolsky, R. 2018, *MNRAS*, **473**, 4868
- Zhao, B., Caselli, P., Li, Z.-Y., et al. 2016, *MNRAS*, **460**, 2050
- Zhao, B., Tomida, K., Hennebelle, P., et al. 2020, *Space Science Reviews*, **216**, 43